



D 2024

THEORETICAL AND NUMERICAL STUDIES OF VISCOELASTIC FLUID FLOWS

ÂNGELA MARGARIDA VERGAS RIBAU

DOCTORAL THESIS SUBMITTED TO THE
FACULDADE DE ENGENHARIA DA UNIVERSIDADE DO PORTO
IN MECHANICAL ENGINEERING

FACULDADE DE ENGENHARIA DA UNIVERSIDADE DO PORTO

Theoretical and numerical studies of viscoelastic fluid flows

Ângela Margarida Vergas Ribau



Doctoral Program in Mechanical Engineering

Supervisor: Alexandre Miguel Prior Afonso

**Co-supervisors: Fernando Manuel Coutinho Tavares de Pinho
Manuel António Moreira Alves**

January, 2024

Theoretical and numerical studies of viscoelastic fluid flows

Ângela Margarida Vergas Ribau

Doctoral Program in Mechanical Engineering

January, 2024

Abstract

Viscoelastic materials, such as polymer melts, polymer solutions and biofluids display complex behaviour described by rheological constitutive models. These models can be classified as differential and/or integral. Differential models are based on partial differential equations and use the local deformation field whereas integral models use direct information from the past history of deformation. Both types have advantages and disadvantages: differential models usually allow a faster numerical solution of the differential equations involved, while integral models are computationally expensive and may lead to error propagation, but otherwise allow a better rheological modelling. A new generation of models that attempts to improve the situation by providing a better description of fluid rheology, while keeping the cost of computations under control, is based on fractional calculus. One such constitutive equation is the generalised Phan-Thien–Tanner (gPTT) model and one contribution from this thesis is in providing semi-analytical and numerical solutions in canonical flows for the purpose of benchmarking. The gPTT viscoelastic model considers the Mittag–Leffler function instead of the classical linear and exponential functions of the trace of the extra-stress tensor and uses two new fitting parameters. The Mittag–Leffler function allows a wider range of variation in the rates of destruction of network junctions of the polymer network, providing additional fitting flexibility. In this work, semi-analytical solutions were developed for Couette–Poiseuille flows (with no-slip and with asymmetric slip), for electro-osmotic flow in microchannels of viscoelastic fluids and in annular flows, and a parametric study was also carried out on the influence of the new parameters of model. The derived solutions allow a better understanding of how a fluid described by this model behaves with the considered flows. These solutions are used to validate the numerical methods used in computational fluid dynamics (CFD) codes.

CFD investigations can produce vast amounts of data that often overwhelm the user while hiding important information. In particular it is important to identify and characterise relevant flow structures, and this is especially expensive under transient flow conditions, where the structures are continuously evolving in space and time. To overcome this problem, the entire dataset can be decomposed into smaller sets and important structures present in the main flow and structures with periodic behaviour, like vortices, can be identified. One way to do it is through model order reduction methods such as the proper orthogonal decomposition (POD) method that is very popular in CFD. POD enables the decomposition of any flow into a infinite set of eigenfunctions or modes, effectively reducing the problem, capturing the essential information using less data and less computational resources. After the analytical studies presented in the first part of this work, the POD method was applied to the flow around two parallel side-by-side cylinders with different radii, where a Newtonian fluid and two non-Newtonian power-law fluids, with $n = 0.7$ and $n = 1.3$, were considered. In addition, the flow past one cylinder of a fluid described by a gPTT model at very low Reynolds number ($Re = 0.01$) and two different Weissenberg numbers ($Wi = 1.2$ and 1.25) were also investigated through the use of POD method. In both studies a reconstruction of the flows was conducted, followed by a frequency analysis of specific modes. Additionally, for the flow past a cylinder, using the POD analysis made for the flow with $Wi = 1.2$, a prediction of the reconstruction of the flow at $Wi = 1.25$ was obtained and compared with the original simulation

at $Wi = 1.25$. The performed analysis showed that the POD method can be used to better identify meaningful flow structures and to obtain new data at different conditions with significantly lower cost.

Resumo

Materiais viscoelásticos, como polímeros fundidos, soluções poliméricas e biofluidos, apresentam um comportamento complexo descrito por modelos reológicos constitutivos. Esses modelos podem ser classificados como diferenciais e/ou integrais. Os modelos diferenciais são descritos pelo uso de equações diferenciais parciais e o campo de deformação local é utilizado, enquanto os modelos integrais usam informação direta da história de deformação. Ambos os tipos têm vantagens e desvantagens: os modelos diferenciais geralmente permitem uma solução numérica mais rápida das equações diferenciais envolvidas, enquanto os modelos integrais são computacionalmente mais demorados e podem levar à propagação de erros, mas por outro lado permitem uma melhor modelação reológica. Uma nova geração de modelos que tenta melhorar a situação, fornecendo uma melhor descrição da reologia dos fluidos, ao mesmo tempo que mantém os cálculos computacionais controlados, é baseada no cálculo fracionário. Uma dessas equações constitutivas é o modelo generalizado de Phan-Thien-Tanner (gPTT) e uma contribuição desta tese é fornecer soluções semi-analíticas e numéricas em escoamentos canônicos para fins de referência. Este modelo considera a função Mittag-Leffler, em vez das funções lineares e exponenciais clássicas, do traço do tensor de tensão e usa dois novos parâmetros de ajuste. A função Mittag-Leffler permite uma maior variação nas taxas de destruição das junções da rede de polímero, proporcionando um ajuste mais flexível. Neste trabalho, foram desenvolvidas soluções semi-analíticas para escoamentos de Couette–Poiseuille (sem escorregamento e com escorregamento assimétrico), para escoamento eletro-osmótico em microcanais de fluidos viscoelásticos e em escoamentos anelares, e foi também realizado um estudo paramétrico sobre a influência dos novos parâmetros do modelo. As soluções obtidas permitem um melhor conhecimento de como um fluido descrito por este modelo se comporta nos escoamentos considerados. Estas soluções podem ser utilizadas para validar os métodos numéricos usados em códigos de dinâmica de fluidos computacional (CFD).

As investigações de CFD podem produzir grandes quantidades de dados que muitas vezes sobrecarregam o utilizador, ao mesmo tempo que ocultam informações importantes. Em particular, é importante identificar e caracterizar estruturas de escoamento relevantes, e isto é especialmente custoso em condições de escoamento transitório, onde as estruturas estão em constante evolução no espaço e no tempo. Para superar este problema, todo o conjunto de dados pode ser decomposto em conjuntos menores e estruturas importantes presentes no escoamento principal e estruturas com comportamento periódico, como vórtices, podem ser identificadas. Uma maneira de o fazer é através de métodos de redução de ordem, como a decomposição ortogonal própria (POD), que é muito popular em CFD. O POD permite a decomposição de qualquer escoamento num conjunto infinito de funções próprias ou modos, reduzindo efetivamente o problema, capturando as informações essenciais usando menos dados e menos recursos computacionais. Após os estudos analíticos apresentados na primeira parte deste trabalho, o POD foi aplicado ao escoamento em torno de dois cilindros paralelos e lado-a-lado com raios diferentes, onde um fluido Newtoniano e dois fluidos não-Newtonianos descritos por um modelo de lei de potência, sendo $n = 0.7$ e $n = 1.3$, foram considerados. Também se analisou o escoamento em torno de um cilindro, de um fluido descrito pelo modelo gPTT em que o número de Reynolds é muito baixo ($Re = 0.01$) e onde foram

considerados dois números de Weissenberg diferentes ($Wi = 1.2$ e 1.25). Em ambos os estudos foi realizada uma reconstrução dos escoamentos, seguida de uma análise de frequência de modos específicos. Adicionalmente, para o escoamento em torno de um cilindro, utilizando a análise realizada com o POD para o escoamento com $Wi = 1.2$, foi obtida uma previsão da reconstrução do escoamento para $Wi = 1.25$ e comparada com a simulação original para $Wi = 1.25$. A análise realizada mostrou que o POD pode ser utilizado para identificar estruturas relevantes do escoamento e obter novos dados em diferentes condições com um custo significativamente menor.

Acknowledgements

Firstly, I would like to express my sincere gratitude to the Portuguese Foundation for Science and Technology (FCT) for their financial support. This acknowledgment extends to various projects, including LA/P/0045/2020 (ALiCE), UIDB/00532/2020, and UIDP/00532/2020 (CEFT), funded by national funds through FCT/MCTES (PIDDAC). Additional support came through PTDC/EMS-ENE/3362/2014 and POCI-01-0145-FEDER-016665, funded by FEDER funds through COMPETE2020 - Programa Operacional Competitividade e Internacionalização (POCI). I am also grateful for the scholarship SFRH/BD/143950/2019, co-financed by the State Budget fund and the European Social Fund (ESF) under the PORTUGAL2020 programme, particularly under Programa Operacional Regional do Norte (NORTE 2020).

I would like to express my sincere gratitude to my advisors, Professor Alexandre Afonso, and my co-advisors, Professor Fernando Pinho and Professor Manuel Alves. From all three, I gained invaluable insights into engineering and rheology. I appreciate Professor Alexandre for his pedagogical and scientific knowledge, as well as his guidance. He was always available to address my doubts, and his patience in listening to me during stressful times when there was a lot of work to be done is truly commendable. To Professor Fernando and Professor Manuel, I thank for their pedagogical and scientific skills, their knowledge made me look at things in a different way, making my work scientifically better.

I acknowledge and sincerely express my gratitude to Professor Luís Ferrás for his pedagogical and scientific skills. Professor Luís is a long-time friend who, in addition to always being available to help and being a true source of work and knowledge, always makes me laugh with his creativity in interpreting the Portuguese language.

I thank Professor Luísa Morgado and Professor Magda Rebelo for their availability to collaborate on my papers and for all their scientific contributions.

I thank all my co-workers at CEFT in the Mechanical Department at FEUP - Tomás, Schuller, Francisco, Saeed, Rui, Miguel and Pedro (and others) - for their patience and also for their help when I couldn't manage things related with the installation of some software.

Finally, I would like to express my gratitude to my family. I thank my parents for their support and all their love. I thank my husband, Nelson, for his love, friendship, and patience, always being there for me and supporting me along this journey, and also for his scientific knowledge. Finally, I thank my son, Leonardo, a little human being who every day teaches me something new, making me see that what really matters in life is love.

Publications

Some ideas and figures developed in this thesis have appeared previously in the following publications:

- A.M. Ribau, L.L. Ferrás, M.L. Morgado, M. Rebelo, and A.M. Afonso. Semi-Analytical Solutions for the Poiseuille-Couette Flow of a Generalised Phan-Thien–Tanner Fluid. *Fluids*, 4(3):129, Jul. 2019; on section 4.1
- A.M. Ribau, L.L. Ferrás, M.L. Morgado, M. Rebelo, and A.M. Afonso. Analytical and numerical studies for slip flows of a generalised Phan-Thien–Tanner fluid. *ZAMM - Journal of Applied Mathematics and Mechanics/Zeitschrift für Angewandte Mathematik und Mechanik*, 100(3), Jan. 2020; on section 4.2
- A.M. Ribau, L.L. Ferrás, M.L. Morgado, M. Rebelo, M.A. Alves, F.T. Pinho, and A.M. Afonso. A study on mixed electro-osmotic/pressure-driven microchannel flows of a generalised Phan-Thien–Tanner fluid. *Journal of Engineering Mathematics*, 127(1), Mar. 2021; on section 4.4
- A.M. Ribau, N.D. Gonçalves, L.L. Ferrás, and A.M. Afonso. Flow structures identification through proper orthogonal decomposition: The flow around two distinct cylinders. *Fluids*, 6(11):384, 2021; on section 5.1
- A.M. Ribau, L.L. Ferrás, M.L. Morgado, M. Rebelo, F.T. Pinho, and A.M. Afonso. Analytical study of the annular flow of a generalised Phan-Thien–Tanner fluid. *Acta Mech* 235, 1307–1317, 2024; on section 4.3
- A.M. Ribau, L.L. Ferrás, M.L. Morgado, M. Rebelo, F.T. Pinho, and A.M. Afonso. The effect of asymmetric zeta potentials on the electro-osmotic flow of complex fluids. Submitted to *Journal of Engineering Mathematics*; on section 4.5
- A.M. Ribau, N.D. Gonçalves, L.L. Ferrás, M.A. Alves, F.T. Pinho, and A.M. Afonso. Flow around a cylinder: a POD study with complex fluids. Under preparation to submit to *Physics of Fluids*.

Contents

Abstract	i
Resumo	iii
Acknowledgements	v
Publications	vii
Table of Contents	x
Nomenclature	xi
Abbreviations	xv
I Introduction	1
1 Introduction	3
1.1 Objectives	4
1.2 Dissertation outline	5
II Theoretical and numerical studies of viscoelastic fluid flows	7
2 Theoretical studies	9
2.1 Mathematical modelling of complex fluids	9
2.1.1 Governing equations	9
2.1.2 Complex fluids	10
2.1.3 Constitutive equations	11
2.2 Couette-Poiseuille flow	20
2.2.1 Problem definition	20
2.2.2 Analytical solution	21
2.2.3 Couette-Poiseuille flow: no-slip case	22
2.2.4 Couette-Poiseuille flow: asymmetric slip	23
2.3 Annular flow	26
2.3.1 Problem definition	26
2.3.2 Analytical solution	26
2.4 Electro-osmotic flow	34
2.4.1 Problem definition	35
2.4.2 Analytical solution	35

2.4.3	EO flow: under symmetric zeta potentials	37
2.4.4	EO flow: under asymmetric zeta potentials	41
3	Numerical studies	49
3.1	Model order reduction (MOR)	49
3.1.1	Introduction	49
3.1.2	Proper orthogonal decomposition (POD)	50
3.2	Flow structures identification through POD for the flow around two distinct cylinders	53
3.2.1	Governing equations, numerical method and POD	54
3.2.2	Problem definition	56
3.2.3	Results and discussion	57
3.3	Flow of complex fluids past a cylinder in a channel	65
3.3.1	Governing equations, numerical method and POD	66
3.3.2	Problem definition	67
3.3.3	Results and discussion	68
III	More on theoretical and numerical studies of viscoelastic fluid flows	77
4	More on theoretical studies	81
4.1	Semi-analytical solutions for the Poiseuille–Couette flow of a generalised Phan-Thien–Tanner	81
4.2	Analytical and numerical studies for slip flows of a generalised Phan-Thien–Tanner fluid	92
4.3	Analytical study of the annular flow of a generalised Phan-Thien–Tanner fluid . .	104
4.4	A study on mixed electro-osmotic/pressure-driven microchannel flows of a generalised Phan-Thien–Tanner fluid	116
4.5	The effect of asymmetric zeta potentials on the electro-osmotic flow of complex fluids	132
5	More in numerical studies	147
5.1	Flow structures identification through proper orthogonal decomposition: the flow around two distinct cylinders	147
IV	Conclusions and outlook	169
6	Conclusions	171
7	Outlook	173
V	References	175
	References	185

Nomenclature

Roman symbols	Definition
a	Consistency index in the power-law model; geometric parameter
\mathbf{A}	Matrix of the time coefficients
$\tilde{\mathbf{A}}$	Matrix with the more relevant time coefficients
$a_{m,t}$	Time coefficients of the proper orthogonal decomposition method associated to mode m and time-step t
a_i	Time coefficient of mode i
b	Parameter of the Carreau-Yasuda model; velocity profile parameter
c	Integration constant
C	Courant number
c_1	Stress constant
c_2	Integration constant
C_d	Drag coefficient
D	Diameter of the cylinder
\mathbf{D}	Rate of deformation tensor
$\frac{D}{Dt}$	Material derivative
De	Deborah number
e	Elementary charge
\mathbf{E}	Electric field
E_α	One-parameter Mittag-Leffler function
$E_{\alpha,\beta}$	Mittag-Leffler function
E_x	Streamwise gradient of the electric potential
f	Vortex shedding frequency
\mathbf{F}	Body force per unit volume
f_{kj}	Auxiliary function
$f(\tau_{kk})$	Function of the trace of the extra-stress tensor for the Phan-Thien and Tanner models (linear, exponential and quadratic)
G	Modulus of elasticity
H	Half-channel width
h_{kj}	Auxiliary function
k	Friction coefficient of the nonlinear Navier slip law
k_1	Friction coefficient of the nonlinear Navier slip law for the bottom wall
k_2	Friction coefficient of the nonlinear Navier slip law for the upper wall
k_B	Boltzmann constant
$K(\tau_{kk})$	Function of the trace of the extra-stress tensor for the generalised Phan-Thien and Tanner model
L	Characteristic length scale
\mathbf{L}	Matrix of the eigenvalues of the autocovariance matrix \mathbf{R}

m	Coefficient of the nonlinear Navier slip law
\mathbf{M}	Matrix with the dataset for the proper orthogonal decomposition method
$\tilde{\mathbf{M}}$	Reconstruction of matrix \mathbf{M} with the first more relevant modes
m_1	Coefficient of the nonlinear Navier slip law for the bottom wall
m_2	Coefficient of the nonlinear Navier slip law for the upper wall
n	Power-law index
n_0	Ion density
N_E	Number of control volumes of the mesh
N_m	Number of modes of the proper orthogonal decomposition method
N_{modes}	Number of modes of the proper orthogonal decomposition method
N_p	Number of rows of the dataset
N_t	Number of time steps
p	Pressure
P	Property on the calculation of the root mean square error for the proper orthogonal decomposition method
P_{rec}	Reconstructed property on the calculation of the root mean square error for the proper orthogonal decomposition method
P_x	Constant streamwise pressure gradient
P_z	Constant streamwise pressure gradient in cylindrical coordinates
r	Radial coordinate
R	Radius of the outer cylinder in annular flow; radius of the cylinder
\mathbf{R}	Autocovariance matrix
Re	Reynolds number
Re_{gen}	Generalised Reynolds number
R_ξ	Ratio of zeta potentials
St	Strouhal number
t	Time
T	Absolute temperature
\mathbf{S}	Autocovariance matrix
u	First component of the velocity vector
\mathbf{u}	Velocity vector
U	Characteristic velocity
U_c	Characteristic velocity
u_{max}	Maximum velocity
u_{sh}	Helmholtz-Smoluchowski electro-osmotic velocity
u_w	Velocity at the wall for the nonlinear Navier slip law
v	Second component of the velocity vector
v_j	Eigenvector
\mathbf{V}	Matrix of eigenvectors of autocovariance matrix \mathbf{R}
\mathbf{w}	Mode vector of the proper orthogonal decomposition method
\mathbf{W}	Matrix of modes of the proper orthogonal decomposition method
$\tilde{\mathbf{W}}$	Matrix with the most important modes
w_i	Eigenvector
Wi	Weissenberg number
x	Streamwise coordinate
y	Transverse coordinate
z	Spanwise coordinate; longitudinal coordinate in cylindrical coordinates; Valence of the ions
$\bar{\cdot}$	The overline represents a dimensionless quantity

Greek symbols	Definition
α	Parameter of the Mittag–Leffler function
α_G	Mobility parameter on Giesekus model
β	Parameter of the Mittag–Leffler function
β_η	Viscosity ratio
$\dot{\gamma}$	Shear rate in simple shear flows; second invariant of the rate of deformation tensor
γ_e	Deformation on the Maxwell model
$\dot{\gamma}_e$	Rate of deformation on the Maxwell model
$\dot{\gamma}_v$	Rate of deformation for the liquid part of the material on the Maxwell model
Γ	Gamma function
δ	Gap between the two cylinders in the annular flow
δt_{CFD}	Time-steps of the computational fluid dynamics simulation
δx	Mesh element size
ε	Extensibility parameter of Phan-Thien and Tanner models (linear, exponential, quadratic and generalised)
ϵ	Dielectric constant of a solution
η_0	Zero shear-rate viscosity
$\eta(\dot{\gamma})$	Viscosity function
η_∞	Infinite-shear-rate viscosity
η_p	Polymeric viscosity coefficient
η_s	Newtonian solvent viscosity
θ	Azimuthal coordinate
κ^2	Debye–Hückel parameter
λ	Time constant for the fluid; characteristic relaxation of a fluid
λ_D	Electric double layer thickness
λ_i	Eigenvalue associated to mode i
λ_r	Retardation time
λ_t	Approximate measure of the residence time
μ	Viscosity
$\mu(\dot{\gamma})$	First normal stress difference coefficient
ξ	Parameter that accounts for the slip between the molecular network and the continuous medium in the Gordon–Schowalter derivative
ξ_1	Zeta potential at the bottom wall
ξ_2	Zeta potential at the top wall
ρ	Fluid density
ρ_e	Electric charge density in the fluid
τ	Shear stress
$\boldsymbol{\tau}$	Extra-stress tensor
τ_1	Shear constant
τ_{kk}	Trace of the extra-stress tensor
τ_{xx}	Streamwise normal stress
τ_{yy}	Transverse normal stress
τ_{xy}	Shear stress
$\tau_{\theta\theta}$	Azimuthal normal stress
τ_{rr}	Radial normal stress
τ_{rz}	Shear stress in cylindrical coordinates
τ_{zz}	Spanwise normal stress; longitudinal normal stress in cylindrical coordinates

τ_p	Polymeric contribution of the extra-stress tensor
τ_s	Solvent contribution of the extra-stress tensor
$\overset{\nabla}{\tau}$	Upper-convected derivative of the extra-stress tensor
$\overset{\square}{\tau}$	Gordon–Schowalter derivative
Υ	Non-dimensional parameter that represents the ratio of pressure to electro-osmotic driving forces
ϕ	General property; electric potential generated by the electrodes
Φ	Electric potential
ψ	Charge distribution near the walls
Ψ_1	Constant that depends of the ratio of zeta potentials
$\Psi_1(\dot{\gamma})$	First normal-stress difference coefficient
Ψ_2	Constant that depends of the ratio of zeta potentials
$\Psi_2(\dot{\gamma})$	Second normal-stress difference coefficient
ψ_{wall}	Zeta potential at the wall
Ω^\pm	Hyperbolic function

Abbreviations

2D	Two-dimensional
3D	Three-dimensional
CFD	Computational fluid dynamics
DMD	Dynamic mode decomposition
EO	Electro-osmotic; electro-osmosis
expPTT	Exponential Phan-Thien–Tanner
FENE-P	Finite extensible nonlinear elastic model with Peterlin’s approximation
FFT	Fast Fourier transform
GNF	Generalised Newtonian fluids
gPTT	Generalised Phan-Thien–Tanner
HFPOD	Hybrid filtered proper orthogonal decomposition
linearPTT	Linear Phan-Thien–Tanner
ML	Machine learning
MOR	Model order reduction
mPOD	Multi-scale proper orthogonal decomposition
MRA	Multiresolution analysis
PCA	Principal components analysis
POD	Proper orthogonal decomposition
PTT	Phan-Thien–Tanner
quadraticPTT	Quadratic Phan-Thien–Tanner
RMSE	Root mean squared error
SPOD	Spectral proper orthogonal decomposition
SSA	Singular systems analysis (SSA)
SVD	Singular value decomposition
UCM	Upper-convected Maxwell

Part I

Introduction

Chapter 1

Introduction

To mimic and predict the behavior of physical phenomena, mathematical modelling can be applied. This is also true when dealing with complex fluids, and along the years, several rheological constitutive models were proposed to predict their behavior. These models can be more or less complex, and rely on the physical properties of the fluids that are considered.

For this work, the main interest is viscoelastic materials [1], such as polymer melts, polymer solutions and bio-fluids, like blood, saliva, synovial fluid and solutions containing long molecules like proteins. For such fluids, many constitutive models have been proposed in the past. The constitutive models used to describe viscoelastic fluids can be classified as: differential, when described by partial differential equations that make use of the local deformation rate field; integral, which need to integrate over time the past history of deformations. These two types of models have advantages and disadvantages. The differential models normally allow a faster numerical solution of the differential equations involved, improving the modelling of complex viscoelastic materials, whereas integral models can perform better, but are computationally more expensive and may lead to error propagation, in this way influencing the fitting quality of the model and the computational effort to numerically solve them [2].

In this work the concern is with differential type models, and a new type of equation is adopted that provides flexibility through the use of fractional calculus. In particular, new semi-analytical and numerical solutions for viscoelastic fluids described by the generalised Phan-Thien–Tanner (gPTT) [3] viscoelastic model are presented, which serves the purpose of providing benchmark results for canonical flows, while showing the advantages of this new type of model relative to classical rheological equations.

The gPTT model was first presented by Ferrás et al. [3], where a generalization form of the Phan-Thien and Tanner (PTT) model was proposed, considering a new function of the trace of the stress tensor. This new function includes the generalized Mittag–Leffler function [4], that includes the exponential form of the PTT, but has two new fitting constants, providing additional fitting flexibility. Ferrás et al. [3] showed that the gPTT model provide a better fit to experimental rheological data, when compared with the exponential PTT (expPTT), to the shear viscosity and first normal stress difference, when steady simple shear flows were considered and also to extensional deformations. In that same work, Ferrás et al. [3] presented the analytical solution for the gPTT

model in rectilinear channel/pipe flows and studied the influence of the new parameters of the model on the velocity and in stress profiles. In what concerns the gPTT model, more considerations on the model will be presented in the Section 2.1.

When considering physical problems, the large number of dependent and independent dimensions that appear, is one of the prominent disadvantages in scientific computing. The dimensionality curse [5], a well-known constraint, has significantly hindered the adoption of direct computation methods for complex materials in favor of more simplified approaches. However, several mathematical techniques can be employed to overcome this challenge of dimensionality [6, 7], including the use of model order reduction (MOR) methods, which aim to capture the fundamental

characteristics of a problem. Therefore, when the reduction process starts, the fundamental characteristics of the original problem must already be present, but with the smallest of approximations. At some point, the reduction process stops, and at that moment all essential properties of the original problem must be captured with enough precision. This whole process is done automatically [8]. In this work, one of the most popular MOR methods is applied: the proper orthogonal decomposition (POD) method, also known as Karhunen–Loève decomposition, principal components analysis (PCA), singular systems analysis (SSA) or singular value decomposition (SSV). The POD method was first introduced by Lumley in 1967 [9] for the analysis of coherent flow structures under turbulent conditions, and it enables the decomposition of any flow into an infinite set of eigenfunctions or modes. The aim of the POD method is to effectively reduce the size of the model data set, capturing essential information using less data and computational resources. The technique remained rather limited, and only gained momentum in computational fluid dynamics (CFD) especially as machine learning (ML) methods started to be developed, due to its ability to reduce the simulation time and accurately reproduce coherent structures in turbulent flows based on the most significant modes. Identifying these flow structures, particularly in transient situations, presents a complex challenge, because such structures change in time and space, with new structures continuously being formed while others are destroyed. By decomposing the entire data set into smaller sets, important structures present in the main flow and structures with periodic behaviour, like vortices, can be identified. So, by analysing the frequency of each of these components and using a smaller number of components, a better and global understanding of the flow is obtained.

1.1 Objectives

Being the gPTT a relatively new rheological model, there is a lack of analytical solutions for canonical flows in the literature. Therefore, one of the main objectives of this thesis is to obtain new analytical, semi-analytical and numerical solutions of flows of viscoelastic fluids governed by the gPTT viscoelastic model. In particular this is carried out through a parametric study on the influence of the rheological constitutive model parameters, on canonical flows, such as, Couette–Poiseuille flows, with no-slip and under asymmetric slip, in annular flow and electro-osmotic (EO) flows in microchannels, with symmetric and asymmetric zeta potentials. The solutions allow the

full characterization of the velocity and stress profiles of a gPTT fluid in different types of flows and can be used to validate the numerical methods used in CFD codes.

Another objective is to numerically study Newtonian and non-Newtonian fluid flows and apply MOR methods to reduce the huge amount of data that comes out of a numerical simulation, by performing a decomposition of the entire data set into smaller sets and then to identify important structures that are present in the main flow. For that, the study of the flow past two parallel side-by-side cylinders with different radii is performed, and by grouping specific modes, a reconstruction is done and an identification of complex flow structures is analyzed. For this study the fluids considered are a Newtonian fluid and two non-Newtonian power-law fluids with $n = 0.7$ and $n = 1.3$, for a Reynolds number (Re , a non-dimensional parameter that measures the ratio between inertial and viscous forces [10]) equal to 100. For this Reynolds number, it is expected to occur periodic oscillation. So, the idea is to fully understand the mode decomposition in an oscillatory flow around two parallel cylinders of different dimensions. The MOR method applied in this work is the POD method, which is used to identify important flow structures that appear in the numerical simulations of viscoelastic flows.

Next, the analysis is extended to a gPTT fluid, with low Reynolds number and two different Weissenberg number (Wi , a non-dimensional parameter that measures the elasticity of a fluid and indicates the degree of anisotropy or orientation generated by the deformation [10]) equal to 1.2 and 1.25, but now considering the flow around a single cylinder at low Re . Furthermore, the performed analysis for the gPTT fluid with $Wi = 1.2$ will be used to predict the reconstruction of the flow for the gPTT fluid with $Wi = 1.25$. A root mean squared error (RMSE), between the original and the reconstructed normal stresses field, below 1 was obtained. The outcomes derived from these studies are to apply the original POD method for decomposing complex flows, better identify significant flow structures and to use it as a step to obtain new data with much less information.

1.2 Dissertation outline

The present dissertation falls into the category of multi-paper (or paper-based) dissertations, built up as a collection of seven peer-review journal papers, published or under evaluation, in international scientific journals. A complete list of the included papers can be found in page vii. The included papers were prepared in the course of this PhD thesis and correspond to specific stages and parts of the above mentioned objectives.

The present dissertation is organized in four main parts:

Part I: Introduction

Part II: Theoretical and numerical studies of viscoelastic fluid flows

Part III: More on theoretical and numerical studies of viscoelastic fluid flows

Part IV: Conclusions and outlook

The present section closes the introductory part (Part I). In Part II the main contributions of each paper will be described, on the following topics: Chapter 2 is dedicated to the theoretical studies, where the analytical solutions with the gPTT model are presented; Chapter 3 is dedicated to the numerical studies, where the MOR methods are presented and applied. Part III presents the integral versions of the papers already published, or in the process of submission or review (Chapter 4 and 5). The conclusion and the outlook of the thesis are presented in Part IV, including suggestions for future work.

Part II

Theoretical and numerical studies of viscoelastic fluid flows

Chapter 2

Theoretical studies

2.1 Mathematical modelling of complex fluids

For modelling physical phenomena of complex polymeric materials, the governing equations describing the phenomena, including the mass conservation and the momentum equations, together with the thermal energy equation if heat transfer is involved, which is not the case in this thesis, need to be solved. In addition, the momentum equation requires a description of the material stress tensor, which is provided by the rheological constitutive equation. The whole set of equations is normally complex and difficult to solve analytically, therefore a numerical study is usually required. However, for flows in simple geometries it is often possible to benefit from simplifications of the governing equations that allow fully analytical or at least semi-analytical solutions for specific fluids to be obtained [11]. In this section, the governing equations are presented and also the types of fluids and the corresponding rheological mathematical models are described.

2.1.1 Governing equations

The main physical laws required to describe a flow field are the:

- the conservation of mass;
- the conservation of momentum (Newton's second law of motion);
- the conservation of energy (first law of thermodynamics).

The first two laws are the ones used to solve an isothermal problem and the last one is essential to solve non-isothermal problems [12].

The conservation of mass states that in a closed system, the system mass must be the same as time goes by, which means that the mass is preserved over time. This law is given, in differential form by the following equation:

$$\frac{\partial \rho}{\partial t} + \nabla \cdot \rho \mathbf{u} = 0, \quad (2.1)$$

where \mathbf{u} is the velocity vector, ρ is the fluid density and t is the time. This equation is known as the continuity equation, and for incompressible fluids reduces to:

$$\nabla \cdot \mathbf{u} = 0. \quad (2.2)$$

The momentum balance states that the quantity of momentum only changes by the action of forces, as described by Newton's law of motion. This law is given by the Cauchy equation:

$$\rho \frac{D\mathbf{u}}{Dt} = -\nabla p + \nabla \cdot \boldsymbol{\tau} + \mathbf{F}, \quad (2.3)$$

where p is the pressure, \mathbf{F} represents a body force per unit volume and $\boldsymbol{\tau}$ is the extra-stress tensor. $\frac{D}{Dt}$ is the material derivative of a general property ϕ ,

$$\frac{D\phi}{Dt} = \frac{\partial \phi}{\partial t} + \mathbf{u} \cdot \nabla \phi. \quad (2.4)$$

2.1.2 Complex fluids

The main interest when developing new analytical equations is that they are capable of modelling the flow of complex polymeric materials, like the flow of viscoelastic fluids.

The motion of fluids is the result of the transfer of momentum to and between molecules. If the length scale of flows is much larger than the size of molecules, those fluids are described as a continuous medium (continuum hypothesis) [13].

The measure of the resistance of a fluid to deformation is the viscosity. Viscosity is one of the most important properties of a fluid, because not only describes the nature of the fluid, but also relates the behavior of the shear stress with respect to the deformation of the fluid [11].

Rheology is the scientific field that studies the deformation and the flow of matter. In this field the main concern is the study of the flow behavior of complex fluids, like polymers, pastes, emulsions and other materials [12]. So, the principal object of study in Rheology is between the Newton's law of viscosity and the Hooke's law of elasticity. In fact any fluid can be considered as Newtonian fluid or approaching the behavior of an elastic solid, depending on the shear, on the deformation process applied and on time scales [10].

There are several models to deal with the relationship between the stress and the deformation tensors of complex fluids. These models are the constitutive equations, that depend on the structure of the fluid [10]. These models also depend on the nature of the fluid. In that way, fluids can be Newtonian or non-Newtonian. The most common non-Newtonian effect on fluids is the shear thinning behavior, that is the tendency of some materials to decrease the viscosity when they are driven into flow at high deformation rates. Some examples of fluids that show this effect are ketchup, paints and blood. Other materials show shear thickening, that is when the materials show higher viscosity when they are made to flow at high deformation rates [12]. An example that shows this effect is the mixture of cornstarch and water. Other common behavior is the Bingham plastic (named after Eugene C. Bingham [14]) where the fluid will not flow until a stress exceeding a yield stress is applied [12]. An example of fluid showing this behaviour is toothpaste. Fig. 2.1

represents a classification of fluids with shear stress as a function of the shear rate, according with the referred behaviors.

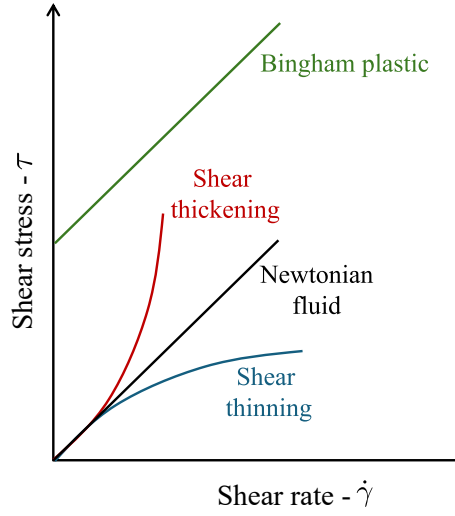


Figure 2.1: Classification of fluids with shear stress as a function of shear rate: shear thinning, shear thickening, Newtonian fluids and Bingham plastic.

Other effect is thixotropy, which is the decreasing of the viscosity over time, when a constant shear stress is applied [11, 13]. The non-Newtonian fluids can also be inelastic or viscoelastic fluids, and as described before, the latter ones being the object of study of this thesis. In the next section, different types of fluids and their constitutive equations are presented.

2.1.3 Constitutive equations

The stress tensor $\boldsymbol{\tau}$, can be described by different rheological models depending on the fluid. When an equation is specified for $\boldsymbol{\tau}$, that equation is known as the constitutive equation for that fluid. The simplest constitutive equation for incompressible Newtonian fluids (like water, air, etc) is given by:

$$\boldsymbol{\tau} = 2\mu\mathbf{D}, \quad (2.5)$$

where $\mathbf{D} = \frac{1}{2}(\nabla\mathbf{u} + (\nabla\mathbf{u})^T)$ is the rate of deformation tensor, $\nabla\mathbf{u}$ is the velocity gradient tensor and μ is the viscosity. For a Newtonian fluid, the viscosity, μ , is constant (for a given temperature and pressure). This means that, the applied stress is linearly proportional to the rate of deformation, as originally hypothesized by Newton [15], and the viscosity, μ , is the constant of proportionality. For a Newtonian fluid, the Reynolds number, Re , that is a dimensionless parameter that relates inertial forces with viscous forces [10] is given by:

$$Re = \frac{\rho UL}{\mu} \quad (2.6)$$

where U is the characteristic velocity and L is a characteristic length scale.

There are other constitutive equations where the viscosity is not constant (for a given temperature and pressure), and depend on the invariants of the rate of deformation tensor. The fluids

following this constitutive equation are known as generalised Newtonian fluids (GNF). In this case, the constitutive equation for τ is given by:

$$\tau = 2\eta(\dot{\gamma})\mathbf{D}, \quad (2.7)$$

where $\eta(\dot{\gamma})$ is the viscosity function and $\dot{\gamma}$ is the second invariant of the rate of deformation tensor. For simple shear flows, $\dot{\gamma}$ is just the shear rate.

There are many viscosity functions for the GNF, with different degrees of complexity. One of such model is the power-law model [1], where viscosity is a power law function of $\dot{\gamma}$:

$$\eta(\dot{\gamma}) = a\dot{\gamma}^{n-1}, \quad (2.8)$$

where a is the consistency index and n is the power-law index.

Another viscosity model is the Carreau-Yasuda model [1], given by:

$$\eta(\dot{\gamma}) = \eta_\infty + (\eta_0 - \eta_\infty) \left[1 + (\lambda\dot{\gamma})^b \right]^{\frac{n-1}{b}}, \quad (2.9)$$

where η_∞ is the infinite-shear-rate viscosity, b is a parameter describing the smoothness of the transition between the first Newtonian plateau and the power-law region and λ is a time constant for the fluid, that determines the shear rate at which the transition from the zero-shear-rate plateau to the power-law region occurs.

The GNF models are not suitable for flows where elastic effects are relevant [11], like the case of viscoelastic fluids. So, for viscoelastic fluids, the constitutive equations have in consideration the viscosity and the elastic (memory) effects.

For viscoelastic fluids, the stress tensor τ of Eq. (2.3) is given by $\tau = \tau_p + \tau_s$, with τ_p representing the polymeric contribution and τ_s the solvent contribution. Since the stress tensor is the sum of the solvent and polymer stress contributions, the viscosity ratio, β_η , can be defined as the ratio between the Newtonian solvent viscosity, η_s , and the zero shear-rate viscosity, η_0 . The viscosity ratio is given by:

$$\beta_\eta = \frac{\eta_s}{\eta_0} = \frac{\eta_s}{\eta_s + \eta_p} \quad (2.10)$$

where η_p is the polymeric viscosity coefficient. η_0 , the total zero shear-rate viscosity, is equal to $\eta_p + \eta_s$. So, for a viscoelastic fluid, the Reynolds number, Re , is usually defined by:

$$Re = \frac{\rho UL}{\eta_0}. \quad (2.11)$$

From now on, the notation τ will be used for τ_p .

One well known viscoelastic model is the Maxwell model. Maxwell [16] combined the ideas of viscosity and elasticity to obtain an equation for a viscoelastic fluid, because he initially thought that gases might be viscoelastic [1]. The main idea behind this model is that a fluid behaves as

a purely Hookean elastic material, with modulus of elasticity G , for fast deformations, and as Newtonian fluid for slow deformations. Therefore, for linear solids the stress is given by:

$$\tau = G\gamma_e, \quad (2.12)$$

that means that the stress is proportional to the deformation (γ_e). When the deformation is slow and the material behaves like a liquid, the rate of deformation, $\dot{\gamma}_v$, is used instead of the deformation, so the stress is given by:

$$\tau = \eta_p \dot{\gamma}_v. \quad (2.13)$$

This lead us to the total rate of deformation:

$$\dot{\gamma} = \dot{\gamma}_e + \dot{\gamma}_v. \quad (2.14)$$

So, the scalar version of the Maxwell model is:

$$\dot{\gamma} = \frac{1}{G} \frac{d\tau}{dt} + \frac{\tau}{\eta_p}. \quad (2.15)$$

Integrating Eq. (2.15), the following equation is obtained:

$$\tau(t) = \int_{-\infty}^t \frac{\eta_p}{\lambda} \exp\left(-\left(\frac{t-s}{\lambda}\right)\right) \dot{\gamma}(s) ds. \quad (2.16)$$

Therefore, this equation means, that at certain moment, the stress depends on the strain (deformation) history. The dependence is controlled by $\frac{\eta_p}{\lambda} \exp\left(-\left(\frac{t-s}{\lambda}\right)\right)$, that is a memory function and $\lambda = \frac{\eta_p}{G}$ is the relaxation time [11]. Using a tensor form, the Maxwell model given by Eq. (2.15) can be rewritten as,

$$\boldsymbol{\tau} + \lambda \frac{\partial \boldsymbol{\tau}}{\partial t} = 2\eta_p \mathbf{D}. \quad (2.17)$$

To measure the influence of the relaxation time, the Deborah number, De , is used, and is given by:

$$De = \frac{\lambda L}{U}, \quad (2.18)$$

where λ is the characteristic relaxation of a fluid and L/U is the time scale of an observed phenomena. When talking about the relaxation time, another dimensionless parameter appears, the Weissenberg number, Wi , that is a parameter that measures the elasticity of a fluid and indicates the degree of anisotropy or orientation generated by the deformation [10]. For a steady simple shear flow, for example, the dominant elastic force is due to the first normal-stress difference, $\Psi_1 = \tau_{xx} - \tau_{yy}$, and the viscous force is simply the shear stress τ_{xy} [17]. This way, the Weissenberg number is given by:

$$Wi = \frac{\Psi_1}{\tau_{xy}}. \quad (2.19)$$

So, depending on the rheological model used, the Weissenberg number can be:

$$Wi = \frac{\lambda U}{L}, \quad (2.20)$$

which depends on the characteristic relaxation of a fluid and on the velocity and length scales. Deborah number and Weissenberg number have different origins and they quantify different effects, but they are frequently used as synonyms. To know more about this subject, please see the work of Poole [17].

The Maxwell model was applicable for small deformations, so later Oldroyd [18] generalised it for large deformations [11, 19]. Since then is called upper-convected Maxwell (UCM) model and the equation gets the following form:

$$\boldsymbol{\tau} + \lambda \overset{\nabla}{\boldsymbol{\tau}} = 2\eta_p \mathbf{D}, \quad (2.21)$$

where $\overset{\nabla}{\boldsymbol{\tau}}$ is the upper-convected derivative, given by

$$\overset{\nabla}{\boldsymbol{\tau}} = \frac{D\boldsymbol{\tau}}{Dt} - \boldsymbol{\tau} \cdot \nabla \mathbf{u} - (\nabla \mathbf{u})^T \cdot \boldsymbol{\tau}. \quad (2.22)$$

The upper-convected derivative allows a frame-invariant method by taking into account the deformation that the fluid particles experience in flow [12].

Oldroyd [18] also proposed another constitutive model based on Jeffreys model [1]. Jeffreys model is the model formed by adding a Newtonian solvent stress to the polymer stress given by the Maxwell model, that is the time derivative of the rate deformation tensor, and is given by:

$$\boldsymbol{\tau} + \lambda \frac{\partial \boldsymbol{\tau}}{\partial t} = 2\eta_p \left(\mathbf{D} + \lambda_r \frac{\partial \mathbf{D}}{\partial t} \right) \quad (2.23)$$

where $\lambda_r = \lambda \frac{\eta_s}{\eta_p}$ is the retardation time.

So, the model proposed by Oldroyd for invariant conditions is given by:

$$\boldsymbol{\tau} + \lambda \overset{\nabla}{\boldsymbol{\tau}} = 2\eta_p \left(\mathbf{D} + \lambda_r \overset{\nabla}{\mathbf{D}} \right), \quad (2.24)$$

and is known as Oldroyd-B model.

There are other constitutive equations, like the ones that can be derived from the molecular theory. One of those models is the Giesekus model [20] and its constitutive equation is given by:

$$\boldsymbol{\tau} + \frac{\alpha_G \lambda}{\eta_p} (\boldsymbol{\tau} \cdot \boldsymbol{\tau}) + \lambda \overset{\nabla}{\boldsymbol{\tau}} = 2\eta_p \mathbf{D}, \quad (2.25)$$

where α_G is the so-called mobility parameter. This model reproduces well many of the characteristics of polymeric fluids [11].

Phan-Thien and Tanner derived a model from the Lodge–Yamamoto type of network theory for polymeric fluids, in which the network junctions of the polymeric network allow a certain effective slip and the rate of destruction of junctions depends on the state of stress in the network [21]. The constitutive equation proposed by Phan-Thien and Tanner, for the case of an isothermal flow, is given by:

$$f(\tau_{kk})\boldsymbol{\tau} + \lambda \overset{\square}{\boldsymbol{\tau}} = 2\eta_p \mathbf{D} \quad (2.26)$$

with

$$f(\tau_{kk}) = 1 + \frac{\varepsilon\lambda}{\eta_p} \tau_{kk}, \quad (2.27)$$

where $f(\tau_{kk})$ is the function that represents the rate of destruction of junctions, $\tau_{kk} = \tau_{xx} + \tau_{yy} + \tau_{zz}$ is the trace of the extra-stress tensor, ε represents the extensibility parameter and $\overset{\square}{\boldsymbol{\tau}}$ represents the Gordon–Schowalter derivative, defined by:

$$\overset{\square}{\boldsymbol{\tau}} = \frac{\partial \boldsymbol{\tau}}{\partial t} + \mathbf{u} \cdot \nabla \boldsymbol{\tau} - (\nabla \mathbf{u})^T \cdot \boldsymbol{\tau} - \boldsymbol{\tau} \cdot (\nabla \mathbf{u}) + \xi (\boldsymbol{\tau} \cdot \mathbf{D} + \mathbf{D} \cdot \boldsymbol{\tau}) \quad (2.28)$$

and parameter ξ accounts for the slip between the molecular network and the continuous medium. This model is known as the linear Phan-Thien–Tanner (PTT) model (linearPTT).

Later, Phan-Thien proposed a new model, based on an exponential function form [22] and showed that this new function would be quite adequate to represent the rate of destruction of junctions, but the parameter ε should be of the $O(10^{-2})$. Therefore, for that model function $f(\tau_{kk})$ is now given by:

$$f(\tau_{kk}) = \exp\left(\frac{\varepsilon\lambda}{\eta_p} \tau_{kk}\right) \quad (2.29)$$

and this model is known as exponential PTT (expPTT) model.

These classical functions of PTT have been frequently used in the literature, and in fact Ferrás et al. [23] considered a new quadratic version of the PTT (quadraticPTT) model, i.e. a second-order expansion of the exponential model, given by:

$$f(\tau_{kk}) = 1 + \frac{\varepsilon\lambda}{\eta_p} \tau_{kk} + \frac{1}{2} \left(\frac{\varepsilon\lambda}{\eta_p} \tau_{kk} \right)^2. \quad (2.30)$$

In 2019, Ferrás et al. [3] considered a more general function for the rate of destruction of junctions, that explores the generalities of the Mittag–Leffler function. This new function has two fitting constants, in order to achieve additional fitting flexibility [3]. The Mittag–Leffler function is defined by,

$$E_{\alpha,\beta}(z) = \sum_{j=0}^{\infty} \frac{z^j}{\Gamma(\alpha j + \beta)}, \quad (2.31)$$

with α, β real and positive and Γ is the Gamma function, defined by $\Gamma(t) = \int_0^\infty x^{t-1} e^{-x} dx$. When $\alpha = \beta = 1$, the Mittag–Leffler [24] function reduces to the exponential function and when $\beta = 1$, the original one-parameter Mittag–Leffler function, E_α , is obtained. Thus, the new function of the trace of stress tensor, that now will be denoted by $K(\cdot)$ instead of $f(\cdot)$ (to distinguish from the classical cases) and that describes the network destruction of junctions is written as:

$$K(\tau_{kk}) = \Gamma(\beta) E_{\alpha, \beta} \left(\frac{\varepsilon \lambda}{\eta_p} \tau_{kk} \right), \quad (2.32)$$

where the normalisation $\Gamma(\beta)$ is used to ensure that $K(0) = 1$, for all choices of β .

Fig. 2.2 presents the variation of function $K(z)$, considering $z = \frac{\varepsilon \lambda}{\eta_p} \tau_{kk}$, for different values of α and β . When the values of α and β decrease, different rates of increase in the rate of destruction of junctions are obtained. Notice that when the exponential function ($\alpha = \beta = 1$) is compared with different values of α and β , the Mittag–Leffler function allows for a wider range of variation of such rates and thus more flexibility in fitting the experimental data [3].

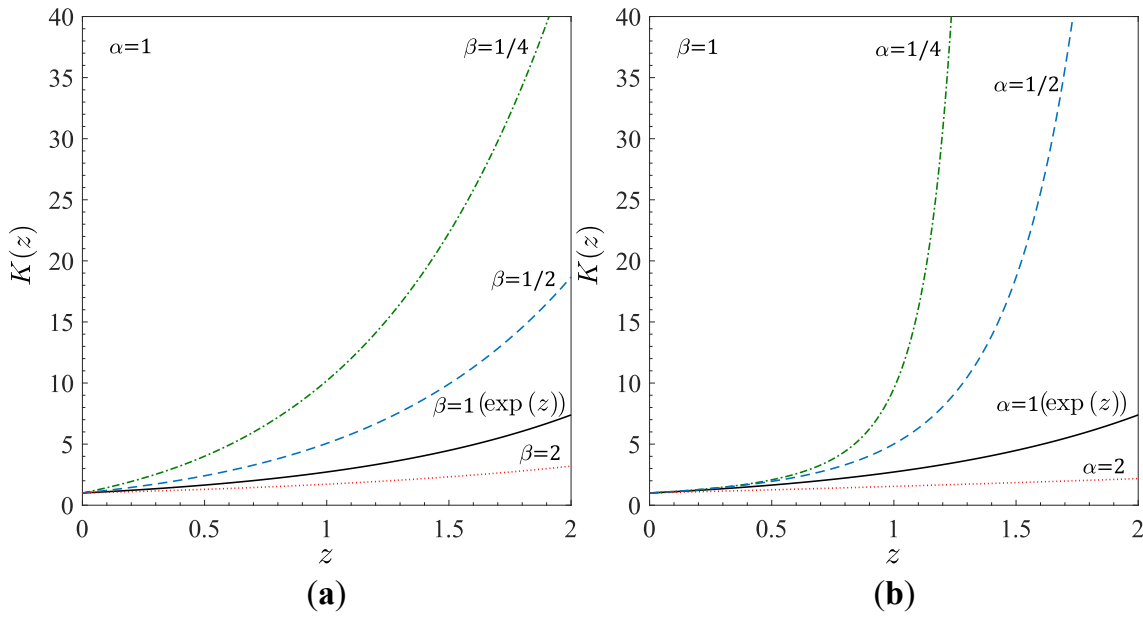


Figure 2.2: Influence of α and β in the shape of $K(z)$ with $z = \frac{\varepsilon \lambda}{\eta_p} \tau_{kk}$: (a) $\alpha = 1$; (b) $\beta = 1$.

Now, the gPTT model, given by Eq. (2.32), will be compared with the linear, the exponential and the quadratic versions of the PTT, given by Eqs. (2.27), (2.29) and (2.30), respectively.

To compare these models, the dimensionless material properties in steady shear flow of the three versions of the PTT model are studied and compared with the gPTT model, considering different values of α and β .

The material functions can be obtained considering a steady-state flow in the x -direction, with the velocity vector, $\mathbf{u} = (\dot{\gamma}y, 0, 0)$, where $\dot{\gamma}$ is the shear rate. For this canonical flow, considering the parameter $\xi = 0$, the constitutive Eq. (2.26) reduces to:

$$\begin{cases} K(\tau_{kk})\tau_{xx} = 2\lambda\dot{\gamma}\tau_{xy} \\ K(\tau_{kk})\tau_{xy} = \eta_p\dot{\gamma} \\ \tau_{yy} = \tau_{zz} = \tau_{xz} = \tau_{yz} = 0 \end{cases} \quad (2.33)$$

From Eq. (2.33), $\tau_{kk} = \tau_{xx}$ and applying some algebra in the first two equations, a relationship between the shear stress and the normal stress is found,

$$\tau_{xx} = 2\frac{\lambda}{\eta_p}\tau_{xy}^2. \quad (2.34)$$

The viscometric material functions can also be obtained: the steady shear viscosity, $\mu(\dot{\gamma})$, the first normal stress difference coefficient, $\Psi_1(\dot{\gamma})$, and the second normal stress difference coefficient, $\Psi_2(\dot{\gamma})$, which are given by:

$$\mu(\dot{\gamma}) = \frac{\tau_{xy}}{\dot{\gamma}}, \quad (2.35)$$

$$\Psi_1(\dot{\gamma}) = \frac{\tau_{xx} - \tau_{yy}}{\dot{\gamma}^2}, \quad (2.36)$$

$$\Psi_2(\dot{\gamma}) = \frac{\tau_{yy} - \tau_{zz}}{\dot{\gamma}^2}. \quad (2.37)$$

As for other versions of the PTT models for which $\xi = 0$, the second normal stress coefficient is null, $\Psi_2(\dot{\gamma}) = 0$, so, it is only needed to find $\mu(\dot{\gamma})$ and $\Psi_1(\dot{\gamma})$. Therefore, manipulating the second equation of the system of equations (Eq. (2.33)) the shear stress can be obtained,

$$\tau_{xy} = \frac{\eta_p\dot{\gamma}}{K(\tau_{xx})}. \quad (2.38)$$

The dimensionless expression for the steady shear viscosity becomes,

$$\frac{\mu(\dot{\gamma})}{\eta_p} = \frac{\tau_{xy}}{\eta_p\dot{\gamma}} = \frac{1}{K(\tau_{xx})} \quad (2.39)$$

and the dimensionless first normal stress coefficient is given by,

$$\frac{\Psi_1(\dot{\gamma})}{2\eta_p\lambda} = \frac{\tau_{xx}}{2\eta_p\lambda\dot{\gamma}^2} = \frac{1}{[K(\tau_{xx})]^2}. \quad (2.40)$$

Ferrás et al. [23], showed that, for the linearPTT, the quadraticPTT and the expPTT, the dimensionless material functions depend on the generalised Deborah number, $\sqrt{\varepsilon}(\lambda\dot{\gamma})$. Here, it will be shown that the same happens for the gPTT model. To obtain the material functions for the gPTT model, the non-linear system of equations (Eq. (2.33)) is solved, and is written in terms of τ_{xx} in the non-linear form:

$$\frac{1}{2}K(\tau_{xx})^2\frac{\varepsilon\lambda}{\eta_p}\tau_{xx} = \varepsilon(\lambda\dot{\gamma})^2. \quad (2.41)$$

Giving values to $\frac{\varepsilon\lambda}{\eta_p}\tau_{xx}$, $\sqrt{\varepsilon}(\lambda\dot{\gamma})$ is found using Eq. (2.41). Then, the function $K(\tau_{xx})$ is directly calculated, allowing us to obtain the material functions given by Eqs. (2.39) and (2.40).

Fig. 2.3 presents the dimensionless material properties for a steady-state planar Couette flow using the three versions of the PTT (linear, quadratic, and exponential) and also the gPTT model. In Fig. 2.3 (a), $\beta = 1$ and different values of α are used, and, in Fig. 2.3 (b), $\alpha = 1$ and different values of β are used.

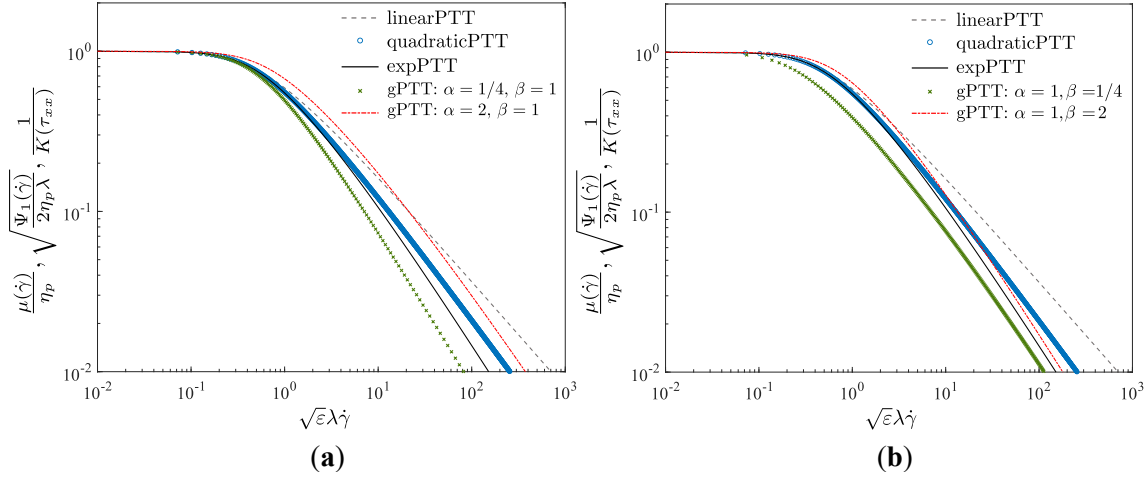


Figure 2.3: Dimensionless material functions in a steady-state Couette flow using the three versions of the PTT and the gPTT model: (a) $\beta = 1$; (b) $\alpha = 1$.

It is observed that the gPTT model allows a broader description of the thinning properties of the fluid. Both the thinning rate and the onset of the thinning behavior can be controlled by the new model parameters. Therefore, this new model must be further explored for canonical flows.

This model was extensively studied for strong flows in [3], where an explanation on the influence of the new model parameters was provided.

Note that the expPTT model was developed to take into account the strong destruction of network junctions, which occurs, for example, in strong flows (e.g., extensional flows). Although the expPTT model was derived for such strong flows, it was shown in [3] that the gPTT model could slightly improve the fitting for shear (weak) flows, considering polymer solutions. In this thesis will be considered polymer melts.

Fig. 2.4 shows that the gPTT model provides a much better fitting to weak flows of polymer melts (low density polyethylene melt [25]), even when using only one extra parameter (α).

To quantify the error incurred during the fitting process, a mean square error was used, given by:

$$error = \sum_i^{N_\mu} [\log \mu(\dot{\gamma})_i - \log \mu(\dot{\gamma})_{fit_i}]^2 + \sum_j^{N_{\Psi_1}} [\log \Psi_1(\dot{\gamma})_j - \log \Psi_1(\dot{\gamma})_{fit_j}]^2, \quad (2.42)$$

$$error_\mu = \sum_i^{N_\mu} [\log \mu(\dot{\gamma})_i - \log \mu(\dot{\gamma})_{fit_i}]^2, \quad (2.43)$$

$$error_{\Psi_1} = \sum_j^{N_{\Psi_1}} [\log \Psi_1(\dot{\gamma})_j - \log \Psi_1(\dot{\gamma})_{fit_j}]^2, \quad (2.44)$$

with N_μ and N_{Ψ_1} representing the number of experimental points obtained for $\mu(\dot{\gamma})$ and $\Psi_1(\dot{\gamma})$, respectively. The notation *fit* is used to denote the fitted results.

A better fit was obtained for the gPTT model when compared to the original expPTT model. The total mean square error obtained for the expPTT was 29.7, being five times the error obtained for gPTT, for which a value of 6.0 was obtained. The gPTT model allows a better fit for low and high shear rates for the first normal stress difference (where the $error_{\Psi_1}$ obtained for the expPTT model is 20 times higher than the error obtained for the gPTT). For the shear viscosity, the gPTT model predicts a lower value (when compared to experimental data) for high shear rates (although it should be remarked that the $error_\mu$ is four times smaller when compared to the expPTT model).

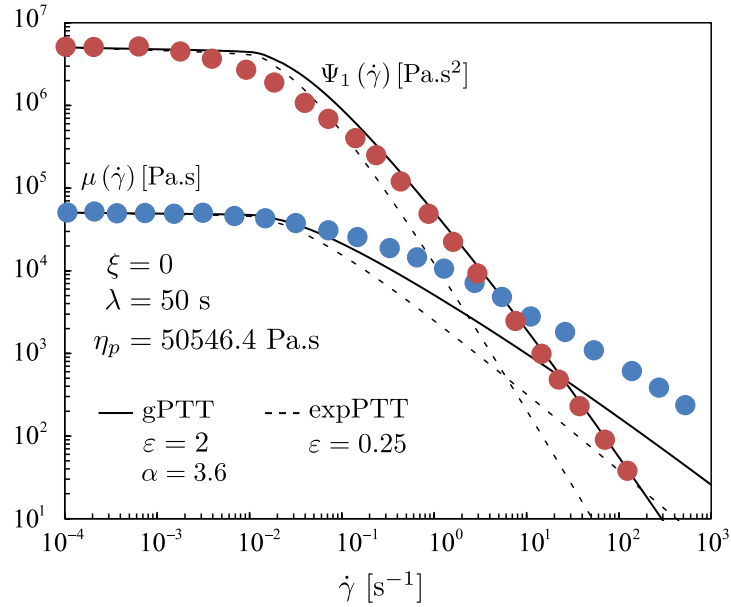


Figure 2.4: Fitting of the shear viscosity and the first normal stress difference coefficient to rheological data from Laun [25]. The gPTT model only considers the one-parameter Mittag–Leffler function, E_α . By adding only one parameter, a fitting error (Eq. (2.42)) of 29.7 and 6 for the expPTT and gPTT models, respectively, was obtained. The symbols represent the experimental data from Laun [25] for a low density polyethylene melt.

Based on what is described above, this thesis presents analytical and semi-analytical solutions for canonical flows, described by the gPTT constitutive equation. In the next sections, the gPTT model is applied to the Couette–Poiseuille flow in section 2.2, to annular flow in section 2.3 and to EO flow in section 2.4. The capability of this model to describe such flows is studied by performing a parametric study on the influence of the gPTT parameters.

2.2 Couette-Poiseuille flow

In this section, new semi-analytical solution for Couette-Poiseuille flow using the gPTT constitutive model are presented. A parametric study is performed, studying the influence of the gPTT parameters.

Each contribution related to the work objectives, presented in section 2.2, are explained in detail. Given that the present dissertation falls into the category of *multi-paper dissertation*, and in order to keep repetition of information at a minimum level, the complete paper related to this section is presented in Part III of this thesis.

2.2.1 Problem definition

The Couette flow is the flow of a fluid in the space between two parallel plates in which one of the plates is moving tangentially to the other. The motion of the plate creates a shear stress on the fluid, so the flow is driven by the action of the viscous forces that act on the fluid. Fig. 2.5 illustrates the geometry of the Couette flow.

Fig. 2.5 (a) represents a planar Couette flow, where the pressure gradient is null. If a pressure gradient is applied to the flow, a planar Couette-Poiseuille flow is obtained, as it is represented in Fig. 2.5 (b). There can also be some slip between the fluid and the wall, and that is the situation represented in Fig. 2.5 (c).

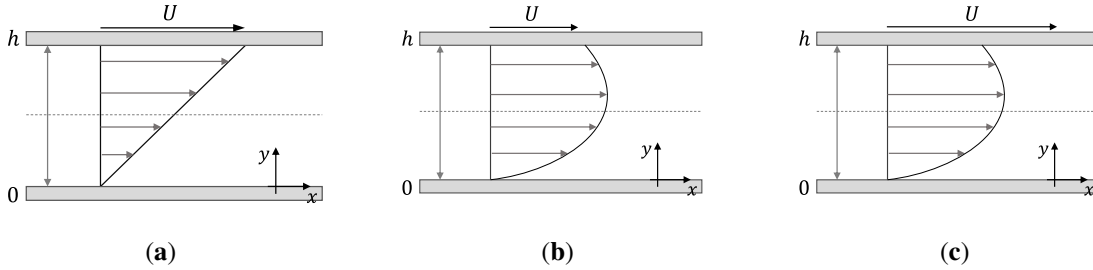


Figure 2.5: Illustration of the geometry of: (a) planar Couette flow; (b) Couette flow with an imposed pressure gradient (Couette–Poiseuille flow); (c) Couette flow with an imposed pressure gradient and asymmetric wall slip (Couette–Poiseuille flow with wall slip).

To obtain the velocity profile for the Couette–Poiseuille flow, the following no-slip boundary conditions, are applied, that is null velocity at the immobile wall:

$$u(0) = 0 \quad (2.45)$$

and an imposed constant velocity, U , at the moving wall,

$$u(h) = U. \quad (2.46)$$

To obtain the velocity profile for the Couette–Poiseuille flow under asymmetric slip, the slip boundary conditions applied are the linear and nonlinear Navier slip laws. The nonlinear Navier

slip law [26] states that the friction coefficient, k , is a function of the shear stress τ_{xy} , providing a non-linear power function given by:

$$u_w = k \left(\mp \tau_{xy,w} \right)^m, \quad (2.47)$$

where $m > 0$ ($m \in \mathbb{R}^+$), the signs \mp stand for the upper $-$ and bottom $+$ walls, assuming there is flow between parallel plates, and the coordinate system is given as in Fig. 2.5 (c). Note that, when $m = 1$, the Navier linear slip law [27] is recovered.

2.2.2 Analytical solution

The equations governing the flow of an isothermal incompressible fluid are the continuity,

$$\nabla \cdot \mathbf{u} = 0 \quad (2.48)$$

and the momentum equation,

$$\rho \frac{D\mathbf{u}}{Dt} = -\nabla p + \nabla \cdot \boldsymbol{\tau}, \quad (2.49)$$

where \mathbf{u} is the velocity vector, ρ is the density, $\frac{D}{Dt}$ is the material derivative, p is the pressure, $\boldsymbol{\tau}$ is the extra-stress tensor and t is the time.

The constitutive equation for the gPTT model is given by:

$$K(\tau_{kk}) \boldsymbol{\tau} + \lambda \overset{\square}{\boldsymbol{\tau}} = 2\eta_p \mathbf{D} \quad (2.50)$$

where

$$K(\tau_{kk}) = \Gamma(\beta) E_{\alpha,\beta} \left(\frac{\varepsilon \lambda}{\eta_p} \tau_{kk} \right), \quad (2.51)$$

is the function of the trace of extra-stress tensor and

$$E_{\alpha,\beta}(z) = \sum_{j=0}^{\infty} \frac{z^j}{\Gamma(\alpha j + \beta)}, \quad (2.52)$$

is the Mittag-Leffler function with α, β real and positive and Γ is the Gamma function. τ_{kk} is the trace of the extra-stress tensor, η_p is the polymeric viscosity coefficient, \mathbf{D} is the rate of deformation tensor, ε represents the extensibility parameter and λ is the relaxation time of the fluid. $\overset{\square}{\boldsymbol{\tau}}$ represents the Gordon-Schowalter derivative (Eq. (2.28)).

Considering a Cartesian coordinate system where x , y , and z are the streamwise, transverse and spanwise directions, respectively, and assuming that the flow is fully-developed, the governing equations can be further simplified since:

$$\frac{\partial}{\partial x} = 0 \text{ (except for pressure)}, \frac{\partial v}{\partial y} = 0, \frac{\partial p}{\partial y} = 0. \quad (2.53)$$

Therefore, Eq. (2.49) can be integrated, leading to the following general equation for the shear stress:

$$\tau_{xy} = P_x y + c_1, \quad (2.54)$$

where P_x is the pressure gradient in the x direction, τ_{xy} is the shear stress and c_1 is a stress constant. This equation is valid regardless of the rheological constitutive equation.

The constitutive equations (Eq. (2.50)) describing this flow can be further simplified leading to:

$$K(\tau_{kk})\tau_{xx} = (2 - \xi)(\lambda\dot{\gamma})\tau_{xy}, \quad (2.55)$$

$$K(\tau_{kk})\tau_{yy} = -\xi(\lambda\dot{\gamma})\tau_{xy}, \quad (2.56)$$

$$K(\tau_{kk})\tau_{xy} = \eta_p \dot{\gamma} + \left(1 - \frac{\xi}{2}\right)(\lambda\dot{\gamma})\tau_{yy} - \frac{\xi}{2}(\lambda\dot{\gamma})\tau_{xx}, \quad (2.57)$$

where the shear rate $\dot{\gamma}$ is a function of y ($\dot{\gamma}(y) \equiv \frac{du}{dy}$) and $\tau_{kk} = \tau_{xx} + \tau_{yy} + \tau_{zz}$. Under fully developed flow conditions $\tau_{zz} = 0$. Assuming that $\xi = 0$, Eq. (2.56) implies that $\tau_{yy} = 0$, and the trace of the extra-stress tensor becomes $\tau_{kk} = \tau_{xx}$. Dividing Eq. (2.55) by Eq. (2.57), $K(\tau_{xx})$ cancels out, and an explicit relationship between the streamwise normal stress and the shear stress is obtained:

$$\tau_{xx} = 2 \frac{\lambda}{\eta_p} \tau_{xy}^2. \quad (2.58)$$

Now, combining Eq. (2.57), (2.58), (2.54) and (2.51) the following shear rate profile is obtained,

$$\dot{\gamma}(y) = \Gamma(\beta) E_{\alpha, \beta} \left(\frac{2\epsilon\lambda^2}{\eta_p^2} (P_x y + c_1)^2 \right) \frac{(P_x y + c_1)}{\eta_p}. \quad (2.59)$$

2.2.3 Couette-Poiseuille flow: no-slip case

Now, applying the no-slip boundary conditions given by Eq. (2.45) and Eq. (2.46) and after some simplifications, the dimensionless velocity profile is obtained:

$$\bar{u}(\bar{y}) = \frac{\Gamma(\beta)}{\bar{P}_x} \sum_{j=0}^{\infty} \left(\left(2\epsilon Wi^2 \right)^j \frac{1}{\Gamma(\alpha j + \beta)} \frac{\left(\bar{P}_x \bar{y} + \bar{c}_1 \right)^{2j+2} - \bar{c}_1^{2j+2}}{2j+2} \right) \quad (2.60)$$

with $\bar{y} = \frac{y}{h}$, $\bar{u}(y) = \frac{\bar{u}(\bar{y})}{U}$, $\bar{c}_1 = \frac{c_1 h}{\eta_p U}$, $\bar{P}_x = \frac{P_x h^2}{\eta_p U}$ and $Wi = \frac{\lambda U}{h}$ representing the Weissenberg number. The stress constant \bar{c}_1 is obtained, by solving numerically the following equation:

$$1 = \frac{\Gamma(\beta)}{\bar{P}_x} \sum_{j=0}^{\infty} \left(\left(2\epsilon Wi^2 \right)^j \frac{1}{\Gamma(\alpha j + \beta)} \frac{\left(\bar{P}_x + \bar{c}_1 \right)^{2j+2} - \bar{c}_1^{2j+2}}{2j+2} \right). \quad (2.61)$$

Now, the influence of the Mittag-Leffler function parameters α and β on the velocity profile of the Couette-Poiseuille flow is investigated.

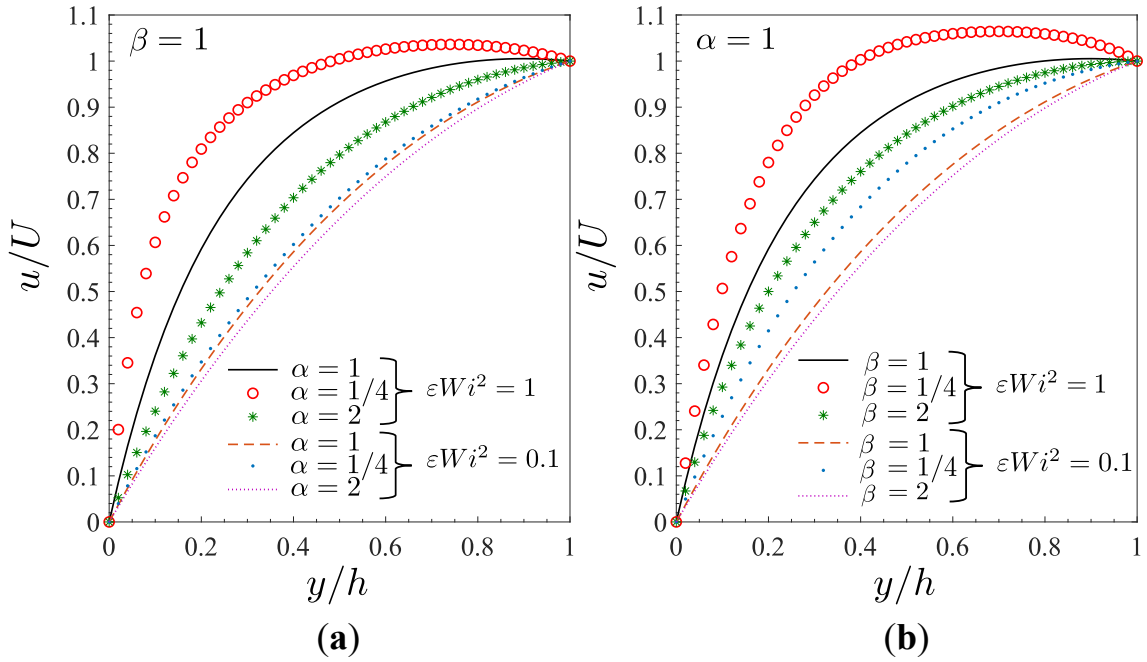


Figure 2.6: Velocity profiles calculated using Eq. (2.60) for Couette–Poiseuille flow considering two different values of ϵWi^2 and $\bar{P}_x = -1$: (a) $\beta = 1$; (b) $\alpha = 1$. The velocity profiles with $\alpha = \beta = 1$ correspond to the expPTT model.

Fig. 2.6 shows the velocity profiles obtained for the Couette–Poiseuille flow considering two different ϵWi^2 values, $\bar{P}_x = -1$ and different values of α (Fig. 2.6 (a)) and β (Fig. 2.6 (b)). In Fig. 2.6 (a), with $\beta = 1$, the flow rate decreases for $\alpha > 1$, while for $\alpha < 1$ it increases. As expected, for a constant pressure gradient, the flow rate increases with the increasing of ϵWi^2 due to shear thinning. In Fig. 2.6 (b), with $\alpha = 1$, the trends are similar to the ones obtained in Fig. 2.6 (a), but now the velocity profile is less sensitive to large values of β (with $\beta > 1$).

2.2.4 Couette-Poiseuille flow: asymmetric slip

For the Couette-Poiseuille flow under asymmetric slip, the velocity profile can be obtained integrating the shear rate subject to the nonlinear Navier slip law. Using Eq. (2.47) at the immobile bottom wall, the boundary condition is:

$$u(0) = k_1(\tau_{xy})^{m_1}, \quad (2.62)$$

and at the moving upper wall,

$$u(h) = k_2(-\tau_{xy})^{m_2}, \quad (2.63)$$

where k_1 and k_2 correspond to friction coefficients. At the immobile bottom wall, $y = 0$, and the shear stress constant c_1 is recovered, becoming:

$$u(0) = k_1(c_1)^{m_1}. \quad (2.64)$$

At the moving upper wall, $y = h$, it is obtained:

$$u(h) = k_2(-(\bar{P}_x h + \bar{c}_1))^{m_2}. \quad (2.65)$$

After some simplifications, this leads to the following dimensionless velocity profile:

$$\bar{u}(\bar{y}) = \bar{k}_2(-(\bar{P}_x + \bar{c}_1))^{m_2} + \frac{\Gamma(\beta)}{\bar{P}_x} \sum_{j=0}^{\infty} \left((2\varepsilon Wi^2)^j \frac{(\bar{P}_x \bar{y} + \bar{c}_1)^{2j+2} - (\bar{P}_x + \bar{c}_1)^{2j+2}}{(\Gamma(\alpha j + \beta))(2j+2)} \right), \quad (2.66)$$

and the stress constant \bar{c}_1 can be obtained numerically, by solving the following equation:

$$\bar{k}_2(-(\bar{P}_x + \bar{c}_1))^{m_2} - \bar{k}_1(\bar{c}_1)^{m_1} = \frac{\Gamma(\beta)}{\bar{P}_x} \sum_{j=0}^{\infty} \left((2\varepsilon Wi^2)^j \frac{(\bar{P}_x + \bar{c}_1)^{2j+2} - \bar{c}_1^{2j+2}}{(\Gamma(\alpha j + \beta))(2j+2)} \right), \quad (2.67)$$

with $\bar{k}_i = k_i U^{m_i-1} \left(\frac{\eta_P}{h} \right)^{m_i}$, for $i = \{1, 2\}$.

Now, the influence of the Mittag-Leffler function parameters α and β on the velocity profile of this flow is investigated.

Fig. 2.7 shows the velocity profiles obtained for the Couette–Poiseuille flow under asymmetric slip, for $\bar{k}_1 = 0.1$, $m_1 = 2$, $\bar{P}_x = -1$ and two different values of εWi^2 are considered.

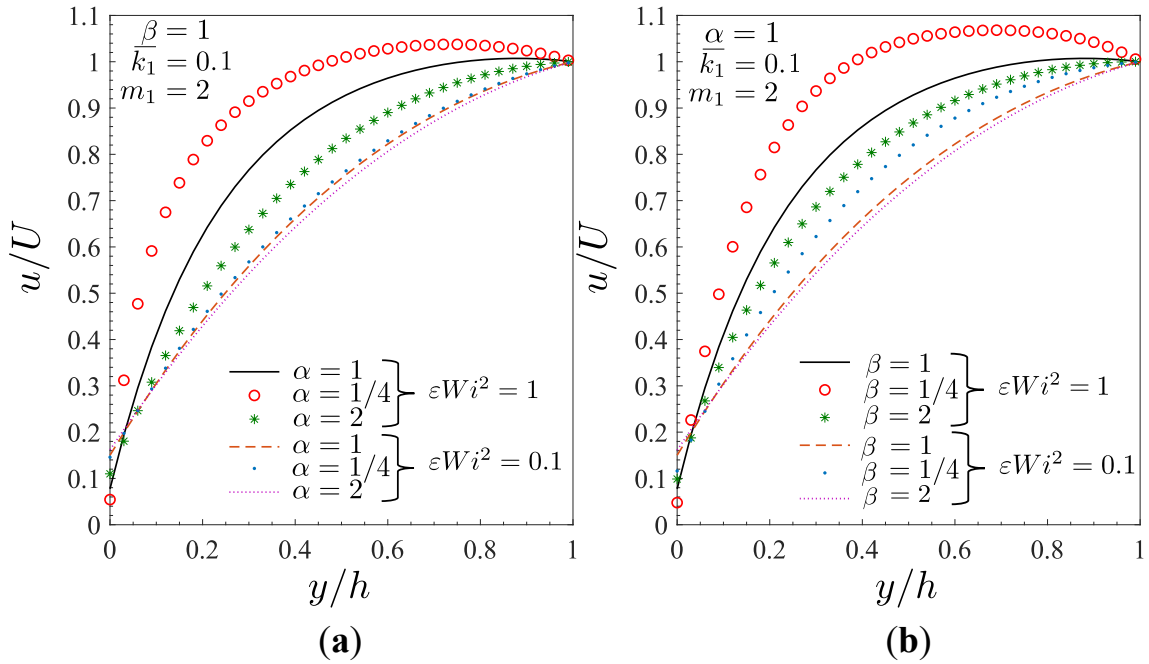


Figure 2.7: Velocity profiles calculated using Eq. (2.66) for Couette–Poiseuille flow under asymmetric slip considering two different values of εWi^2 , $\bar{P}_x = -1$, $\bar{k}_1 = 0.1$ and $m_1 = 2$: (a) $\beta = 1$; (b) $\alpha = 1$. The velocity profiles with $\alpha = \beta = 1$ correspond to the expPTT model.

Fig. 2.7 shows the velocity profiles obtained for the Couette–Poiseuille flow under asymmetric slip considering two different values of εWi^2 , $\bar{P}_x = -1$, $\bar{k}_1 = 0.1$, $m_1 = 2$ and different values of α (Fig. 2.7 (a)) and β (Fig. 2.7 (b)). In Fig. 2.7 (a), with $\beta = 1$, as εWi^2 increases, the influence of the other parameters on the velocity profile also increases. This effect is enhanced as α decreases. From Fig. 2.7 (b), with $\alpha = 1$, it is observed that the effect of decreasing β is similar to the one presented in Fig. 2.7 (a).

Fig. 2.8 presents the variation of \bar{c}_1 obtained numerically from Eq. (2.67), as a function of \bar{k}_1 , for $\bar{P}_x = -1$ and $m_1 = 1$. It is observed that the increase of the slip velocity, implies the decrease of the shear stress coefficient. This effect is more significant for lower values of εWi^2 , presenting (almost) linear dependence for $\varepsilon Wi^2 = 1$.

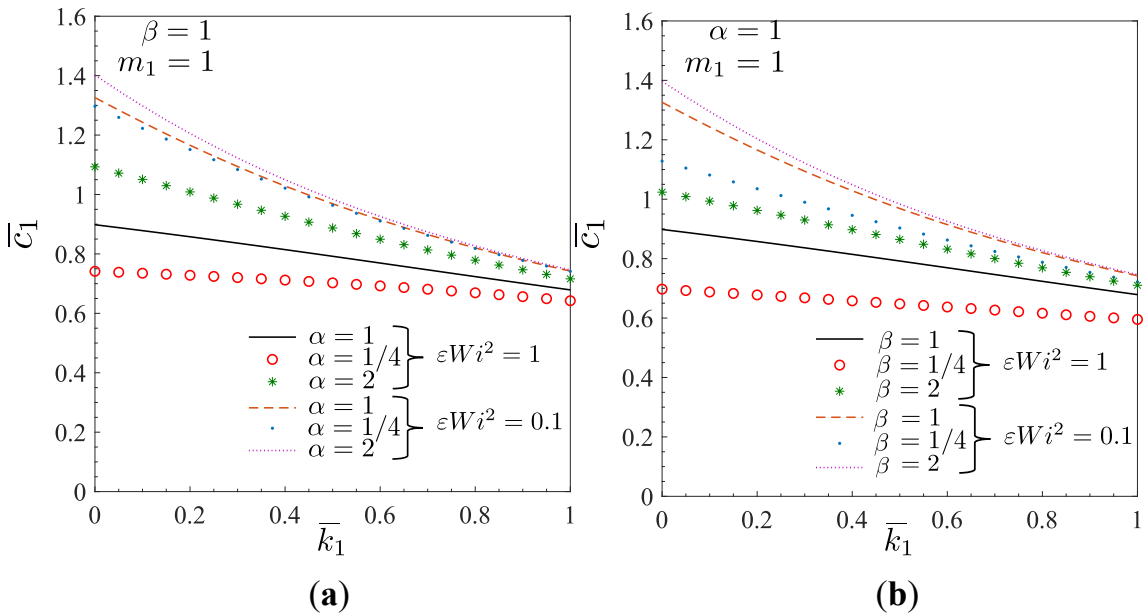


Figure 2.8: Variation of \bar{c}_1 as a function of slip coefficient \bar{k}_1 for Couette–Poiseuille flow with slip at the immobile wall and no-slip at the moving wall. **(a)** Variation of α with $\beta = 1$; **(b)** variation of β with $\alpha = 1$. The velocity profiles with $\alpha = \beta = 1$ correspond to the expPTT model.

These works are published on papers [28] and [29], which can be found in Part III of this thesis.

2.3 Annular flow

Annular fluid flows are usually found in industrial processes such as cable coating, food processing and drilling. Usually in the drilling process, there is rotation of the inner cylinder together with cylinder eccentricity, but in this thesis is going to be considered the simplified case. In these processes, the fluids are mixtures of various substances, such as water, particles, oils, and other long-chain molecules, that gives the fluid non-Newtonian properties.

Many analytical and numerical solutions for annular flows using different constitutive rheological models or different boundary conditions can be found in the literature [19, 23, 30–38]. Among these works, all the different variants of the PTT model have already been studied: linear, quadratic and exponential. The exception is for the gPTT model [3], that uses the Mittag–Leffler function (Eq. 2.31).

In this section, new semi-analytical solution for the annular flow using the gPTT constitutive model are presented. For that, a parametric study is performed studying the influence of the gPTT parameters.

Each contribution related to the work objectives, presented in section 2.3, is explained in detail. Given that the present dissertation falls into the category of *multi-paper dissertation*, and in order to keep repetition of information at a minimum level, the complete paper related to this section is presented in Part III of this thesis.

2.3.1 Problem definition

Fig. 2.9 illustrates a pressure-driven annular flow of a viscoelastic gPTT fluid, being R the radius of the outer cylinder and aR the radius of the inner cylinder, with $0 < a < 1$.

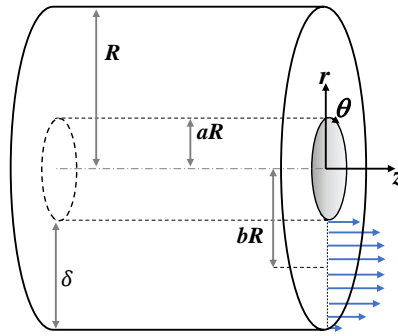


Figure 2.9: Schematic of the flow in an annular region.

The boundary conditions considered are the no-slip boundary conditions at the inner and the outer cylinders, that means, $u(R) = 0$ and $u(aR) = 0$.

2.3.2 Analytical solution

To derive the analytical solution for the gPTT model, a steady fully-developed pressure-driven annular flow is considered (cf. Fig. 2.9). For that, a unidirectional flow in cylindrical coordinates

is considered, where the outer radius is R and the inner radius is aR .

The equations governing the flow of an isothermal incompressible fluid are the continuity,

$$\nabla \cdot \mathbf{u} = 0 \quad (2.68)$$

and the momentum equation,

$$\rho \frac{D\mathbf{u}}{Dt} = -\nabla p + \nabla \cdot \boldsymbol{\tau}, \quad (2.69)$$

where \mathbf{u} is the velocity vector, ρ is the density, $\frac{D}{Dt}$ is the material derivative, p is the pressure, $\boldsymbol{\tau}$ is the extra-stress tensor and t is the time.

The constitutive equation for the gPTT model is given by:

$$K(\tau_{kk}) \boldsymbol{\tau} + \lambda \overset{\square}{\boldsymbol{\tau}} = 2\eta_p \mathbf{D} \quad (2.70)$$

where

$$K(\tau_{kk}) = \Gamma(\beta) E_{\alpha,\beta} \left(\frac{\varepsilon \lambda}{\eta_p} \tau_{kk} \right), \quad (2.71)$$

is the function of the trace of extra-stress tensor and

$$E_{\alpha,\beta}(z) = \sum_{j=0}^{\infty} \frac{z^j}{\Gamma(\alpha j + \beta)}, \quad (2.72)$$

is the Mittag-Leffler function with α, β real and positive and Γ is the Gamma function. τ_{kk} is the trace of the extra-stress tensor, η_p is the polymeric viscosity coefficient, \mathbf{D} is the rate of deformation tensor, ε represents the extensibility parameter and λ is the characteristic relaxation of the fluid. $\overset{\square}{\boldsymbol{\tau}}$ represents the Gordon-Schowalter derivative (Eq. (2.28)).

The momentum equation, Eq. (2.69), simplifies to

$$\frac{1}{r} \frac{d(r\tau_{rz})}{dr} = P_z, \quad (2.73)$$

where $P_z \equiv \frac{dp}{dz}$ is the constant streamwise pressure gradient and τ_{rz} is the shear stress.

In order to obtain closed form analytical solutions, the slip parameter in the Gordon-Schowalter derivative (Eq. 2.28) is set to $\xi = 0$. Therefore, the constitutive equation for the gPTT model for this flow can be further simplified, leading to:

$$K(\tau_{kk})\tau_{zz} = 2\lambda\dot{\gamma}\tau_{rz}, \quad (2.74)$$

$$K(\tau_{kk})\tau_{rr} = 0, \quad (2.75)$$

$$K(\tau_{kk})\tau_{rz} = \eta_p \dot{\gamma}, \quad (2.76)$$

where the velocity gradient $\dot{\gamma}$ is a function of r ($\dot{\gamma}(r) \equiv \frac{du}{dr}$) and $\tau_{kk} = \tau_{\theta\theta} + \tau_{zz} + \tau_{rr}$ is the trace of the extra-stress tensor. Under fully-developed flow conditions, $\tau_{\theta\theta} = 0$ and $\tau_{rr} = 0$, thus the trace of the extra-stress tensor becomes $\tau_{kk} = \tau_{zz}$.

Integrating the momentum equation results in,

$$\tau_{rz} = \frac{P_z}{2}r + \frac{c}{r} \quad (2.77)$$

where c is a constant that results from the integration. Assuming that $\tau_{rz} = 0$ at $r = bR$ (the location of the velocity maximum, see Fig. 2.9), with $a < b < 1$, the integration constant ($c = -(P_z/2)b^2R^2$), is calculated, resulting in the following shear stress distribution,

$$\tau_{rz} = \frac{-P_z bR}{2} \left(\frac{bR}{r} - \frac{r}{bR} \right). \quad (2.78)$$

Dividing Eq. (2.74) by Eq. (2.76) results in the following relationship between normal and shear stresses,

$$\tau_{zz} = \frac{2\lambda}{\eta_p} \tau_{rz}^2. \quad (2.79)$$

Solving Eq. (2.74) for $\dot{\gamma}$, and using Eq. (2.78) and Eq. (2.79), results in the following velocity gradient distribution:

$$\frac{du}{dr} = -\frac{\Gamma(\beta)}{\eta_p} E_{\alpha,\beta} \left(\frac{2\varepsilon\lambda^2}{\eta_p^2} \left(\frac{P_z bR}{2} \left(\frac{bR}{r} - \frac{r}{bR} \right) \right)^2 \right) \frac{P_z bR}{2} \left(\frac{bR}{r} - \frac{r}{bR} \right). \quad (2.80)$$

The velocity gradient is written in dimensionless form, using the Weissenberg number, that for this case is defined as, $Wi = \lambda U_c / \delta$, where $U_c = -P_z \delta^2 / \eta_p$ is a characteristic velocity of the flow and δ is the gap between the two cylinders in the annulus. It is also defined that $\bar{u} = u/U_c$ and $\bar{r} = r/\delta$ as the normalized radius/distance between the inner and outer cylinders ($\bar{R} = R/\delta$). This gives the following dimensionless velocity gradient:

$$\frac{d\bar{u}}{d\bar{r}} = \frac{\Gamma(\beta)}{2} \left(\frac{b^2 \bar{R}^2}{\bar{r}} - \bar{r} \right) E_{\alpha,\beta} \left(\frac{\varepsilon Wi^2}{2} \left(\frac{b^2 \bar{R}^2}{\bar{r}} - \bar{r} \right)^2 \right). \quad (2.81)$$

The velocity profile is now obtained numerically, solving the nonlinear problem, where given εWi^2 and a , the value of b needs to be found and satisfies,

$$\int_{a\bar{R}}^{\bar{R}} \frac{d\bar{u}}{d\bar{r}} d\bar{r} = 0. \quad (2.82)$$

Using the value of b , then the velocity profile is computed:

$$\bar{u}(\bar{r}) = \int_{a\bar{R}}^{\bar{r}} \frac{\Gamma(\beta)}{2} \left(\frac{b^2 \bar{R}^2}{\bar{r}} - \bar{r} \right) E_{\alpha,\beta} \left(\frac{\varepsilon Wi^2}{2} \left(\frac{b^2 \bar{R}^2}{\bar{r}} - \bar{r} \right)^2 \right) d\bar{r}, \quad (2.83)$$

where $0 < a < 1$ is defined by the user. Eq. (2.83) results from the no-slip boundary condition, $\bar{u}(\bar{R}) = 0$. The velocity profile, Eq. (2.83), can be easily approximated numerically by a simple quadrature rule. The solution of Eq. (2.82) can be obtained by defining $F(b) = \int_{a\bar{R}}^{\bar{R}} \frac{d\bar{u}}{d\bar{r}} d\bar{r}$. So, there exists $0 < a < b < 1$ such that $F(b) = 0$.

Eq. (2.81) is further expanded using the definition of the Mittag–Leffler function, resulting in:

$$\frac{d\bar{u}}{d\bar{r}} = \frac{\Gamma(\beta)}{2} \left(\frac{b^2 \bar{R}^2}{\bar{r}} - \bar{r} \right) \sum_{j=0}^{\infty} \frac{1}{\Gamma(\alpha j + \beta)} \left(\frac{\varepsilon W i^2}{2} \left(\frac{b^2 \bar{R}^2}{\bar{r}} - \bar{r} \right)^2 \right)^j \quad (2.84)$$

$$= \frac{\Gamma(\beta)}{2} \sum_{j=0}^{\infty} \frac{1}{\Gamma(\alpha j + \beta)} \left(\frac{\varepsilon W i^2}{2} \right)^j \left(\frac{b^2 \bar{R}^2}{\bar{r}} - \bar{r} \right)^{2j+1} \quad (2.85)$$

and the velocity profile is obtained from the integration of each term in this sum, leading to the following expression:

$$\bar{u}(\bar{r}) = \frac{\Gamma(\beta)}{2} \sum_{j=0}^{\infty} \frac{1}{\Gamma(\alpha j + \beta)} \left(\frac{\varepsilon W i^2}{2} \right)^j \int_{a\bar{R}}^{\bar{r}} \left(\frac{b^2 \bar{R}^2}{\bar{r}} - \bar{r} \right)^{2j+1} d\bar{r}. \quad (2.86)$$

The integral $\int \left(\frac{A}{\bar{r}} - \bar{r} \right)^{2j+1} d\bar{r}$, with $A = b^2 \bar{R}^2$, is easily computed using the Newton's binomial. So, the velocity profile, is given by:

$$\bar{u}(\bar{r}) = \frac{\Gamma(\beta)}{2} \sum_{j=0}^{\infty} \frac{1}{\Gamma(\alpha j + \beta)} \left(\frac{\varepsilon W i^2}{2} \right)^j \left[\sum_{k=0}^{2j+1} \binom{2j+1}{k} \int_{a\bar{R}}^{\bar{r}} \left(\frac{b^2 \bar{R}^2}{\bar{r}} \right)^{2j+1-k} (-\bar{r})^k d\bar{r} \right] \quad (2.87)$$

and is rewritten as:

$$\bar{u}(\bar{r}) = \frac{\Gamma(\beta)}{2} \sum_{j=0}^{\infty} \frac{1}{\Gamma(\alpha j + \beta)} \left(\frac{\varepsilon W i^2}{2} \right)^j \left[\sum_{k=0}^{2j+1} \binom{2j+1}{k} (-1)^k (b^2 \bar{R}^2)^{2j+1-k} f_{kj}(a, \bar{r}) \right] \quad (2.88)$$

where:

$$f_{kj}(a, \bar{r}) = \begin{cases} \ln \left(\frac{\bar{r}}{a\bar{R}} \right), & \text{if } k = j \\ \frac{\bar{r}^{2(k-j)} - (a\bar{R})^{2(k-j)}}{2(k-j)}, & \text{if } k \neq j \end{cases}. \quad (2.89)$$

Although Eq. (2.88) is an infinite series, a solution with a fair number of correct decimal places is obtained (depending on the problem and the parameters used). The numerical solution of the velocity profile given by Eq. (2.83) is compared with the analytical solution of Eq. (2.88). These results are obtained using the *Mathematica* software version 13.3 and first it is considered a high-precision numerical solution, where the value of b is obtained using the secant method, and

then Eq. (2.81) is numerically integrated. This highly accurate numerical solution of the velocity profile is then used as a reference to perform an investigation of the influence of the number of terms in the series on the error of the solution. The new truncated solution is obtained from Eq. (2.88), truncating the sum with $j + 1$ terms. It is considered 200 equidistant mesh points along the cylinder gap and the maximum relative error obtained at these points (boundaries excluded) is measured.

The error is calculated by $\frac{|\bar{u}(\bar{r})_{num} - \bar{u}(\bar{r})_t|}{\bar{u}(\bar{r})_{num}}$, where $\bar{u}(\bar{r})_{num}$ is the approximate value of the velocity and $\bar{u}(\bar{r})_t$ is the velocity value from the truncated series. Three different values of εWi^2 are considered: 0.05, 3.2 and 5. It is assumed that $\beta = 1$, and two different values of α , 0.5 and 1.5, are tested. The values of α are the ones changed, because this parameter induces more changes in the series. The value of $a = 0.5$ is used in all cases.

Table 2.1 shows the maximum relative errors, in percentage. For $\varepsilon Wi^2 = 0.05$, the error is low, even when considering a single term in the series (Eq. (2.88)). For $\alpha = 1.5$ the error is much smaller, with the decrease in error becoming less pronounced as the number of terms in the series increases. This is due to the number of significant digits considered.

Table 2.1: Maximum relative errors (in percentage) for $\varepsilon Wi^2 = 0.05$.

j	$\alpha = 0.5$	$\alpha = 1.5$
1	5.669×10^{-1}	9.405×10^{-2}
2	1.342×10^{-2}	4.757×10^{-4}
4	4.550×10^{-4}	4.432×10^{-4}

Tables 2.2 and 2.3 show the maximum relative errors in percentage for $\varepsilon Wi^2 = 3.2$ and 5, respectively. As εWi^2 increases, the series solution shows convergence problems, and as α increases (see Table 2.3) the error decreases faster as the number of terms in the series increases (note also that in this case, a higher εWi^2 value is considered). The corresponding velocity profiles are shown in Fig. 2.10, where u/U_c is the velocity profile normalised by the characteristic velocity, using the highly accurate numerical solution. These particular results indicate that the velocity profile converges to the correct profile as the number of terms in the series increases, and that this convergence is slower for low values of α .

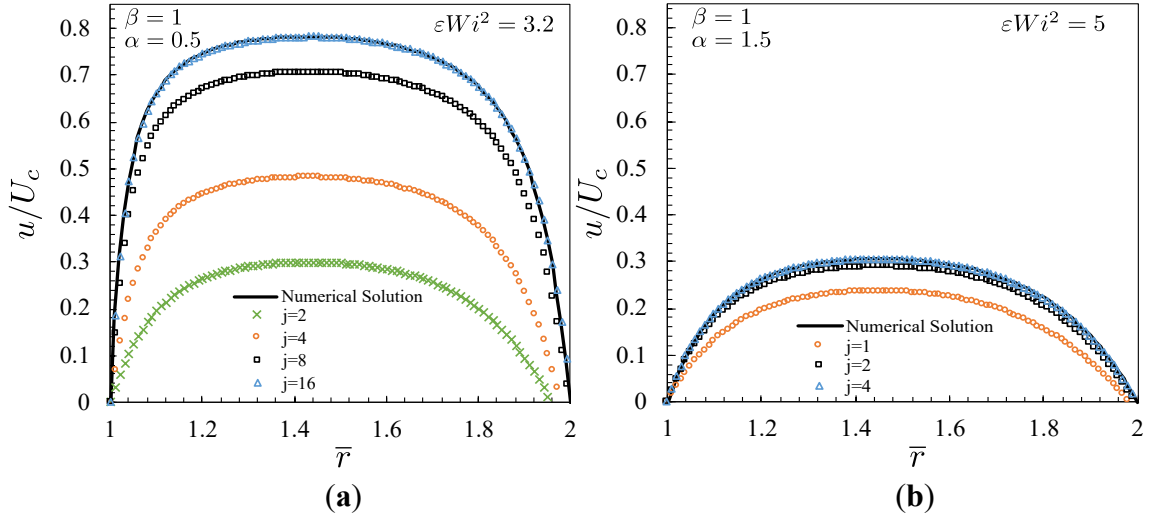
Table 2.2: Maximum relative errors (in percentage) for $\varepsilon Wi^2 = 3.2$.

j	$\alpha = 0.5$
2	1.782×10^2
4	1.580×10^2
8	5.874×10^1
16	8.681×10^{-1}

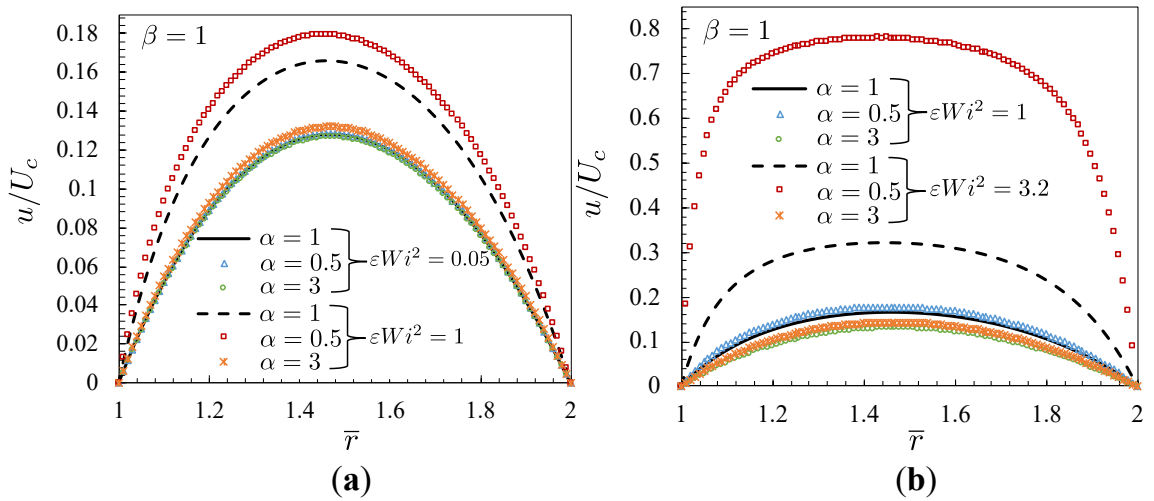
Therefore, the sum of Eq. (2.88) is truncated with $j + 1$ terms, and to present the results $j = 15$ is considered.

Table 2.3: Maximum relative errors (in percentage) for $\varepsilon Wi^2 = 5$.

j	$\alpha = 1.5$
1	1.414×10^2
2	4.773×10^1
4	1.409×10^0
8	4.275×10^{-4}

Figure 2.10: Velocity profiles for $\beta = 1$, two different values of α , 0.5 and 1.5 and two different values of εWi^2 , 3.2 and 5: (a) $\alpha = 0.5$; (b) $\alpha = 1.5$.

Now, the influence of the Mittag–Leffler function parameters α and β on the velocity profile of this flow is studied. Fig. 2.11 shows the velocity profiles for $\beta = 1$, three different values of α , 0.5, 1 and 3 and three different values of the εWi^2 , 0.05, 1 and 3.2.

Figure 2.11: Velocity profiles calculated using Eq. (2.88) for the annular flow considering $\beta = 1$, different values of εWi^2 and different values of α : (a) $\varepsilon Wi^2 = 0.05$ and 1; (b) $\varepsilon Wi^2 = 1$ and 3.2. The velocity profiles with $\alpha = \beta = 1$ correspond to the expPTT model.

For $\varepsilon Wi^2 = 0.05$ (Fig. 2.11 (a)) the velocity profiles almost overlap, but when εWi^2 increases to 1, that does not happen, and the highest velocity and flow rate is obtained for $\alpha = 0.5$. This behaviour is more pronounced when the elasticity increases (see Fig. 2.11 (b)). When $\varepsilon Wi^2 = 3.2$, the differences in the flow rates are obvious, except for $\alpha = 3$, where the velocity profile almost overlaps with the case with $\varepsilon Wi^2 = 1$. It is interesting to see that for $\alpha = \beta = 1$ a parabolic velocity profile typical of Newtonian fluids still appears, while decreasing α a very pronounced plug-like profile is observed.

Figures 2.12 (a), (b) and (c) show the influence of β on the velocity profile. The results are similar to the ones obtained for the variation of α . For a small value of εWi^2 (Fig. 2.12 (a)), the velocity profiles almost overlap for all values of β , but as εWi^2 increases (Fig. 2.12 (b) and (c)), the velocity and the flow rate increase when the values of β decrease. This effect is more pronounced for $\beta = 0.5$.

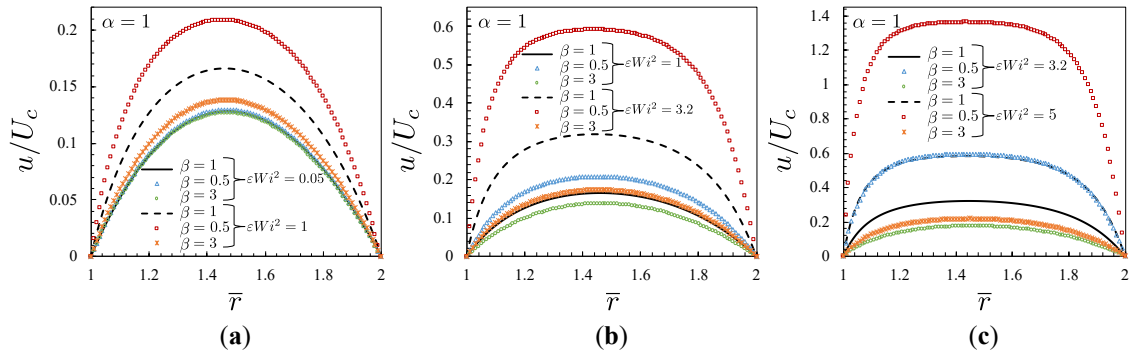


Figure 2.12: Velocity profiles calculated using Eq. (2.88) for the annular flow considering $\alpha = 1$, different values of εWi^2 and different values of β : (a) $\varepsilon Wi^2 = 0.05$ and 1; (b) $\varepsilon Wi^2 = 1$ and 3.2; (c) $\varepsilon Wi^2 = 3.2$ and 5. The velocity profiles with $\alpha = \beta = 1$ correspond to the expPTT model.

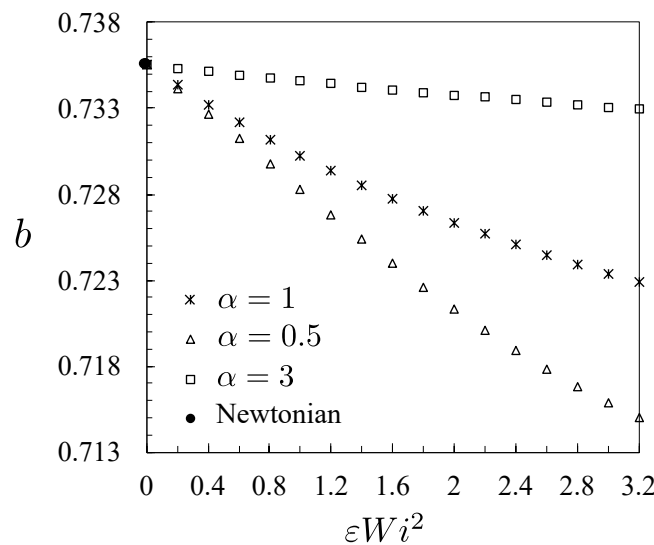


Figure 2.13: Variation of b with the variation εWi^2 for different values of α . The dotted symbol corresponds to value of b obtained for a Newtonian fluid [30, 39].

Another aspect studied is the value obtained for b when εWi^2 increases (see Fig. 2.13). Three different values of α , 0.5, 1 and 3, are considered and b is calculated for different values of εWi^2 . It can be seen that the value of b decreases with the increase of εWi^2 , and that for $\alpha = 3$ the relation is almost linear. Notice also that, when $\alpha = 0.5$, the decrease is more pronounced. Figure 2.13 shows that b decreases with the increase of the fluid elasticity, a trend also observed on the velocity profiles of Figs. 2.12, since the values of b represent the radial position of the maximum value for the velocity profile. Therefore, the point of maximum velocity approaches the inner cylinder walls as the elasticity of the fluid increases.

This work is published on paper [40], which can be found in Part III of this thesis.

2.4 Electro-osmotic flow

Electro-osmosis (EO) is a type of flow that occurs at micro- and nano-devices and is particularly useful for applications in medicine, biochemistry and miniaturised industrial processes. Generically, EO is a basic electrokinetic phenomenon, where the flow of an electrolyte is driven by an external potential difference between the inlet and outlet of the channel, acting on ions that are imbalanced in the near-wall region of the fluid due to the interaction between the dielectric channel walls and the fluid, as represented in Fig. 2.14.

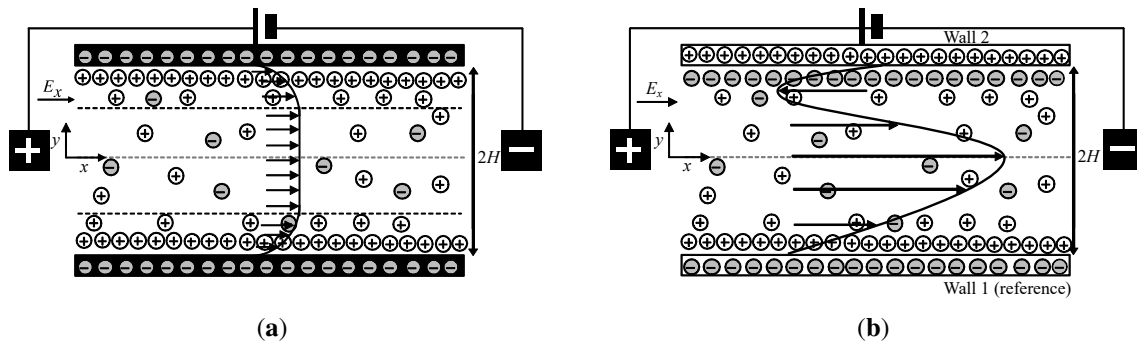


Figure 2.14: Schematic of the flow in a planar microchannel. (a) EO flow with symmetric zeta potentials at the walls; (b) EO flow with asymmetric zeta potentials at the walls.

Specifically, these are layers of higher concentration of counter-ions within the fluid, that move under the action of the applied electric field, which then drags by viscous forces the neutral core as a solid body [41].

As can be seen in Fig. 2.14 (a), the ion separation appears due to the interaction between the walls and the fluid. Here, the illustrated negatively charged walls of the microchannel attract counter-ions forming layers of positively charged fluid near the walls and with the co-ions predominantly staying at the core. At such dilute concentrations, the fluid core remains essentially neutral. The Stern layers, that are very thin layers of immobile counter-ions that remain at the walls, are followed by thicker more diffuse layers of mobile counter-ions. The electric double layer (EDL) is formed by these two layers near the wall.

A DC potential difference between the two electrodes at the inlet and outlet generates an external electric field that exerts a body force on the counter-ions of the EDL, which flow along the channel dragging the neutral liquid core. The pressure difference that can also be applied between the inlet and outlet can act in the same direction of the electric field or in the opposite direction.

There is a vast literature dealing with EO flow for Newtonian fluids [42–49] and as reviewed by Zhao and Yang [50], there is also a fair amount of literature that deals with EO flows of non-Newtonian fluids, as can be seen in [51–57]. In what concerns EO flow where the zeta potentials at the walls are asymmetric, Afonso et al. [58] provided analytical solutions for combined EO and pressure-driven flows, where asymmetric boundary conditions with unequal zeta potentials at the channel walls were considered, and the analyzed fluids were characterized by the linearPTT model and the finite extensible nonlinear elastic model with Peterlin's approximation (FENE-P).

Escandón et al. [59] presented both analytical and numerical solutions for transient EO flows in microchannels, using a Maxwell fluid and they covered symmetric and asymmetric uniform zeta potentials. Sadek and Pinho [60] presented analytical solutions for the oscillatory shear flow of viscoelastic fluids induced by EO forcing, specifically exploring the case of a straight microchannel with asymmetric wall zeta potentials, considering for the rheological behavior of the fluid, a multi-mode UCM model. Sanchez et al. [61] obtained analytical solutions for an electrokinetic battery comprising parallel plates, driven by osmotic flow, where the Debye–Hückel approximation to calculate the EDL potential coupled with asymmetric hydrodynamic slippage were used. The authors explicitly addressed both asymmetries in the Navier slip lengths and zeta potentials, providing insights into the interplay of these boundary conditions.

There are new recent studies where the gPTT model has been studied for EO flow. Teodoro et al. [62] derived an approximate solution for laminar viscoelastic fluid flow through a parallel flat plate microchannel driven by EO and external pressure forces, and incorporated a nonlinear Navier slip law at the wall, depicting a power-law behavior on shear stress. The Debye–Hückel approximation for the EDL is applied, assuming symmetric zeta potentials at the wall. Furthermore, Hernandez et al. [63] investigated EO flow in a microchannel with a viscoelastic fluid, using the gPTT model as a constitutive equation, where the thermodiffusion effect is explored and the results compared with those obtained through the linearPTT model (as seen in [64]).

In this section, new analytical and numerical equations for the EO flow of a gPTT fluid are presented and a parametric study is performed, studying the influence of the gPTT parameters on this flow. For that, it is considered the case where the zeta potentials at the walls are symmetric and the case where the zeta potentials at the walls are asymmetric.

Each contribution related to the work objectives, presented in section 2.4, are explained in detail. Given that the present dissertation falls into the category of *multi-paper dissertation*, and in order to keep repetition of information at a minimum level, the complete papers related to this section is presented in Part III of this thesis.

2.4.1 Problem definition

Fig. 2.14 illustrates a combined EO/pressure-driven channel flow of a viscoelastic gPTT fluid in a microchannel. Here x , y and z represent the streamwise, transverse and spanwise directions, respectively, and the channel width is $2H$. The channel size in the spanwise direction is much larger than H , so the flow is assumed to be fully-developed.

The boundary conditions applied to obtain the analytical solution are the no-slip condition at the walls. Since the flow is fully-developed, the velocity and stress fields only depend on the transverse coordinate y [51, 52].

2.4.2 Analytical solution

The equations governing the flow of an isothermal incompressible fluid are the continuity equation,

$$\nabla \cdot \mathbf{u} = 0 \quad (2.90)$$

and the momentum equation, that for EO flow has a new term that accounts the electric part and is given by:

$$\rho \frac{D\mathbf{u}}{Dt} = -\nabla p + \nabla \cdot \boldsymbol{\tau} + \rho_e \mathbf{E}, \quad (2.91)$$

where \mathbf{u} is the velocity vector, ρ is the density, $\frac{D}{Dt}$ is the material derivative, p is the pressure, $\boldsymbol{\tau}$ is the extra-stress tensor, t is the time, \mathbf{E} is the electric field and ρ_e is the electric charge density in the fluid.

The constitutive equation for the gPTT model is given by:

$$K(\tau_{kk}) \boldsymbol{\tau} + \lambda \overset{\square}{\boldsymbol{\tau}} = 2\eta_p \mathbf{D} \quad (2.92)$$

where

$$K(\tau_{kk}) = \Gamma(\beta) E_{\alpha,\beta} \left(\frac{\varepsilon \lambda}{\eta_p} \tau_{kk} \right), \quad (2.93)$$

is the function of the trace of extra-stress tensor and

$$E_{\alpha,\beta}(z) = \sum_{j=0}^{\infty} \frac{z^j}{\Gamma(\alpha j + \beta)}, \quad (2.94)$$

is the Mittag-Leffler function with α, β real and positive and Γ is the Gamma function. τ_{kk} is the trace of the extra-stress tensor, η_p is the polymeric viscosity coefficient, \mathbf{D} is the rate of deformation tensor, ε represents the extensibility parameter and λ is the relaxation time of the fluid. $\overset{\square}{\boldsymbol{\tau}}$ represents the Gordon-Schowalter derivative (Eq. (2.28)).

2.4.2.1 Electric potential

The electrostatic field, \mathbf{E} is related with the electric potential, Φ , through:

$$\mathbf{E} = -\nabla \Phi \quad (2.95)$$

where Φ is governed by:

$$\nabla^2 \Phi = -\frac{\rho_e}{\epsilon} \quad (2.96)$$

with ϵ representing the dielectric constant of the solution. The electric potential includes two different contributions, $\Phi = \phi + \psi$, where ϕ is the electric potential generated by the electrodes, placed at the inlet and outlet of the flow geometry, and ψ is associated with the charge distribution near the walls. Therefore, the imposed potential is described by a Laplace equation, $\nabla^2 \phi = 0$, and the induced potential is described by a Poisson equation:

$$\nabla^2 \psi = -\frac{\rho_e}{\epsilon}. \quad (2.97)$$

In some circumstances, such as when the flow and the ion distributions are fully-developed, the EDLs are thin and do not overlap at the centre of the channel. Significant variations of ψ only

occur in the transverse direction, and a stable Boltzmann distribution of ions occurs in the EDL. So, the net electric charge density, ρ_e , for an electrolyte in equilibrium near a charged surface is given by the following Boltzmann distribution [41]:

$$\rho_e = -2n_0ez \sinh\left(\frac{ez}{k_BT}\psi\right), \quad (2.98)$$

where n_0 is the ion density, e the elementary charge, z the valence of the ions, T the absolute temperature and k_B the Boltzmann constant.

Combining Eq. (2.97) for the induced potential equation, that for fully-developed steady flow becomes,

$$\frac{d^2\psi}{dy^2} = -\frac{\rho_e}{\epsilon}, \quad (2.99)$$

with Eq. (2.98), leads to the Poisson-Boltzmann equation, given by:

$$\frac{d^2\psi}{dy^2} = \frac{2n_0ez}{\epsilon} \sinh\left(\frac{ez}{k_BT}\psi\right). \quad (2.100)$$

Assuming the Debye-Hückel linearization principle, a valid approximation for low values of ψ [51, 52, 65], the Poisson-Boltzmann equation (Eq. (2.100)) for the, two-dimensional (2D) channel flow becomes,

$$\frac{d^2\psi}{dy^2} = \kappa^2\psi, \quad (2.101)$$

where $\kappa^2 = 2n_0e^2z^2/\epsilon k_BT$ is the Debye-Hückel parameter, which is related to the thickness of the Debye layer, $\lambda_D = 1/\kappa$, also called the EDL thickness.

2.4.3 EO flow: under symmetric zeta potentials

In this section, the analytical solution for the gPTT model considering fully-developed pure EO flow is derived assuming symmetric zeta potentials at the walls (see Fig. 2.14 (a)).

When symmetric zeta potential at the walls are assumed, for the Poisson-Boltzmann equation, the boundary conditions are: at the symmetry plane, $\frac{d\psi}{dy}|_{y=0} = 0$ and the zeta potential at the wall is $\psi_{wall} = \psi_0$. Integrating Eq. (2.101) and applying these boundary conditions, leads to the following induced electric field, ψ :

$$\psi(y) = \psi_0 \frac{\cosh(\kappa y)}{\cosh(\kappa H)}, \quad (2.102)$$

for $|y| \leq H$. So, the electric charge density, ρ_e is given by:

$$\rho_e = -\epsilon\psi_0\kappa^2 \frac{\cosh(\kappa y)}{\cosh(\kappa H)}. \quad (2.103)$$

The momentum equation, Eq. (2.91), becomes:

$$\frac{d\tau_{xy}}{dy} = P_x - \rho_e E_x, \quad (2.104)$$

where $E_x \equiv \frac{d\phi}{dx}$ is the imposed constant streamwise gradient of electric potential. This equation is valid regardless of the rheological constitutive equation considered.

Using Eq. (2.103) and considering that the shear stress at the centreline is zero, Eq. (2.104) is integrated, leading to the following shear stress distribution:

$$\tau_{xy} = \epsilon\psi_0 E_x \kappa \frac{\sinh(\kappa y)}{\cosh(\kappa H)} + P_x y. \quad (2.105)$$

The constitutive equations for the gPTT model are Eq. (2.55), (2.56) and (2.57) (see section 2.2). In order to obtain closed form analytical solutions, the slip parameter in the Gordon-Schowalter derivative (Eq. (2.28)) is set to $\xi = 0$. So, with the same procedure described in section 2.2, Eq. (2.106) is obtained:

$$\tau_{xx} = 2 \frac{\lambda}{\eta_p} \tau_{xy}^2. \quad (2.106)$$

Now combining Eqs. (2.57), (2.106), (2.105) and (2.93) the following velocity gradient profile is obtained,

$$\dot{\gamma}(y) = \frac{\Gamma(\beta)}{\eta_p} E_{\alpha,\beta} \left(\frac{2\epsilon\lambda^2}{\eta_p^2} \left(\epsilon\psi_0 E_x \kappa \frac{\sinh(\kappa y)}{\cosh(\kappa H)} + P_x y \right)^2 \right) \left(\epsilon\psi_0 E_x \kappa \frac{\sinh(\kappa y)}{\cosh(\kappa H)} + P_x y \right). \quad (2.107)$$

The dimensionless velocity gradient becomes:

$$\frac{d\bar{u}}{d\bar{y}} = \Gamma(\beta) E_{\alpha,\beta} \left(\frac{2\epsilon Wi^2}{\bar{\kappa}^2} \left(\Upsilon \bar{y} - \bar{\kappa} \frac{\sinh(\bar{\kappa} \bar{y})}{\cosh(\bar{\kappa})} \right)^2 \right) \left(\Upsilon \bar{y} - \bar{\kappa} \frac{\sinh(\bar{\kappa} \bar{y})}{\cosh(\bar{\kappa})} \right), \quad (2.108)$$

where $Wi = \lambda \kappa u_{sh}$ is the Weissenberg number and u_{sh} is the Helmholtz-Smoluchowski electro-osmotic velocity, defined as $u_{sh} = -\frac{\epsilon\psi_0 E_x}{\eta_p}$, $\bar{u} = \frac{u}{u_{sh}}$, $\bar{y} = \frac{y}{H}$ and $\bar{\kappa} = \kappa H$. The non-dimensional parameter $\Upsilon = -\frac{H^2}{\epsilon\psi_0} \left(\frac{P_x}{E_x} \right)$ represents the ratio of pressure to EO driving forces.

Eq. (2.108) has an analytical solution only for pure EO flow and provided further assumptions are made, whereas for the combined situation with a pressure gradient, the solution is obtained numerically (see [56]).

For pure EO flow, $\Upsilon = 0$ and the velocity profile is obtained integrating the velocity gradient profile, subjected to the no-slip boundary condition at the top (+) or bottom (-) walls, $\bar{u}(\bar{y} = \pm 1) = 0$. Simplifying Eq. (2.108), the equation to be integrated is:

$$\bar{u}(\bar{y}) = \int_{\bar{y}}^1 \left(\Gamma(\beta) \bar{\kappa} \sum_{j=0}^{\infty} \left(2\epsilon Wi^2 \right)^j \left(\frac{\sinh(\bar{\kappa} \bar{z})}{\cosh(\bar{\kappa})} \right)^{2j+1} \frac{1}{\Gamma(\alpha j + \beta)} \right) d\bar{z}. \quad (2.109)$$

To compute the integral in Eq. (2.109), the approximation $\sinh(\bar{\kappa} \bar{y}) \approx \frac{1}{2} \exp(\bar{\kappa} \bar{y})$ is used, which is usually accurate because in most micro-devices the thickness of the EDL is very small, about 1 to 3 orders of magnitude smaller than the width of the microchannel, so $\bar{\kappa}$ is a large value. However, close to the centreline ($\bar{y} \sim 0$) the approximation becomes less adequate (in this case, the Simpson's quadrature rule is used to obtain the approximate solution of the differential equation).

Assuming $\sinh(\bar{\kappa} z) \approx \frac{1}{2} \exp(\bar{\kappa} z)$, $z \in (\bar{y}, 1)$, the integration (Eq. (2.109)) gives the following velocity profile:

$$\bar{u}(\bar{y}) \approx \frac{\Gamma(\beta)}{2 \cosh(\bar{\kappa})} \sum_{j=0}^{\infty} \left(\frac{\varepsilon W i^2}{2 \cosh^2(\bar{\kappa})} \right)^j \frac{((\exp(\bar{\kappa}))^{2j+1} - (\exp(\bar{\kappa} \bar{y}))^{2j+1})}{2j+1} \frac{1}{\Gamma(\alpha j + \beta)}. \quad (2.110)$$

Before doing a study on the influence of the different parameters on the fluid flow, first a discussion on the validity of the approximate analytical solution given by Eq. (2.110) will be performed. Fig. 2.15 presents a comparison between the results obtained with this equation and the results obtained numerically by discretizing Eq. (2.109) with the Simpson's quadrature rule. For the approximation of the infinite series performing numerical tests, it was observed that the use of 20-40 terms would allow to obtain an accurate sum up to the sixth decimal place.

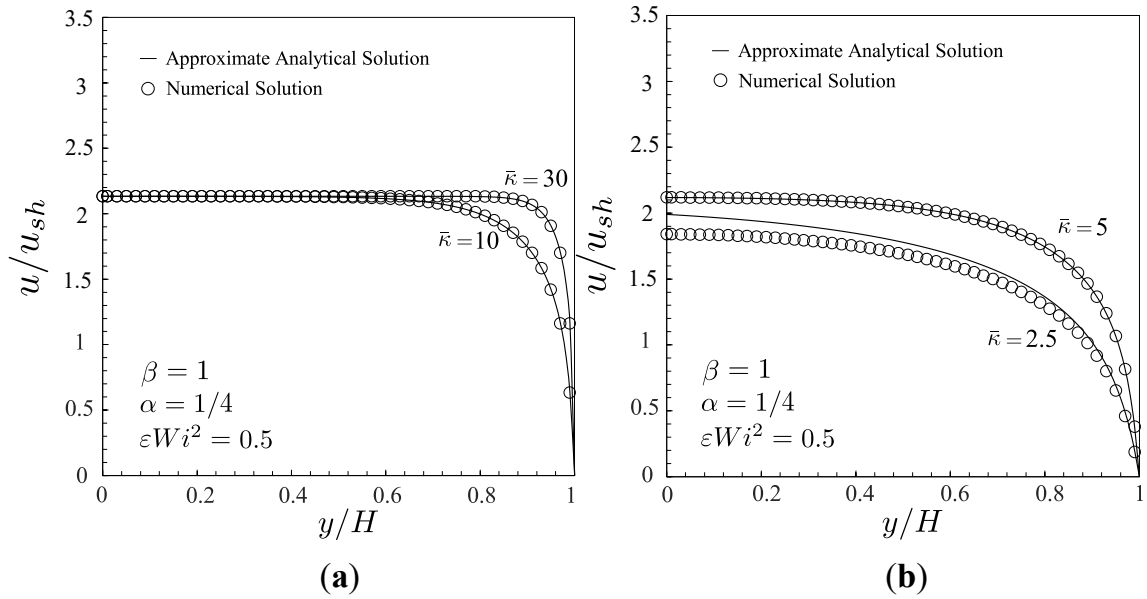


Figure 2.15: Velocity profiles calculated using Eqs. (2.110) (lines) and (2.109) (symbols) for the pure EO flow considering $\varepsilon W i^2 = 0.5$ and different values of $\bar{\kappa}$ for $\alpha = 1/4$ and $\beta = 1$: (a) $\bar{\kappa} = 10$ and 30; (b) $\bar{\kappa} = 2.5$ and 5.

From Fig. 2.15, it can be seen that only for low values of $\bar{\kappa}$ ($\bar{\kappa} \leq 5$) the thin layer approximation of the analytical solution fails to predict the correct velocity profile. Therefore, the values of $\bar{\kappa}$ used along this work are greater or equal to 10.

Now, an investigation on the influence of the Mittag-Leffler function parameters, α and β , on the velocity profile distribution across the channel, for different values of $\varepsilon W i^2$ and $\bar{\kappa}$ is presented.

Fig. 2.16 compares the velocity profiles obtained for EO flow considering two different εWi^2 values and different values of α (Fig. 2.16 (a)) and β (Fig. 2.16 (b)) at $\bar{\kappa} = 10$.

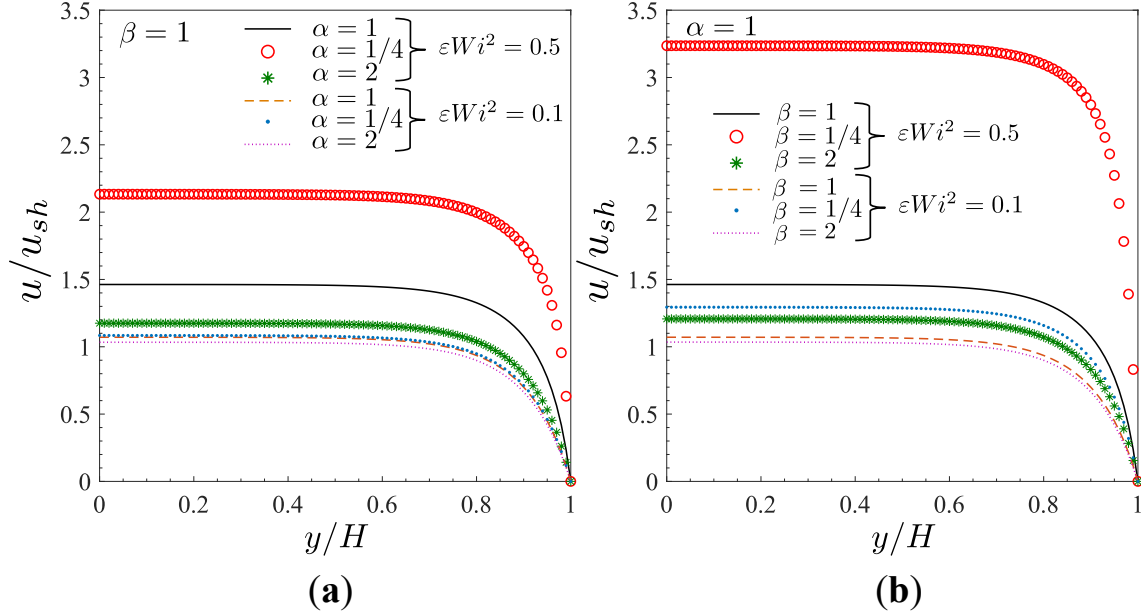


Figure 2.16: Velocity profiles calculated using Eq. (2.110) for the pure EO flow considering two different values of εWi^2 and different values of α and β for $\bar{\kappa} = 10$: (a) $\beta = 1$; (b) $\alpha = 1$. The velocity profiles with $\alpha = \beta = 1$ correspond to the expPTT model.

In Fig. 2.16 (a), with $\beta = 1$, it is observed that for increasing εWi^2 and decreasing α the flow rate increases, which is due to enhanced shear-thinning at the shear rates prevailing within the EDL. In Fig. 2.16 (b), with $\alpha = 1$, on increasing εWi^2 and decreasing β , the flow rate increases, but there are quantitative differences with the effect of β being stronger than the effect of α . Note that both α and β play a role similar to ε in the classical PTT model, that is, increasing α and β , leads to an increase of the net rate of destruction of network junctions in the physical model of the polymer, and therefore the fluid becomes more thinning, reducing the friction between junctions [3]. The fact that β plays a stronger role on the thinning effect is actually because the new function of the trace of the extra-stress tensor presents higher numerical values for $\beta \ll 1$ when the argument is smaller than ≈ 1 (the case of the EO flow presented here).

Fig. 2.17 compares transverse velocity profiles for the EO flow considering three different values of $\bar{\kappa}$, at fixed $\varepsilon Wi^2 = 0.5$: Fig. 2.17 (a) refers to fixed $\beta = 1$, and by increasing $\bar{\kappa}$ the expected thinning of the EDL is observed. Similar results are observed in Fig. 2.17 (b). The highest shear rates occur near the walls and in this region the effects of α and β are felt more strongly, as discussed in [3]. Smaller values of these parameters mean that the rate of destruction of junctions increases, that is, the friction between the molecules of the polymer solution decreases, leading to a less resistive flow (stronger shear-thinning). These effects are qualitatively similar to those observed with other shear thinning fluids, even if quantitatively different.

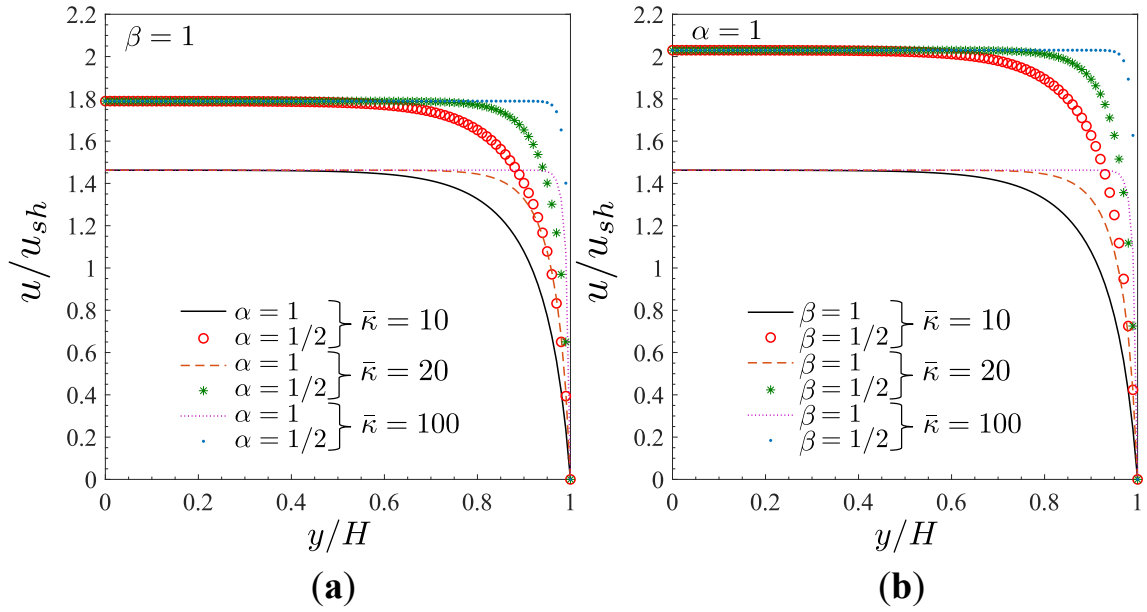


Figure 2.17: The effect of $\bar{\kappa}$ on transverse velocity profiles for EO at $\varepsilon Wi^2 = 0.5$: (a) $\beta = 1$; (b) $\alpha = 1$. The velocity profiles were obtained from Eq. (2.110). The velocity profiles with $\alpha = \beta = 1$ correspond to the expPTT model.

2.4.4 EO flow: under asymmetric zeta potentials

In this section, the analytical solution for the gPTT model considering fully-developed pure EO flow is derived, considering asymmetric zeta potentials at the walls (see Fig. 2.14 (b)).

When asymmetric zeta potentials at the walls are assumed, for the Poisson-Boltzmann equation, the boundary conditions are: at the walls, $\psi|_{y=-H} = \xi_1$ and $\psi|_{y=H} = \xi_2$, that leads to the following induced electric field, ψ :

$$\psi(y) = \xi_1 (\Psi_1 e^{\kappa y} - \Psi_2 e^{-\kappa y}) \quad (2.111)$$

with $\Psi_1 = \frac{R_\xi e^{\kappa H} - e^{-\kappa H}}{2 \sinh(2\kappa H)}$ and $\Psi_2 = \frac{R_\xi e^{-\kappa H} - e^{\kappa H}}{2 \sinh(2\kappa H)}$, where $R_\xi = \frac{\xi_2}{\xi_1}$ denotes the ratio of zeta potentials of the two walls. This equation is valid for $-H \leq y \leq H$, and when $R_\xi = 1$, the symmetric potential profile obtained in section 2.4.3 is recovered [51, 56].

In this case, the electric charge density, ρ_e , is given by:

$$\rho_e = -\epsilon \kappa^2 \xi_1 (\Psi_1 e^{\kappa y} - \Psi_2 e^{-\kappa y}) = -\epsilon \kappa^2 \xi_1 \Omega^-(y) \quad (2.112)$$

where the operator $\Omega^\pm(y) = \Psi_1 e^{\kappa y} \pm \Psi_2 e^{-\kappa y}$ is a hyperbolic function of the transverse variable y which depends on the ratio of zeta potentials and the thickness of the Debye layer.

The momentum equation is given by Eq. (2.104) and using Eq. (2.112), Eq. (2.104) is integrated resulting in the following shear stress distribution:

$$\tau_{xy} = \epsilon \kappa \xi_1 E_x \Omega^+(y) + P_x y + c_1, \quad (2.113)$$

where c_1 is a shear-stress integration constant that will be obtained later from the boundary conditions.

The constitutive equations are for the gPTT model Eq. (2.55), (2.56) and (2.57) (see section 2.2). In order to obtain closed form analytical solutions, the slip parameter in the Gordon-Schowalter derivative (Eq. (2.28)) is set to $\xi = 0$. So, with the same procedure described in section 2.2, Eq. (2.114) is obtained:

$$\tau_{xx} = 2 \frac{\lambda}{\eta_p} \tau_{xy}^2. \quad (2.114)$$

Now combining Eqs. (2.57), (2.114), (2.113) and (2.93) the following velocity gradient profile is obtained,

$$\dot{\gamma}(y) = \frac{\Gamma(\beta)}{\eta_p} E_{\alpha,\beta} \left(\frac{2\varepsilon\lambda^2}{\eta_p^2} (\epsilon\kappa\xi_1 E_x \Omega^+(y) + P_x y + c_1)^2 \right) (\epsilon\kappa\xi_1 E_x \Omega^+(y) + P_x y + c_1). \quad (2.115)$$

The dimensionless velocity gradient becomes:

$$\frac{d\bar{u}}{d\bar{y}} = \Gamma(\beta) E_{\alpha,\beta} \left(\frac{2\varepsilon Wi^2}{\bar{\kappa}^2} (\bar{\Upsilon}\bar{y} - \bar{\kappa}\bar{\Omega}^+(\bar{y}) + \bar{\tau}_1)^2 \right) (\bar{\Upsilon}\bar{y} - \bar{\kappa}\bar{\Omega}^+(\bar{y}) + \bar{\tau}_1), \quad (2.116)$$

where $\bar{\tau}_1 = \frac{\tau_1 H}{u_{sh}}$ ($\tau_1 = c_1/\eta_p$), $\bar{\Omega}^+(\bar{y}) = \bar{\Psi}_1 e^{\bar{\kappa}\bar{y}} + \bar{\Psi}_2 e^{-\bar{\kappa}\bar{y}}$, with $\bar{\Psi}_1 = \frac{R_\xi e^{\bar{\kappa}} - e^{-\bar{\kappa}}}{2\sinh(2\bar{\kappa})}$ and $\bar{\Psi}_2 = \frac{R_\xi e^{-\bar{\kappa}} - e^{\bar{\kappa}}}{2\sinh(2\bar{\kappa})}$.

Eq. (2.116) has an analytical solution only for pure EO flow and the velocity profile can be obtained by integrating the velocity gradient profile, subjected to the no-slip boundary condition at both walls, $\bar{u}(\bar{y} = \pm 1) = 0$. Simplifying Eq. (2.116) and applying integration, the following equation is obtained:

$$\bar{u}(\bar{y}) = \int_{-1}^{\bar{y}} \left(\Gamma(\beta) \sum_{j=0}^{\infty} \left(\frac{2\varepsilon Wi^2}{\bar{\kappa}^2} \right)^j \frac{1}{\Gamma(\alpha j + \beta)} (-\bar{\kappa}\bar{\Omega}^+(\bar{z}) + \bar{\tau}_1)^{2j+1} \right) d\bar{z}, \quad (2.117)$$

with z a dummy variable.

This way, the velocity profile is given by:

$$\bar{u}(\bar{y}) = \Gamma(\beta) \left(\sum_{j=0}^{\infty} \frac{2\varepsilon Wi^2}{\bar{\kappa}^2 (\Gamma(\alpha j + \beta))} \left[\sum_{m=0}^{2j+1} \binom{2j+1}{m} (\bar{\tau}_1^m) \left\{ \sum_{i=0}^{2j+1-m} \binom{2j+1-m}{i} \frac{(-\bar{\kappa}\bar{\Psi}_1)^{2j-m-i+1} (-\bar{\kappa}\bar{\Psi}_2)^i}{\bar{\kappa} (2j-2i-m+1)} e^{(2j-2i-m+1)\bar{\kappa}\bar{y}} \right\} \right] \right) + c_2. \quad (2.118)$$

with c_2 obtained using $\bar{u}(1) = 0$, and given by,

$$c_2 = -\Gamma(\beta) \left(\sum_{j=0}^{\infty} \frac{2\varepsilon Wi^2}{\bar{\kappa}^2 (\Gamma(\alpha j + \beta))} \left[\sum_{m=0}^{2j+1} \binom{2j+1}{m} (\bar{\tau}_1^m) \left\{ \sum_{i=0}^{2j+1-m} \binom{2j+1-m}{i} \frac{(-\bar{\kappa}\bar{\Psi}_1)^{2j-m-i+1} (-\bar{\kappa}\bar{\Psi}_2)^i}{\bar{\kappa} (2j-2i-m+1)} e^{(2j-2i-m+1)\bar{\kappa}} \right\} \right] \right). \quad (2.119)$$

$\bar{\tau}_1$ is obtained by solving numerically $\bar{u}(-1) = 0$.

Although Eq. (2.118) is an infinite series, a solution with a fair number of correct decimal places can be obtained (depending on the problem and the parameters used).

Therefore, now the velocity profile given by Eq. (2.117) (obtained by a numerical quadrature rule, and referred to as *numerical solution*), will be compared with the analytical solution given by Eq. (2.118). The numerical results were obtained using the *Mathematica* software version 13.3.

For the *numerical solution*, first $\bar{\tau}_1$ is obtained using the secant method to find the root of,

$$\Gamma(\beta) \sum_{j=0}^{\infty} \left(\frac{2\varepsilon Wi^2}{\bar{\kappa}^2} \right)^j \frac{1}{\Gamma(\alpha j + \beta)} \left(\int_{-1}^1 (-\bar{\kappa}\bar{\Omega}^+(\bar{z}) + \bar{\tau}_1)^{2j+1} d\bar{z} \right) = 0. \quad (2.120)$$

The $\bar{\tau}_1$ value obtained is then substituted in Eq. (2.117), and the numerical velocity profile is finally obtained.

The analytical solution given by Eq. (2.118) is composed by an infinite series. Therefore, it is important to access the number of terms required in the series to achieve a precise and accurate solution. To do this, the *numerical solution* is used as a reference.

The new truncated solution is obtained from Eq. (2.118), truncating the sum with $j + 1$ terms. To validate the solution it was considered 201 equidistant mesh points along the channel height ($2H$) and measured the root mean squared error (RMSE) obtained at these points. The error is calculated by,

$$RMSE = \sqrt{\frac{1}{n} \sum_{i=1}^n (\bar{u}(\bar{y})_{num} - u(\bar{y})_t)^2},$$

where $\bar{u}(\bar{y})_{num}$ is the numerical value of the velocity and $\bar{u}(\bar{y})_t$ is the velocity value for the truncated series.

Three different values of εWi^2 are considered ($\varepsilon Wi^2 = 0.5, 1$ and 2) and two different values for R_ξ ($R_\xi = -1$ and 0.5), considering $\beta = 1$ and two different values of α ($\alpha = 0.5$ and 1.5). The values of α are varied, because this parameter is the most sensitive to changes in the series.

Tables 2.4, 2.5, 2.6 show the RMSE, in percentage, for $\varepsilon Wi^2 = 0.5, 1$ and 2 respectively, and considering $\alpha = 0.5, R_\xi = 0.5$ and -1 . As the number of terms in the series (Eq. (2.118)) increase, the error decreases. This parametric study provides insights into the behavior of the truncated solution. For instance, when εWi^2 increases (Table 2.5 and 2.6) and $R_\xi = 0.5$, the series solution

Table 2.4: RMSE (in percentage) for $\varepsilon Wi^2 = 0.5$ and $\alpha = 0.5$.

j	$R_\xi = 0.5$	$R_\xi = -1$
2	8.834×10^0	5.197×10^0
4	1.819×10^0	8.889×10^{-1}
8	4.78×10^{-2}	1.597×10^{-2}
16	2.207×10^{-4}	1.472×10^{-4}

Table 2.5: RMSE (in percentage) for $\varepsilon Wi^2 = 1$ and $\alpha = 0.5$.

j	$R_\xi = 0.5$	$R_\xi = -1$
2	1.038×10^2	4.550×10^1
4	5.23×10^1	1.889×10^1
8	9.679×10^0	2.433×10^0
16	1.092×10^{-1}	1.198×10^{-2}
20	6.757×10^{-3}	5.342×10^{-4}

Table 2.6: RMSE (in percentage) for $\varepsilon Wi^2 = 2$ and $\alpha = 0.5$.

j	$R_\xi = 0.5$	$R_\xi = -1$
2	1.503×10^3	2.660×10^2
4	1.226×10^3	1.585×10^2
8	6.571×10^2	4.63×10^1
16	7.132×10^1	2.118×10^0
20	1.546×10^1	3.042×10^{-1}

shows slower convergence. On the other hand, for lower εWi^2 values, the series solution converges much more rapidly.

Table 2.7 shows the RMSE in percentage, for $\varepsilon Wi^2 = 2$, $\alpha = 1.5$ and considering $R_\xi = 0.5$ and -1 . Notably, as α increases (see Table 2.7), the error decreases more rapidly with an increase in the number of terms in the series (even for high values of εWi^2). It was also experimented with a higher number of terms in the series for cases with high εWi^2 and low α , and found that a favorable balance between computation time, simplicity, and solution accuracy could be achieved for $j = 20$.

Table 2.7: RMSE (in percentage) for $\varepsilon Wi^2 = 2$ and $\alpha = 1.5$.

j	$R_\xi = 0.5$	$R_\xi = -1$
2	7.898×10^0	4.268×10^0
4	2.231×10^{-1}	9.7×10^{-2}
8	2.635×10^{-4}	1.927×10^{-4}

The velocity profiles computed by the *numerical solution* of Eq. (2.117) and the analytical solution obtained by Eq. (2.118) for different j are shown in Figs. 2.18 and 2.19, where u/u_{sh} is the normalised velocity profile. These particular results indicate that the velocity profile converges

to the correct profile as the number of terms in the series increases, and that this convergence is slower for lower values of α .

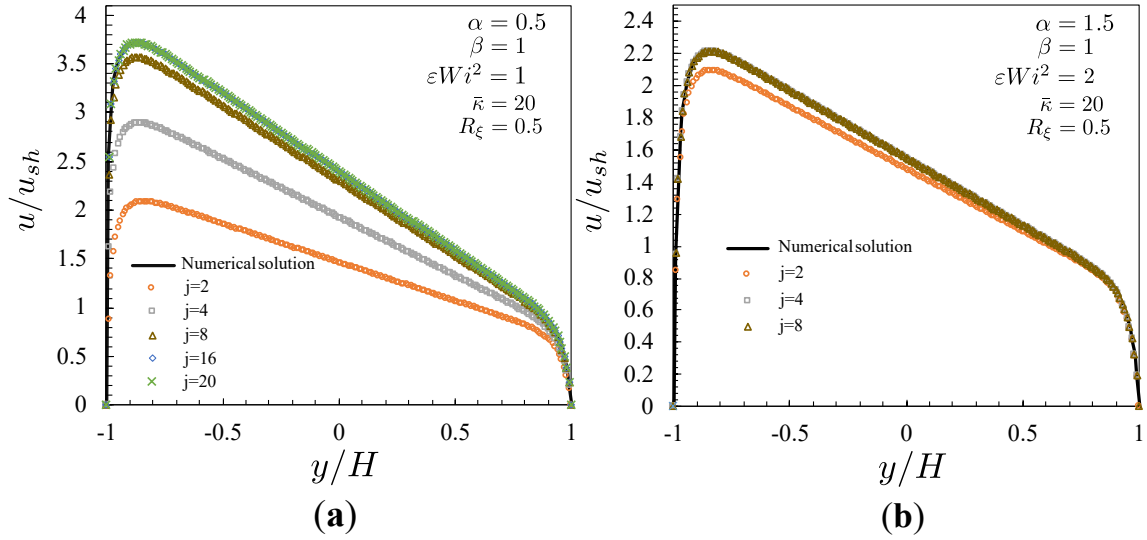


Figure 2.18: Velocity profiles for $\beta = 1$, $R_\xi = 0.5$ and $\bar{\kappa} = 20$: (a) $\alpha = 0.5$, $\varepsilon Wi^2 = 1$; (b) $\alpha = 1.5$, $\varepsilon Wi^2 = 2$.

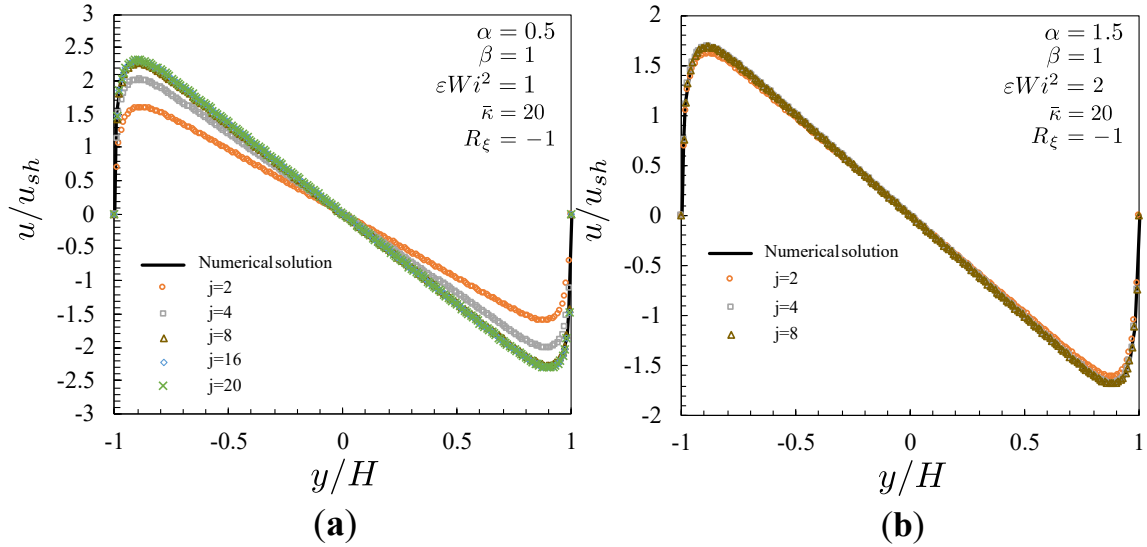


Figure 2.19: Velocity profiles for $\beta = 1$, $R_\xi = -1$ and $\bar{\kappa} = 20$: (a) $\alpha = 0.5$, $\varepsilon Wi^2 = 1$; (b) $\alpha = 1.5$, $\varepsilon Wi^2 = 2$.

Now, the influence of the Mittag–Leffler function parameters α and β on the velocity profile is studied. Fig. 2.20 shows the velocity profiles for $\beta = 1$, different values of α , 0.5, 1 and 1.5, $R_\xi = 0.5$, $\bar{\kappa} = 20$ and different values of εWi^2 , 0.5 and 1.

In Fig. 2.20 (a), with $\beta = 1$, it is observed that for increasing εWi^2 and decreasing α the flow rate increases, leading to an increase of the *skewed pluglike* profile. In Fig. 2.20 (b), with $\alpha = 1$, a similar behaviour is obtained, i.e., on increasing εWi^2 and decreasing β , the flow rate increases. However, there are some differences with the effect of α being stronger than the effect of β .

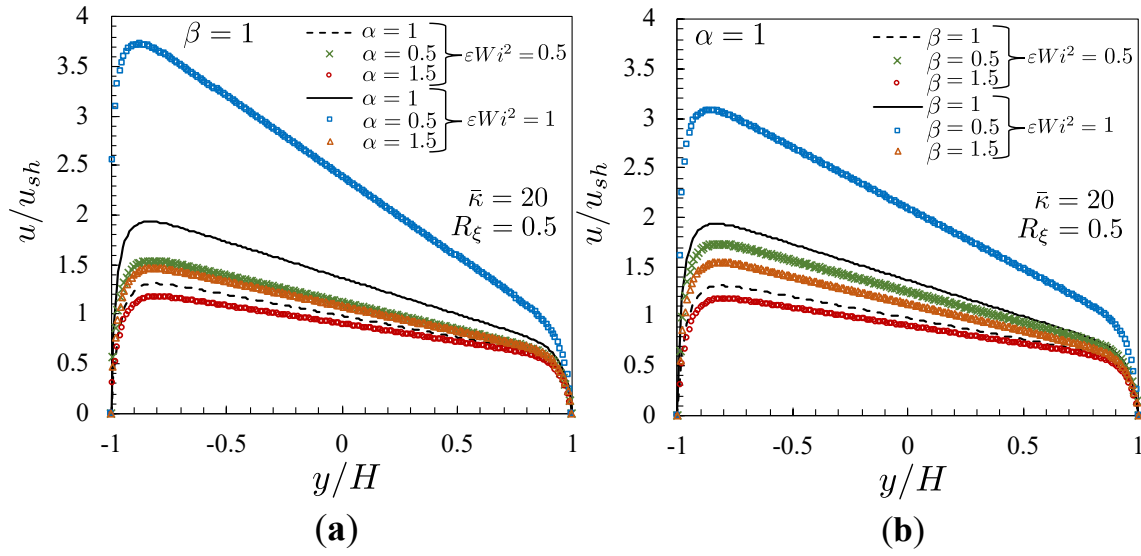


Figure 2.20: Velocity profiles calculated using Eq. (2.118) for pure EO flow with $R_\xi = 0.5$ considering two different values of εWi^2 and different values of α and β for $\bar{k} = 20$: (a) $\beta = 1$; (b) $\alpha = 1$. The velocity profiles with $\alpha = \beta = 1$ correspond to the expPTT model.

Fig. 2.21 shows the velocity profiles for $\alpha = 1$, different values of β , 0.5, 1 and 1.5, $R_\xi = -1$, $\bar{k} = 20$ and different values of εWi^2 , 0.5 and 1.

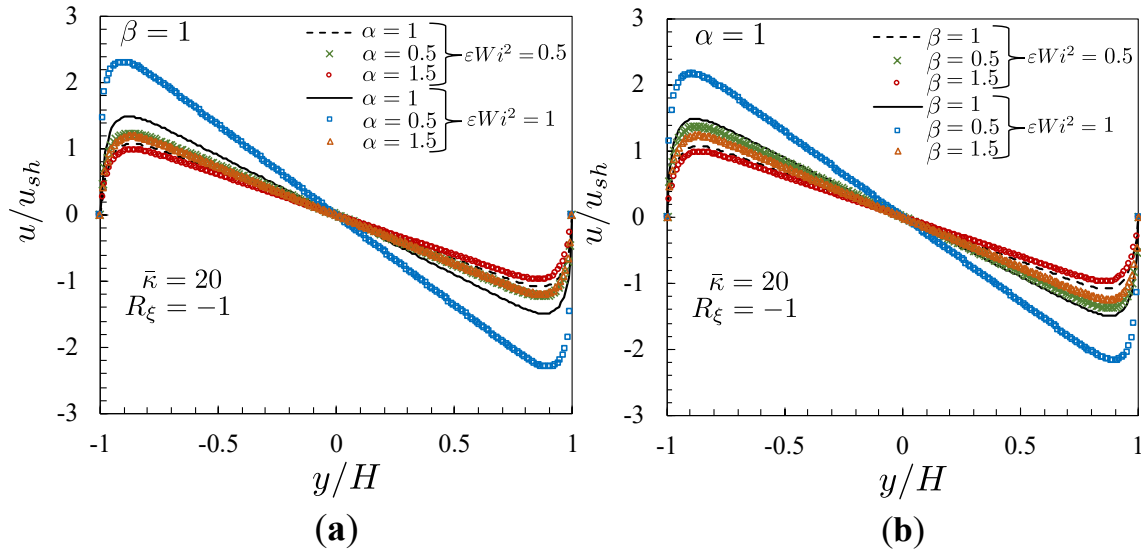


Figure 2.21: Velocity profiles calculated using Eq. (2.118) for pure EO flow with $R_\xi = -1$ considering two different values of εWi^2 and different values of α and β for $\bar{k} = 20$: (a) $\beta = 1$; (b) $\alpha = 1$. The velocity profiles with $\alpha = \beta = 1$ correspond to the expPTT model.

In Fig. 2.21 (a), with $\beta = 1$, it is observed that for increasing εWi^2 and decreasing α the flow rate increases, leading to an increase of an *anti-symmetric pluglike* profile. In Fig. 2.21 (b), with $\alpha = 1$ a similar behaviour is obtained, i.e., on increasing εWi^2 and decreasing β , the flow rate increases. However, there are some differences, with the effect of α being stronger than the effect of β . The pronounced flow with the increasing of εWi^2 is associated with the shear-thinning

behaviour of the fluid.

These works are published on paper [56] and on manuscript [66], which can be found in Part III of this thesis.

Chapter 3

Numerical studies

3.1 Model order reduction (MOR)

One of the most popular model order reduction (MOR) methods is the proper orthogonal decomposition (POD) method. The method was first introduced by Lumley [9], and it allows to decompose almost any flow into a infinite set of eigenfunctions or modes. The objective of the POD method is to reduce the model in a way that it can capture the most important and reliable information with much less data and effort. In recent years, because of the development of machine learning (ML) techniques, this method became very popular in CFD problems, because it reduces the simulation time and allows to predict the fluid flow based only on the most important modes.

Performing a numerical simulation produces a huge amount of data and some important flow structures can be ignored. To identify these flow structures, mainly in transient situations, is a complex task, because such structures change in time and space, with new structures continuously being formed while others are destroyed. Performing a decomposition of the entire data set into smaller sets, important structures present in the main flow and structures with periodic behaviour, like vortices, can be identified. Therefore, through the analysis of the frequency of each of these components and using a smaller number of components, a better and global understanding of the flow can be achieved.

In this section an introduction of the POD model is done and then the mathematical theory behind the POD method used in this thesis is described.

3.1.1 Introduction

The method has become very popular and has been applied to a large variety of engineering problems, from fluid mechanics to bio-engineering, having different names for the same procedure: Karhunen–Loève decomposition, principal components analysis (PCA), singular systems analysis (SSA) or singular value decomposition (SSV) (for more details, please see the review papers [67, 68]).

Several versions of the POD method, and even new methods, were proposed in the literature, since its first introduction in 1967, being adapted to specific cases and branches of engineering. In

the first fifteen years, the only works on this topic are from Lumley itself and some co-workers [69]. One of these new methods is from Aradag et al. [70] who developed a couple of methods: the hybrid filtered POD (HFPOD) approach (see also [71]) and the fast Fourier transform (FFT)-based 3D filtered POD (FFTPOD). These methods deal with the difficulty encountered when using simple POD for three-dimensional (3D) structures. Using the HFPOD method, large-scale structures associated with von Kármán's vortex street, as well as their phase and amplitude variations, can be identified quantitatively, and FFTPOT enables modelling 3D flows without being contaminated by small-scale turbulent structures while capturing the large-scale features of the flow, like von Kármán's vortex street. Another new method based on POD is the spectral POD (SPOD) method, which is used for a space-time POD problem for statistically stationary flows, and it was investigated by Aaron et al. [72]. This model produces modes that oscillate at a single frequency, and in their study the authors demonstrated how SPOD modes articulate coherently with development in space and time, in contrast to general POD space-modes. Moreover, SPOD modes were found to be optimally averaged dynamic mode decompositions (DMD), resulting from an ensemble model DMD problem for stationary flows. So, SPOD modes represent dynamic structures in the same sense as DMD modes, while also incorporating the statistical variability of turbulent flows.

Another method based on POD was presented by Mendez et al. [73–75], that developed the multi-scale POD (mPOD), which uses multiresolution analysis (MRA) on the correlation matrix to produce a set of PODs at multiple scales.

In recent years, new methods appeared in the literature to predict complex fluid flows with less effort, like ML techniques, and POD being a feature selection method that reduces the dimension of the process [76], has become a valuable tool. In this area, the POD method goes by the name of PCA. This way, by combining the CFD simulations and ML algorithms to simultaneously reduce computational cost and time, retain physical insight by focusing on the prediction of flow-fields, and keep the ability to access information or to make adjustments is already a reality [77].

In the literature, new works have been published with the combination of POD and ML methods. Hijazi et al. [78] recently presented a model for solving inverse problems for the Navier–Stokes equations, in a reduced order setting by integrating the structure of the POD–Galerkin reduced order models (ROMs) into physics informed neural networks (PINNs). They incorporated the POD–Galerkin reduced order equations into the loss function of the PINNs. This way, the reduced model is able to approximate unknown parameters, such as physical constants or boundary conditions. Another study is from Wu et al. [79] that proposed a method that obtains a snapshot of the solution through numerical simulation, then uses the POD method to generate basis functions that optimally represent the solution and a transformer neural network learns the physical dynamics.

In the next section, the mathematical theory behind the POD method is introduced.

3.1.2 Proper orthogonal decomposition (POD)

To implement the POD method, it is assumed that all data are saved in a matrix with N_p by N_t entries, each column representing one time step:

$$\mathbf{M} = \begin{bmatrix} M_{1,1} & M_{1,2} & \cdots & M_{1,N_t} \\ M_{2,1} & M_{2,2} & \cdots & M_{2,N_t} \\ \vdots & \vdots & \ddots & \vdots \\ M_{N_p,1} & M_{N_p,2} & \cdots & M_{N_p,N_t} \end{bmatrix} \quad (3.1)$$

where N_p is the number of rows of data and N_t the number of time steps.

Each column of \mathbf{M} can be written as a linear combination of orthonormal, i.e. unitary and orthogonal, vectors or modes, \mathbf{w} . Therefore, the matrix of the modes, \mathbf{W} , is given by

$$\mathbf{W} = \begin{bmatrix} w_{1,1} & w_{1,2} & \cdots & w_{1,N_m} \\ w_{2,1} & w_{2,2} & \cdots & w_{2,N_m} \\ \vdots & \vdots & \ddots & \vdots \\ w_{N_p,1} & w_{N_p,2} & \cdots & w_{N_p,N_m} \end{bmatrix} \quad (3.2)$$

where N_m is the number of modes. This way, matrix \mathbf{M} can be rewritten as the product of two matrices:

$$\mathbf{M} = \mathbf{W} \cdot \mathbf{A} \quad (3.3)$$

where each element of \mathbf{M} is given by:

$$M_{i,t} = \sum_{m=1}^{N_m} w_{i,m} a_{m,t} \quad (3.4)$$

with $i \in \{1, 2, \dots, N_p\}$, $t \in \{1, 2, \dots, N_t\}$ and $a_{m,t}$ are the time coefficients and the elements of matrix \mathbf{A} :

$$\mathbf{A} = \begin{bmatrix} a_{1,1} & a_{1,2} & \cdots & a_{1,N_t} \\ \vdots & \vdots & \ddots & \vdots \\ a_{N_m,1} & a_{N_m,2} & \cdots & a_{N_m,N_t} \end{bmatrix}. \quad (3.5)$$

Matrices \mathbf{W} and \mathbf{A} are obtained from the calculation of the autocovariance matrix \mathbf{S} , that is a N_p by N_p matrix given by:

$$\mathbf{S} = \mathbf{M} \cdot \mathbf{M}^T. \quad (3.6)$$

By definition, \mathbf{S} is a symmetric positive definite matrix with real, nonnegative ordered eigenvalues $\lambda_1 \geq \dots \geq \lambda_{N_p} \geq 0$. The corresponding eigenvectors $w_i, i = 1, \dots, N_p$, are given by [8]:

$$\mathbf{S}w_i = \lambda_i w_i, i = 1, \dots, N_p. \quad (3.7)$$

Due to the special structure of \mathbf{S} , vectors $w_i, i = 1, \dots, N_p$ represent the desired orthonormal vectors or modes, which together form matrix \mathbf{W} . However, obtaining these modes by directly solving the eigenvalue problem for the N_p by N_p matrix \mathbf{S} would be computationally expensive. Therefore, the

method of snapshots proposed by Sirovich [80] is employed, which involves solving the eigenvalue problem using the autocovariance matrix \mathbf{R} instead of \mathbf{S} , i.e.,

$$\mathbf{R}v_j = \lambda_j v_j, j = 1, \dots, N_t \quad (3.8)$$

where $v_j, j = 1, \dots, N_t$ are the eigenvectors of \mathbf{R} , which are computed as follows:

$$\mathbf{R} = \mathbf{M}^T \cdot \mathbf{M}. \quad (3.9)$$

The autocovariance matrix \mathbf{R} has dimensions N_t by N_t and has the same non-zero eigenvalues as \mathbf{S} [8]. Matrix \mathbf{W} of the modes is now given by,

$$\mathbf{W} = \mathbf{M} \cdot \mathbf{V} \cdot (\mathbf{L})^{-\frac{1}{2}}, \quad (3.10)$$

where the columns of matrix \mathbf{V} are the eigenvectors of \mathbf{R} and \mathbf{L} is the matrix of eigenvalues of \mathbf{R} , sorted by descending order. Finally, matrix \mathbf{A} is obtained by:

$$\mathbf{A} = \mathbf{W}^T \cdot \mathbf{M}. \quad (3.11)$$

The distribution of the matrix \mathbf{W} columns is directly related to the corresponding eigenvalues, with the first columns corresponding to higher variations of the time coefficients, and therefore those gathering more relevant information. Thus, the reconstruction of matrix \mathbf{M} is performed, but keeping only the first more relevant modes (the user decides on the number of modes, which affects both accuracy and cost). Since $N_m < N_p$, it brings:

$$\mathbf{M} \approx \tilde{\mathbf{W}} \cdot \tilde{\mathbf{A}} = \tilde{\mathbf{M}} \quad (3.12)$$

where the tilde is used to denote the matrices reconstructed only with data corresponding to the more relevant modes.

In the next sections, two problems are presented where the POD method is applied.

3.2 Flow structures identification through POD for the flow around two distinct cylinders

In the literature many studies have been made of the flow around one cylinder (e.g. [81]). Concerning recent literature on the use of POD to study the flow around bluff bodies, Bergmann et al. [82] studied the optimal rotary control of the cylinder wake using POD and Huan Ping et al. [83] also studied the wake dynamics behind a rotary oscillating cylinder. They used POD to extract the energetic modes that govern the dynamics of the flow, and also to characterize the spatially evolving nature of the forced wake as it undergoes a transition from the near-wake two-layer shedding pattern to the far-wake Kármán-like shedding pattern. They concluded that only a few modes allowed for reconstructing the near-wake accurately, while more modes must be retained to ensure an accurate approximation of the far-wake. Riches et al. [84] used POD to analyze the wake-dynamics of a low-mass ratio circular cylinder undergoing vortex-induced vibrations. Recently, most of the works are in flow around cylinders with different surface texture/geometry.

For the flow around two cylinders, there are works on flows around side-by-side circular cylinders with the same dimensions [85–87], and also a study with two cylinders in a staggered configuration, where the data processed by the POD method were obtained from experimental measurements of flow fields using particle image velocimetry [88].

In this section, a simple POD method is used to compute the 2D flow around two parallel side-by-side cylinders with different radii. The main idea is:

- to use the POD not to reduce and compile the amount of information on the flow as happens in most studies, but instead to show that the POD can be used to capture flow structures and flow physics that would be impossible to *observe* without a mode analysis, highlighting, in this way, this ability of the POD method;
- to understand the flow around two parallel side-by-side cylinders with different radii, through the use of POD and classical CFD. Thus, by decomposing this complex 2D flow, a better understanding of the impact of a given obstacle on the areas of interest can be achieved.

Therefore, a detailed study on complex 2D flow is presented, and it is shown that the energy drop-off for higher order modes is much less steep when the complexity of the 2D flow increases.

It should be mentioned that turbulent flows are not studied in here. The main idea is to fully understand the mode decomposition in an oscillatory flow around two parallel side-by-side cylinders of different dimensions.

This section is organized as follows: a numerical study for the 2D flow past two parallel side-by-side cylinders of different radii is performed, considering a Newtonian fluid and two non-Newtonian power-law fluids with $n = 0.7$ and $n = 1.3$. Then, the most important modes are identified and a reconstruction with the main modes is performed. Using this specific flow, destroys the possibility of forming a symmetric pattern over time and increases the difficulty in grouping different modes. Finally, a discussion of the dynamics of the fluid flow and of the reconstruction procedure is detailed.

Each contribution related to the work objectives, presented in section 3.2, are explained in detail. Given that the present dissertation falls into the category of *multi-paper dissertation*, and in order to keep repetition of information at a minimum level, the complete paper related to this section is presented in Part III of this thesis.

3.2.1 Governing equations, numerical method and POD

The equations governing the flow of an isothermal incompressible fluid, are the continuity,

$$\nabla \cdot \mathbf{u} = 0 \quad (3.13)$$

where \mathbf{u} is the velocity vector, and the momentum equation,

$$\rho \frac{D\mathbf{u}}{Dt} = -\nabla p + \nabla \cdot \boldsymbol{\tau}, \quad (3.14)$$

where ρ is the density, $\frac{D}{Dt}$ is the material derivative, p is the pressure, $\boldsymbol{\tau}$ is the extra-stress tensor and t is the time.

A Newtonian fluid and a power-law fluid were considered. For the Newtonian fluid, the constitutive equation is given by:

$$\boldsymbol{\tau} = 2\mu\mathbf{D}, \quad (3.15)$$

where \mathbf{D} is the rate of deformation tensor and μ is the viscosity. For the power-law fluid, the constitutive equation is:

$$\boldsymbol{\tau} = 2\eta(\dot{\gamma})\mathbf{D}, \quad (3.16)$$

where $\dot{\gamma}$ is the second invariant of the rate of deformation tensor and $\eta(\dot{\gamma})$ is the viscosity function given by:

$$\eta(\dot{\gamma}) = a\dot{\gamma}^{n-1}, \quad (3.17)$$

where a is the consistency index and n is the power-law index.

In this section, for the power-law fluid, a generalised Reynolds number [89, 90] is considered:

$$Re_{gen} = \frac{6\rho U^{(2-n)} L^n}{a [(4n+2)/n]^n}, \quad (3.18)$$

where U is the imposed mean velocity at the inlet and L is a characteristic linear dimension.

When studying the von Kármán vortex street, that is a repeating pattern of swirling vortices occurring due to vortex shedding, which is responsible for the unsteady separation of the fluid flow around a blunt body, another important dimensionless numbers appears: the Strouhal number. The Strouhal number is a key parameter for oscillating flows, because it describes the relation between the length-scale of the blunt body, the vortex shedding frequency and the flow velocity [77], and is defined as:

$$St = \frac{fL}{U}, \quad (3.19)$$

where f is the vortex shedding frequency. This dimensionless number depends on the Reynolds number, Re . According to Roshko [91], for the range $50 < Re < 150$, the relationship between St and Re is given by

$$St = 0.212 \left(1 - \frac{21.2}{Re} \right). \quad (3.20)$$

The system of equations, Eqs. (3.13), (3.14), together with the constitutive equations (3.15) for the Newtonian fluid and (3.16) for the power-law fluid, are solved numerically using the software ANSYS Fluent version 2020 R2. To perform the simulations, the velocity and pressure fields at $t = 0$ are obtained in the following manner:

- First, a steady-state solution is calculated for $Re = 100$;
- Second, the previous solution is used as an initial guess ($t = 0$) for the velocity and pressure fields, in the steady-state numerical simulation considering $Re = 500$. This simulation allows the development of the characteristic von Kármán vortex street.
- Third, the steady-state solution obtained for $Re = 500$ is used as the initial guess for the transient simulation with $Re = 100$.

The pressure–velocity coupling is done using the SIMPLE method. To discretize the pressure gradient, the least squares cell based scheme is used, and for the discretization of the advective terms, the second-order upwind scheme is considered. The transient term is approximated by a first order implicit scheme.

The POD analysis is performed with MATLAB R2018a. The data saved in matrix \mathbf{M} correspond to the velocity components, u and v , and the pressure field, p , that are obtained after performing the CFD simulation. Thus, each column of matrix \mathbf{M} , contains the following data:

$$(u_1, u_2, \dots, u_{N_E}, v_1, v_2, \dots, v_{N_E}, p_1, p_2, \dots, p_{N_E})^T$$

where N_E is the number of control volumes of the mesh.

In this study, the implementation of the POD method is a little different of the one presented in section 3.1.2. For this work the autocovariance matrix \mathbf{S} , is computed in the following form:

$$\mathbf{S} = \frac{1}{N_p} \mathbf{M} \cdot \mathbf{M}^T \quad (3.21)$$

where N_p is the number of rows of data. This way, the matrix of modes are the eigenvectors of matrix \mathbf{S} and the time coefficients are obtained by Eq. (3.11). With these two matrices, the reconstruction is then performed using Eq. (3.12).

In the next section, more details are presented regarding the geometry, the mesh and the rheological properties of the fluids used for this study.

3.2.2 Problem definition

The geometry is represented in Fig. 3.1. There are two cylinders with different radii that are parallel and side-by-side, one at the bottom of the channel and other at the top of the channel. Assuming that the characteristic linear dimension considered here is the diameter, i.e. $L = D$, the bottom cylinder has a diameter $D = 0.1$ m and is placed $5D$ away from the inlet and $15D$ from the outlet. The inlet has a $10D$ height.

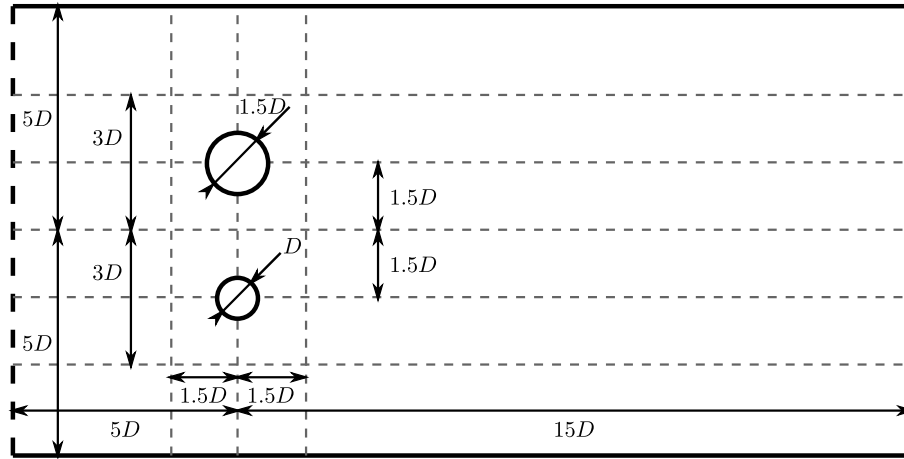


Figure 3.1: Geometry of the flow around two cylinders. The left dashed line represents the inlet and the right dashed one the outlet.

Fig. 3.2 (a) presents a global view of the chosen mesh and Fig. 3.2 (b) shows a zoomed view around the two cylinders. The cell size is set to $0.025D$ along the cylinders' surface region, $0.1D$ along bold lines of Fig. 3.2 (a) and $0.2D$ on the rest of the domain. The cell size growth rate is 1.2. Along the bold edges (Fig. 3.2 (b)), a bias type procedure is used with a bias factor of 10. The mesh obtained has 23944 elements.

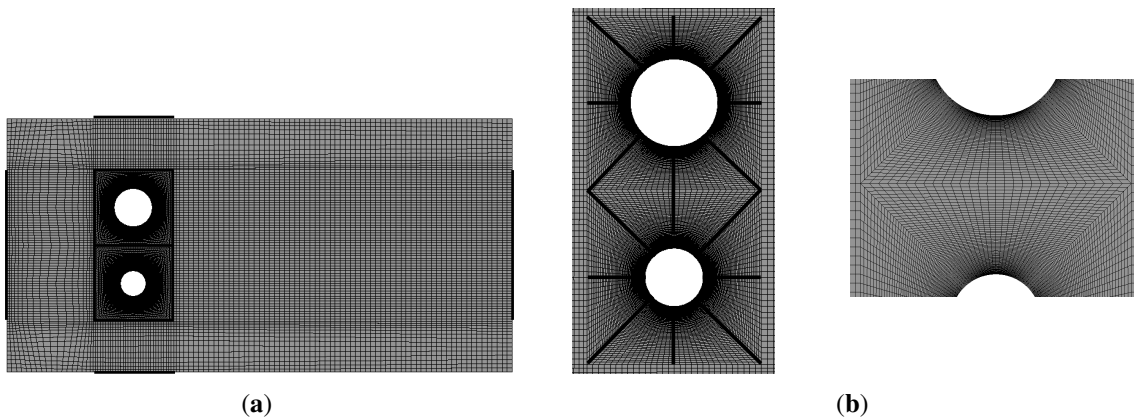


Figure 3.2: Mesh of the flow around two cylinders with 23944 elements. (a) Global view with black lines with $0.1D$ mm elements; (b) close view around and between the cylinders.

For the boundary conditions, an imposed pressure at the outlet is considered, and at the inlet an imposed uniform velocity profile that is constant in time. Full slip is considered at the top and

bottom walls of the channel, and the usual empirical no-slip boundary condition is assumed at the walls of the cylinders.

The numerical simulations are performed considering a Newtonian fluid and a non-Newtonian power-law fluid. For the Newtonian case, the rheological properties of water at a temperature of 20 °C are considered, ($\rho = 10^3 \text{ kg.m}^{-3}$ and $\mu = 10^{-3} \text{ Pa.s}$), and it is assumed that near the bottom cylinder, $Re = 100$ and near the top cylinder, $Re = 150$. For the non-Newtonian power-law case, is assumed $Re_{gen} = 100$, where $\rho = 10^3 \text{ kg.m}^{-3}$, $D = 0.1 \text{ m}$ and $U = 10^{-3} \text{ m.s}^{-1}$. Considering two fixed values for the power-law index n , 0.7 and 1.3, from Eq. (3.18), where $L = D$, $a = 0.00039 \text{ Pa.s}^{0.7}$ and $0.0026 \text{ Pa.s}^{1.3}$ are obtained, respectively.

3.2.3 Results and discussion

The transient simulation is performed, and the first $10\lambda_t$ seconds ($\lambda_t = \frac{20D}{D \times U} \text{ s}$) are neglected to avoid the strong influence of the initial conditions. The subsequent $10\lambda_t$ seconds of data are then analysed. Note that λ_t is an approximate measure of the residence time, that is, the average time a element takes to go from the inlet to the outlet. The study and analysis is focused on the subsequent $10\lambda_t$ seconds of data. To set the maximum time step of the numerical simulation, a maximum Courant number (C) of 1 is considered. Using $C \leq 1$ leads to $\delta t_{CFD} \leq \frac{\delta x}{u_{max}} = \frac{0.0025}{0.001} = 2.5 \text{ s}$. To use the POD method, the data of every 20 time-steps is considered, i.e., $\delta t_{POD} = 50 \text{ s}$, resulting into 400 time-steps to be analyzed.

Fig. 3.3 (a)–(c) presents the streamlines and the vorticity sign map for the flow around two cylinders, for the Newtonian fluid and of the power-law fluids with $n = 0.7$ and $n = 1.3$, respectively. The oscillatory behaviour downstream the cylinders is perceptible and the vortices detach from each cylinder rear, with different sizes. Later in time, the vortices that arise from both cylinders interact and new structures are formed, where the individual influence of each cylinder is no more clear. From Eq. (3.20) for $Re = 100$, that corresponds to the smaller cylinder, $St \approx 0.17$ and consequently the structures behind the cylinder are about six times bigger than the cylinder itself. Near the bigger cylinder, with diameter $1.5D$, a $Re = 150$ corresponds to $St \approx 0.18$ and vortices are slightly bigger.

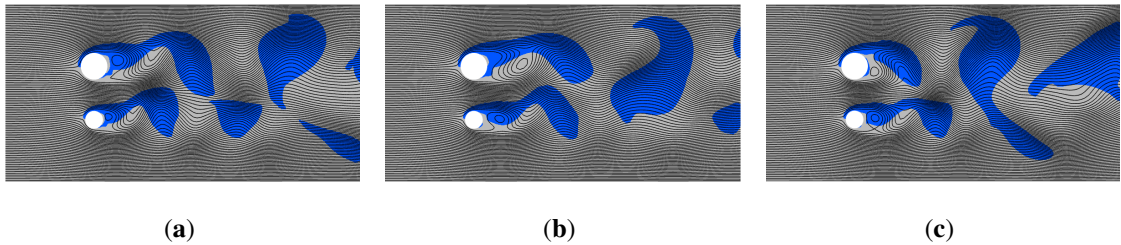


Figure 3.3: Streamlines and vorticity sign (blue represents positive values and grey negative values) at $t = 20\lambda_t$ for: (a) Newtonian fluid; (b) power-law fluid with $n = 0.7$; (c) power-law fluid with $n = 1.3$.

Some snapshots/instants of the evolution in time of the velocity component u are shown in Fig. 3.4. The figures are numbered from 1 to 15, with 1 representing $t \approx 0 \text{ s}$ and 15 representing

$t \approx 2.3$ s of simulation. From instants 1 to 5, the flow in the wake of the cylinders is similar, although the different scales generate different structures that lead to the asynchronous flow verified at instant 6. These asynchronous flow resulted in the formation of higher-velocity structures that (detached) from the main flow in the wake of the cylinder. This analysis alone is still insufficient to fully understand the influence of one cylinder on the other. Therefore, a detailed analysis based on POD is presented, which shows that these methods allow to unveil the origin and evolution of different structures.

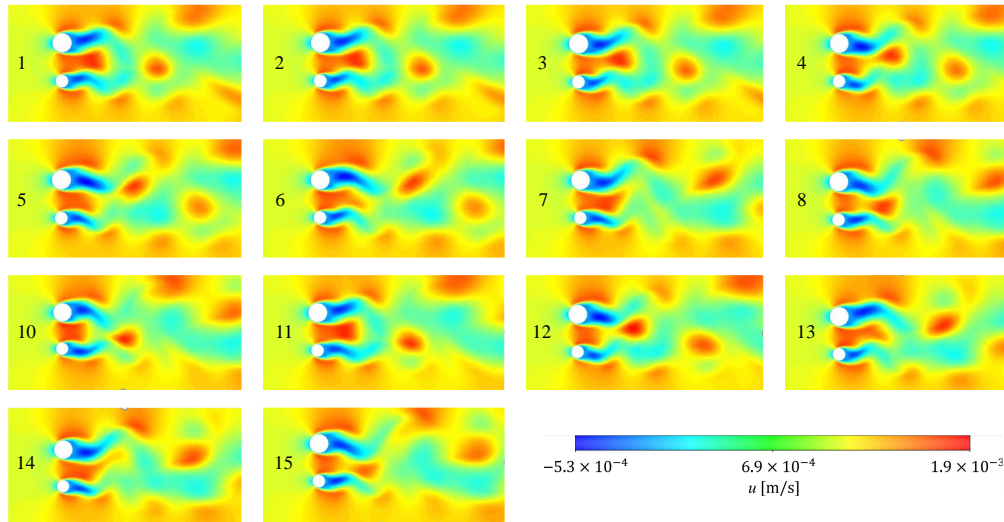


Figure 3.4: Evolution, in time, of the first component, u , of the velocity profile for the Newtonian fluid. The numbers 1 to 15 establish the order of occurrence, with 1 representing $t \approx 0$ s and 15 representing $t \approx 2.3$ s.

3.2.3.1 Eigenvalues, modes and partial reconstruction

For this study only the first 20 eigenvalues and modes are considered. Fig. 3.5 shows the relative weight of the eigenvalues associated with each mode, for a Newtonian fluid, a power-law fluid with $n = 0.7$ and a power-law fluid with $n = 1.3$, respectively. In the three cases, a fast decay of the relative weight of the eigenvalues associated with each mode can be seen. For the Newtonian fluid, the weights attributed to the first, second and third eigenvalues are 95.7%, 1.21% and 0.98%, respectively. For the power-law fluid with $n = 0.7$, the weights are 97.5%, 0.79% and 0.67%. And, for the power-law fluid with $n = 1.3$, the weights are 94.5%, 1.5% and 1.2%. The existence of a second cylinder with different frequencies associated and the interaction of the structures that emerge from the distinct cylinders lead to the use of a higher number of frequencies and modes, to correctly predict/reconstruct the flow.

Table 3.1 shows the most important modes of u , v and p , for the flow around two cylinders (for each component u , v and p , from left to right, it is represented: a Newtonian fluid, a power-law fluid with $n = 0.7$ and a power-law fluid with $n = 1.3$).

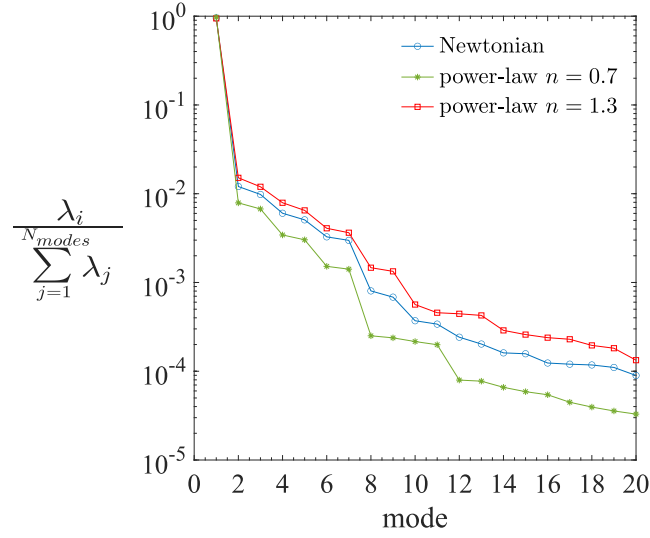
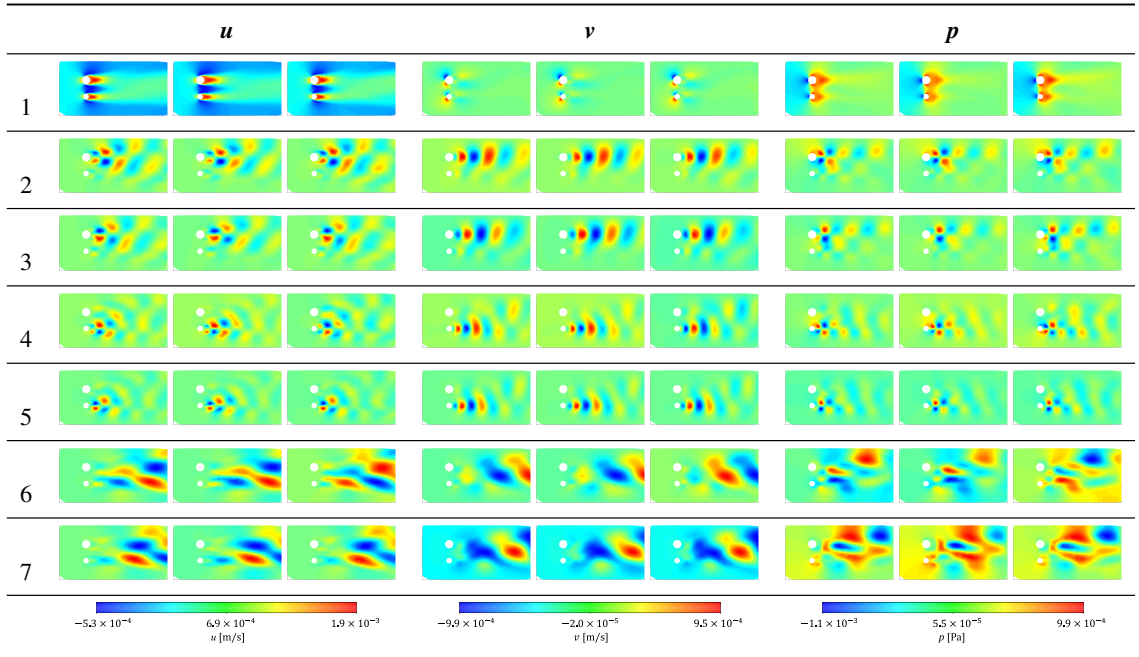


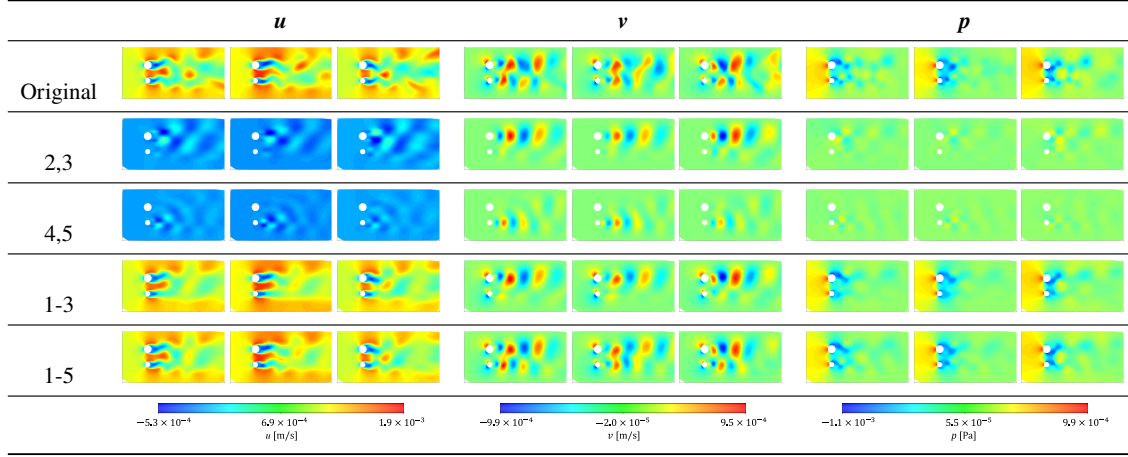
Figure 3.5: Relative weight of the eigenvalues associated with each mode.

Table 3.1: Most important modes (1 to 7) of u , v and p for the flow around two cylinders. For each component u , v and p , from left to right it is represented: a Newtonian fluid, a power-law fluid with $n = 0.7$ and a power-law fluid with $n = 1.3$.



From the analysis of Table 3.1, the first mode has the main features of the flow, but without the oscillating components. Mode 1 is in close agreement with the ensemble average (as expected). Notice that the values of u , v and p for mode 1 are symmetrical of what is *supposed* to happen, because this mode is multiplied by the time coefficients that, in this case, are negative. Modes 2 and 3 are related to vortices that detach from the top cylinder, whereas modes 4 and 5 can be associated with the bottom cylinder. In modes 2 and 3, flow structures of the top cylinder in front of

Table 3.2: Comparison between the original (first row of images) data versus the partial reconstruction at $t = 20\lambda_t$ (the modes used in the reconstruction are shown in the first column). For each component u , v and p , from left to right it is considered: a Newtonian fluid, a power-law fluid with $n = 0.7$ and a power-law fluid with $n = 1.3$.



the bottom cylinder can be seen, and that type of influence is hard to see without a decomposition by modes like is performed in this study. Modes after mode 5 are not *similar by pairs* neither easily associated with some meaningful flow structure.

To better understand this phenomena, Table 3.2 shows a comparison between the original data and the partial reconstruction at $t = 20\lambda_t$, for the three fluids (for each component u , v and p from left to right it is represented: a Newtonian fluid, a power-law fluid with $n = 0.7$ and a power-law fluid with $n = 1.3$). From these results, it is concluded that the partial reconstruction with just modes 2 and 3 recovers the bigger vortices traveling along the domain associated with the top cylinder. When modes 4 and 5 are considered, the smaller vortices downstream the bottom cylinder are captured, in a short distance from the cylinder. In the reconstruction with the first five modes almost all the structures are perceptible, although slight corrections are missing.

Due to the different vortices that are formed along time and space, the task of finding a direct relationship between the modes and the exact structures is really hard to perform. However the velocity fields obtained for the Newtonian fluid at $t = 10\lambda_t$, $t = 15\lambda_t$ and $t = 20\lambda_t$ were plotted, together with the velocity fields obtained for modes 2 and 3, and, modes 4 and 5. These results are shown in Fig. 3.6.

From Fig. 3.6, it is clear that the relationship between modes 2,3 and modes 4,5 and the top and bottom cylinders prevails along time. In addition, it may be concluded that both reconstructions still have information on both cylinders. The isolated vortices are not completely retrieved, but the association is clear. It is also noticeable that if the spatial characteristics are preserved, the temporal ones are merged. The intensity of each vortex pattern (represented by the vector lengths) is proportional to the vortices at this position in the decomposed dataset. When the velocity components are decomposed, the intensity of the vectors (vector length) coincides with the local averaged kinetic energy. Notice that the original data for variables u , v and p , with 23944 elements along 400 time steps are saved into a matrix with $(3 \times 23944 \times 400)$ about 28.7 million values that

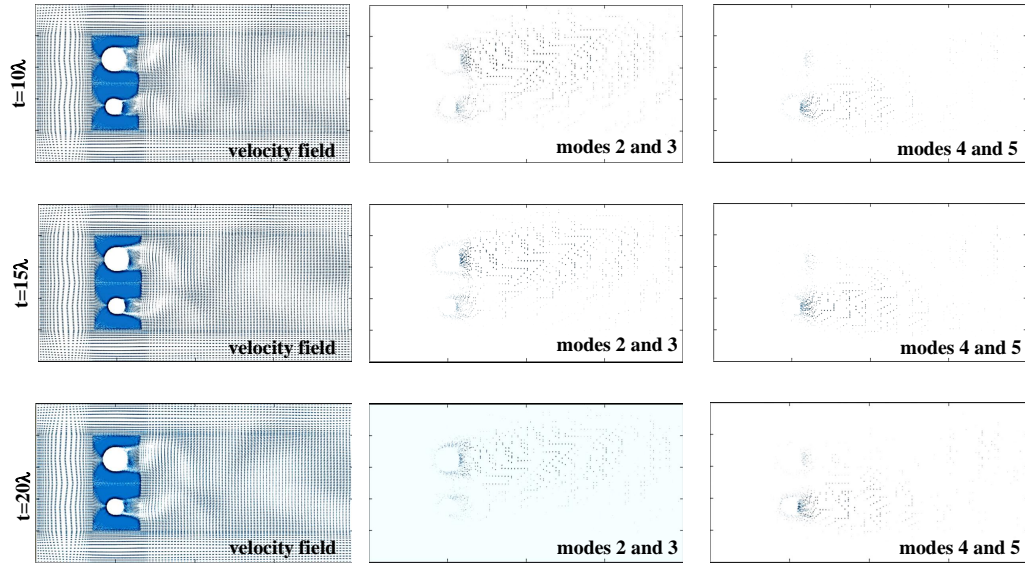


Figure 3.6: Velocity fields obtained for the Newtonian fluid at $t = 10\lambda_t$, $t = 15\lambda_t$ and $t = 20\lambda_t$ (together with the velocity fields obtained for modes 2 and 3, and, modes 4 and 5).

need to be stored. Due to computational limitations of the MATLAB software in the calculations of the elements applying the POD method it was considered one fifth of the elements. The data were saved into a matrix of $(3 \times 4789 \times 400)$ about 5.7 million entries. The reconstruction made with just five modes only needs $(3 \times 4789 \times 5)$ 71835 values to be stored. This is a reduction of 98.75% with no significant loss of information, resulting in significant savings. Next, a frequency analysis on the modes is performed.

3.2.3.2 Analysis of the frequencies of the modes time coefficients

Fig. 3.7 represents an analysis of the frequencies of the modes time coefficients. The Strouhal numbers presented in the figures are calculated considering the frequency with higher energy, the diameter of the bottom cylinder, D , and the mean velocity U .

By Eq. (3.20), the Strouhal number for $Re = 100$ is about 0.17 and for $Re = 150$ the Strouhal number is 0.18. These predicted Strouhal numbers can be related to the ones presented in Fig. 3.7 (a) for the Newtonian fluid. Therefore, analysing the frequencies of modes 2 and 3, it can be seen that $St = 0.155$ and the difference to the predicted Strouhal for the top cylinder (considering the diameter $1.5D$) is about 30%. For modes 4 and 5, $St = 0.22$, that when compared with the value predicted by Eq. (3.20) for the bottom cylinder, shows a deviation of about 30%.

Fig. 3.7 also shows that modes greater than one seem to be organized in pairs, revealing the need for the combination of two structures to correctly model the evolution of the flow structures along the domain.

From Fig. 3.7, it is also seen that for the three fluids the Strouhal numbers are very similar, meaning that the flow characteristics induced by the two cylinders are more important than the rheology of the fluids.

Tables 3.1 and 3.2 show that modes 2 and 3 were associated with the top cylinder. Thus, taking that into account, some conclusions related to the Strouhal numbers and how do they relate with the other modes represented in Fig. 3.7 can be derived. Therefore, it is seen that modes 6 and 7 have a Strouhal number approximately half the Strouhal number of modes 2 and 3 ($St_{6,7} \approx 0.5St_{2,3}$), whereas the Strouhal number of modes 10 and 11 is twice the value obtained for modes 2 and 3 ($St_{10,11} = 2St_{2,3}$). So, it is concluded that modes 6 and 7 and modes 10 and 11 are related to the same flow structures of modes 2 and 3.

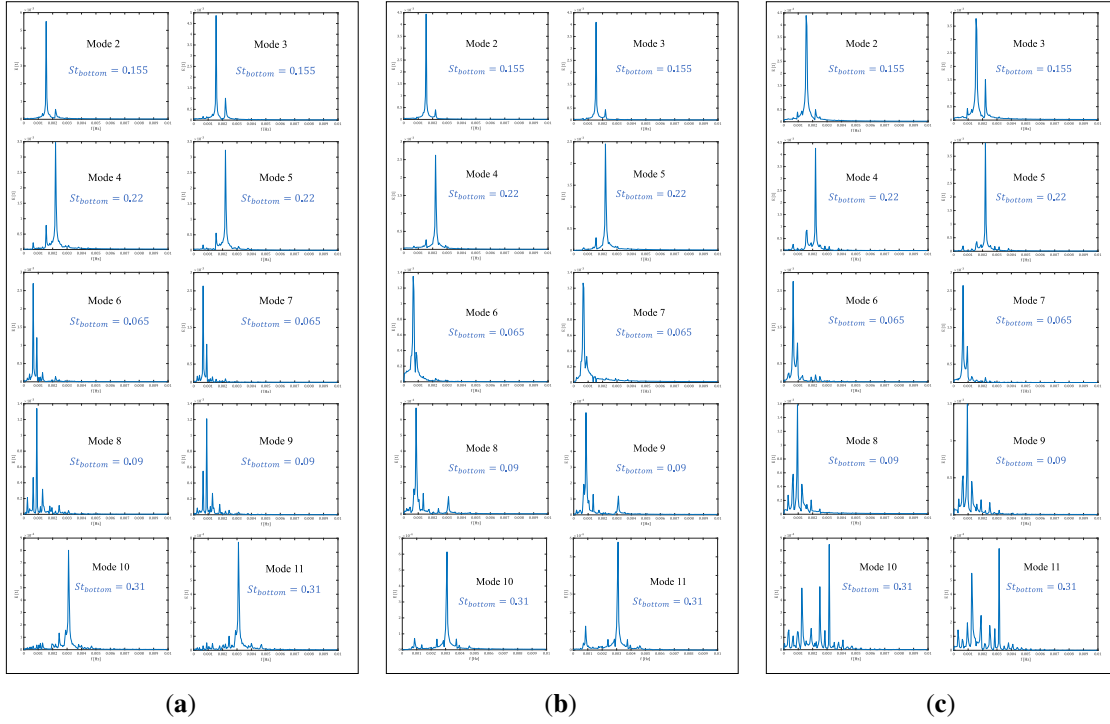


Figure 3.7: Analysis of frequencies of the modes time coefficients: (a) Newtonian fluid; (b) power-law fluid with $n = 0.7$; (c) power-law fluid with $n = 1.3$.

In Fig. 3.7 (a), that is the case of a Newtonian fluid, it can also be noticed that the Strouhal number calculated for the second most important frequency of modes 2 and 3 is the Strouhal number associated with modes 4 and 5, and vice versa. This means that the flow structure associated with modes 4 and 5 interferes with the flow structures associated with modes 2 and 3, and vice versa. The same happens to modes 6 and 7 and modes 8 and 9. This means that the flow structures associated with modes 8 and 9 interfere with the flow structure associated with modes 6 and 7, and vice versa.

In Fig. 3.7 (b), that is the case of a power-law fluid with $n = 0.7$, it is noticed that the Strouhal number calculated for the second most important frequency of modes 2 and 3 is the Strouhal number associated with modes 4 and 5 (the flow structure associated with modes 4 and 5 interferes with the flow structure associated with modes 2 and 3, and vice versa), but this relationship is not observed for the other modes. This is due to the use of a different constitutive model for the viscosity.

Finally, for Fig. 3.7 (c), the case of the power-law fluid with $n = 1.3$, it can be seen that the Strouhal number calculated for the second most important frequency of modes 2 and 3 is the Strouhal number associated with modes 4 and 5, but not the other way around. However, for modes 6 and 7, the Strouhal number calculated for the second most important frequency is associated with modes 8 and 9, and vice versa. This means that the flow structure associated with modes 8 and 9 interferes with the flow structures associated with modes 6 and 7, and vice versa. This is again due to the use of a different constitutive model for the viscosity.

Visually, it seems that the different modes are related to the upper or lower cylinder, thus allowing to use POD to detect and predict flow feature with much less information.

Fig. 3.8 (a)–(c) shows the pairs of time coefficients of consecutive modes, according to the frequencies represented in Fig. 3.7 for the Newtonian fluid, the power-law fluid with $n = 0.7$ and the power-law fluid with $n = 1.3$, respectively.

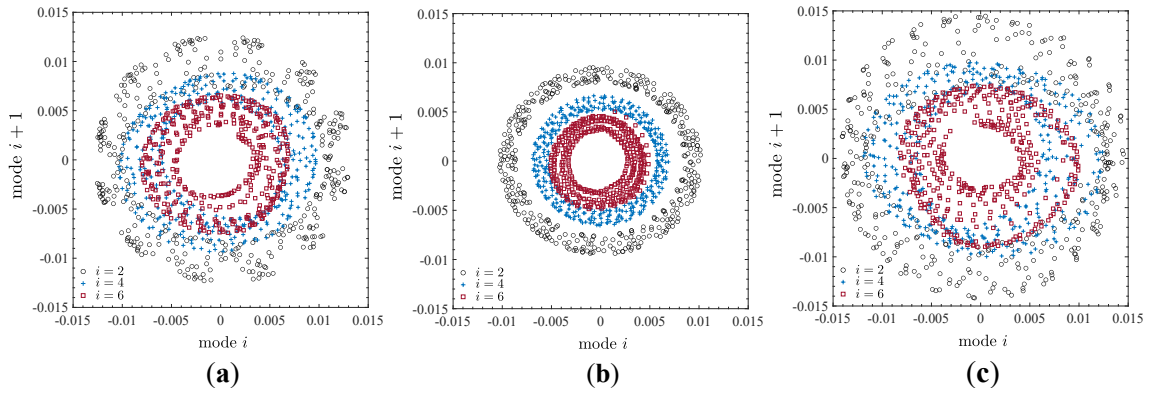


Figure 3.8: Pairs of time coefficients of consecutive modes: **(a)** Newtonian fluid; **(b)** power-law fluid with $n = 0.7$; **(c)** power-law fluid with $n = 1.3$.

Fig. 3.8 shows the oscillatory and alternating behaviour for pairs of time coefficients a_2 and a_3 , a_4 and a_5 , and a_6 and a_7 , that have similar frequency and amplitude, but with a phase between them. Therefore, to compare their relative contribution, if the values $\sqrt{a_1^2}$, $\sqrt{a_2^2 + a_3^2}$, $\sqrt{a_4^2 + a_5^2}$ and $\sqrt{a_6^2 + a_7^2}$ are considered, they remain similar along time. So, Eq. (3.22) is considered to compare the time coefficients of the modes having into account their oscillatory behaviour:

$$\sqrt{a_1^2} + \sqrt{a_2^2 + a_3^2} + \sqrt{a_4^2 + a_5^2} + \sqrt{a_6^2 + a_7^2}. \quad (3.22)$$

Modes higher than 7 were not considered due to their small contributions. For the Newtonian fluid, mode 1, without the oscillatory information, has about 75% of the information in Eq. (3.22), whereas modes 2 and 3 have approximately 11.2% of the information in Eq. (3.22) (referring to $\sqrt{a_2^2 + a_3^2}$), modes 4 and 5 have approximately 8% of the information in Eq. (3.22) (referring to $\sqrt{a_4^2 + a_5^2}$) and modes 6 and 7 have approximately 6% of the information in Eq. (3.22) (referring to $\sqrt{a_6^2 + a_7^2}$).

For the non-Newtonian power-law fluid with $n = 0.7$, mode 1, without the oscillatory information, has about 79.5% of the information in Eq. (3.22), whereas modes 2 and 3 have approximately

9.7% of the information in Eq. (3.22) (referring to $\sqrt{a_2^2 + a_3^2}$), modes 4 and 5 have approximately 6.5% of the information in Eq. (3.22) (referring to $\sqrt{a_4^2 + a_5^2}$) and modes 6 and 7 have approximately 4.3% of the information in Eq. (3.22) (referring to $\sqrt{a_6^2 + a_7^2}$). When comparing with the Newtonian fluid, the time weights show a smaller decrease, for pairs of modes after mode 1, but an increase for mode 1.

Finally, for the non-Newtonian power-law fluid with $n = 1.3$, mode 1, without the oscillatory information, has about 72.7% of the information in Eq. (3.22), whereas modes 2 and 3 have approximately 12.1% of the information in Eq. (3.22) (referring to $\sqrt{a_2^2 + a_3^2}$), modes 4 and 5 have approximately 8.8% of the information in Eq. (3.22) (referring to $\sqrt{a_4^2 + a_5^2}$) and modes 6 and 7 have approximately 6.3% of the information in Eq. (3.22) (referring to $\sqrt{a_6^2 + a_7^2}$). When comparing with the Newtonian fluid and with the non-Newtonian power-law where $n = 0.7$, the time weights show a smaller decrease on mode 1, but an increase on the pairs of modes after mode 1.

Looking at the results obtained for the Newtonian fluid, the non-Newtonian power-law fluid with $n = 0.7$, and with the non-Newtonian power-law fluid with $n = 1.3$, it can be concluded that the first modes are the ones that carry most of the information and with only a few modes, the simulation can be reconstructed.

By using two cylinders with different radii, different hidden structures in the flow are obtained, and using the modes and the frequencies of the modes time coefficients, some structures can be related to the influence of one cylinder over the other. This gives a better understanding of the flow.

This work is published on paper [92], which can be found in Part III of this thesis.

3.3 Flow of complex fluids past a cylinder in a channel

The planar flow past a cylinder is a benchmark problem proposed nearly three decades ago [93]. Numerous numerical studies have been published since then, predominantly employing the Oldroyd-B model to investigate creeping flow conditions, with a solvent viscosity ratio of 0.59. This selection is primarily driven by the simplicity of the problem, the availability of precise benchmark data, and the lack of singular points in the flow domain, particularly within the low Weissenberg range [94].

Within the creeping flow regime, the fluid elasticity becomes the primary cause of nonlinear behaviour, leading to the emergence of various flow phenomena that have received limited attention. These include, but are not limited to, flow instabilities, such as symmetry breaking, secondary flow, time dependency, elastic instability and elastic turbulence [95]. Several studies have already been conducted on the flow of non-Newtonian fluids around confined cylinders, and it is important to highlight some recent findings from the literature.

Varchanis et al. [96] carried out an investigation to assess how fluid rheological properties influence the development of laterally asymmetric flows past confined cylinders. They considered three non-Newtonian constitutive models: a shear-thinning inelastic Carreau–Yasuda model, which showed that shear-thinning alone is insufficient to cause flow asymmetry; a non-linear elastic dumbbell model, leading to a thin layer of highly elastic stresses downstream of the cylinder rear stagnation point, but no significant lateral asymmetries of the flow around the sides of the cylinder; and a viscoelastic shear-thinning linear PTT model, where lateral symmetry is retained, only below a critical low flow rate, together with the growth of an elastic downstream wake. Above the critical flow rate, this flow bifurcates to one of two steady laterally asymmetric states. These numerical results were compared with experimental data, and the conclusion was that both shear thinning and fluid elasticity are essential for the occurrence of flow asymmetry.

Recently, Peng et al. [95] investigated numerically the viscoelastic fluid flow instabilities observed experimentally upstream of the front stagnation point of the cylinder in a narrow channel. They used the FENE-P model to describe the rheological behaviour of a dilute polymer solution.

In this section, an extended work on the investigation of section 3.2 is presented. For that purpose, simulations in a planar flow past a 2D cylinder confined in a channel for a gPTT fluid are carried out at a low Reynolds number ($Re = 0.01$) and Weissenberg numbers of 1.2 and 1.25. Visualization of the transient flow during the simulations showed the presence of vortex shedding, bearing similarities with the von Kármán vortex street downstream of a cylinder for Newtonian fluids at higher Reynolds numbers. The presence of such coherent structures makes this problem a good candidate for applying the POD method. For each of the fluids, a reconstruction is performed and a frequency analysis of specific modes is obtained.

By applying the POD method, it was possible to detect and characterize large coherent structures through the flow decomposing into a generator base and the corresponding time coefficients and then by performing a frequency analysis of a limited number of modes for each of the flows, the one $Wi = 1.2$ and the other with $Wi = 1.25$. These values were used for the Weissenberg number,

because they are within a range that contains the transition from a steady state to the appearance of small vortices.

This section is organized as follows: first, the governing equations for the fluid and the constitutive model used in the simulations are presented, followed by the numerical method and the POD method applied. Following that, numerical simulations are conducted for the planar flow past a cylinder, considering two fluids: one with $Wi = 1.2$ and other with $Wi = 1.25$. The identification of the most significant modes is carried out, followed by a reconstruction of the flow and frequency analysis of specific modes. Finally, a change in the frequencies of the modes time coefficients of the POD for the fluid with $Wi = 1.2$ are applied, resulting in a new reconstruction. This reconstructed flow is then compared to the simulation results for the fluid with $Wi = 1.25$.

Each contribution related to the work objectives, presented in section 3.3, are explained in detail.

3.3.1 Governing equations, numerical method and POD

The equations governing the flow of an isothermal incompressible fluid, are the continuity,

$$\nabla \cdot \mathbf{u} = 0 \quad (3.23)$$

where \mathbf{u} is the velocity vector, and the momentum equation,

$$\rho \frac{D\mathbf{u}}{Dt} = -\nabla p + \nabla \cdot \boldsymbol{\tau}, \quad (3.24)$$

where ρ is the density, $\frac{D}{Dt}$ is the material derivative, p is the pressure, $\boldsymbol{\tau}$ is the extra-stress tensor and t is the time. The fluid considered is a gPTT fluid, whose constitutive equation is given by

$$K(\tau_{kk}) \boldsymbol{\tau} + \lambda \overset{\square}{\boldsymbol{\tau}} = 2\eta_p \mathbf{D}, \quad (3.25)$$

where

$$K(\tau_{kk}) = \Gamma(\beta) E_{\alpha, \beta} \left(\frac{\varepsilon \lambda}{\eta_p} \tau_{kk} \right), \quad (3.26)$$

is the function of the trace of stress tensor and

$$E_{\alpha, \beta}(z) = \sum_{j=0}^{\infty} \frac{z^j}{\Gamma(\alpha j + \beta)}, \quad (3.27)$$

is the Mittag–Leffler function with α, β real and positive and Γ is the Gamma function. τ_{kk} is the trace of the extra-stress tensor, η_p is the polymeric viscosity coefficient, \mathbf{D} is the rate of deformation tensor, ε represents the extensibility parameter and λ is the relaxation time of the fluid. $\overset{\square}{\boldsymbol{\tau}}$ represents the Gordon–Schowalter derivative (Eq. (2.28)).

Equations (3.23) and (3.24) together with the constitutive equation Eq. (3.25) are solved numerically using RheoTool, an open-source toolbox based on OpenFOAM® to simulate GNF and viscoelastic fluids under pressure-driven and/or electrically-driven flows [97–99].

The POD analysis is performed with MATLAB R2018a, whose implementation is described in section 3.1.2. The data saved in matrix \mathbf{M} corresponds to the velocity components, u and v , the pressure field, p , τ_{xx} and τ_{xy} , that are obtained after performing the CFD simulation. Thus, in each column of matrix \mathbf{M} , the following vector is saved:

$$\left(u_1, u_2, \dots, u_{N_E}, v_1, v_2, \dots, v_{N_E}, p_1, p_2, \dots, p_{N_E}, \tau_{xx_1}, \tau_{xx_2}, \dots, \tau_{xx_{N_E}}, \tau_{xy_1}, \tau_{xy_2}, \dots, \tau_{xy_{N_E}} \right)^T$$

where N_E is the number of elements of the mesh.

In the planar flow around a cylinder, a von Kármán vortex street can be observed above a sufficiently high Reynolds number that depends on blockage ratio and other relevant dimensionless numbers, such as the Weissenberg number if the fluid is viscoelastic. To quantify the periodic behaviour, the dimensionless Strouhal number is usually employed. The Strouhal number is defined by Eq. (3.19) and in this section, the characteristic linear dimension considered to calculate this non-dimensional number is the radius of the cylinder, R . Later, this definition is also used to normalise the frequencies obtained from the frequency analysis of the modes that come out of the POD method.

3.3.2 Problem definition

To the best of our knowledge, there were no studies published in the literature on numerical simulations performed with the gPTT model. Since a fundamental part of this thesis concerns that rheological model, to perform the numerical simulations, a gPTT fluid is considered with $\xi = 0$, $\beta_\eta = 0.9$, $\varepsilon = 0.02$, $\alpha = 1.26$ and $\beta = 1.2$, at $Re = 0.01$ and $Wi = \{1.2, 1.25\}$. The values for α and β are defined in accordance with the results presented by Ferrás et al. [3], that by performing a fitting to the extensional viscosity using the expPTT model and the gPTT model with $\alpha = 1.26$ and $\beta = 1.2$, showed that the gPTT model was a better fitting to the rheological data. In that fitting the mean square error was calculated being the error with the gPTT model 24 times smaller than the fitting with the expPTT model.

The geometry used in this study is a benchmark problem in computational rheology, corresponding to a planar flow past a confined cylinder [93]. This geometry, shown in Fig. 3.9, includes a channel with a cylinder of radius R , that is vertically centered between its walls, spaced apart $4R$ and placed at a distance of $20R$ downstream the inlet. The channel has a length of $60R$ downstream of the cylinder.

A 2D flow in the xy -plane is assumed and the following boundary conditions: at the inlet, the polymeric extra-stresses are null, and a zero-gradient is applied to the pressure; at the walls of the channel and of the cylinder, no-slip and non-porous conditions were set (velocity is null, the polymeric extra-stresses are linearly extrapolated to the walls and a zero-gradient is imposed for pressure); at the outlet, all variables have a zero-gradient, except for pressure that is fixed at $p = 0$.

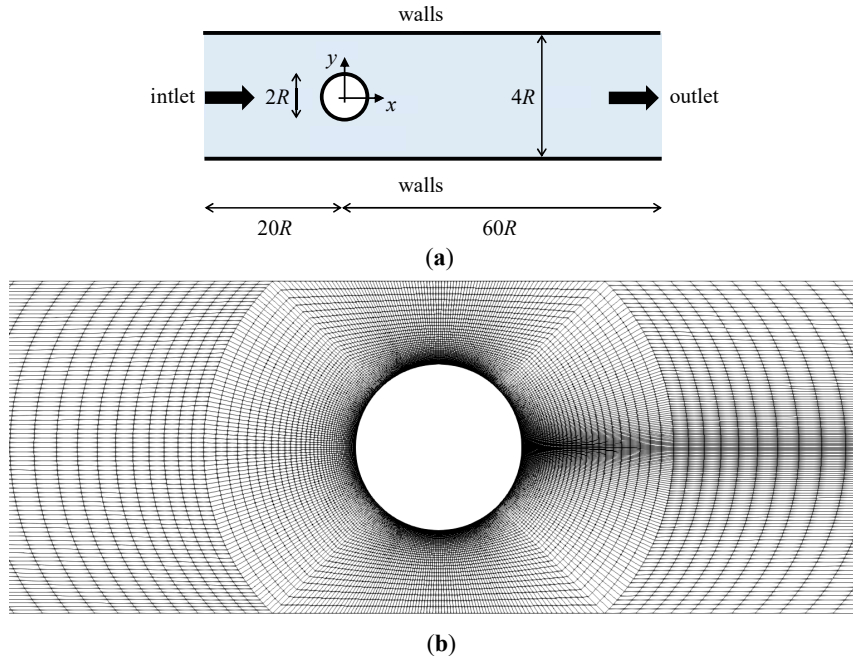


Figure 3.9: Flow around one cylinder with 50% blockage ratio. (a) Geometry; (b) closure view of the mesh around the cylinder. See user guide of RheoTool [100].

3.3.3 Results and discussion

The mesh considered for the numerical simulations and POD analysis has 24894 elements and is the one considered in the tutorial of the RheoTool [97]. For this mesh and with $Re = 0.01$, simulations at different Weissenberg numbers (Wi) are performed, to obtain the drag coefficient (C_d) for each simulation. The results are presented in Fig. 3.10.

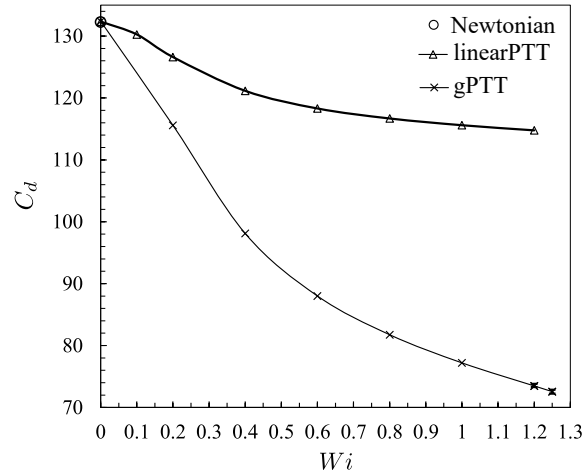


Figure 3.10: Variation of C_d with Wi . The circle (\circ) corresponds to a Newtonian fluid [101], triangles (Δ) correspond to values of Afonso et al. [102] for the linearPTT ($\varepsilon = 0.02$ and a mesh with 45120 elements), and the cross (\times) are the results for the gPTT. The error bars represent the amplitude of the oscillations for the unsteady cases and lines are a guide to the eye.

A maximum value for Wi at 1.25 was used because the simulation at $Wi = 1.3$ diverged. The

values for C_d in each simulation are calculated until the flow becomes steady. Fig. 3.10 shows that the drag coefficient decreases as the Weissenberg number increases, which aligns with the results obtained from the linearPTT model [102]. It is worth noting that these results for the gPTT model differ from those of Afonso et al. [102] for a linearPTT model with $\beta_\eta = 0.59$ due to the change of rheology of the model.

3.3.3.1 POD with $Wi=1.2$ and $Wi=1.25$

To apply the POD method, transient simulations with 1200 time-steps are performed, considering $\Delta t/\lambda \approx 0.0083$ for $Wi = 1.2$ and $\Delta t/\lambda = 0.008$ for $Wi = 1.25$, so that a periodic flow without the strong influence of the initial conditions could be obtained. Then the simulation continued and 800 snapshots of our simulation are saved with increments of 10 time-steps each. To better understand the presence of a vortex shedding bearing similarities with the von Kármán vortex street downstream of the cylinder for Newtonian fluids at higher Reynolds number, Fig. 3.11 presents the drag coefficient as a function of t/λ .

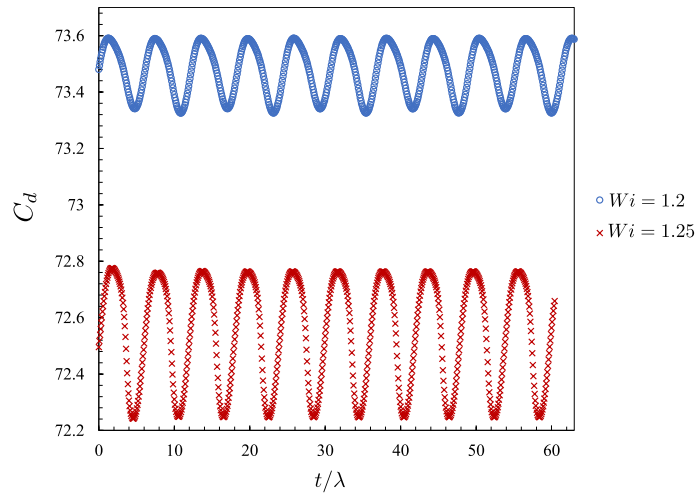


Figure 3.11: Variation of C_d with t/λ for the fluid with $Wi = 1.2$ and $Wi = 1.25$.

Fig. 3.11 shows that the flow is periodic at $Wi = 1.2$ and 1.25 .

To perform the POD, only 400 snapshots are considered, i.e. the data of every 20 time-steps is read.

For this study, only the first 20 eigenvalues and modes are considered. Fig. 3.12 shows the relative weight of the eigenvalues associated with each mode, for $Wi = 1.2$ and $Wi = 1.25$, respectively. In both cases, and as expected, there is a fast decay of the relative weight associated with each mode. For the fluid with $Wi = 1.2$, the weights of the first, second and third modes are 99.9996%, 0.0004% and 0.0000205% respectively and for the fluid with $Wi = 1.25$ the weights of the first, second and third modes are 99.9987%, 0.00121% and 0.0000605%, respectively. For both cases the weights attributed to the remaining modes are residual, showing that these first three modes may be sufficient to perform the reconstruction of the flow.

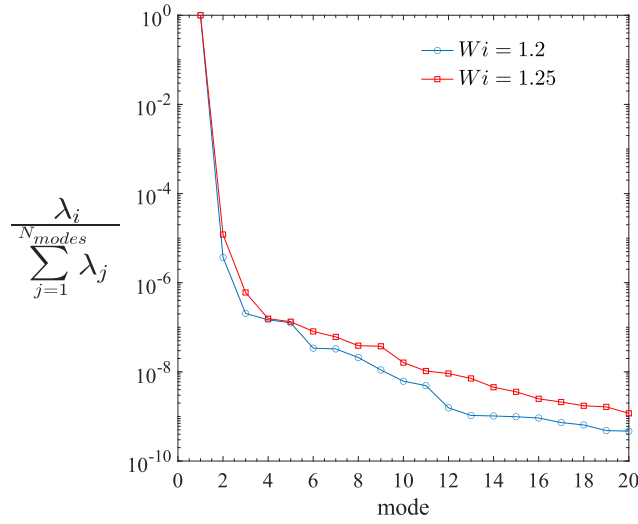
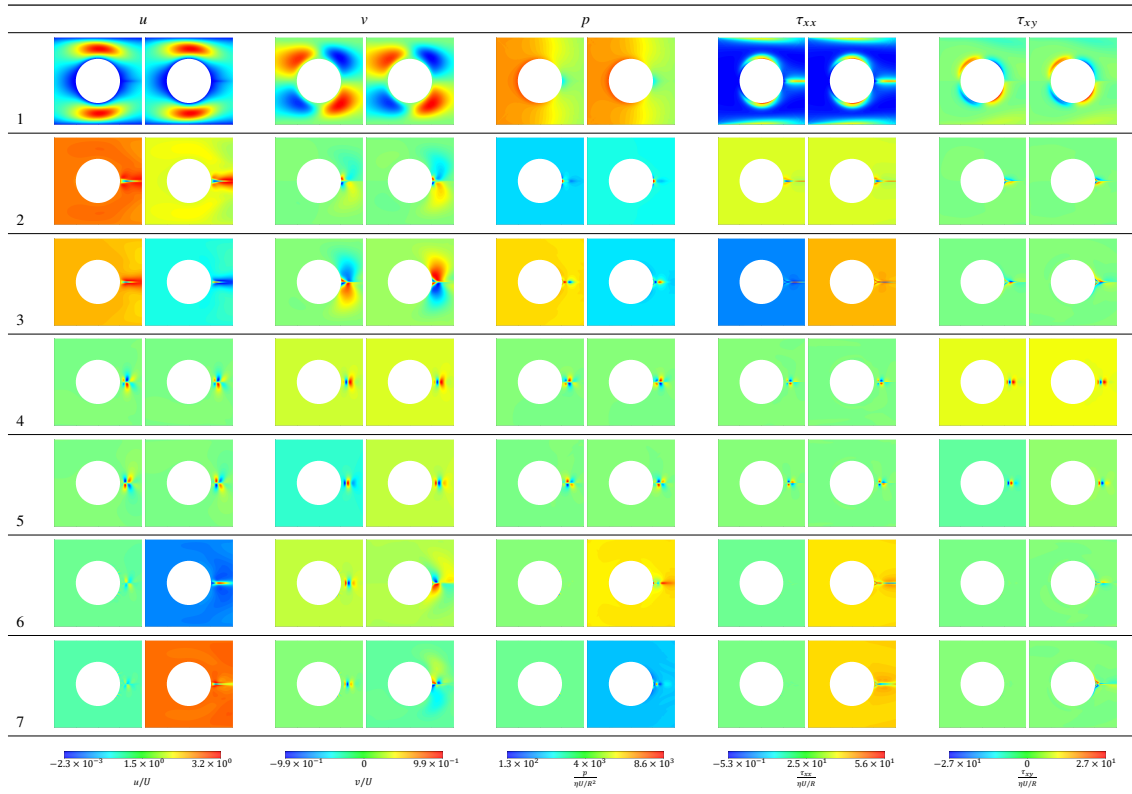


Figure 3.12: Relative weight of the eigenvalues associated with each mode.

Table 3.3 presents the most important modes for u , v , p , τ_{xx} and τ_{xy} (for each component u , v , p , τ_{xx} and τ_{xy} , from left to right, represents the case simulation with $Wi = 1.2$ and $Wi = 1.25$).

Table 3.3: Most important modes (1 to 7) of u , v , p , τ_{xx} and τ_{xy} for the flow around the cylinder. For each component u , v , p , τ_{xx} and τ_{xy} , from left to right, represents the case simulation with $Wi = 1.2$ and $Wi = 1.25$.

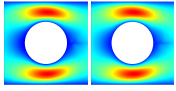
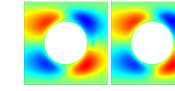
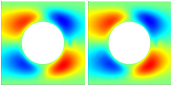
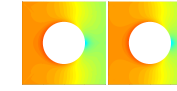
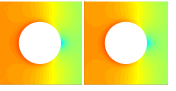
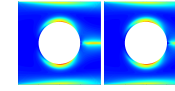
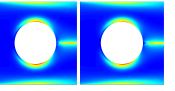
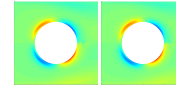
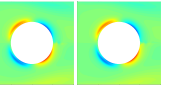







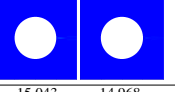




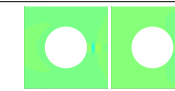
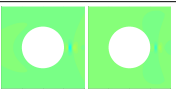
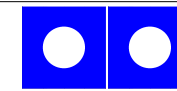
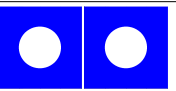
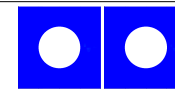
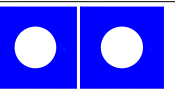
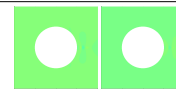
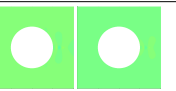

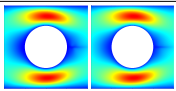
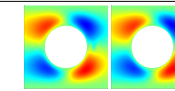
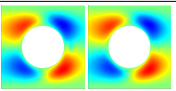
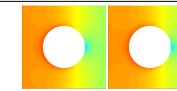
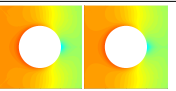
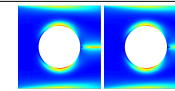
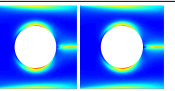
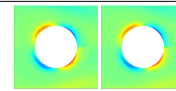
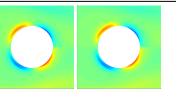

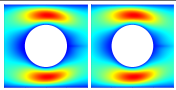
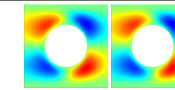
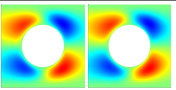
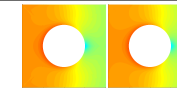
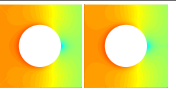
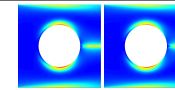
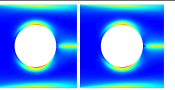
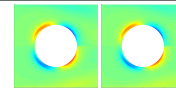
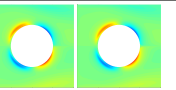

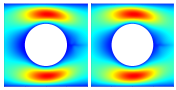
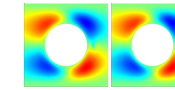
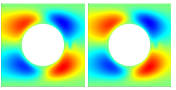
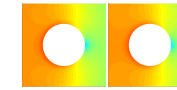
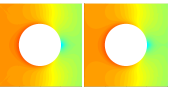
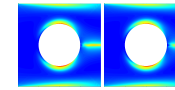
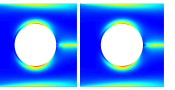
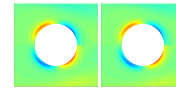
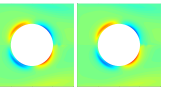

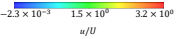

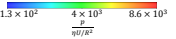
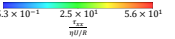
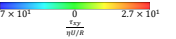


By analysing Table 3.3, it is seen that the first mode is symmetric and has the main features of

the flow without the oscillating part, having the same behaviour of the study presented in section 3.2. The results are similar between the cases with $Wi = 1.2$ and $Wi = 1.25$, but analysing the modes there are some differences between them. For both cases, the modes after mode 1 are similar by pairs (meaning 2,3 and 4,5) with some delay between them. For modes 6 and 7, comparing the two fluids, a different behaviour is observed. Specifically for p , τ_{xx} and τ_{xy} , the case with $Wi = 1.25$ shows some structures downstream of the cylinder, which seem to be absent for $Wi = 1.2$.

In Table 3.4 a comparison is made between the original data obtained from the simulation and a partial reconstruction at the last time step, for each quantity, u , v , p , τ_{xx} and τ_{xy} . From left to right, the simulation cases with $Wi = 1.2$ and $Wi = 1.25$ are represented. The value shown below each reconstruction is the RMSE at the last time step, for each quantity u , v , p , τ_{xx} and τ_{xy} relative to the corresponding original data for each flow simulation. Various reconstructions are shown, namely with modes 2 and 3, modes 4 and 5, modes 1 and 5, modes 1 to 3 and modes 1 to 5.

Table 3.4: Comparison between the original (first row of images) data versus the partial reconstruction (the modes used in the reconstruction are shown in the first column). For each component u , v , p , τ_{xx} and τ_{xy} , from left to right it is considered the simulation case with $Wi = 1.2$ and $Wi = 1.25$ and the RMSE for each reconstruction.

	u		v		p		τ_{xx}		τ_{xy}	
Original										
2,3										
RMSE _{2,3}	1.184	1.183	0.313	0.313	5754.705	5722.864	15.043	14.968	6.012	6.013
4,5										
RMSE _{4,5}	1.183	1.183	0.312	0.311	5754.722	5722.869	15.053	14.958	6.003	5.992
1,5										
RMSE _{1,5}	0.006	0.008	0.015	0.015	14.581	8.511	0.381	0.376	0.183	0.191
1-3										
RMSE ₁₋₃	0.007	0.005	0.021	0.015	3.630	3.637	0.160	0.192	0.188	0.144
1-5										
RMSE ₁₋₅	0.001	0.002	0.004	0.002	1.913	2.888	0.084	0.170	0.062	0.076
<div>  u/U  v/U  $\frac{p}{\rho U^2}$  $\frac{\tau_{xx}}{\rho U^2}$  $\frac{\tau_{xy}}{\rho U^2}$ </div>										

RMSE is calculated with Eq. (3.28):

$$RMSE = \sqrt{\frac{1}{n} \sum_{i=1}^n (P - P_{rec})^2} \quad (3.28)$$

where P can be u , v , p , τ_{xx} and τ_{xy} and P_{rec} (“rec” indicates *reconstruction*) is the corresponding reconstructed value. For any fields, the reconstruction with modes 2 and 3, does not show any hidden structures of the flow, but in the reconstruction with modes 4 and 5, for v and τ_{xy} , small vortices downstream of the cylinder are perceptible. The best reconstructions are with modes 1 and 5, modes 1 to 3, and modes 1 to 5, where all reconstructed fields approach the original data and exhibit the lowest RMSE. When comparing to the work in section 3.2, the reconstruction with modes 1 and 5 was added to assess if only with modes 1 and 5 the reconstruction was good enough to identify all the structures of the flow. It is seen that the reconstruction is very similar to the original, but some differences can be noted, mainly for the $Wi = 1.25$ case. The best reconstruction is with modes 1 to 5, where the differences are not visible. By looking at the RMSE for each quantity, it is verified what the figures represented on the table show, and can be concluded that the best prediction of the flow is for the reconstruction with modes 1 to 5 since in that case the RMSE is lower.

Fig. 3.13 presents an analysis of the frequencies of the modes time coefficients for the two fluids. The Strouhal numbers (Eq. (3.19)) plotted in Fig. 3.13 are calculated considering the frequency with higher energy in each mode.

In Fig. 3.13 mode 1 was not considered because the time coefficient of this mode is constant in time. By analysing Fig. 3.13, it can be seen that pairs of modes 2 and 3, 4 and 5, 6 and 7, 8 and 9 have common Strouhal numbers, for both flows, which shows that each pair is associated with the same flow structure, being in agreement with the conclusions of section 3.2. For the fluid with $Wi = 1.2$, the Strouhal number of modes 4 and 5 is about 8 times the Strouhal number of modes 2 and 3 ($St_{4,5} \approx 8St_{2,3}$) and the Strouhal number of modes 8 and 9 is twice the Strouhal number of modes 2 and 3 ($St_{8,9} = 2St_{2,3}$). For the fluid with $Wi = 1.25$, the Strouhal number of modes 4 and 5 is about 8 times the Strouhal number of modes 2 and 3 ($St_{4,5} \approx 8St_{2,3}$) and the Strouhal number of modes 6 and 7 is about twice the Strouhal number of modes 2 and 3 ($St_{6,7} \approx 2St_{2,3}$). Comparing the fluids, it can be seen that the Strouhal numbers are similar, except for modes 6 and 7, and modes 8 and 9 that are swapped, from one fluid to the other, i.e. the Strouhal number of modes 6 and 7 in the fluid with $Wi = 1.2$ is equal to the Strouhal number of modes 8 and 9 in the $Wi = 1.25$ case, and the Strouhal number of modes 8 and 9 in the $Wi = 1.2$ case is approximated to the Strouhal number of modes 6 and 7 for $Wi = 1.25$.

The modes obtained from the POD are unitary vectors that when combined with the time coefficients form the original data set. These coefficients can provide information regarding the importance of the modes. Considering Fig. 3.13, the modes can be grouped by consecutive pairs according to the Strouhal number, and those pairs are plotted in 3.14.

Fig. 3.14 shows that the oscillatory and alternating behaviour is observed for modes higher than 3. Looking, to modes 6 and 7, in Fig. 3.14 (a) the elliptical shape of curves of the time coefficients is characteristic of two sinusoidal waves, its vertical stretch is due to different amplitudes and their rotation is a phase influence, both on correspondent time coefficients. It can be noticed in Fig. 3.13 (a) that they have a single peak. For modes 2 and 3 the representation is not elliptical, as a consequence of some secondary peaks close to the main frequencies as seen in Fig. 3.13 (a) for

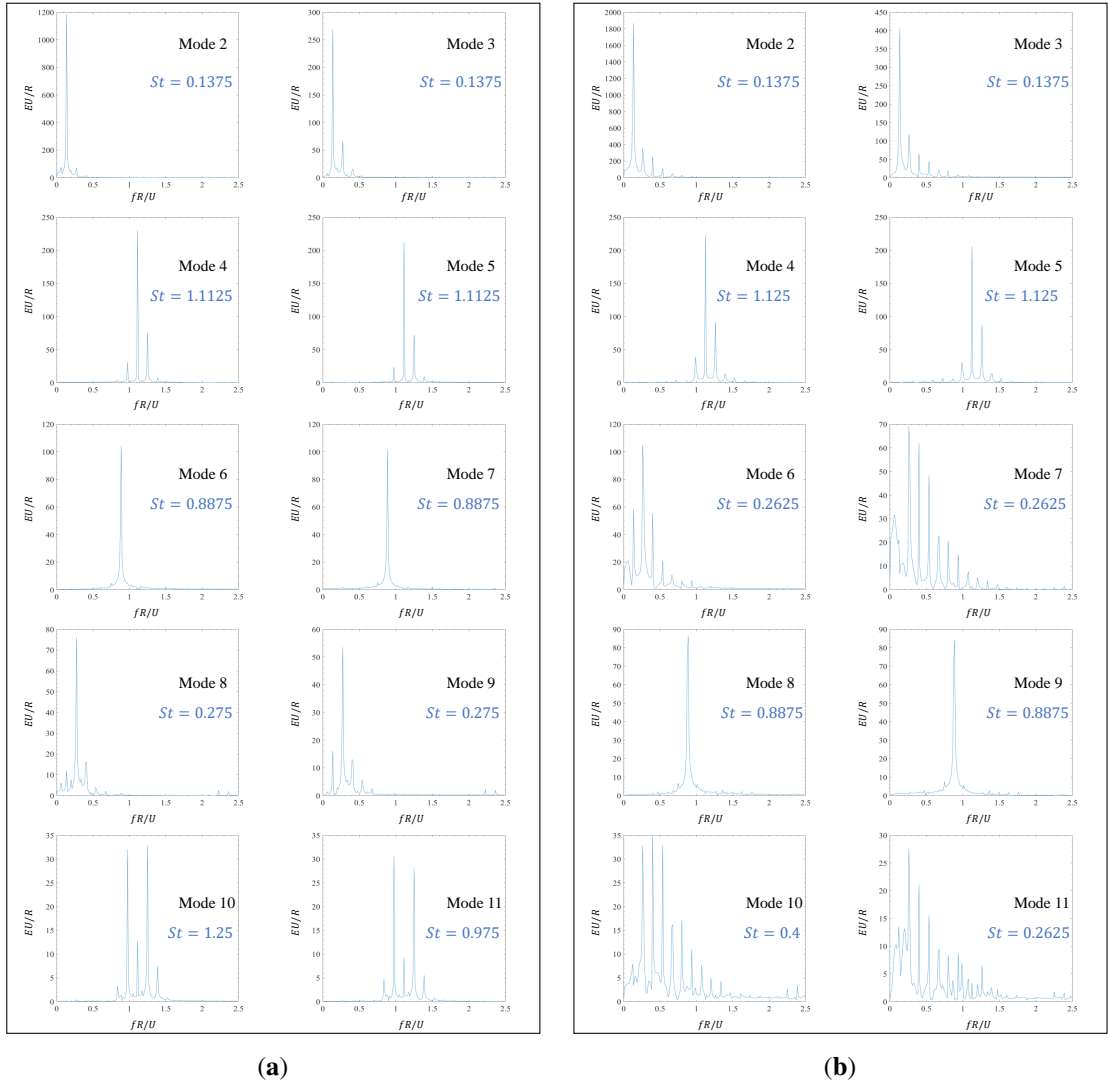


Figure 3.13: Analysis of frequencies of the *time coefficients* of the modes through fast Fourier transform: **(a)** $Wi = 1.2$; **(b)** $Wi = 1.25$.

modes 2 and 3.

The pairs of coefficients a_2 and a_3 , a_4 and a_5 and a_6 and a_7 vary into an oscillatory way, with a phase between them, as can be seen in Fig. 3.14. However, they have similar frequency and amplitude, so to compare their relative contribution, if the values $\sqrt{a_1^2}$, $\sqrt{a_2^2 + a_3^2}$, $\sqrt{a_4^2 + a_5^2}$ and $\sqrt{a_6^2 + a_7^2}$ are considered, they remain similar along time. Therefore, to compare the time coefficients of the modes having into account their oscillatory behaviour, Eq. (3.29) is considered:

$$\sqrt{a_1^2} + \sqrt{a_2^2 + a_3^2} + \sqrt{a_4^2 + a_5^2} + \sqrt{a_6^2 + a_7^2}. \quad (3.29)$$

As seen before, modes greater than 7 have small contributions, so they are not considered. For the fluid with $Wi = 1.2$, mode 1, that is the one where doesn't appear the oscillating part, has about 99.7% of the information in Eq. (3.29) (regarding $\sqrt{a_1^2}$), while modes 2 and 3 have approximately

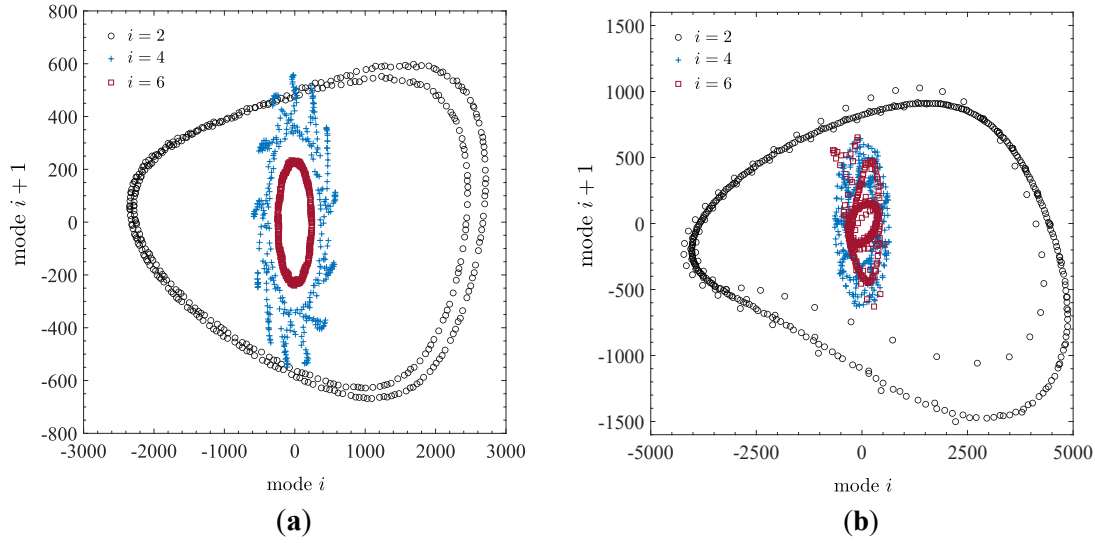


Figure 3.14: Pairs of time coefficients of consecutive modes: (a) $Wi = 1.2$; (b) $Wi = 1.25$.

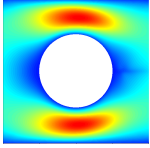
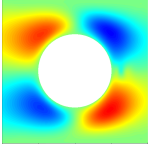
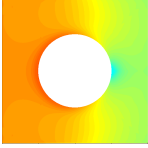
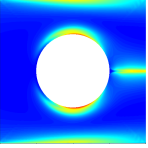
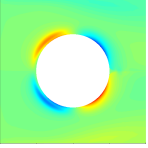
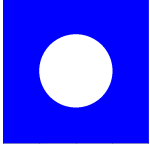
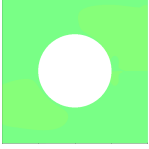
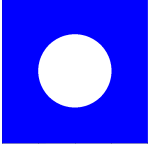


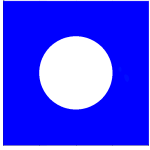

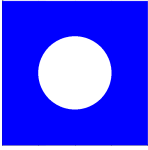
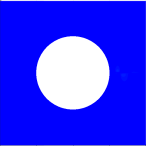

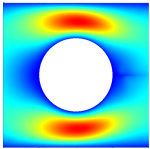
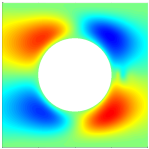
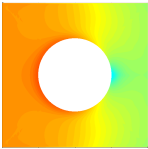
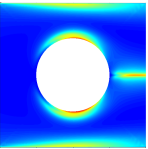
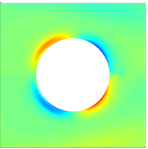
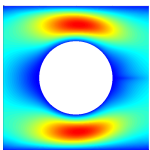
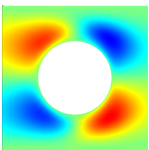
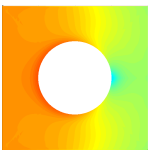
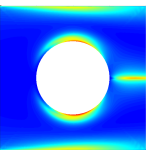
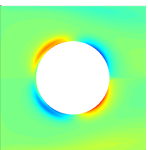
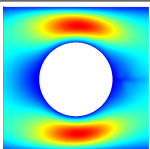
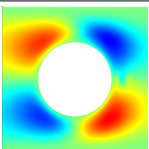
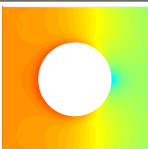
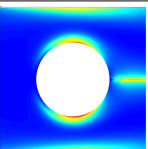
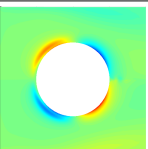
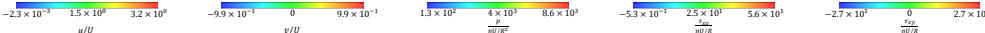
0.18% of the information in Eq. (3.29) (regarding $\sqrt{a_2^2 + a_3^2}$), modes 4 and 5 have approximately 0.051% of the information in Eq. (3.29) (regarding $\sqrt{a_4^2 + a_5^2}$), and finally, modes 6 and 7 have approximately 0.026% of the information in Eq. (3.29) (regarding $\sqrt{a_6^2 + a_7^2}$). For the fluid with $Wi = 1.25$, mode 1, has about 99.6% of the information in Eq. (3.29) (regarding $\sqrt{a_1^2}$), while modes 2 and 3 have approximately 0.33% of the information in Eq. (3.29) (regarding $\sqrt{a_2^2 + a_3^2}$), modes 4 and 5 have approximately 0.052% of the information in Eq. (3.29) (regarding $\sqrt{a_4^2 + a_5^2}$), and finally, modes 6 and 7 have approximately 0.034% of the information in Eq. (3.29) (regarding $\sqrt{a_6^2 + a_7^2}$). When both fluids are compared, there is a small increase for the fluid with $Wi = 1.25$.

3.3.3.2 Changing the POD of the fluid with $Wi=1.2$ to reconstruct the simulation of the fluid with $Wi=1.25$.

In this section, a reconstruction of the simulation of the flow with $Wi = 1.25$ having as initial data the POD of the flow with $Wi = 1.2$ is conducted. For that, a change of the modes frequencies in the POD of the fluid with $Wi = 1.2$ is applied, by multiplying the interval considered of the frequencies by $1.25/1.2$, followed by an inverse of the fast Fourier transform, to obtain a new matrix for the time coefficients. Then, with that new matrix, a new reconstruction is obtained and compared with the original simulation case of $Wi = 1.25$.

Table 3.5 presents the obtained results. The original data for the fluid with $Wi = 1.25$ is represented on the first row and in Table 3.5 the reconstruction with modes 2 and 3, modes 4 and 5, modes 1 and 5, modes 1 to 3 and modes 1 to 5, for u , v , p , τ_{xx} and τ_{xy} are represented. RMSE is calculated for each variable for the last time step, by considering the u , v , p , τ_{xx} and τ_{xy} from the original data of the simulation case with $Wi = 1.25$, with u , v , p , τ_{xx} and τ_{xy} reconstructed with modes 2 and 3, modes 4 and 5, modes 1 and 5, modes 1 to 3 and modes 1 to 5. RMSE is calculated by Eq. (3.28).

Table 3.5: Comparison between the original data (first row of images) for $Wi = 1.25$ versus the partial reconstruction (the modes used in the reconstruction are shown in the first column) with the change in the frequencies and the RMSE for each reconstruction.

	u	v	p	τ_{xx}	τ_{xy}
Original					
2,3					
RMSE _{2,3}	1.183	0.312	5722.899	14.955	6.001
4,5					
RMSE _{4,5}	1.183	0.312	5722.869	14.958	5.993
1,5					
RMSE _{1,5}	0.008	0.018	34.023	0.394	0.211
1-3					
RMSE ₁₋₃	0.006	0.016	38.749	0.501	0.210
1-5					
RMSE ₁₋₅	0.005	0.012	38.720	0.499	0.196
					

Looking at Table 3.5 it can be seen that the reconstructions that are similar to the original data are the ones with modes 1 and 5, modes 1 to 3 and modes 1 to 5. Looking at the RMSE and comparing these three reconstructions, the one that shows in the majority of the variables a better prediction for the last time step is the reconstruction with modes 1 to 5. So, considering that reconstruction and to better understand the results, the RMSE for all time steps was calculated, for τ_{xx} from the original data of the simulation case with $Wi = 1.25$ and τ_{xx} reconstructed with modes 1 to 5. The error was calculated with Eq. (3.28), where P was τ_{xx} .

It was also considered τ_{xx} from the original data of the simulation case with $Wi = 1.25$ and

τ_{xx} reconstructed with modes 1 to 5, for point (1.7,0.004,0), that is a point placed downstream of the cylinder.

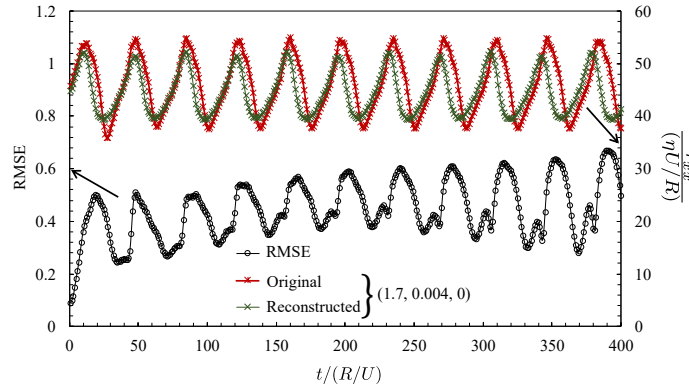


Figure 3.15: RMSE calculated for the original τ_{xx} of the simulation with $Wi = 1.25$ and for the τ_{xx} reconstructed with modes 1 to 5 (left vertical axis). In the right vertical axis it is represented the values of τ_{xx} from the original data of the simulation for the fluid with $Wi = 1.25$ and τ_{xx} reconstructed with modes 1 to 5, for point (1.7,0.004,0), that is a point placed downstream the cylinder.

The results are plotted in Fig. 3.15. Looking at Fig. 3.15, the RMSE is greater when stresses are at their maximum. This is expected, but with this representation is more evident. So, it can be concluded that the forecast is worst when the fields are close to the maximum value of the oscillations. Comparing τ_{xx} from the original data of the simulation case with $Wi = 1.25$ and τ_{xx} reconstructed with modes 1 to 5, in point (1.7,0.004,0), that effect is best visualized, but also, a good prevision of the fluid flow with this reconstruction is obtained.

Part III

More on theoretical and numerical studies of viscoelastic fluid flows

The present dissertation falls into the category of *multi-paper dissertations*, and in the Part III of this dissertation, called “More on theoretical and numerical studies of viscoelastic fluid flows”, includes the complete and integral version of the papers written in the course of this PhD work. These papers were explained and contextualized in the previous Part II in section 2.2, 2.3, 2.4 and 3.2.

Part III is further divided into six main sections. In section 4.1, the following paper, related with analytical and semi-analytical solutions for the Couette and Poiseuille–Couette flows, described by the viscoelastic model gPTT are presented.

- A.M. Ribau, L.L. Ferrás, M.L. Morgado, M. Rebelo, and A.M. Afonso. Semi-Analytical Solutions for the pure Poiseuille-Couette Flow of a Generalised Phan-Thien–Tanner Fluid. *Fluids*, 4(3):129, jul 2019.

In section 4.2, the following paper, related with analytical and semi-analytical solutions for the pure Couette and Poiseuille–Couette flows under slip, described by the viscoelastic model gPTT are presented.

- A.M. Ribau, L.L. Ferrás, M.L. Morgado, M. Rebelo, and A.M. Afonso. Analytical and numerical studies for slip flows of a generalised Phan-Thien–Tanner fluid. *ZAMM - Journal of Applied Mathematics and Mechanics/Zeitschrift für Angewandte Mathematik und Mechanik*, 100(3), jan 2020.

In section 4.3, the following paper, related with analytical and semi-analytical solutions for the annular flow, described by the viscoelastic model gPTT are presented.

- A.M. Ribau, L.L. Ferrás, M.L. Morgado, M. Rebelo, F.T. Pinho, and A.M. Afonso. Analytical study of the annular flow of a generalised Phan-Thien–Tanner fluid. *Acta Mech* 235, 1307–1317, 2024.

In section 4.4, the following paper, related with semi-analytical solutions for the combined fully-developed electro-osmotic pressure-driven flow in microchannels of viscoelastic fluids, described by the gPTT model are presented.

- A.M. Ribau, L.L. Ferrás, M.L. Morgado, M. Rebelo, M.A. Alves, F.T. Pinho, and A.M. Afonso. A study on mixed electro-osmotic/pressure-driven microchannel flows of a generalised Phan-Thien–Tanner fluid. *Journal of Engineering Mathematics*, 127(1), mar 2021.

In section 4.5, the following paper, related with semi-analytical solutions for the combined fully-developed electro-osmotic pressure-driven flow in microchannels of viscoelastic fluids under asymmetric zeta potentials, described by the gPTT model are presented.

- A.M. Ribau, L.L. Ferrás, M.L. Morgado, M. Rebelo, F.T. Pinho, and A.M. Afonso. The effect of asymmetric zeta potentials on the electro-osmotic flow of complex fluids. Submitted to *Journal of Engineering Mathematics*.

In section 5.1, the following paper, related with the decomposition of the von Kármán vortex street into a generator base and the correspondent analysis through the POD for the 2D flow around a cylinder and the 2D flow around two cylinders with different radii are presented.

- A.M. Ribau, N.D. Gonçalves, L.L. Ferrás, and A.M. Afonso. Flow structures identification through proper orthogonal decomposition: The flow around two distinct cylinders. *Fluids*, 6(11):384, 2021.

Chapter 4

More on theoretical studies

4.1 Semi-analytical solutions for the Poiseuille–Couette flow of a generalised Phan-Thien–Tanner¹

Abstract: This work presents new analytical and semi-analytical solutions for the pure Couette and Poiseuille–Couette flows, described by the recently proposed (Ferrás et al., A Generalised Phan-Thien–Tanner Model, JNNFM 2019) viscoelastic model, known as the generalised Phan-Thien–Tanner constitutive equation. This generalised version considers the Mittag–Leffler function instead of the classical linear or exponential functions of the trace of the stress tensor, and provides one or two new fitting constants in order to achieve additional fitting flexibility. The analytical solutions derived in this work allow a better understanding of the model, and therefore contribute to improve the modelling of complex materials, and will provide an interesting challenge to computational rheologists, to benchmarking and to code verification.

Keywords: generalised simplified PTT; Phan-Thien–Tanner (PTT) model; Mittag–Leffler; Couette flow; Poiseuille–Couette flow

4.1.1 Introduction

It is well known that much can be learned about a physical phenomenon if a mathematical model exists that can mimic and predict its behavior. The world of complex fluids is no different, and, therefore, several models have been proposed over the years for that purpose. These models can be more or less complex, depending on the properties of the fluids that are taken into account.

In this work, we are interested in viscoelastic materials [1], for which several models have been proposed in the past. One can classify these models as: differential (that make use of the local deformation field only) and integral (that take into account all the past deformation at each instant). Differential models usually allow a faster numerical solution of the differential equations involved,

¹A.M. Ribau, L.L. Ferrás, M.L. Morgado, M. Rebelo, and A.M. Afonso. Semi-analytical solutions for the Poiseuille–Couette flow of a generalised Phan-Thien–Tanner fluid. *Fluids*, 4(3):129, jul 2019.

while integral models are computationally expensive and may lead to error propagation. On the other hand, integral models allow a better modelling, since they incorporate the real world fluid memory (the present state is influenced by all past weighted deformations). It is therefore of major importance to improve the fitting capabilities of differential models and reduce the computational effort needed to compute integral models.

In a recent work, Ferrás et al. [3] proposed an improved differential model based on the model by Nhan Phan-Thien and Roger Tanner (PTT [21]), derived from the Lodge–Yamamoto type of network theory for polymeric fluids. The constitutive equation proposed by Nhan Phan-Thien and Roger Tanner, for the case of an isothermal flow, is given by:

$$f(\tau_{kk})\boldsymbol{\tau} + \lambda \dot{\boldsymbol{\tau}} = 2\eta_p \mathbf{D} \quad (4.1)$$

with

$$f(\tau_{kk}) = 1 + \frac{\varepsilon \lambda}{\eta_p} \tau_{kk}, \quad (4.2)$$

where \mathbf{D} is the rate of deformation tensor, $\boldsymbol{\tau}$ is the stress tensor, λ is a relaxation time, η_p is the polymeric viscosity, τ_{kk} is the trace of the stress tensor, ε represents the extensibility parameter and $\dot{\boldsymbol{\tau}}$ represents the Gordon–Schowalter derivative defined as

$$\dot{\boldsymbol{\tau}} = \frac{\partial \boldsymbol{\tau}}{\partial t} + \mathbf{u} \cdot \nabla \boldsymbol{\tau} - (\nabla \mathbf{u})^T \cdot \boldsymbol{\tau} - \boldsymbol{\tau} \cdot (\nabla \mathbf{u}) + \xi (\boldsymbol{\tau} \cdot \mathbf{D} + \mathbf{D} \cdot \boldsymbol{\tau}). \quad (4.3)$$

Here, \mathbf{u} is the velocity vector, $\nabla \mathbf{u}$ is the velocity gradient and the parameter ξ accounts for the slip between the molecular network and the continuous medium (it should be remarked that for the derivation of the analytical solutions we will consider $\xi = 0$). Later, Phan-Thien proposed a new model, based on an exponential function form [22] and showed that this new function would be quite adequate to represent the rate of destruction of junctions, but the parameter ε should be of the order 0.01. The function $f(\tau_{kk})$ is given by:

$$f(\tau_{kk}) = \exp\left(\frac{\varepsilon \lambda}{\eta_p} \tau_{kk}\right). \quad (4.4)$$

Ferrás et al. [3] considered a more general function for the rate of destruction of junctions, the Mittag–Leffler function where one or two fitting constants are included, in order to achieve additional fitting flexibility [3]. The Mittag–Leffler function is defined by,

$$E_{\alpha, \beta}(z) = \sum_{k=0}^{\infty} \frac{z^k}{\Gamma(\alpha k + \beta)}, \quad (4.5)$$

with α, β real and positive. When $\alpha = \beta = 1$, the Mittag–Leffler [24] function reduces to the exponential function. When $\beta = 1$, the original one-parameter Mittag–Leffler function, E_{α} , is obtained. Thus, the new function of the trace of stress tensor (now denoted by $K(\cdot)$ instead of $f(\cdot)$, to distinguish from the classical cases) describing the network destruction of junctions is written as:

$$K(\tau_{kk}) = \Gamma(\beta) E_{\alpha,\beta} \left(\frac{\varepsilon\lambda}{\eta_p} \tau_{kk} \right), \quad (4.6)$$

where Γ is the Gamma function and the normalisation $\Gamma(\beta)$ is used to ensure that $K(0) = 1$, for all choices of β .

The linear and the exponential model of the Phan-Thien–Tanner has been frequently used in the literature, and in fact Ferrás et al. [23] considered a new quadratic version of the PTT model, i.e., a second-order expansion of the exponential model given by:

$$f(\tau_{kk}) = 1 + \frac{\varepsilon\lambda}{\eta_p} \tau_{kk} + \frac{1}{2} \left(\frac{\varepsilon\lambda}{\eta_p} \tau_{kk} \right)^2. \quad (4.7)$$

Here, we compare the generalised Phan-Thien–Tanner (gPTT), given by Eq. (4.6), with the linear, the exponential and the quadratic versions of the PTT (Eqs. (4.2), (4.4) and (4.7), respectively).

To compare these models, we study the dimensionless material properties in steady shear flow of the three versions of the PTT model and compare them with the new gPTT model, considering different values of α and β .

The material functions can be obtained considering a steady-state Couette flow in the x -direction, $\mathbf{u} = (\dot{\gamma}y, 0, 0)$, where $\dot{\gamma}$ is the shear rate. For this flow, considering the parameter $\xi = 0$, the constitutive Eq. (4.1) reduces to:

$$\begin{cases} K(\tau_{kk})\tau_{xx} = 2\lambda\dot{\gamma}\tau_{xy} \\ K(\tau_{kk})\tau_{xy} = \eta_p\dot{\gamma} \\ \tau_{yy} = \tau_{zz} = \tau_{xz} = \tau_{yz} = 0 \end{cases} \quad (4.8)$$

From the system of Eq. (4.8), $\tau_{kk} = \tau_{xx}$ and applying some algebra in the first two equations, a relationship between the shear stress and the normal stress is found,

$$\tau_{xx} = 2 \frac{\lambda}{\eta_p} \tau_{xy}^2. \quad (4.9)$$

We can also obtain the viscometric material functions: the steady shear viscosity, $\mu(\dot{\gamma})$, the first normal stress difference coefficient, $\Psi_1(\dot{\gamma})$, and the second normal stress difference coefficient, $\Psi_2(\dot{\gamma})$, which are given by:

$$\mu(\dot{\gamma}) = \frac{\tau_{xy}}{\dot{\gamma}}, \quad (4.10)$$

$$\Psi_1(\dot{\gamma}) = \frac{\tau_{xx} - \tau_{yy}}{\dot{\gamma}^2}, \quad (4.11)$$

$$\Psi_2(\dot{\gamma}) = \frac{\tau_{yy} - \tau_{zz}}{\dot{\gamma}^2}. \quad (4.12)$$

As for other versions of the simplified PTT models for which $\xi = 0$, the second normal stress coefficient is null, $\Psi_2(\dot{\gamma}) = 0$, so, we only need to find $\mu(\dot{\gamma})$ and $\Psi_1(\dot{\gamma})$. Therefore, manipulating the second equation of the system of Eqs. (4.8) we get,

$$\tau_{xy} = \frac{\eta_p \dot{\gamma}}{K(\tau_{xx})}. \quad (4.13)$$

The dimensionless expression for the steady shear viscosity becomes,

$$\frac{\mu(\dot{\gamma})}{\eta_p} = \frac{\tau_{xy}}{\eta_p \dot{\gamma}} = \frac{1}{K(\tau_{xx})} \quad (4.14)$$

and the dimensionless first normal stress coefficient is given by,

$$\frac{\Psi_1(\dot{\gamma})}{2\eta_p \lambda} = \frac{\tau_{xx}}{2\eta_p \lambda \dot{\gamma}^2} = \frac{1}{[K(\tau_{xx})]^2}. \quad (4.15)$$

In [23], it was shown that, for the linear PTT, the quadratic PTT and the exponential PTT, the dimensionless material functions depend on the generalised Deborah number, $\sqrt{\varepsilon}(\lambda\dot{\gamma})$. We show that the same happens for the gPTT model. To obtain the material function for the gPTT model, we need to solve the non-linear system of equations (Eq. (4.8)), which can be written in terms of τ_{xx} in the non-linear form:

$$\frac{1}{2} K(\tau_{xx})^2 \frac{\varepsilon \lambda}{\eta_p} \tau_{xx} = \varepsilon (\lambda \dot{\gamma})^2. \quad (4.16)$$

Giving values to $\frac{\varepsilon \lambda}{\eta_p} \tau_{xx}$, we can find $\sqrt{\varepsilon}(\lambda\dot{\gamma})$ using Eq. (4.16). Then, the function $K(\tau_{xx})$ is directly calculated, allowing us to obtain the material functions given by Eqs. (4.14) and (4.15).

Fig. 4.1 presents the dimensionless material properties for the steady-state Couette flow using three versions of the PTT (linear, quadratic, and exponential) and also the gPTT model. In Fig. 4.1 (a), we set $\beta = 1$ and use different values of α , and, in Fig. 4.1 (b), we set $\alpha = 1$ and use different values to β .

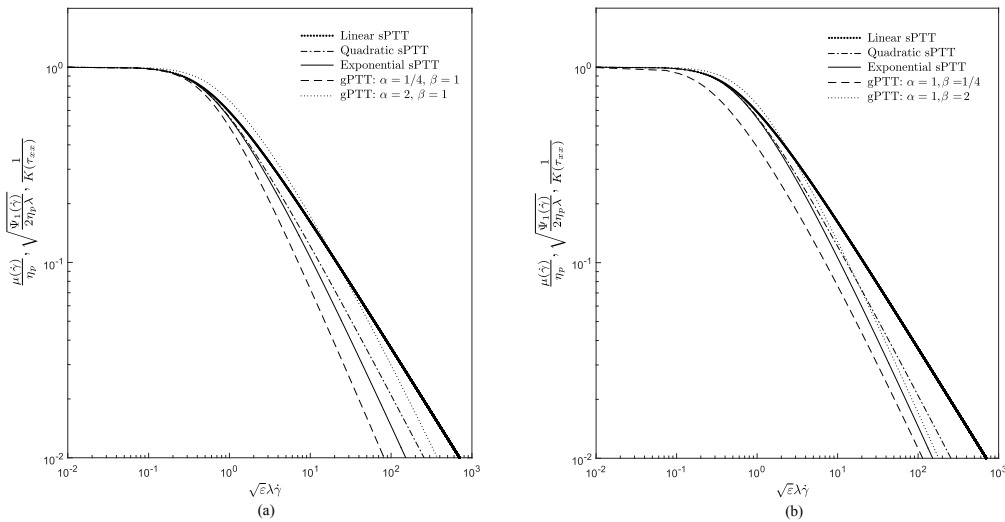


Figure 4.1: Dimensionless material properties in steady-state Couette flow using the three versions of the sPTT and for the gPTT model: **(a)** $\beta = 1$; and **(b)** $\alpha = 1$.

We observe that the new generalised function allows a broader description of the thinning properties of the fluid. Both the thinning rate and the onset of the thinning behavior can be controlled by the new model parameters. Therefore, this new model must be further explored for weak flows, such as Couette flows.

This model was extensively studied for strong flows in [3], where an explanation on the influence of the new model parameters was provided.

Note that the exponential version of the model was developed to take into account the strong destruction of network junctions, which occurs, for example, in strong flows (e.g., extensional flows). Although the exponential model was derived for such strong flows, it was shown in [3] that the gPTT model could slightly improve the fitting for shear (weak) flows, considering polymer solutions. Here, we consider polymer melts.

Fig. 4.2 shows that the gPTT model provides a much better fitting to weak flows of polymer melts (low density polyethylene melt [25]), even when using only one extra parameter (α).

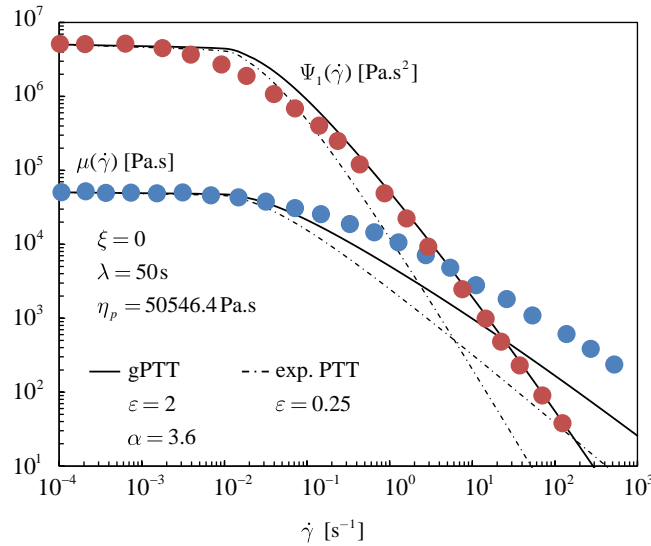


Figure 4.2: Fitting of the shear viscosity and the first normal stress difference coefficient to rheological data from Laun [25]. The generalised PTT model only considers the one-parameter Mittag–Leffler function, E_α . By adding only one parameter, we obtain a fitting error (Eq. (4.17)) of 29.7 and 6 for the exponential and gPTT models, respectively. The symbols represent the experimental data from Laun [25] for a low density polyethylene melt.

To quantify the error incurred during the fitting process, we used a mean square error given by

$$error = \sum_i^{N_\mu} [\log \mu(\dot{\gamma})_i - \log \mu(\dot{\gamma})_{fit_i}]^2 + \sum_j^{N_{\Psi_1}} [\log \Psi_1(\dot{\gamma})_j - \log \Psi_1(\dot{\gamma})_{fit_j}]^2, \quad (4.17)$$

$$error_\mu = \sum_i^{N_\mu} [\log \mu(\dot{\gamma})_i - \log \mu(\dot{\gamma})_{fit_i}]^2, \quad (4.18)$$

$$error_{\Psi_1} = \sum_j^{N_{\Psi_1}} \left[\log \Psi_1(\dot{\gamma})_j - \log \Psi_1(\dot{\gamma})_{fit_j} \right]^2, \quad (4.19)$$

with N_μ and N_{Ψ_1} the number of experimental points obtained for $\mu(\dot{\gamma})$ and $\Psi_1(\dot{\gamma})$, respectively.

A better fit was obtained for the new generalised model when compared to the original exponential PTT model. The total mean square error obtained for the exponential PTT model was 29.7, being five times the error obtained for its generalised version (for which a value of 6.0 was obtained). The new model allows a better fit for low and high shear rates for the first normal stress difference (where the $error_{\Psi_1}$ obtained for the exponential PTT model is 20 times higher than the error obtained for the gPTT). For the shear viscosity, the gPTT model predicts a lower value (when compared to experimental data) for high shear rates (although it should be remarked that the $error_\mu$ is four times smaller when compared to the exponential model).

Based on what is described above, this work presents analytical and semi-analytical solutions for pure Couette and Poiseuille–Couette flows, described by the generalised Phan-Thien–Tanner constitutive equation. It is well known that the rate of destruction of junctions increases for strong flows (e.g., extensional flows), but, in this case, we consider weak flows, and study the capability of this new model to describe them. This is done by performing a parametric study for the influence of the gPTT parameters.

4.1.2 Analytical solution for the gPTT model in Couette flow

In this section, we derive the analytical solution for the fully developed flow of the gPTT model considering both Couette and Poiseuille–Couette flows (cf. Fig. 4.3). To obtain closed form analytical solutions, the slip parameter in the Gordon–Schowalter derivative is set to $\xi = 0$.

The equations governing the flow of an isothermal incompressible fluid are the continuity,

$$\nabla \cdot \mathbf{u} = 0 \quad (4.20)$$

and the momentum equation,

$$\rho \frac{D\mathbf{u}}{Dt} = -\nabla p + \nabla \cdot \boldsymbol{\tau} \quad (4.21)$$

together with the constitutive equation,

$$\Gamma(\beta) E_{\alpha,\beta} \left(\frac{\varepsilon \lambda}{\eta_p} \tau_{kk} \right) \boldsymbol{\tau} + \lambda \dot{\boldsymbol{\tau}} = 2\eta_p \mathbf{D}, \quad (4.22)$$

where $\frac{D}{Dt}$ is the material derivative, p is the pressure, t is the time and ρ is the fluid density.

We consider a Cartesian coordinate system with x , y , and z being the streamwise, transverse and spanwise directions, respectively. The flow is assumed to be fully-developed and therefore the governing equations can be further simplified since

$$\frac{\partial}{\partial x} = 0 (\text{except for pressure}), \quad \frac{\partial v}{\partial y} = 0, \quad \frac{\partial p}{\partial y} = 0. \quad (4.23)$$

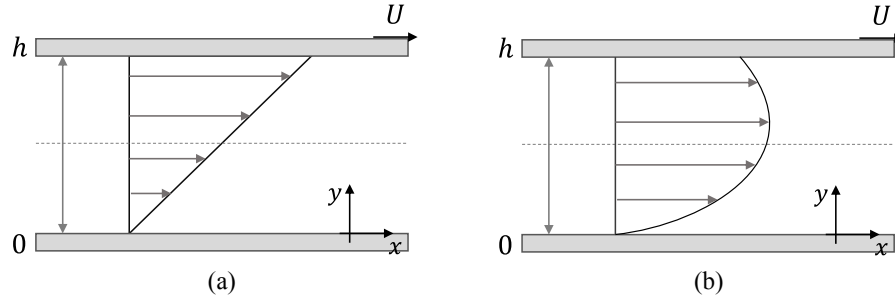


Figure 4.3: Geometry of: **(a)** the pure Couette flow; and **(b)** the Couette flow with an imposed pressure gradient (Poiseuille–Couette flow).

Therefore, Eq. (4.21) can be integrated, leading to the following general equation for the shear stress:

$$\tau_{xy} = P_x y + c_1, \quad (4.24)$$

where P_x is the pressure gradient in the x direction, τ_{xy} is the shear stress and c_1 is a stress constant. This equation is valid regardless of the rheological constitutive equation. The constitutive equations for the generalised PTT model describing this flow can be further simplified leading to:

$$K(\tau_{kk})\tau_{xx} = (2 - \xi)(\lambda\dot{\gamma})\tau_{xy}, \quad (4.25)$$

$$K(\tau_{kk})\tau_{yy} = -\xi(\lambda\dot{\gamma})\tau_{xy}, \quad (4.26)$$

$$K(\tau_{kk})\tau_{xy} = \eta_p \dot{\gamma} + \left(1 - \frac{\xi}{2}\right)(\lambda\dot{\gamma})\tau_{yy} - \frac{\xi}{2}(\lambda\dot{\gamma})\tau_{xx}, \quad (4.27)$$

where the shear rate $\dot{\gamma}$ is a function of y ($\dot{\gamma}(y) \equiv \frac{du}{dy}$) and $\tau_{kk} = \tau_{xx} + \tau_{yy}$ is the trace of the stress tensor. Assuming $\xi = 0$, Eq. (4.26) implies that $\tau_{yy} = 0$, and the trace of the stress tensor becomes $\tau_{kk} = \tau_{xx}$. Dividing Eq. (4.25) by Eq. (4.27), $K(\tau_{xx})$ cancels out, and we get the explicit relationship between the streamwise normal stress and the shear stress given by Eq. (4.9).

Now, combining Eqs. (4.9), (4.24) and (4.27), the following shear rate profile is obtained,

$$\dot{\gamma}(y) = \Gamma(\beta) E_{\alpha, \beta} \left(\frac{2\varepsilon\lambda^2}{\eta_p^2} (P_x y + c_1)^2 \right) \frac{(P_x y + c_1)}{\eta_p}. \quad (4.28)$$

The velocity profile can be obtained integrating the shear rate subject to the Couette boundary conditions (null velocity at the immobile wall),

$$u(0) = 0 \quad (4.29)$$

and an imposed constant velocity, U , at the moving wall,

$$u(h) = U. \quad (4.30)$$

This leads to the following velocity profile:

$$u(y) = U - \frac{\Gamma(\beta)}{\eta_p P_x} \sum_{k=0}^{\infty} \left(\left(\frac{2\varepsilon \lambda^2}{\eta_p^2} \right)^k \frac{(P_x h + c_1)^{2k+2} - (P_x y + c_1)^{2k+2}}{\Gamma(\alpha k + \beta) (2k+2)} \right), \quad (4.31)$$

where c_1 can be obtained by solving numerically the following equation,

$$U = \frac{\Gamma(\beta)}{\eta_p P_x} \sum_{k=0}^{\infty} \left(\left(\frac{2\varepsilon \lambda^2}{\eta_p^2} \right)^k \frac{1}{\Gamma(\alpha k + \beta)} \frac{(P_x h + c_1)^{2k+2} - c_1^{2k+2}}{2k+2} \right). \quad (4.32)$$

Combining Eqs. (4.31) and (4.32) leads to the following dimensionless velocity profile:

$$\bar{u}(\bar{y}) = \frac{\Gamma(\beta)}{\bar{P}_x} \sum_{k=0}^{\infty} \left((2\varepsilon Wi^2)^k \frac{1}{\Gamma(\alpha k + \beta)} \frac{(\bar{P}_x \bar{y} + \bar{c}_1)^{2k+2} - \bar{c}_1^{2k+2}}{2k+2} \right) \quad (4.33)$$

with $\bar{y} = \frac{y}{h}$, $\bar{u}(\bar{y}) = \frac{u(\bar{y})}{U}$, $\bar{c}_1 = \frac{c_1 h}{\eta_p U}$, $\bar{P}_x = \frac{P_x h^2}{\eta_p U}$ and $Wi = \frac{\lambda U}{h}$ the Weissenberg number.

Remark: Note that, if $c_1 = -P_x \frac{h}{2}$, Eq. (4.31) becomes,

$$u(y) = U - \frac{\Gamma(\beta)}{\eta_p P_x} \sum_{k=0}^{\infty} \left(\left(\frac{2\varepsilon \lambda^2}{\eta_p^2} \right)^k \frac{1}{\Gamma(\alpha k + \beta)} \frac{\left(P_x \frac{h}{2} \right)^{2k+2} - \left(P_x \left(y - \frac{h}{2} \right) \right)^{2k+2}}{2k+2} \right), \quad (4.34)$$

and Eq. (4.32) leads to $u(h) = 0$, corresponding to Poiseuille flow with no slip boundary conditions.

The velocity profile can be written in dimensionless form as:

$$\bar{u}(\bar{y}) = \frac{\Gamma(\beta)}{\bar{P}_x} \sum_{k=0}^{\infty} \left((2\varepsilon Wi^2)^k \frac{1}{\Gamma(\alpha k + \beta)} \frac{\left(\bar{P}_x \left(\bar{y} - \frac{1}{2} \right) \right)^{2k+2} - \left(\frac{\bar{P}_x}{2} \right)^{2k+2}}{2k+2} \right). \quad (4.35)$$

When we consider $\alpha = \beta = 1$, this equation reduces to the one presented by Oliveira and Pinho [103] for the planar channel flow of an exponential PTT fluid:

$$\bar{u}(\bar{y}) = \frac{1}{4\varepsilon Wi^2 \bar{P}_x} \left(\exp \left(2\varepsilon Wi^2 \bar{P}_x^2 \left(\bar{y} - \frac{1}{2} \right)^2 \right) - \exp \left(\frac{2\varepsilon Wi^2 \bar{P}_x^2}{4} \right) \right). \quad (4.36)$$

Fig. 4.4 shows a comparison between the gPTT model and exponential PTT (Eqs. (4.35) and (4.36)) for different values of εWi^2 . As expected, the results are identical, confirming the solution limit for $\alpha = \beta = 1$ on the Mittag-Leffler function.

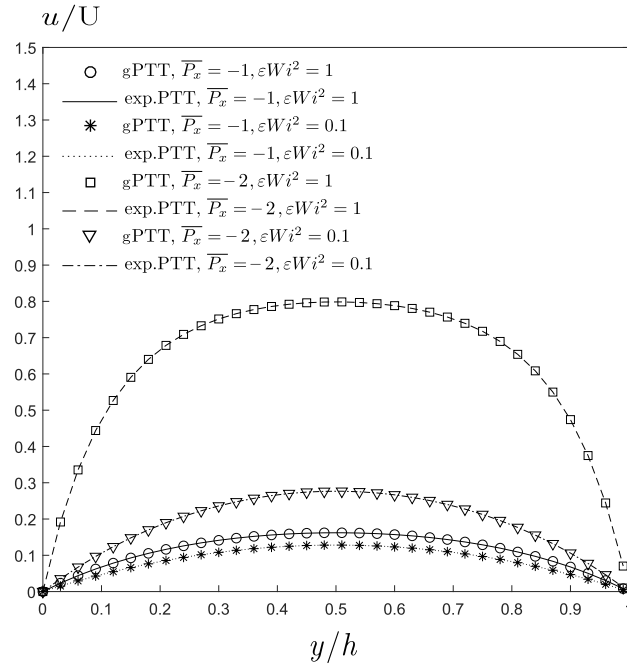


Figure 4.4: Comparison between the gPTT model and exponential PTT considering a Poiseuille flow with different values of εWi^2 and different values of imposed \bar{P}_x .

4.1.3 Analytical solution for the gPTT model in pure Couette flow.

For the pure Couette flow, $P_x = 0$, therefore Eq. (4.24) becomes,

$$\tau_{xy} = c_1. \quad (4.37)$$

The shear rate is then given by Eq. (4.38),

$$\dot{\gamma}(y) = \Gamma(\beta) E_{\alpha, \beta} \left(\frac{2\varepsilon\lambda^2}{\eta_p^2} c_1^2 \right) \frac{c_1}{\eta_p}. \quad (4.38)$$

Integrating Eq. (4.38) and taking into account Eq. (4.29), the velocity field for the pure Couette flow is obtained,

$$u(y) = \frac{\Gamma(\beta)}{\eta_p} \sum_{k=0}^{\infty} \left(\left(\frac{2\varepsilon\lambda^2}{\eta_p^2} \right)^k \frac{c_1^{2k+1}}{\Gamma(\alpha k + \beta)} y \right). \quad (4.39)$$

Making use of the boundary condition given in Eq. (4.30), we obtain the following nonlinear equation on c_1 , which must be solved numerically,

$$\frac{U}{h} = \frac{\Gamma(\beta)}{\eta_p} \sum_{k=0}^{\infty} \left(\left(\frac{2\varepsilon\lambda^2}{\eta_p^2} \right)^k \frac{c_1^{2k+1}}{\Gamma(\alpha k + \beta)} \right). \quad (4.40)$$

Eqs. (4.39) and (4.40) can be written in dimensionless form as:

$$\bar{u}(\bar{y}) = \Gamma(\beta) \bar{c}_1 \bar{y} \sum_{k=0}^{\infty} \left(\left(2\varepsilon Wi^2 \bar{c}_1^2 \right)^k \frac{1}{\Gamma(\alpha k + \beta)} \right) \quad (4.41)$$

and

$$1 = \Gamma(\beta) \bar{c}_1 \sum_{k=0}^{\infty} \left(\left(2\varepsilon Wi^2 \bar{c}_1^2 \right)^k \frac{1}{\Gamma(\alpha k + \beta)} \right), \quad (4.42)$$

respectively.

4.1.4 Discussion of results

In the previous section, semi-analytical equations were derived for the gPTT model in Poiseuille–Couette flow. In this section, we investigate the influence of the Mittag–Leffler function parameters α and β on the velocity profile of the Poiseuille–Couette flow. We consider different εWi^2 values, and also different values of α and β , and we compare the results with the ones obtained for the exponential PTT model. Fig. 4.5 shows the velocity profiles obtained for the Poiseuille–Couette flow considering two different εWi^2 values and different values of α ($\beta = 1$).

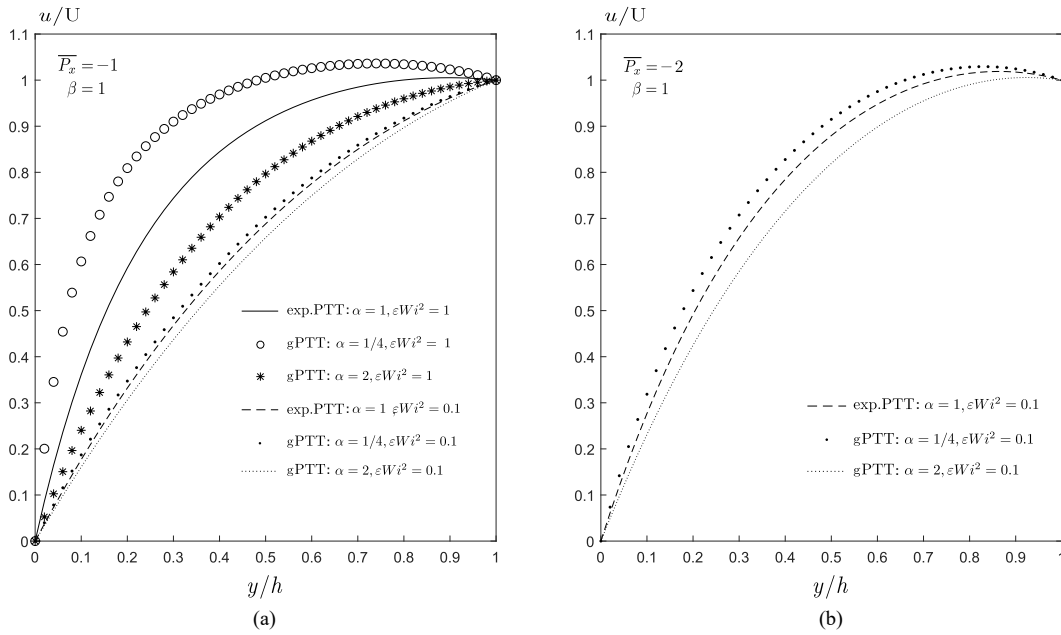


Figure 4.5: Velocity profiles obtained for the Poiseuille–Couette flow considering different values of εWi^2 and different values of α ($\beta = 1$): (a) $\bar{P}_x = -1$; and (b) $\bar{P}_x = -2$.

Fig. 4.6 shows the velocity profiles obtained for the Poiseuille–Couette flow considering two different εWi^2 and different values of β ($\alpha = 1$).

We observe in Fig. 4.5 (a) that for $\alpha > 1$ the flow rate decreases while for $\alpha < 1$ it increases. As expected, for a constant pressure drop, the flow rate increases with εWi^2 . In Fig. 4.5 (b), we can observe that with the increase of the absolute value of the pressure drop, the velocity profile becomes more sensitive to small changes in α .

For the case of constant $\alpha = 1$ and varying β (Fig. 4.6), the trends are similar to the ones obtained in Fig. 4.5 (varying α), but now the velocity profile is less sensitive to large values of β (with $\beta > 1$). In Fig. 4.6 (b), we observe that the combined effects of pressure drop and large values of εWi^2 lead to a substantial increase of the flow rate for $\beta < 1$.

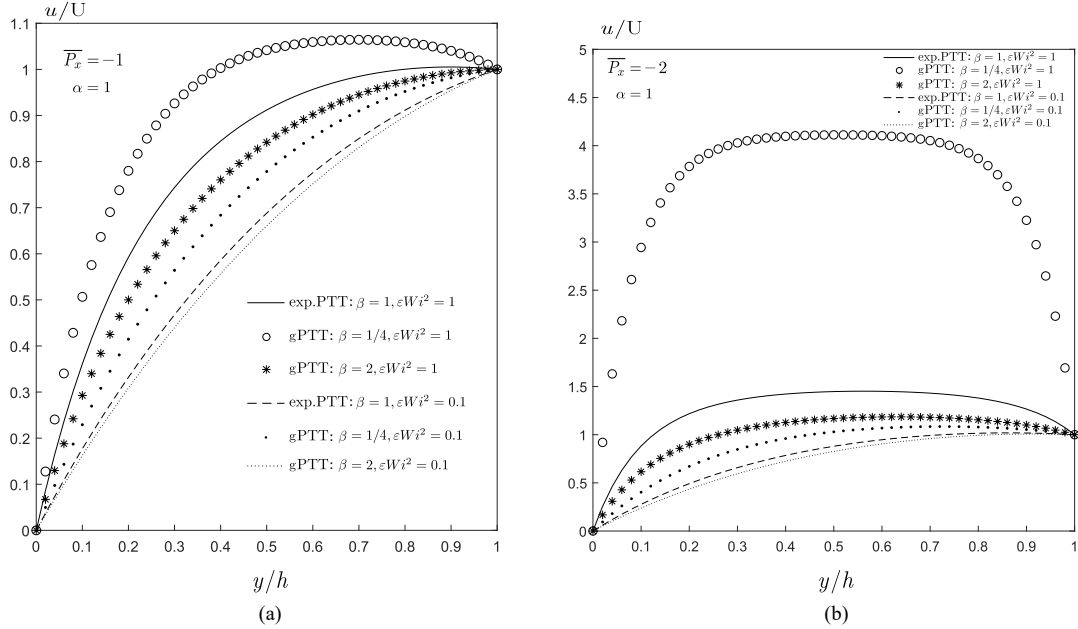


Figure 4.6: Velocity profiles obtained for the Poiseuille–Couette flow considering different values of εWi^2 and different values of β ($\alpha = 1$): (a) $\bar{P}_x = -1$; and (b) $\bar{P}_x = -2$.

4.1.5 Conclusions

In this work, we develop new analytical solutions for the Poiseuille–Couette flow of a viscoelastic fluid modelled by the generalised PTT model. We study the influence of the model's new parameters on the velocity profile and we discuss the role of the new function of the stress tensor on weak flows. The new model allows a broader description of flow behavior, and therefore it should be considered in the modelling of complex viscoelastic flows. The analytical solutions developed in this work are helpful for validating CFD codes, and also allow a further understanding of the model behavior in weak flows.

4.2 Analytical and numerical studies for slip flows of a generalised Phan-Thien–Tanner fluid²

Abstract: This work presents analytical and numerical studies for pure Couette and combined Poiseuille-Couette flows under slip. The fluid behaviour is described by the recently proposed viscoelastic model, known as the generalised simplified Phan-Thien-Tanner constitutive equation, that considers the Mittag–Leffler function instead of the classical linear and exponential functions of the trace of the stress tensor, and provides one or two new fitting constants in order to achieve additional fitting flexibility. The solutions derived in this work allow a better understanding of the model and its influence on the slippery behaviour of some complex fluids, contributing in this way to improve the modeling of complex fluids.

Keywords: Couette flow, generalised simplified PTT, Mittag–Leffler, Poiseuille-Couette flow, PTT model, wall slip

4.2.1 Introduction

Different mathematical models were proposed along the years to deal with complex viscoelastic fluids [1](e.g. polymer solutions and melts). These models can be classified as: differential and integral. The differential models make use of the local deformation field and in general allow a faster numerical solution of the differential equations involved, and the integral models allow a better modelling (at every instant they consider all past deformations), but they are computationally expensive and may lead to error propagation [104]. It is important to improve the fitting capabilities of differential models and reduce the computational effort needed to compute the integral models. In a recent work, Ferrás et al. [3] proposed the generalised Phan-Thien-Tanner (gPTT), an improved differential model based on the Nhan Phan-Thien and Roger Tanner constitutive equation (PTT model [21]), derived from the Lodge-Yamamoto type of network theory for polymeric fluids. This model considers the Mittag–Leffler function as a function of the trace of the stress tensor (instead of the classical linear and exponential functions), and provide one or two new fitting constants in order to obtain additional fitting flexibility. In this work, we propose new analytical and semi-analytical solutions for the pure Couette and Poiseuille-Couette flows under slip for the gPTT constitutive equation [3]. The analytical solutions derived in this work allow a better understanding of the model and its influence on the slippery behaviour of some complex fluids, and also improve the modelling capabilities of differential constitutive equations. Using this new model, Ribau et al. [28] proposed semi-analytical solutions for pure Couette and combined Poiseuille-Couette flows. Now, we extend the application of this model for pure Couette and combined Poiseuille-Couette flows under slip.

²A.M. Ribau, L.L. Ferrás, M.L. Morgado, M. Rebelo, and A.M. Afonso. Analytical and numerical studies for slip flows of a generalised Phan-Thien–Tanner fluid. *ZAMM - Journal of Applied Mathematics and Mechanics/Zeitschrift für Angewandte Mathematik und Mechanik*, 100(3), jan 2020.

The original constitutive equation proposed by Nhan Phan-Thien and Roger Tanner [21, 22], for the case of an isothermal flow, is given by:

$$f(\tau_{kk})\boldsymbol{\tau} + \lambda \dot{\boldsymbol{\tau}} = 2\eta_p \mathbf{D}, \quad (4.43)$$

with

$$f(\tau_{kk}) = 1 + \frac{\varepsilon\lambda}{\eta_p} \tau_{kk}, \quad (4.44)$$

where \mathbf{D} is the rate of deformation tensor, $\boldsymbol{\tau}$ is the stress tensor, λ is a relaxation time, η_p is the polymeric viscosity, τ_{kk} is the trace of the stress tensor, ε represents the extensibility parameter and $\dot{\boldsymbol{\tau}}$ represents the Gordon-Schowalter derivative, defined as

$$\dot{\boldsymbol{\tau}} = \frac{\partial \boldsymbol{\tau}}{\partial t} + \mathbf{u} \cdot \nabla \boldsymbol{\tau} - (\nabla \mathbf{u})^T \cdot \boldsymbol{\tau} - \boldsymbol{\tau} \cdot (\nabla \mathbf{u}) + \xi (\boldsymbol{\tau} \cdot \mathbf{D} + \mathbf{D} \cdot \boldsymbol{\tau}). \quad (4.45)$$

In Eq. (4.45) \mathbf{u} is the velocity vector, $\nabla \mathbf{u}$ is the velocity gradient, t the time and the parameter ξ accounts for the slip between the molecular network and the continuous medium. Later, a new model was proposed, by Phan-Thien [22], based on an exponential function form. This new function showed to be quite adequate to represent the rate of destruction of junctions, but with the parameter ε of the $\sim O(10^{-2})$. In this case, the function $f(\tau_{kk})$ is given by:

$$f(\tau_{kk}) = \exp\left(\frac{\varepsilon\lambda}{\eta_p} \tau_{kk}\right). \quad (4.46)$$

The new model considers a more general function for the rate of destruction of junctions, the Mittag-Leffler function with one or two fitting constants,

$$E_{\alpha,\beta}(z) = \sum_{k=0}^{\infty} \frac{z^k}{\Gamma(\alpha k + \beta)}, \quad (4.47)$$

with α, β real and positive. When $\alpha = \beta = 1$, the Mittag-Leffler function reduces to the exponential function. And, when $\beta = 1$ the original one-parameter Mittag-Leffler function, E_{α} is obtained. So, the new function that describes the network destruction of junctions is:

$$K(\tau_{kk}) = \Gamma(\beta) E_{\alpha,\beta}\left(\frac{\varepsilon\lambda}{\eta_p} \tau_{kk}\right), \quad (4.48)$$

where Γ is the Gamma function and the normalization $\Gamma(\beta)$ is used to ensure that $K(0) = 1$, for all choices of β .

Fig. 4.7 shows the variation of $\Gamma(\beta) E_{\alpha,\beta}(z)$, for three situations: when we have the exponential

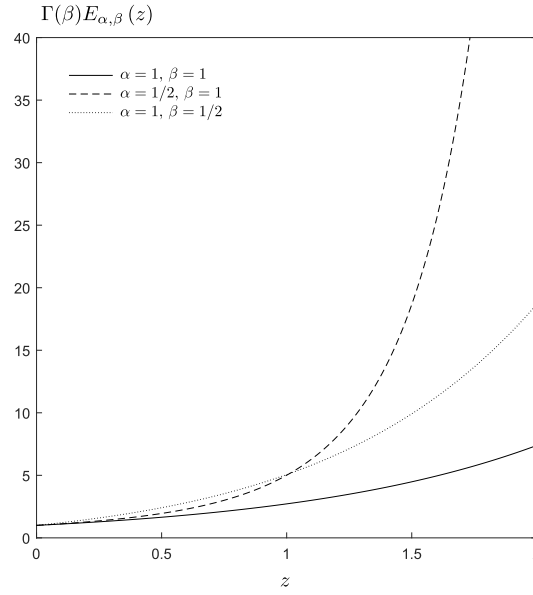


Figure 4.7: Influence of α and β on the shape of $\Gamma(\beta) E_{\alpha,\beta}(z)$ with $z = \frac{\varepsilon \lambda}{\eta p} \tau_{kk}$.

function, where $\alpha = \beta = 1$, when $\alpha = 1/2$, $\beta = 1$ and when $\beta = 1/2$, $\alpha = 1$. We observe different rates of increase in the destruction of junctions, when we decrease values of α and β to $1/2$, in comparison to the exponential function. Note that, for z values between 0 and 1, the behaviour of the functions $\Gamma(1) E_{1/2,1}(z)$ and $\Gamma(1/2) E_{1,1/2}(z)$ are similar. But, when z is bigger than 1 the function $\Gamma(1) E_{1/2,1}(z)$ increases more quickly than the function $\Gamma(1/2) E_{1,1/2}(z)$.

The rate of destruction of junctions increases for strong flows (e.g. extensional flows), but, here we consider weak flows under slip, and study the capability of this new model to describe such flows. For that, we are going to develop new analytical solutions and perform a parametric study on the influence of the model parameters.

4.2.2 Analytical solution for the gPTT model in Couette flow under slip

In this section, the analytical solution for the fully developed flow of the gPTT model considering both Couette and Poiseuille-Couette flows under slip will be derived (cf. Fig. 4.8). The slip parameter in the Gordon-Schowalter derivative is set to $\xi = 0$ in order to obtain closed form analytical solutions.

The equations governing the flow of an isothermal incompressible fluid are the continuity,

$$\nabla \cdot \mathbf{u} = 0, \quad (4.49)$$

and the momentum equation,

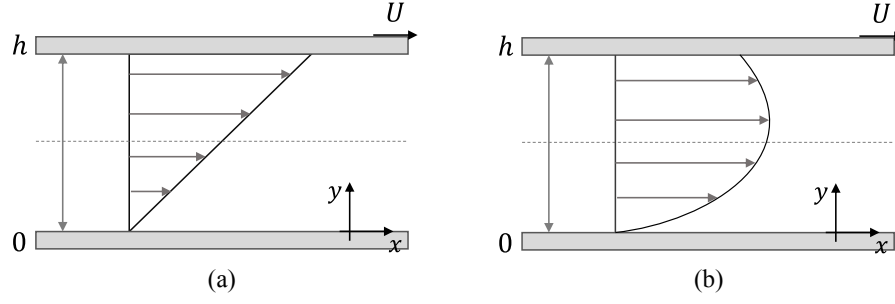


Figure 4.8: Geometry of the Pure Couette flow (a). Geometry of the Couette flow with imposed pressure gradient (b).

$$\rho \frac{D\mathbf{u}}{Dt} = -\nabla p + \nabla \cdot \boldsymbol{\tau}, \quad (4.50)$$

where $\frac{D}{Dt}$ is the material derivative, p is the pressure and ρ the fluid density, together with the constitutive equation,

$$\Gamma(\beta) E_{\alpha,\beta} \left(\frac{\varepsilon \lambda}{\eta_p} \tau_{kk} \right) \boldsymbol{\tau} + \lambda \dot{\boldsymbol{\tau}} = 2\eta_p \mathbf{D}. \quad (4.51)$$

The slip boundary conditions investigated here are the linear and nonlinear Navier slip laws. The nonlinear Navier slip law [26] states that the friction coefficient, k , is a function of the shear stress τ_{xy} , providing a non-linear power function given by:

$$u_w = k (\mp \tau_{xy,w})^m, \quad (4.52)$$

where $m > 0$ ($m \in \mathbb{R}$), the signs \mp stand for the upper $-$ and bottom $+$ walls, assuming there is flow between parallel plates, and the coordinate system is given as in Fig. 4.8. Note that, when $m = 1$ we have the Navier linear slip law [27].

In the cartesian coordinate system x, y, z , are the streamwise, transverse and spanwise directions, respectively. The flow is assumed to be fully-developed and therefore, the governing equations can be further simplified since,

$$\frac{\partial}{\partial x} = 0 (\text{except for pressure}), \quad \frac{\partial v}{\partial y} = 0, \quad \frac{\partial p}{\partial y} = 0. \quad (4.53)$$

So, Eqs. (4.49) and (4.50) can be simplified and integrated, leading to the following general equation for the shear stress:

$$\tau_{xy} = P_x y + c_1, \quad (4.54)$$

where $P_x \equiv -\frac{\partial p}{\partial x}$ is the pressure gradient in the x direction, τ_{xy} is the shear stress and c_1 is a shear stress constant, to be determined using the boundary condition at the wall. This equation is valid regardless of the rheological constitutive equation. The constitutive equations for the gPTT model describing this flow, can be further simplified leading to:

$$K(\tau_{kk})\tau_{xx} = (2 - \xi)(\lambda\dot{\gamma})\tau_{xy}, \quad (4.55)$$

$$K(\tau_{kk})\tau_{yy} = -\xi(\lambda\dot{\gamma})\tau_{xy}, \quad (4.56)$$

$$K(\tau_{kk})\tau_{xy} = \eta_p \dot{\gamma} + (1 - \frac{\xi}{2})(\lambda\dot{\gamma})\tau_{yy} - \frac{\xi}{2}(\lambda\dot{\gamma})\tau_{xx}, \quad (4.57)$$

where the shear rate $\dot{\gamma}$ is a function of y ($\dot{\gamma}(y) = \frac{du}{dy}$) and $\tau_{kk} = \tau_{xx} + \tau_{yy}$ is the trace of the stress tensor. Since, $\xi = 0$, Eq. (4.56) implies that $\tau_{yy} = 0$, and the trace of the stress tensor becomes $\tau_{kk} = \tau_{xx}$. Dividing Eq. (4.55) by Eq. (4.57), $K(\tau_{xx})$ cancels out, and an explicit relationship between the streamwise normal stress and the shear stress is found:

$$\tau_{xx} = 2 \frac{\lambda}{\eta_p} \tau_{xy}^2. \quad (4.58)$$

Combining Eqs. (4.57), (4.58) and (4.54) the following shear rate is obtained,

$$\dot{\gamma}(y) = \Gamma(\beta) E_{\alpha, \beta} \left(\frac{2\varepsilon\lambda^2}{\eta_p^2} (P_x y + c_1)^2 \right) \frac{(P_x y + c_1)}{\eta_p}. \quad (4.59)$$

The velocity profile can be obtained integrating the shear rate subject to the nonlinear Navier slip law. Therefore, the boundary condition that we are going to consider at the immobile wall is

$$u(0) = k_1(\tau_{xy})^{m_1}, \quad (4.60)$$

and at the moving wall,

$$u(h) = k_2(\tau_{xy})^{m_2}. \quad (4.61)$$

At the immobile wall, $y = 0$, and the shear stress constant c_1 is recovered, becoming:

$$u(0) = k_1(c_1)^{m_1}. \quad (4.62)$$

Also, at the moving wall, $y = h$, leading to:

$$u(h) = k_2(P_x h + c_1)^{m_2}. \quad (4.63)$$

This leads to the following velocity profile:

$$u(y) = k_1(c_1)^{m_1} + \frac{\Gamma(\beta)}{\eta_p P_x} \sum_{k=0}^{\infty} \left(\left(\frac{2\varepsilon\lambda^2}{\eta_p^2} \right)^k \frac{(P_x y + c_1)^{2k+2} - c_1^{2k+2}}{\Gamma(\alpha k + \beta)(2k+2)} \right). \quad (4.64)$$

The shear stress constant, c_1 , can be obtained by solving numerically the following equation,

$$k_2(P_x h + c_1)^{m_2} - k_1(c_1)^{m_1} = \frac{\Gamma(\beta)}{\eta_p P_x} \sum_{k=0}^{\infty} \left(\left(\frac{2\varepsilon\lambda^2}{\eta_p^2} \right)^k \frac{1}{\Gamma(\alpha k + \beta)} \frac{(P_x h + c_1)^{2k+2} - c_1^{2k+2}}{2k+2} \right). \quad (4.65)$$

Combining Eqs. (4.65) and (4.64) leads to the following velocity profile,

$$\bar{u}(\bar{y}) = \bar{k}_2(\bar{P}_x + \bar{c}_1)^{m_2} + \frac{\Gamma(\beta)}{\bar{P}_x} \sum_{k=0}^{\infty} \left((2\varepsilon Wi^2)^k \frac{1}{\Gamma(\alpha k + \beta)} \frac{(\bar{P}_x \bar{y} + \bar{c}_1)^{2k+2} - (\bar{P}_x + \bar{c}_1)^{2k+2}}{2k+2} \right), \quad (4.66)$$

and the equation for the stress constant \bar{c}_1 ,

$$\bar{k}_2(\bar{P}_x + \bar{c}_1)^{m_2} - \bar{k}_1(\bar{c}_1)^{m_1} = \frac{\Gamma(\beta)}{\bar{P}_x} \sum_{k=0}^{\infty} \left((2\varepsilon Wi^2)^k \frac{1}{\Gamma(\alpha k + \beta)} \frac{(\bar{P}_x + \bar{c}_1)^{2k+2} - \bar{c}_1^{2k+2}}{2k+2} \right), \quad (4.67)$$

that are written in dimensionless form, with $\bar{y} = \frac{y}{h}$, $\bar{u}(\bar{y}) = \frac{u(\bar{y})}{U}$ (being U the imposed velocity at the moving wall), $\bar{c}_1 = \frac{c_1 h}{\eta_p U}$, $\bar{P}_x = \frac{P_x h^2}{\eta_p U}$, $\bar{k}_i = k_i U^{m_i-1} \left(\frac{\eta_p}{h} \right)^{m_i}$, for $i = \{1, 2\}$ and $Wi = \frac{\lambda U}{h}$ the Weissenberg number.

Remark: Note that if $\bar{k}_1 = \bar{k}_2 = 0$ and $m_1 = m_2 = 1$, the velocity profile (Eq. (4.66)) becomes:

$$\bar{u}(\bar{y}) = \frac{\Gamma(\beta)}{\bar{P}_x} \sum_{k=0}^{\infty} \left((2\varepsilon Wi^2)^k \frac{1}{\Gamma(\alpha k + \beta)} \frac{(\bar{P}_x \bar{y} + \bar{c}_1)^{2k+2} - (\bar{P}_x + \bar{c}_1)^{2k+2}}{2k+2} \right), \quad (4.68)$$

and Eq. (4.67) is given by,

$$\frac{\Gamma(\beta)}{\bar{P}_x} \sum_{k=0}^{\infty} \left((2\varepsilon Wi^2)^k \frac{1}{\Gamma(\alpha k + \beta)} \frac{(\bar{P}_x + \bar{c}_1)^{2k+2} - \bar{c}_1^{2k+2}}{2k+2} \right) = 0. \quad (4.69)$$

If we consider $\bar{c}_1 = -\frac{\bar{P}_x}{2}$ and $\alpha = \beta = 1$, Eq. (4.68) reduces to the velocity profile obtained in [103] for the exponential PTT model (Eq. (4.70)):

$$\bar{u}(\bar{y}) = \frac{1}{4\varepsilon Wi^2 \bar{P}_x} \left(\exp \left(2\varepsilon Wi^2 \bar{P}_x^2 \left(\bar{y} - \frac{1}{2} \right)^2 \right) - \exp \left(\frac{2\varepsilon Wi^2 \bar{P}_x^2}{4} \right) \right). \quad (4.70)$$

4.2.3 Analytical solution for the gPTT model in pure Couette flow under slip

For the pure Couette flow, $P_x = 0$, Eq. (4.54) reduces to:

$$\tau_{xy} = c_1. \quad (4.71)$$

The shear rate is then given in dimensionless form by Eq. (4.72), as follows:

$$\dot{\gamma}(y) = \Gamma(\beta) E_{\alpha, \beta} \left(\frac{2\varepsilon\lambda^2}{\eta_p^2} c_1^2 \right) \frac{c_1}{\eta_p}. \quad (4.72)$$

Integrating Eq. (4.72), the velocity field for the pure Couette flow is obtained,

$$u(y) = \frac{\Gamma(\beta)}{\eta_p} \left(\sum_{k=0}^{\infty} \left(\left(\frac{2\varepsilon\lambda^2}{\eta_p^2} \right)^k \frac{c_1^{2k+1}}{\Gamma(\alpha k + \beta)} y \right) + c_2 \right), \quad (4.73)$$

where c_2 is an integration constant to be determined by the boundary conditions at the wall.

In order to find c_2 , boundary conditions (4.60) and (4.61) will be considered. Here, we have two different boundary conditions, one at the immobile wall:

$$u(0) = k_1(c_1)^{m_1}, \quad (4.74)$$

and other at the moving wall,

$$u(h) = k_2(c_1)^{m_2}. \quad (4.75)$$

We use boundary condition (4.74) to obtain:

$$u(y) = k_1(c_1)^{m_1} + \frac{\Gamma(\beta)}{\eta_p} \sum_{k=0}^{\infty} \left(\left(\frac{2\varepsilon\lambda^2}{\eta_p^2} \right)^k \frac{c_1^{2k+1}}{\Gamma(\alpha k + \beta)} y \right). \quad (4.76)$$

With the help of (4.75), an approximation for constant c_1 can be obtained by solving numerically the following nonlinear equation,

$$\frac{k_2(c_1)^{m_2} - k_1(c_1)^{m_1}}{h} = \frac{\Gamma(\beta)}{\eta_p} \sum_{k=0}^{\infty} \left(\left(\frac{2\varepsilon\lambda^2}{\eta_p^2} \right)^k \frac{c_1^{2k+1}}{\Gamma(\alpha k + \beta)} \right). \quad (4.77)$$

Equations (4.76) and (4.77) can be written in dimensionless form as:

$$\bar{u}(\bar{y}) = \bar{k}_1(\bar{c}_1)^{m_1} + \Gamma(\beta) \bar{c}_1 \bar{y} \sum_{k=0}^{\infty} \left(\left(2\varepsilon Wi^2 \bar{c}_1^2 \right)^k \frac{1}{\Gamma(\alpha k + \beta)} \right), \quad (4.78)$$

and

$$\bar{k}_2(\bar{c}_1)^{m_2} - \bar{k}_1(\bar{c}_1)^{m_1} = \Gamma(\beta) \bar{c}_1 \sum_{k=0}^{\infty} \left(\left(2\varepsilon Wi^2 \bar{c}_1^2 \right)^k \frac{1}{\Gamma(\alpha k + \beta)} \right), \quad (4.79)$$

respectively.

4.2.4 Discussion of results

4.2.4.1 Pure Couette flow

We will now investigate the influence of the Mittag–Leffler function on the velocity profile for pure Couette slip flows.

Fig. 4.9 shows the influence of parameter α on the velocity profile, considering slip velocity at the immobile wall and no-slip at the moving wall.

As expected, when we consider full slip velocity at the moving wall, regardless of the boundary condition at the immobile wall, the only possible solution is $\bar{u}(\bar{y}) = 0$.

Note that, we are only going to study the influence of parameter α , because of what we concluded in Fig. 4.7, where the effect of $\alpha = 1/2$, $\beta = 1$ is similar to the effect of $\alpha = 1$, $\beta = 1/2$, i.e., when the argument of Eq. (4.48) is between 0 and 1, both functions, $\Gamma(1)E_{1/2,1}(z)$ and $\Gamma(1/2)E_{1,1/2}(z)$ have a similar behaviour.

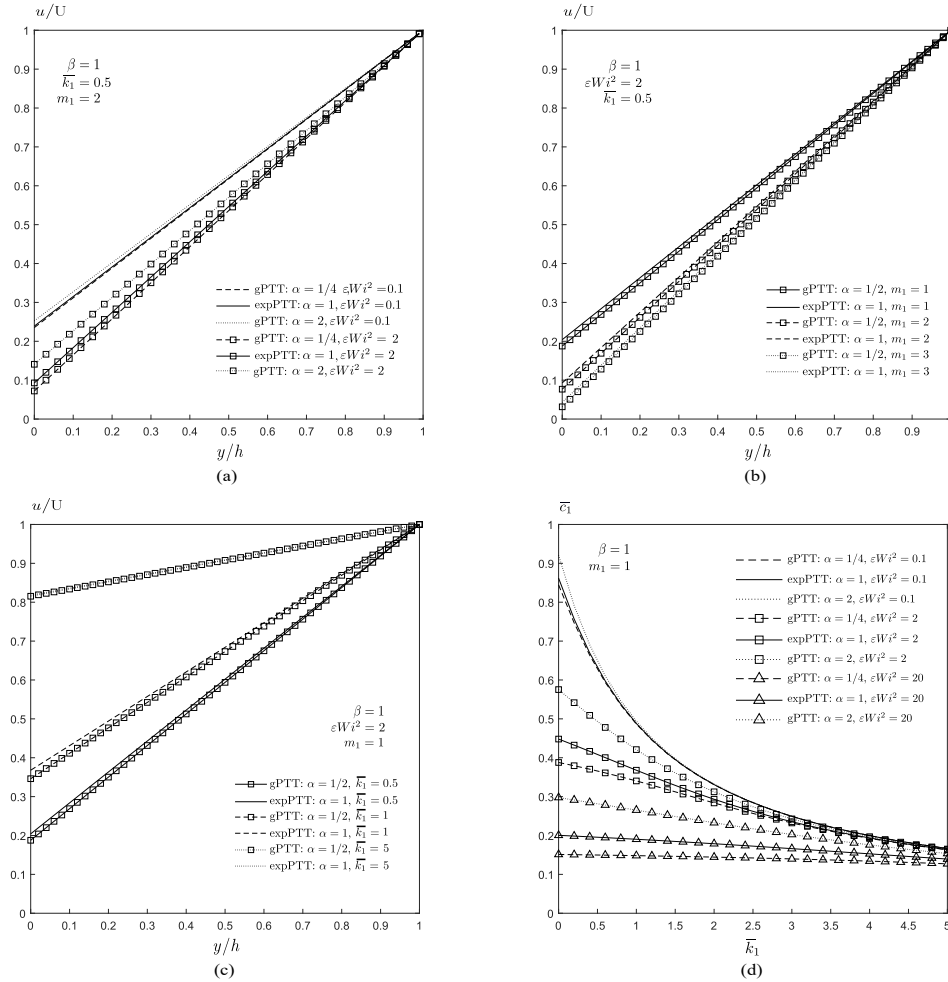


Figure 4.9: Velocity profiles obtained for the pure Couette flow with slip at the immobile wall and no-slip at the moving wall. (a) Variation of α with $\beta = 1$, (b) variation of parameter m_1 , (c) variation of slip coefficient \bar{k}_1 , (d) variation of \bar{c}_1 with \bar{k}_1 .

Fig. 4.9 (a) shows the velocity profiles obtained for the pure Couette flow, for \bar{k}_1 and m_1 fixed and different values for εWi^2 and α are considered, and the results obtained are compared with the exponential PTT ($\alpha = 1$ and $\beta = 1$). We can observe that decreasing elasticity, εWi^2 , increases the influence of the other parameters on the velocity profile. And this effect is more intense as α increases.

Fig. 4.9 (b) shows the velocity profiles obtained for the pure Couette flow for different values of m_1 . In this study, we consider three different values for m_1 , fixed \bar{k}_1 and εWi^2 , and study the influence of the parameter α in the velocity profile. We can observe that increasing m_1 , the velocity profile approaches the velocity profile for pure Couette without slip, i.e. for smaller values of m_1 at the immobile wall, we have higher values of velocity. And if we increase the parameter α the velocity increases.

Fig. 4.9 (c) shows the velocity profiles obtained for the pure Couette flow for different \bar{k}_1 values. In this case, we consider three different values for the \bar{k}_1 , fixed m_1 and εWi^2 , and study the influence of the parameter α in the velocity profile. We can see that when $\bar{k}_1 = 5$, the velocity profiles for the exponential PTT and the gPTT are similar. But, for smaller values of \bar{k}_1 , we observe that, at the immobile wall, the velocity profiles increase, when α increases.

Note that, in Fig. 4.9 (a), (b) and (c) when $\bar{y} = 0$, the velocity is different from zero, and this happens because, we are considering the existence of slip at the immobile wall.

Fig. 4.9 (d) shows the variation of \bar{c}_1 , obtained numerically from Eq. (4.79), with the slip parameter \bar{k}_1 , fixing m_1 and considering different values of α and εWi^2 . We can see that when we increase the slip flow, the shear stress coefficient decreases, and for lower values of elasticity, εWi^2 , this effect is more enhanced.

It should be remarked that α and β parameters will influence the rate of destruction of junctions, therefore, the fluidity of the viscoelastic material will suffer changes. This combined with the slip velocity at the wall will promote a complex motion of molecules in the near wall region. This way, the lower the value of α or β , the higher is the rate of destruction of junctions, and therefore, the fluid is more shear-thinning. Consequently, when we keep all parameters fixed and we decrease α or β , will lead to reduced stresses at the immobile wall, and thus, a lower slip velocity.

4.2.4.2 Combined Poiseuille-Couette flow

We will now investigate the influence of the Mittag-Leffler function parameters on the velocity profile for the combined Poiseuille-Couette flow. We want to know the influence of α and β , on the velocity profile of the Poiseuille-Couette flow with slip velocity at the immobile wall and no-slip at the moving wall.

Fig. 4.10 shows the velocity profiles obtained for the combined Poiseuille-Couette flow, for fixed \bar{k}_1 , m_1 , \bar{P}_x and different values of εWi^2 , α and β , and a comparison with the exponential PTT.

In Fig. 4.10 (a) we consider different values for α and in Fig. 4.10 (b) different values for β . We can observe in Fig. 4.10 (a), that increasing elasticity, εWi^2 , increases the influence of the other parameters on the velocity profile. This effect is enhanced as α decreases. From Fig. 4.10

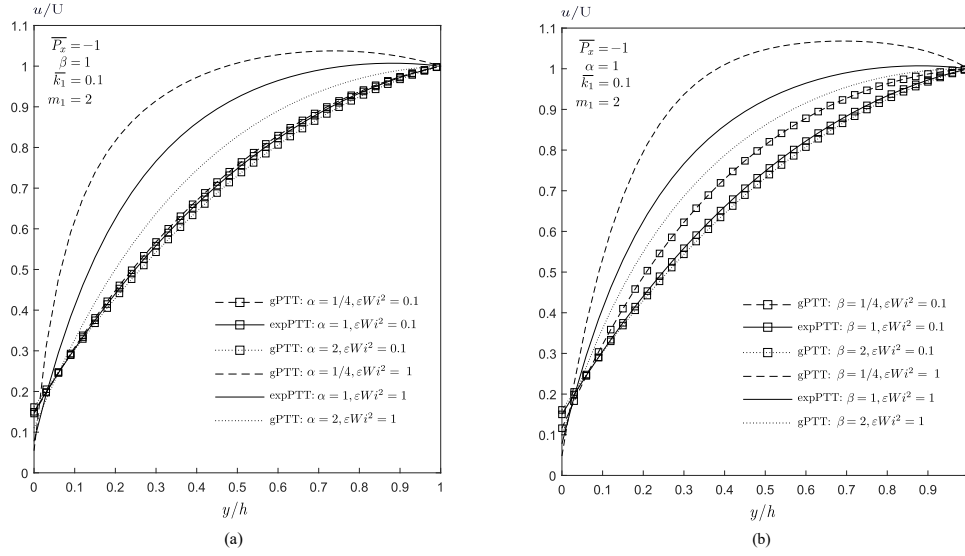


Figure 4.10: Velocity profiles obtained for the Poiseuille-Couette flow with slip at the immobile wall and no-slip at the moving wall. (a) Variation of α with $\beta = 1$, (b) variation of β with $\alpha = 1$.

(b), we can observe that when parameter α is constant, the effect of decreasing β is similar to the one presented in Fig. 4.10 (a).

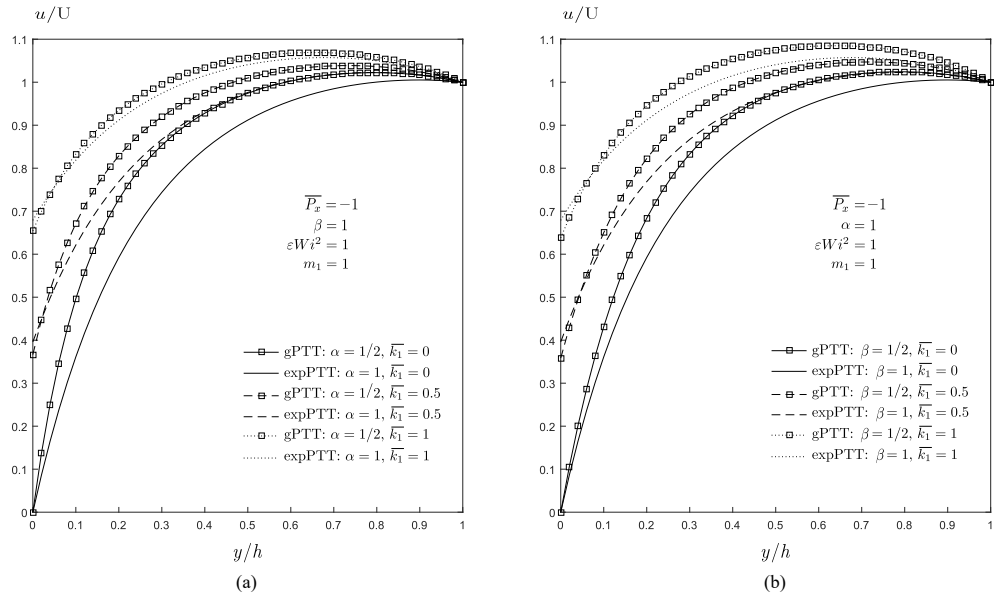


Figure 4.11: Velocity profiles obtained for the Poiseuille-Couette flow with slip at the immobile wall and no-slip at the moving wall for three different values of the slip coefficient \overline{k}_1 . (a) Variation of α with $\beta = 1$, (b) variation of β with $\alpha = 1$.

Fig. 4.11 shows the velocity profiles obtained for the Poiseuille-Couette flow for three different values of \overline{k}_1 , and fixed \overline{P}_x , m_1 and εWi^2 . Fig. 4.11 (a) and Fig. 4.11 (b), present velocity profiles for fixed $\alpha = 1$ and $\beta = 1$, respectively. When β is fixed, the effect of the increase of slip coefficient

is more pronounced for smaller values of α . As observed in Fig. 4.11 (a), when the parameter α is fixed, a similar trend is observed, i.e., the effect on the velocity profile is more pronounced for smaller values of β . This happens because for low values of α (β), the rate of destruction of junctions increases and therefore the internal friction decreases, leading to a less restrictive flow, increasing the flow rate.

Fig. 4.12 presents the variation of the \bar{c}_1 obtained numerically from Eq. (4.67), as a function of \bar{k}_1 , for fixed \bar{P}_x and m_1 . The increase of slip velocity implies the decrease of the shear stress coefficient. This effect is more significant for lower values of εWi^2 , presenting (almost) linear dependence for $\varepsilon Wi^2 = 1$.

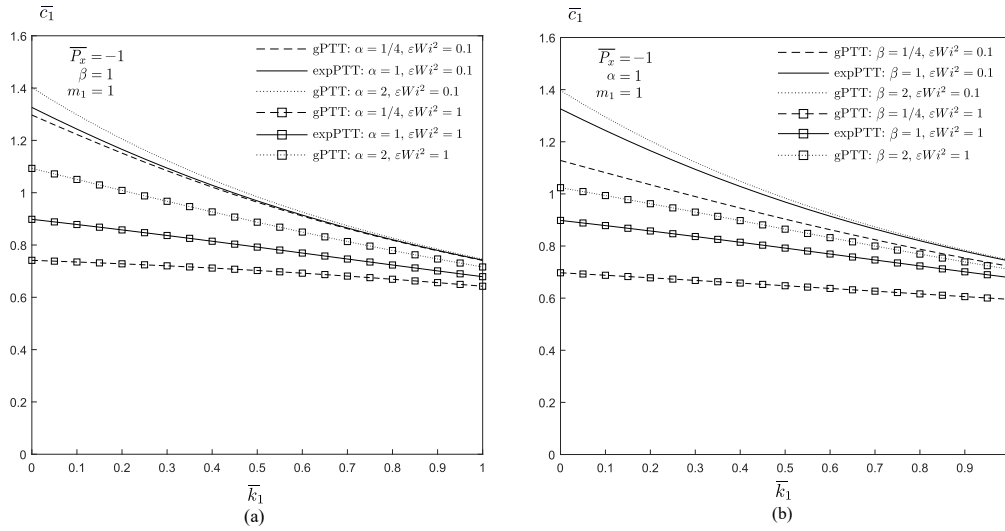


Figure 4.12: Variation of \bar{c}_1 as a function of slip coefficient \bar{k}_1 for Poiseuille-Couette flow with slip at the immobile wall and no-slip at the moving wall. (a) Variation of α with $\beta = 1$, (b) variation of β with $\alpha = 1$.

Fig. 4.13 shows the variation of the shear stress, $\bar{\tau}_{xy}$, and the corresponding normal stress, $\bar{\tau}_{xx}$, for fixed \bar{P}_x , m_1 and εWi^2 . We consider three different values of \bar{k}_1 and this analysis is presented only for varying α , since for the parameter β the results are qualitatively similar.

As explained before, the increase in the rate of destruction of junctions will lead to a decrease of the shear stress, and corresponding viscosity. This leads to a less pronounced effect of slip coefficient.

For the normal stress the conclusions are similar, but now have a nonlinearity, that will invert the role of α , depending if the fluid is near the bottom or top wall.

4.2.5 Conclusions

In this work we developed analytical and semi-analytical solutions for the combined Poiseuille-Couette flow and pure Couette flow of a viscoelastic fluid modelled by the gPTT model, with the influence of slip at the walls. We study the influence of the model's new parameters, on the velocity profile and also discuss the role of the new function of the stress tensor on weak

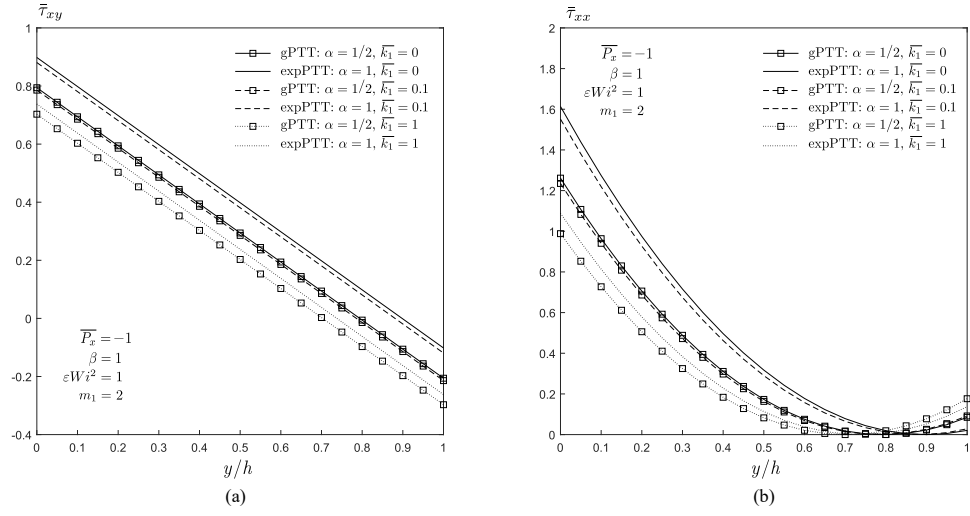


Figure 4.13: Variation of $\bar{\tau}_{xy}$ and $\bar{\tau}_{xx}$ for Poiseuille-Couette flow with slip at the immobile wall and no-slip at the moving wall with different values of \bar{k}_1 . (Note that: $\bar{\tau}_{xy} = \frac{\tau_{xy}h}{\eta_p U}$ and $\bar{\tau}_{xx} = \frac{\tau_{xx}h}{\eta_p U}$)

flows. The combined effects of slip, α and β reveal a new model with improved capability to mimic complex phenomena even for weak flows.

4.3 Analytical study of the annular flow of a generalised Phan-Thien–Tanner fluid³

Abstract: The annular flow of complex viscoelastic fluids, described by the generalised Phan-Thien-Tanner model, is studied. This model considers the Mittag-Leffler function instead of the usual linear or exponential functions of the trace of the stress tensor, and includes two new parameters that provide additional fitting flexibility. We derive a semi-analytical solution that provides a better understanding of the behaviour of this type of fluid in annular flows and also helps to improve the modelling of complex materials.

Keywords: PTT model, Mittag-Leffler, gPTT model, annular pressure driven flows, analytical solutions

4.3.1 Introduction

Viscoelastic materials, such as polymer melts, polymer solutions, and biofluids (e.g. blood, saliva, proteins) have complex behaviour. To better model and understand their rheological behaviour, several constitutive equations have been proposed in the literature. In this study, we consider the study of annular fluid flows that are commonly encountered in industrial processes such as drilling, cable coating, and food processing. In these processes, the fluids are mixtures of various substances, such as water, particles, oils, and other long-chain molecules, that impart the fluid with various non-Newtonian properties.

The literature has many analytical and numerical solutions for annular flows using different constitutive rheological models or different boundary conditions [19, 23, 30–38]. Among them, all the different variants of the Phan-Thien–Tanner (PTT) model have already been studied (linear, quadratic, exponential), except for the more recent PTT model, which uses the Mittag-Leffler function and is called the generalized Phan-Thien–Tanner (gPTT) model [3]. The gPTT model considers the Mittag-Leffler function instead of the classical linear and exponential functions of the trace of the stress tensor (linear PTT and exponential PTT, respectively) to ensure a much wider rheology coverage range and uses two new fitting constants to provide such additional fitting flexibility to the description of the rheological properties of viscoelastic fluids.

Using this constitutive equation, in this work we propose a new approach by deriving a new semi-analytical solution for the annular flow domain. Note that this model was previously studied for Couette and pressure-driven flows, and also in combined electro-osmotic/pressure-driven flows (see [28, 29, 56]). The obtained solutions allow the characterization of the velocity profile in annuli and can be used to validate the numerical methods and results.

³A.M. Ribau, L.L. Ferrás, M.L. Morgado, M. Rebelo, F.T. Pinho, and A.M. Afonso. Analytical study of the annular flow of a generalised Phan-Thien–Tanner fluid. *Acta Mechanica*, 2023.

The remainder of this paper is organized as follows: the next section presents the governing equations, followed by the new analytical solution in section 4.3.3, the discussion of the results in section 4.3.4 and the closure of the paper in section 4.3.5.

4.3.2 Formulation and governing equations

We consider the pressure-driven annular flow of a viscoelastic gPTT fluid, as shown in Fig. 4.14, where R is the radius of the outer cylinder and aR is the radius of the inner cylinder.

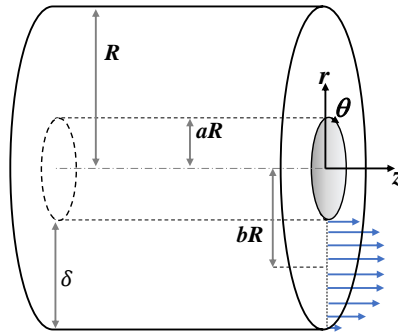


Figure 4.14: Schematic of the flow in an annular region.

The equations governing the flow of an isothermal incompressible fluid are the continuity equation

$$\nabla \cdot \mathbf{u} = 0, \quad (4.80)$$

and the linear momentum equation

$$\rho \frac{D\mathbf{u}}{Dt} = -\nabla p + \nabla \cdot \boldsymbol{\sigma}, \quad (4.81)$$

where \mathbf{u} is the velocity vector, $\frac{D}{Dt}$ is the material derivative, p is the pressure, t is the time, ρ is the fluid density and $\boldsymbol{\sigma}$ is the extra-stress tensor.

4.3.2.1 Constitutive equation

In order to achieve a closed system of equations, a constitutive equation for the extra-stress tensor, $\boldsymbol{\sigma}$, must be defined. Recently, Ferrás et al. [3] proposed a new differential rheological model based on the Phan-Thien–Tanner constitutive equation (PTT model [21, 22]), derived from the Lodge–Yamamoto type of network theory for polymeric fluids. This new model considers a more general function for the rate of destruction of junctions, the Mittag–Leffler function, where two fitting constants are included, in order to achieve additional fitting flexibility [3]. More details about this model are discussed in [3].

The Mittag–Leffler function is defined by

$$E_{\alpha,\beta}(z) = \sum_{j=0}^{\infty} \frac{z^j}{\Gamma(\alpha j + \beta)}, \quad (4.82)$$

where α, β are real and positive values and Γ is the Gamma function. When $\alpha = \beta = 1$, the Mittag–Leffler function reduces to the exponential function, and when $\beta = 1$ the original one-parameter Mittag–Leffler function, E_{α} , is obtained [4].

The constitutive equation of the gPTT model is given by

$$K(\sigma_{kk})\boldsymbol{\sigma} + \lambda \overset{\square}{\boldsymbol{\sigma}} = 2\eta_p \mathbf{D}, \quad (4.83)$$

where σ_{kk} is the trace of the extra stress tensor, λ is the relaxation time and η_p is the polymeric viscosity coefficient. \mathbf{D} is the rate of deformation tensor and function $K(\sigma_{kk})$ is given by

$$K(\sigma_{kk}) = \Gamma(\beta) E_{\alpha,\beta} \left(\frac{\varepsilon \lambda}{\eta_p} \sigma_{kk} \right) \quad (4.84)$$

where the normalization $\Gamma(\beta)$ is used to ensure that $K(0) = 1$ for all choices of β , and ε represents the extensibility parameter. $\overset{\square}{\boldsymbol{\sigma}}$ represents the Gordon-Schowalter derivative, defined as

$$\overset{\square}{\boldsymbol{\sigma}} = \frac{\partial \boldsymbol{\sigma}}{\partial t} + \mathbf{u} \cdot \nabla \boldsymbol{\sigma} - (\nabla \mathbf{u})^T \cdot \boldsymbol{\sigma} - \boldsymbol{\sigma} \cdot (\nabla \mathbf{u}) + \xi (\boldsymbol{\sigma} \cdot \mathbf{D} + \mathbf{D} \cdot \boldsymbol{\sigma}), \quad (4.85)$$

where $\nabla \mathbf{u}$ is the velocity gradient and the constant parameter ξ accounts for the slip between the molecular network and the continuum.

4.3.3 Semi-analytical solution for the gPTT model in annuli

We derive the analytical solution for the gPTT model considering a steady fully-developed pressure-driven annular flow (cf. Fig. 4.14). We consider a unidirectional flow in cylindrical coordinates, where the outer radius is R and the inner radius is aR , with $0 < a < 1$. Therefore, the momentum equation, Eq. (4.81), simplifies to

$$\frac{1}{r} \frac{d(r\sigma_{rz})}{dr} = P_z, \quad (4.86)$$

where $P_z \equiv \frac{dp}{dz}$ is the constant streamwise pressure gradient and σ_{rz} is the shear stress.

In order to obtain closed form analytical solutions the slip parameter in the Gordon-Schowalter derivative, Eq. (4.85) was set to $\xi = 0$. So, the constitutive equation for the gPTT model in this flow (section 4.3.2.1) can be further simplified, leading to:

$$K(\sigma_{kk})\sigma_{zz} = 2\lambda\dot{\gamma}\sigma_{rz}, \quad (4.87)$$

$$K(\sigma_{kk})\sigma_{rr} = 0, \quad (4.88)$$

$$K(\sigma_{kk})\sigma_{rz} = \eta_p \dot{\gamma}, \quad (4.89)$$

where the velocity gradient $\dot{\gamma}$ is a function of r ($\dot{\gamma}(r) \equiv \frac{du}{dr}$) and $\sigma_{kk} = \sigma_{\theta\theta} + \sigma_{zz} + \sigma_{rr}$ is the trace of the extra stress tensor. Under fully-developed flow conditions, $\sigma_{\theta\theta} = 0$ and $\sigma_{rr} = 0$, the trace of the extra stress tensor becomes $\sigma_{kk} = \sigma_{zz}$.

Integration of the momentum equation results in

$$\sigma_{rz} = \frac{P_z}{2}r + \frac{c}{r}, \quad (4.90)$$

where c is a constant of integration. Assuming that $\sigma_{rz} = 0$ at $r = bR$ (the location of the maximum velocity, see Fig. 4.14), with $a < b < 1$, we calculate the integration constant ($c = -(P_z/2)b^2R^2$), resulting in the following shear stress distribution,

$$\sigma_{rz} = \frac{-P_z bR}{2} \left(\frac{bR}{r} - \frac{r}{bR} \right). \quad (4.91)$$

Dividing Eq. (4.87) by Eq. (4.89) results in the following relationship between normal and shear stresses,

$$\sigma_{zz} = \frac{2\lambda}{\eta_p} \sigma_{rz}^2. \quad (4.92)$$

Solving Eq. (4.87) for $\dot{\gamma}$, and using Eq. (4.91) and Eq. (4.92) results in the following velocity gradient distribution:

$$\frac{du}{dr} = -\frac{\Gamma(\beta)}{\eta_p} E_{\alpha,\beta} \left(\frac{2\varepsilon\lambda^2}{\eta_p^2} \left(\frac{P_z bR}{2} \left(\frac{bR}{r} - \frac{r}{bR} \right) \right)^2 \right) \frac{P_z bR}{2} \left(\frac{bR}{r} - \frac{r}{bR} \right). \quad (4.93)$$

The velocity gradient can be written in dimensionless form, using the Weissenberg number, $Wi = \lambda U_c / \delta$, where $U_c = -P_z \delta^2 / \eta_p$ is a characteristic velocity of the flow and δ is the gap between the two cylinders in the annulus. We also define $\bar{u} = u / U_c$ as the dimensionless velocity and $\bar{r} = r / \delta$ as the normalized radius/distance between the inner and outer cylinders ($\bar{R} = R / \delta$). This gives the following dimensionless velocity gradient:

$$\frac{d\bar{u}}{d\bar{r}} = \frac{\Gamma(\beta)}{2} \left(\frac{b^2 \bar{R}^2}{\bar{r}} - \bar{r} \right) E_{\alpha,\beta} \left(\frac{\varepsilon Wi^2}{2} \left(\frac{b^2 \bar{R}^2}{\bar{r}} - \bar{r} \right)^2 \right). \quad (4.94)$$

Now, we can obtain the velocity profile numerically by solving the following nonlinear problem:

Problem 1

Given εWi^2 and a , find the value of b that satisfies,

$$\int_{a\bar{R}}^{\bar{R}} \frac{d\bar{u}}{d\bar{r}} d\bar{r} = 0. \quad (4.95)$$

Using the value of b , compute the velocity profile:

$$\bar{u}(\bar{r}) = \int_{a\bar{R}}^{\bar{r}} \frac{\Gamma(\beta)}{2} \left(\frac{b^2 \bar{R}^2}{\bar{r}} - \bar{r} \right) E_{\alpha, \beta} \left(\frac{\varepsilon Wi^2}{2} \left(\frac{b^2 \bar{R}^2}{\bar{r}} - \bar{r} \right)^2 \right) d\bar{r}, \quad (4.96)$$

where $0 < a < 1$ is defined by the user. Eq. (4.96) results from the no-slip boundary condition, $\bar{u}(\bar{R}) = 0$. The velocity profile in Eq. (4.96) can be easily approximated numerically by a simple quadrature rule. The solution of Eq. (4.95) can be obtained by defining $F(b) = \int_{a\bar{R}}^{\bar{R}} \frac{d\bar{u}}{d\bar{r}} d\bar{r}$. So, there exists $0 < a < b < 1$ such that $F(b) = 0$.

Eq. (4.94) can be further expanded using the definition of the Mittag–Leffler function, resulting in

$$\frac{d\bar{u}}{d\bar{r}} = \frac{\Gamma(\beta)}{2} \left(\frac{b^2 \bar{R}^2}{\bar{r}} - \bar{r} \right) \sum_{j=0}^{\infty} \frac{1}{\Gamma(\alpha j + \beta)} \left(\frac{\varepsilon Wi^2}{2} \left(\frac{b^2 \bar{R}^2}{\bar{r}} - \bar{r} \right)^2 \right)^j \quad (4.97)$$

$$= \frac{\Gamma(\beta)}{2} \sum_{j=0}^{\infty} \frac{1}{\Gamma(\alpha j + \beta)} \left(\frac{\varepsilon Wi^2}{2} \right)^j \left(\frac{b^2 \bar{R}^2}{\bar{r}} - \bar{r} \right)^{2j+1} \quad (4.98)$$

and the velocity profile can be obtained from the integration of each term in this sum, leading to the following expression:

$$\bar{u}(\bar{r}) = \frac{\Gamma(\beta)}{2} \sum_{j=0}^{\infty} \frac{1}{\Gamma(\alpha j + \beta)} \left(\frac{\varepsilon Wi^2}{2} \right)^j \int_{a\bar{R}}^{\bar{r}} \left(\frac{b^2 \bar{R}^2}{\bar{r}} - \bar{r} \right)^{2j+1} d\bar{r}. \quad (4.99)$$

The integral $\int \left(\frac{A}{\bar{r}} - \bar{r} \right)^{2j+1} d\bar{r}$, with $A = b^2 \bar{R}^2$, can be easily computed, using the Newton's binomial. So, the velocity profile, is given by:

$$\bar{u}(\bar{r}) = \frac{\Gamma(\beta)}{2} \sum_{j=0}^{\infty} \frac{1}{\Gamma(\alpha j + \beta)} \left(\frac{\varepsilon Wi^2}{2} \right)^j \left[\sum_{k=0}^{2j+1} \binom{2j+1}{k} \int_{a\bar{R}}^{\bar{r}} \left(\frac{b^2 \bar{R}^2}{\bar{r}} \right)^{2j+1-k} (-\bar{r})^k d\bar{r} \right] \quad (4.100)$$

that can be rewritten as:

$$\bar{u}(\bar{r}) = \frac{\Gamma(\beta)}{2} \sum_{j=0}^{\infty} \frac{1}{\Gamma(\alpha j + \beta)} \left(\frac{\varepsilon Wi^2}{2} \right)^j \left[\sum_{k=0}^{2j+1} \binom{2j+1}{k} (-1)^k \left(b^2 \bar{R}^2 \right)^{2j+1-k} f_{kj}(a, \bar{r}) \right] \quad (4.101)$$

where:

$$f_{kj}(a, \bar{r}) = \begin{cases} \ln\left(\frac{\bar{r}}{a\bar{R}}\right), & \text{if } k = j. \\ \frac{\bar{r}^{2(k-j)} - (a\bar{R})^{2(k-j)}}{2(k-j)}, & \text{if } k \neq j. \end{cases} \quad (4.102)$$

Although Eq. (4.101) is an infinite series, we can obtain an approximated solution with a fair number of correct decimal places by using only $j = 3$ or $j = 4$ (depending on the problem and the parameters used). This will be explored in detail in the next section.

The second relevant problem from a practical point of view is the corresponding inverse problem of determining the pressure gradient for a given flow rate. In this second case, the following equation must be solved,

$$U = \frac{1}{\pi R^2(1-a^2)} \int_{aR}^R u(r) 2\pi r \, dr \quad (4.103)$$

where $\pi R^2(1-a^2)$ is the cross section area of the annular region and U is the average velocity in the annular region. Eq. (4.103) in dimensionless form becomes:

$$\frac{2}{\bar{R}^2(1-a^2)} \int_{a\bar{R}}^{\bar{R}} \bar{u}(\bar{r}) \bar{r} \, d\bar{r} - \frac{U}{U_c} = 0 \quad (4.104)$$

In this scenario, we can formulate the next problem:

Problem 2

Given εWi_U^2 ($Wi_U = \lambda U / \delta$) and a , find b and εWi^2 such that,

$$\bar{u}(\bar{R}) = 0 \quad \wedge \quad \frac{2}{\bar{R}^2(1-a^2)} \int_{a\bar{R}}^{\bar{R}} \bar{u}(\bar{r}) \bar{r} \, d\bar{r} - \frac{U}{U_c} = 0. \quad (4.105)$$

Then use the values of b and εWi^2 to compute the velocity profile given by Eq. (4.101). Note that $U/U_c = Wi_U/Wi$.

4.3.4 Results and discussion

4.3.4.1 Assessment of the series solution

In this subsection, we compare the numerical solution of the velocity profile given by Eq. (4.96), with the analytical solution of Eq. (4.101). These results were obtained using the *Mathematica* software and we first consider a high-precision numerical solution, where we obtain the value of b using the secant method and then we numerically integrate Eq. (4.94). This highly accurate numerical solution of the velocity profile was then used as a reference to perform an investigation of the influence of the number of terms in the series on the error of the solution. The new truncated solution is obtained from Eq. (4.101), truncating the sum with $j + 1$ terms. We considered 200

equidistant mesh points along the cylinder gap and measured the maximum relative error obtained at these points (boundaries excluded).

The error is calculated by $\frac{|\bar{u}(\bar{r})_{num} - \bar{u}(\bar{r})_t|}{\bar{u}(\bar{r})_{num}}$, where $\bar{u}(\bar{r})_{num}$ is the approximate value of the velocity and $\bar{u}(\bar{r})_t$ is the velocity value from the truncated series. Three different values of εWi^2 were considered: 0.05, 3.2 and 5. We set $\beta = 1$ and tested two different values of α , 0.5 and 1.5. We only changed the values of α , because this parameter induces more changes in the series. The value of a used was 0.5 in all cases.

In Table 4.1, we show the maximum relative errors, in percentage. For $\varepsilon Wi^2 = 0.05$, the error was low, even when considering a single term in the series (Eq. (4.101)). For $\alpha = 1.5$ we see that the error is much smaller, with the decrease in error becoming less pronounced as the number of terms in the series increases. This is due to the number of significant digits considered.

Table 4.1: Maximum relative errors (in percentage) for $\varepsilon Wi^2 = 0.05$.

j	$\alpha = 0.5$	$\alpha = 1.5$
1	5.669×10^{-1}	9.405×10^{-2}
2	1.342×10^{-2}	4.757×10^{-4}
4	4.550×10^{-4}	4.432×10^{-4}

Tables 4.2 and 4.3 show the maximum relative errors in percentage for $\varepsilon Wi^2 = 3.2$ and 5, respectively. As we increase εWi^2 , the series solution shows convergence problems, and as we increase α (see Table 4.3), the error decreases faster as the number of terms in the series increases (note also that in this case we even consider a higher εWi^2 value). The corresponding velocity profiles are shown in Fig. 4.15, where u/U_c is the velocity profile normalised by the characteristic velocity, using the highly accurate numerical solution. These particular results indicate that the velocity profile converges to the correct profile as the number of terms in the series increases, and that this convergence is slower for low values of α .

Table 4.2: Maximum relative errors (in percentage) for $\varepsilon Wi^2 = 3.2$.

j	$\alpha = 0.5$
2	1.782×10^2
4	1.580×10^2
8	5.874×10^1
16	8.681×10^{-1}

Based on these observations, we will consider $j = 15$ for the results presented next.

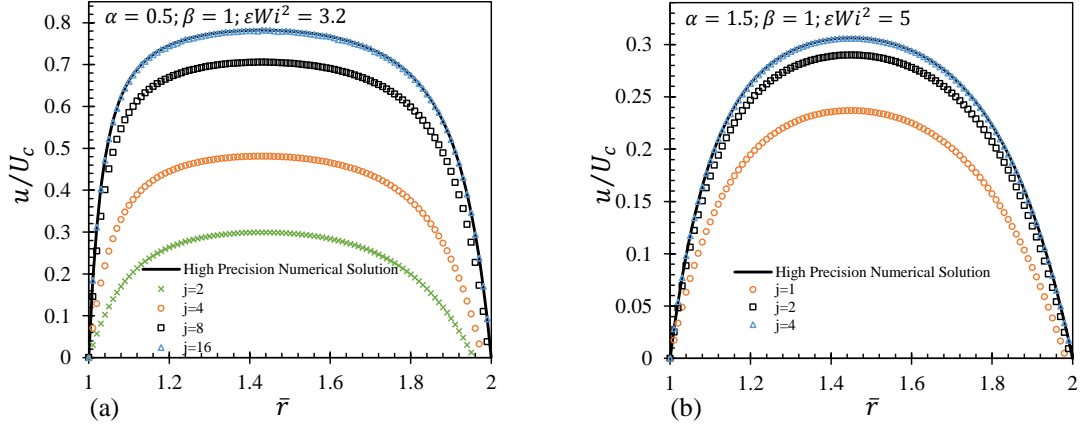
4.3.4.2 Problem 1:

Fig. 4.16 shows the velocity profiles for $\beta = 1$, $\alpha = 0.5, 1, 3$ at three different values of the εWi^2 of 0.05, 1 and 3.2.

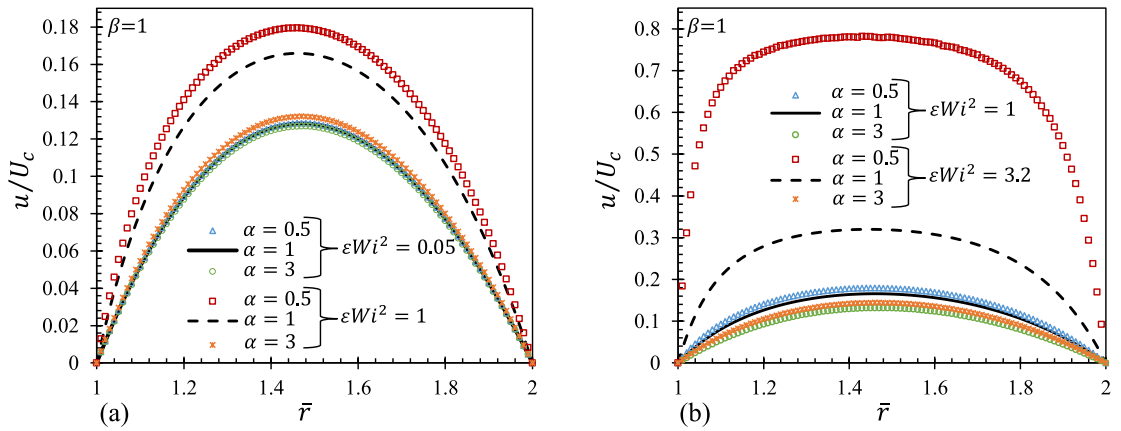
For $\varepsilon Wi^2 = 0.05$ (Fig. 4.16 (a)) the velocity profiles for different values of α almost overlap. However, when we increase εWi^2 to 1, that no longer happens, in fact we obtain the highest velocity

Table 4.3: Maximum relative errors (in percentage) for $\varepsilon Wi^2 = 5$.

j	$\alpha = 1.5$
1	1.414×10^2
2	4.773×10^1
4	1.409×10^0
8	4.275×10^{-4}

Figure 4.15: Velocity profiles for $\beta = 1$, $\alpha = 0.5$, 1.5 and two different values of εWi^2 , 3.2 and 5 . (a) $\alpha = 0.5$; (b) $\alpha = 1.5$.

and flow rate for $\alpha = 0.5$, the case in which we have the highest rate of destruction of junctions. This behaviour is more pronounced when we increase elasticity (see Fig. 4.16 (b)). For $\varepsilon Wi^2 = 3.2$, the differences in the flow rates are obvious, except for $\alpha = 3$, where the velocity profile almost overlaps with the case $\varepsilon Wi^2 = 1$. It is interesting to see that for $\alpha = \beta = 1$ we still have a parabolic velocity profile typical of Newtonian fluids, while decreasing α we observe a very pronounced plug-like profile, which is more typical of shear-thinning fluids.

Figure 4.16: Velocity profiles for $\beta = 1$, $\alpha = 0.5$, 1 , 3 . (a) $\varepsilon Wi^2 = 0.05$ and 1 ; (b) $\varepsilon Wi^2 = 1$ and 3.2 .

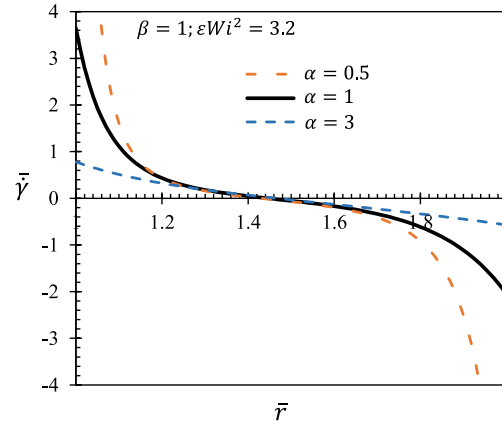


Figure 4.17: Normalized shear rate profiles for $\varepsilon Wi^2 = 3.2$ and $\alpha = 0.5, 1$ and 3 .

To understand the slope variation of the velocity profile across the cylinder gap (for different α values), we also plotted the corresponding normalized shear rate, in Fig. 4.17. This way we have an idea of how much higher shear rates near the wall are for low values of α .

Figs. 4.18 (a) and (b) show the normalized shear and normal stress profiles, for $\beta = 1$, $\alpha = 0.5, 1$ and 3 for $\varepsilon Wi^2 = 3.2$. For the three cases, the dimensionless normal stress is always positive and the dimensionless shear stress shows a quasi-linear profile, being positive near the inner cylinder and negative in the vicinity of the outer cylinder. The shear stress is smaller for low values of α since the values of b decrease with decreasing α (see also Eq. (4.94)).

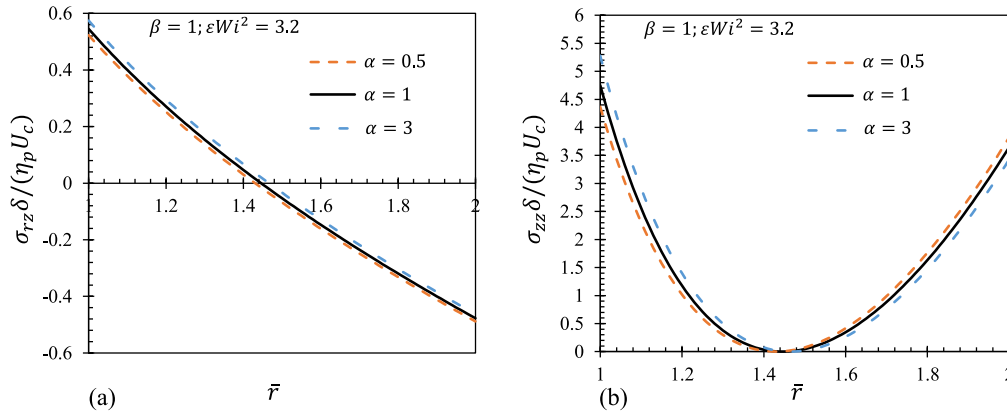


Figure 4.18: Normalized shear and normal stress profiles, for $\beta = 1$, $\alpha = 0.5, 1$ and 3 and $\varepsilon Wi^2 = 3.2$. (a) Normalized shear stress; (b) Normalized normal stress.

Figs. 4.19 (a), (b) and (c) show the influence of β on the velocity profile. The results are similar to those for the variation of α . For a small value of εWi^2 (Fig. 4.19 (a)), the velocity profiles almost overlap for all values of β , but as εWi^2 is increased (Fig. 4.19 (b) and (c)), the velocity and the flow rate increase as we decrease β . That effect is more pronounced for small values of β .

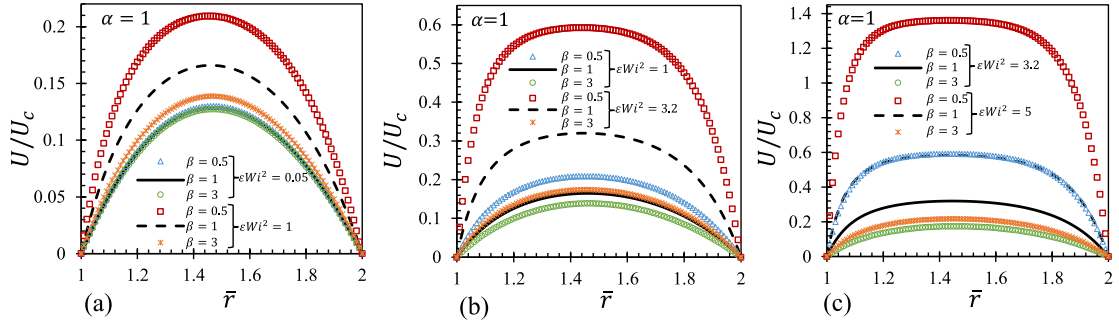


Figure 4.19: Velocity profiles for $\alpha = 1$, $\beta = 0.5$, 1 and 3; (a) $\epsilon Wi^2 = 0.05$ and 1 ;(b) $\epsilon Wi^2 = 1$ and 3.2;(c) $\epsilon Wi^2 = 3.2$ and 5.

The role of β is more complex than that of α . β is used as an argument of the Mittag–Leffler function and to normalize $K(\sigma_{zz})$. This mixed effect of β on the rate of destruction of junctions results in smoother variations of velocity due to the variation of β .

We also study the variations of b with ϵWi^2 (see Fig. 4.20). We considered three different values of α , of 0.5, 1 and 3 and calculated b for different ϵWi^2 . We see that the value of b decreases with the increase of ϵWi^2 , and that for $\alpha = 3$, the variation is almost linear. Notice that, when $\alpha = 0.5$, the reduction is more pronounced. Fig. 4.20 shows that b decreases with the increase of the fluid elasticity, a trend also observed on the velocities profiles of Figs. 4.19, since b represents the radial position of the maximum value for the velocity profile. Therefore, the point of maximum velocity approaches the inner cylinder wall as the elasticity of the fluid increases, because of the direct relationship between elasticity and shear-thinning of the shear viscosity.

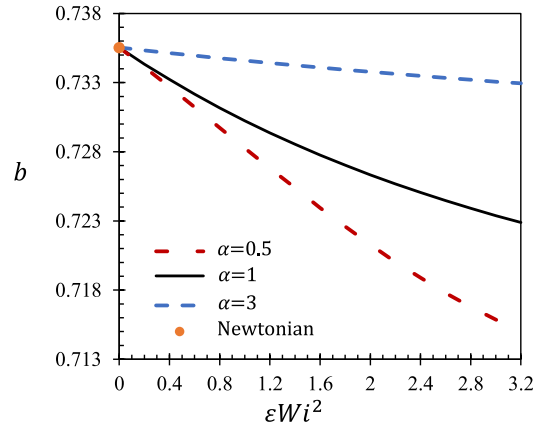


Figure 4.20: Variation of b with the variation ϵWi^2 , for $\alpha = 0.5$, 1 and 3. The closed circle corresponds to value of b obtained for a Newtonian fluid [30, 39].

4.3.4.3 Problem 2:

This problem is harder to solve because for a given value of the flow rate, U , we have to find b and εWi^2 ($\varepsilon Wi^2 = \varepsilon (\lambda U_c / \delta)^2 = \varepsilon (-\lambda \delta P_z / \eta_p)^2$) from a system of two strongly nonlinear equations. The first equation come from the outer wall boundary condition,

$$\frac{\Gamma(\beta)}{2} \sum_{j=0}^{\infty} \frac{1}{\Gamma(\alpha j + \beta)} \left(\frac{\varepsilon Wi^2}{2} \right)^j \left[\sum_{k=0}^{2j+1} \binom{2j+1}{k} (-1)^k (b^2 \bar{R}^2)^{2j+1-k} \left[f_{kj}(a, \bar{R}) \right] \right] = 0; \quad (4.106)$$

and the second from the imposed non-dimensionless flow rate

$$\frac{\Gamma(\beta)}{\bar{R}^2 (1 - a^2)} \sum_{j=0}^{\infty} \frac{1}{\Gamma(\alpha j + \beta)} \left(\frac{\varepsilon Wi^2}{2} \right)^j \left[\sum_{k=0}^{2j+1} \binom{2j+1}{k} (-1)^k (b^2 \bar{R}^2)^{2j+1-k} \left[h_{kj}(a, \bar{R}) \right] \right] - \frac{Wi_U}{Wi} = 0 \quad (4.107)$$

where $h_{kj}(a, \bar{R}) = \bar{R} - a\bar{R}$ if $k = j$ and $h_{kj}(a, \bar{R}) = \frac{\bar{R}^{2(k-j)+1} - (a\bar{R})^{2(k-j)+1}}{2(k-j)+1}$ if $k \neq j$. Note that $U/U_c = Wi_U/Wi$, as in Eq. (4.105).

Since one of the goals of this work is to provide a tool for validating future numerical implementations of this constitutive model in general numerical codes, the *Mathematica* codes used to obtain the solution are provided as supplementary material.

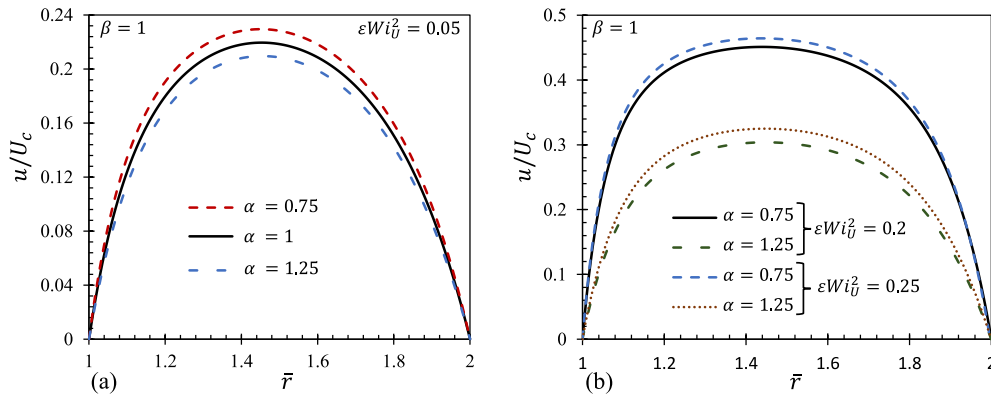


Figure 4.21: Normalized velocity profiles for $\beta = 1$ and $\alpha = 0.75, 1$ and 1.25 . (a) $\varepsilon Wi_U^2 = 0.05$; (b) $\varepsilon Wi_U^2 = 0.2$ and 0.25 .

Fig. 4.21 shows the normalized velocity profiles for $\beta = 1$, $\alpha = 0.75, 1$ and 1.25 , $a = 0.5$, and, for three different values of εWi_U^2 : $0.05, 0.2$ and 0.25 .

For the lowest εWi_U^2 (Fig. 4.21 (a)), the velocity profiles are similar, with higher velocities for lower values of α , and, the plug-like profile typical of non-Newtonian fluids is less pronounced due to the low elasticity. Again, this confirms the idea that the lower values of α lead to more plug-like profiles due to the intense shear-thinning.

This effect is more pronounced in Fig. 4.21 (b), where we compare the results for two moderate values of elasticity. The combination of a higher εWi_U^2 and a lower value of α leads to a less parabolic velocity profile.

The combined effect of elasticity and parameters α and β leads to a complex relationship. Physically, we have that a higher rate of destruction of junctions in the network (lower α) allows for a faster creation of a new network. For Problem 1, this resulted in a higher flow rate, giving the idea that, this high destruction rate results in less resistance of the flow. When the flow rate is imposed, we observe that the information from the boundary conditions travels at a slower velocity, allowing for a more plug-like profile to be possible.

4.3.5 Conclusions

We derived an analytical solution for the velocity profile in series form for the annular flow of a gPTT fluid. A semi-analytic solution is derived for the case where the flow rate is imposed.

We show the influence of the model parameters on the velocity and stress profiles. As expected, the flow velocity increases with the decrease of α and β for the same εWi^2 , resulting in a more pronounced plug-like profile. The influence of β is less pronounced due to its double influence on the proposed rate of destruction of junctions (it is a parameter of the Mittag–Leffler function and is also used as a normalization factor).

The analytical and semi-analytical solutions presented in this work are useful for the validation of CFD codes and also provide a better understanding of the model behaviour in simple shear flows.

4.4 A study on mixed electro-osmotic/pressure-driven microchannel flows of a generalised Phan-Thien–Tanner fluid⁴

Abstract: This work presents new semi-analytical solutions for the combined fully-developed electro-osmotic pressure-driven flow in microchannels of viscoelastic fluids, described by the generalised Phan-Thien–Tanner model (gPTT) recently proposed by Ferrás et al. (Journal of Non-Newtonian Fluid Mechanics, 269: 88-99, 2019). This generalised version of the PTT model presents a new function for the trace of the stress tensor - the Mittag–Leffler function - where one or two new fitting constants are considered in order to obtain additional fitting flexibility. The semi-analytical solution is obtained under sufficiently weak electric potentials that allows the Debye–Hückel approximation for the electrokinetic fields and for thin electric double layers. Based on the solution, the effects of the various relevant dimensionless numbers are assessed and discussed, such as the influence of εWi^2 , of the parameters α and β of the gPTT model, and also of $\bar{\kappa}$, the dimensionless Debye–Hückel parameter. We conclude that the new model characteristics enhance the effects of both εWi^2 and $\bar{\kappa}$ on the velocity distribution across the microchannels. The effects of a high zeta potential and of the finite size of ions are also studied numerically.

Keywords: electro-osmotic flow/pressure driven flows, generalised simplified PTT, high zeta potential, Mittag–Leffler, steric effect

4.4.1 Introduction

Electro-osmosis (EO) is a flow forcing method suitable for flows through micro- and nano-devices that are particularly useful for applications in medicine, biochemistry and miniaturised industrial processes. EO relies on a basic electrokinetic phenomenon, where the flow of an electrolyte is driven by an external potential difference between the inlet and outlet of the channel, acting on ions that are imbalanced in the near-wall region of the fluid due to the interaction between the dielectric channel walls and the fluid. Specifically, these are layers of higher concentration of counter-ions within the fluid, that move under the action of the applied electric field, which then drags by viscous forces the neutral core as a solid body [41]. There is a vast literature dealing with this topic for Newtonian fluids [42–49]. As reviewed by Zhao and Yang [50], there is also a fair amount of literature dealing with electro-osmotic flows of non-Newtonian fluids (see also [51–54]).

In this work, we are interested in viscoelastic materials described by differential constitutive equations [1], which can describe accurately the real behaviour of polymer solutions. In order to reduce the computational effort needed to compute integral models, new differential model were proposed in the literature, such as the generalised Phan-Thien–Tanner (gPTT) [3] model that uses

⁴A.M. Ribau, L.L. Ferrás, M.L. Morgado, M. Rebelo, M.A. Alves, F.T. Pinho, and A.M. Afonso. A study on mixed electro-osmotic/pressure-driven microchannel flows of a generalised Phan-Thien–Tanner fluid. *Journal of Engineering Mathematics*, 127(1), mar 2021.

the Mittag–Leffler function of the trace of the stress tensor (instead of the classical linear and exponential functions [21, 22]), together with one or two new fitting parameters in order to obtain additional fitting flexibility.

This model was previously studied for Couette and pressure driven flows, in the absence EO [28, 29], therefore this work aims to assess the influence of the new model parameters for combined electro-osmotic/pressure driven flows.

The remainder of this paper is organised as follows: the next section presents the governing equations, followed by the new analytical solution in section 4.4.3, the discussion of the results in section 4.4.4 and the conclusions of the paper in section 4.4.5.

4.4.2 Formulation and governing equations

We consider a combined electro-osmotic/pressure-driven channel flow of a viscoelastic gPTT fluid in a microchannel, as shown in Fig. 4.22. Here x , y and z , represent the streamwise, transverse and spanwise directions, respectively, and the channel width is $2H$. We consider that the channel size in the spanwise direction is much larger than H : thus, the flow can be assumed two-dimensional.

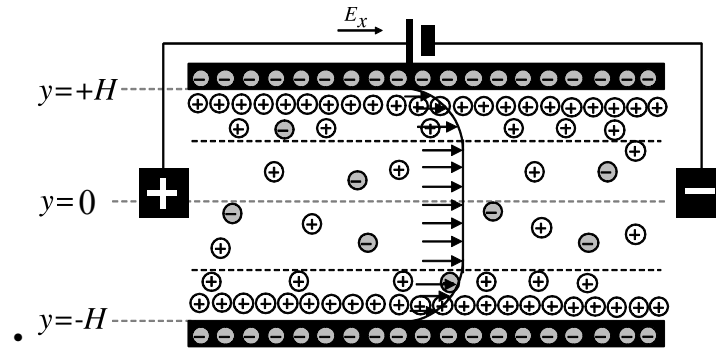


Figure 4.22: Schematic of the flow in a planar microchannel.

As schematically shown in Fig. 4.22, the ion separation arises due to the interaction between the walls and the fluid. Here, the illustrated negatively charged walls of the microchannel attract counter-ions forming layers of positively charged fluid near the walls and with the co-ions predominantly staying at the core. At such dilute concentrations, the fluid core remains essentially neutral. Very thin layers of immobile counter-ions remain at the walls, known as the Stern layers, followed by thicker more diffuse layers of mobile counter-ions; the two layers near the wall form what is called the Electrical Double Layer (EDL).

A DC potential difference between the two electrodes at the inlet and outlet generates an external electric field that exerts a body force on the counter-ions of the EDL, which flow along the channel dragging the neutral liquid core. The pressure difference that can also be applied between the inlet and outlet can act in the same direction of the electric field or in the opposite direction. At the wall, the no-slip condition applies, whereas at the centreplane, the symmetry boundary condition is used. Since the flow is fully-developed, the velocity and stress fields only depend on

the transverse coordinate y [51, 52].

The equations governing the flow of an isothermal incompressible fluid are the continuity equation

$$\nabla \cdot \mathbf{u} = 0, \quad (4.108)$$

and the Cauchy equation

$$\rho \frac{D\mathbf{u}}{Dt} = -\nabla p + \nabla \cdot \boldsymbol{\tau} + \rho_e \mathbf{E}, \quad (4.109)$$

where \mathbf{u} is the velocity vector, $\frac{D}{Dt}$ is the material derivative, p is the pressure, t is the time, ρ is the fluid density, $\boldsymbol{\tau}$ is the extra-stress tensor, \mathbf{E} is the electric field and ρ_e is the electric charge density in the fluid.

4.4.2.1 Constitutive equation

In order to achieve a closed system of equations, a constitutive equation for the extra-stress tensor, $\boldsymbol{\tau}$, is required. Recently, Ferrás et al. [3] proposed a new differential model based on the Phan-Thien–Tanner constitutive equation [21, 22]. This new model considers a more general function for the rate of destruction of junctions, the Mittag–Leffler function, where one or two fitting parameters are included, in order to achieve additional fitting flexibility [3].

The Mittag–Leffler function is defined as,

$$E_{\alpha, \beta}(z) = \sum_{j=0}^{\infty} \frac{z^j}{\Gamma(\alpha j + \beta)}, \quad (4.110)$$

with α, β being real and positive and Γ is the Gamma function. When $\alpha = \beta = 1$, the Mittag–Leffler function reduces to the exponential function, and when $\beta = 1$ the original one-parameter Mittag–Leffler function, E_{α} is obtained.

The constitutive equation is given by:

$$K(\tau_{kk})\boldsymbol{\tau} + \lambda \overset{\square}{\boldsymbol{\tau}} = 2\eta_p \mathbf{D}, \quad (4.111)$$

where τ_{kk} is the trace of the stress tensor, λ is the a relaxation time, η_p is the polymeric viscosity coefficient, \mathbf{D} is the rate of deformation tensor and $\overset{\square}{\boldsymbol{\tau}}$ represents the Gordon-Schowalter derivative defined as

$$\overset{\square}{\boldsymbol{\tau}} = \frac{\partial \boldsymbol{\tau}}{\partial t} + \mathbf{u} \cdot \nabla \boldsymbol{\tau} - (\nabla \mathbf{u})^T \cdot \boldsymbol{\tau} - \boldsymbol{\tau} \cdot (\nabla \mathbf{u}) + \xi(\boldsymbol{\tau} \cdot \mathbf{D} + \mathbf{D} \cdot \boldsymbol{\tau}). \quad (4.112)$$

Here $\nabla \mathbf{u}$ is the velocity gradient and the parameter ξ accounts for the slip between the molecular network and the continuous medium. The stress function, $K(\tau_{kk})$, is given by a new formulation that imparts more flexibility and accuracy to the model predictions, as discussed in [3]. Specifically, it is given by

$$K(\tau_{kk}) = \Gamma(\beta) E_{\alpha, \beta} \left(\frac{\varepsilon \lambda}{\eta_p} \tau_{kk} \right), \quad (4.113)$$

where ε represents the extensibility parameter and the normalization parameter $\Gamma(\beta)$ is used to ensure that $K(0) = 1$, for all choices of β .

4.4.2.2 Electric potential

We can relate the electrostatic field, \mathbf{E} , with the electric potential, Φ , through

$$\mathbf{E} = -\nabla \Phi, \quad (4.114)$$

where Φ is governed by

$$\nabla^2 \Phi = -\frac{\rho_e}{\epsilon} \quad (4.115)$$

with ϵ representing the dielectric constant of the solution. The electric potential includes two different contributions, $\Phi = \phi + \psi$, where ϕ is generated by the electrodes, placed at the inlet and outlet of the flow geometry, and ψ is associated with the charge distribution near the walls. In this way, the imposed potential is described by a Laplace equation, $\nabla^2 \phi = 0$, and the induced potential is described by a Poisson equation:

$$\nabla^2 \psi = -\frac{\rho_e}{\epsilon}. \quad (4.116)$$

In some situations, such as when the flow and the ion distributions are fully-developed, the EDLs are thin and do not overlap at the centre of the channel. Significant variations of ψ only occur in the transverse direction, and a stable Boltzmann distribution of ions occurs in the EDL. Therefore, the net electric charge density, ρ_e , for an electrolyte in equilibrium near a charged surface is given by [41]:

$$\rho_e = -2n_0 e z \sinh \left(\frac{ez}{k_B T} \psi \right), \quad (4.117)$$

where n_0 is the ion density, e the elementary charge, z the valence of the ions, T the absolute temperature and k_B the Boltzmann constant.

Combining Eq. (4.116) for the induced potential equation, that for fully-developed steady flow becomes

$$\frac{d^2 \psi}{dy^2} = -\frac{\rho_e}{\epsilon}, \quad (4.118)$$

with Eq. (4.117), leads to the Poisson-Boltzmann equation:

$$\frac{d^2\psi}{dy^2} = \frac{2n_0ez}{\epsilon} \sinh\left(\frac{ez}{k_BT}\psi\right). \quad (4.119)$$

Assuming the Debye-Hückel linearisation principle, a valid approximation provided for small values of ψ [51, 52, 65], the Poisson-Boltzmann equation (Eq. (4.119)) for the 2D channel flow becomes

$$\frac{d^2\psi}{dy^2} = \kappa^2\psi, \quad (4.120)$$

where $\kappa^2 = (2n_0e^2z^2)/(\epsilon k_BT)$ is the Debye-Hückel parameter, which is related to the thickness of the Debye layer, $\lambda_D = 1/\kappa$, also called the EDL thickness.

The boundary conditions for the Poisson-Boltzmann equation are the following: at the symmetry plane, $d\psi/dy|_{y=0} = 0$; the zeta potential at the wall is $\psi_{wall} = \psi_0$. Integrating Eq. (4.120) and applying these boundary conditions, leads to the following induced electric field, ψ :

$$\psi(y) = \psi_0 \frac{\cosh(\kappa y)}{\cosh(\kappa H)} \quad (4.121)$$

for $|y| \leq H$. The electric charge density, ρ_e is given by

$$\rho_e = -\epsilon\psi_0\kappa^2 \frac{\cosh(\kappa y)}{\cosh(\kappa H)}. \quad (4.122)$$

It should be remarked that the non-dimensionalization of the Nernst-Planck equation which governs the transport of ionic species shows that the relative contribution of the advective strength of the ionic species compared to diffusive strength results in the ionic Peclet number, which can be expressed as $(u_{\text{ref}}H)/D$, where u_{ref} is a reference velocity, H is a reference length scale (the half width of the channel) and D is the ionic diffusivity. For electro-osmotic flows, a typical velocity scale is $u_{\text{ref}} \sim (\epsilon\psi_0 E_x)/\eta_p$. Taking a viscoelastic fluid as a medium with $\epsilon \sim 10^{-9}$ C/V.m and $\eta_p \sim 10^{-2}$ Pa.s, for an electric field of $E_x \sim 10^4$ V/m and for $\psi_0 \sim 20$ mV, we obtain $u_{\text{ref}} \sim 2 \times 10^{-5}$ m/s. Now, with a channel height of $2H \sim 10 \mu\text{m}$ and $D \sim 10^{-8}$ m²/s, the ionic Peclet number is of order $Pe \sim 0.01$, i.e. the contribution of advection on the space distribution of ionic charges can be neglected in the present analysis, when considering the Debye-Hückel approximation.

More details regarding the derivation of these equations can be seen in Afonso et al. [51], Mondal et al. [105] and Mukherjee et al. [106].

4.4.3 Analytical solution for the gPTT model

In this section, we derive the analytical solution for the gPTT model considering fully-developed electro-osmotic/pressure-driven flow (cf. Fig. 4.22).

The momentum equation, Eq. (4.109), becomes

$$\frac{d\tau_{xy}}{dy} = P_x - \rho_e E_x, \quad (4.123)$$

where $P_x \equiv dp/dx$ is the constant streamwise pressure gradient, τ_{xy} the shear stress and $E_x \equiv d\phi/dx$ is the imposed constant streamwise gradient of electric potential. This equation is valid regardless of the rheological constitutive equation.

Now, using Eq. (4.122) and considering that the shear stress at the centreline is zero, Eq. (4.123) can be integrated leading to the following shear stress distribution:

$$\tau_{xy} = \epsilon\psi_0 E_x \kappa \frac{\sinh(\kappa y)}{\cosh(\kappa H)} + P_x y. \quad (4.124)$$

The constitutive equation for the gPTT model for this flow (section 4.4.2.1) can be further simplified, leading to

$$K(\tau_{kk})\tau_{xx} = (2 - \xi)(\lambda\dot{\gamma})\tau_{xy}, \quad (4.125)$$

$$K(\tau_{kk})\tau_{yy} = -\xi(\lambda\dot{\gamma})\tau_{xy}, \quad (4.126)$$

$$K(\tau_{kk})\tau_{xy} = \eta_p \dot{\gamma} + \left(1 - \frac{\xi}{2}\right)(\lambda\dot{\gamma})\tau_{yy} - \frac{\xi}{2}(\lambda\dot{\gamma})\tau_{xx}, \quad (4.127)$$

where the velocity gradient $\dot{\gamma}$ is a function of y ($\dot{\gamma}(y) \equiv du/dy$) and $\tau_{kk} = \tau_{xx} + \tau_{yy} + \tau_{zz}$ is the trace of the stress tensor. Under fully developed flow conditions, $\tau_{zz} = 0$.

4.4.3.1 Electro-osmotic flow with $\xi = 0$

In order to obtain closed form analytical solutions, the slip parameter in the Gordon-Schowalter derivative is set to $\xi = 0$. For $\xi = 0$, Eq. (4.126) implies that $\tau_{yy} = 0$, and the trace of the stress tensor becomes $\tau_{kk} = \tau_{xx}$. Dividing Eq. (4.125) by Eq. (4.127), $K(\tau_{xx})$ cancels out, and an explicit relationship between the streamwise normal stress and the shear stress is found:

$$\tau_{xx} = 2 \frac{\lambda}{\eta_p} \tau_{xy}^2. \quad (4.128)$$

Now combining Eqs. (4.127), (4.128), (4.124) and (4.113), the following velocity gradient profile is obtained:

$$\dot{\gamma}(y) = \frac{\Gamma(\beta)}{\eta_p} E_{\alpha,\beta} \left(\frac{2\epsilon\lambda^2}{\eta_p^2} \left(\epsilon\psi_0 E_x \kappa \frac{\sinh(\kappa y)}{\cosh(\kappa H)} + P_x y \right)^2 \right) \left(\epsilon\psi_0 E_x \kappa \frac{\sinh(\kappa y)}{\cosh(\kappa H)} + P_x y \right). \quad (4.129)$$

The dimensionless velocity gradient becomes:

$$\frac{d\bar{u}}{d\bar{y}} = \Gamma(\beta) E_{\alpha,\beta} \left(\frac{2\epsilon Wt^2}{\bar{\kappa}^2} \left(\Upsilon \bar{y} - \bar{\kappa} \frac{\sinh(\bar{\kappa} \bar{y})}{\cosh(\bar{\kappa})} \right)^2 \right) \left(\Upsilon \bar{y} - \bar{\kappa} \frac{\sinh(\bar{\kappa} \bar{y})}{\cosh(\bar{\kappa})} \right), \quad (4.130)$$

where $Wi = \lambda \kappa u_{sh}$ is the Weissenberg number and u_{sh} is the Helmholtz-Smoluchowski electro-osmotic velocity, defined as $u_{sh} = -\frac{\epsilon \psi_0 E_x}{\eta_p}$, $\bar{u} = \frac{u}{u_{sh}}$, $\bar{y} = \frac{y}{H}$ and $\bar{\kappa} = \kappa H$. The non-dimensional parameter

$$\Upsilon = -\frac{H^2}{\epsilon \psi_0} \left(\frac{P_x}{E_x} \right),$$

represents the ratio of pressure to electro-osmotic driving forces. Eq. (4.130) has an analytical solution only for pure electro-osmotic (EO) flow and provided further assumptions are made, whereas for the combined situation with a pressure gradient (EO+PD), the solution is obtained numerically. Next, we obtain the analytical solution for pure EO and discuss its validity in section 4.4.4, where the combined solution (EO+PD) is also discussed.

For pure EO flow, $\Upsilon = 0$, the velocity profile can be obtained integrating the velocity gradient profile, subjected to the no-slip boundary condition at the top (+) or bottom (-) walls, $\bar{u}(\bar{y} = \pm 1) = 0$. Simplifying Eq. (4.130), the equation to be integrated is:

$$\bar{u}(\bar{y}) = \int_{\bar{y}}^1 \left(\Gamma(\beta) \bar{\kappa} \sum_{j=0}^{\infty} \left(2\epsilon Wi^2 \right)^j \left(\frac{\sinh(\bar{\kappa} z)}{\cosh(\bar{\kappa})} \right)^{2j+1} \frac{1}{\Gamma(\alpha j + \beta)} \right) dz. \quad (4.131)$$

In order to compute the integral in (4.131), we consider $\sinh(\bar{\kappa} \bar{y}) \approx \frac{1}{2} \exp(\bar{\kappa} \bar{y})$ which is usually accurate because in most micro-devices, the thickness of the EDL is very small, about 1 to 3 orders of magnitude smaller than the width of the micro channel, so $\bar{\kappa}$ is a large value. However, close to the centreline, the approximation ($\bar{y} \sim 0$) becomes less adequate (in this case, we can use a numerical method to obtain the approximate solution of the differential equation).

Assuming $\sinh(\bar{\kappa} z) \approx \frac{1}{2} \exp(\bar{\kappa} z)$, the integration (Eq. (4.131)) gives the following velocity profile ($\bar{y} > 0$):

$$\bar{u}(\bar{y}) \approx \frac{\Gamma(\beta)}{2 \cosh(\bar{\kappa})} \sum_{j=0}^{\infty} \left(\frac{\epsilon Wi^2}{2 \cosh^2(\bar{\kappa})} \right)^j \frac{\left((\exp(\bar{\kappa} \bar{y}))^{2j+1} - (\exp(\bar{\kappa}))^{2j+1} \right)}{2j+1} \frac{1}{\Gamma(\alpha j + \beta)}. \quad (4.132)$$

When we consider $\alpha = \beta = 1$, Eq. (4.132) reduces to the one presented in Ferrás et al. [52] for pure EO flow of an exponential PTT fluid:

$$\bar{u}(\bar{y}) \approx \frac{\sqrt{\frac{\pi}{2}} \left(\operatorname{erfi} \left[\frac{B \sqrt{A} \exp(\bar{\kappa})}{\sqrt{2}} \right] - \operatorname{erfi} \left[\frac{B \sqrt{A} \exp(\bar{\kappa} |\bar{y}|)}{\sqrt{2}} \right] \right)}{2 \bar{\kappa} \sqrt{A}}, \quad (4.133)$$

where $\operatorname{erfi}(z) = -i \operatorname{erf}(iz)$ with $\operatorname{erf}(\cdot)$ denoting the error function, $A = (\epsilon Wi^2) / \bar{\kappa}^2$ and $B = \bar{\kappa} / \cosh(\bar{\kappa})$.

4.4.3.2 Electro-osmotic flow with $\xi \neq 0$

For purely EO flow ($P_x = 0$), and considering parameter $\xi \neq 0$ in the Gordon–Schowalter derivative, the behaviour of the solution is different and the EO flow may become unstable above a critical shear rate as previously shown by Dhinakaran et al. [65]. The system of differential equations is

non-linear and the velocity profile must be obtained numerically. Following the steps of Dhinakaran et al. [65] (their equations (12)-(22)), one can obtain the velocity gradient:

$$\frac{du}{dy} = \frac{-\Gamma(\beta)E_{\alpha,\beta} \left[\frac{1}{\chi} \left(1 - \sqrt{1 - \left(a\lambda\kappa u_{sh} \frac{\sinh(\kappa y)}{\cosh(\kappa H)} \right)^2} \right) \right] \kappa u_{sh} \frac{\sinh(\kappa y)}{\cosh(\kappa H)}}{1 - \frac{1}{2} \left(1 - \sqrt{1 - \left(a\lambda\kappa u_{sh} \frac{\sinh(\kappa y)}{\cosh(\kappa H)} \right)^2} \right)}, \quad (4.134)$$

where

$\chi = \frac{\xi(2-\xi)}{\varepsilon(1-\xi)}$ and $a = 2\sqrt{\xi(2-\xi)}$. The velocity gradient can be written in dimensionless form as

$$\frac{d\bar{u}}{d\bar{y}} = \frac{-\Gamma(\beta)E_{\alpha,\beta} \left[\frac{1}{\chi} \left(1 - \sqrt{1 - \left(aWi \frac{\sinh(\bar{\kappa}\bar{y})}{\cosh(\bar{\kappa})} \right)^2} \right) \right] \bar{\kappa} \frac{\sinh(\bar{\kappa}\bar{y})}{\cosh(\bar{\kappa})}}{1 - \frac{1}{2} \left(1 - \sqrt{1 - \left(aWi \frac{\sinh(\bar{\kappa}\bar{y})}{\cosh(\bar{\kappa})} \right)^2} \right)} \quad (4.135)$$

and then the velocity profile, $\bar{u}(\bar{y})$, can be obtained integrating numerically Eq. (4.135) using, for example, Simpson's rule.

The steric effects are presented in Appendix A.

4.4.4 Discussion of results

4.4.4.1 Pure electro-osmotic flow

Before performing a study on the influence of the different parameters on the fluid flow, we briefly discuss the validity of the approximate analytical solution given by Eq. (4.132). We compare in Fig. 4.23 the results obtained with this equation and the results obtained numerically by integrating Eq. (4.131) with the Simpson's quadrature rule. For the approximation of the infinite series, we performed numerical tests and observed that the use of 20-40 terms would allow us to obtain an accurate sum up to the sixth decimal place.

As expected, it can be seen that only for low values of $\bar{\kappa}$, ($\bar{\kappa} \leq 5$), the thin layer approximation of the analytical solution fails to predict the correct velocity profile. Therefore, the values of $\bar{\kappa}$ used along this work will typically be greater or equal than 10 (except for the cases where the solution is numerical or when this effect is considered).

We will now investigate the influence of the Mittag–Leffler function parameters α and β , on the velocity profile distribution across the channel for different values of εWi^2 and $\bar{\kappa}$, and we compare the results with those for the exponential PTT model.

Fig. 4.24 compares the velocity profiles obtained for EO flow considering two different εWi^2 values and different values of α (Fig. 4.24 (a)) and β (Fig. 4.24 (b)) at $\bar{\kappa} = 10$. In Fig. 4.24 (a), $\beta = 1$ and we observe that for increasing εWi^2 and decreasing α , the flow rate increases, which is due to enhanced shear-thinning at the shear rates prevailing within the EDL. In Fig. 4.24 (b) $\alpha = 1$ and a similar qualitative behaviour is obtained, i.e., on increasing εWi^2 and decreasing β , the flow rate increases. However, there are quantitative differences with the effect of β being stronger than

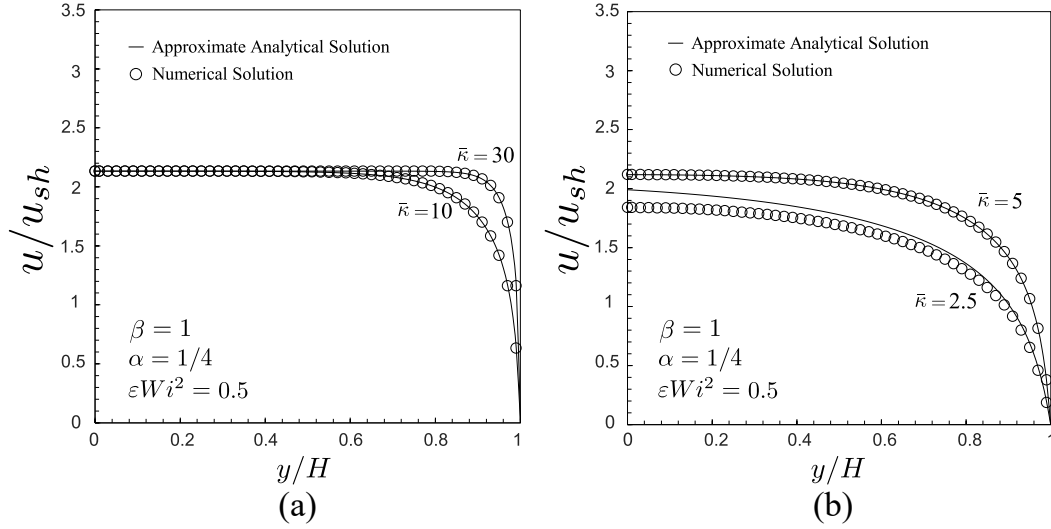


Figure 4.23: Velocity profiles calculated using Eqs. (4.132) (lines) and (4.131) (symbols) for the pure EO flow considering $\epsilon Wi^2 = 0.5$ and different values of \bar{k} for $\alpha = 1/4$ and $\beta = 1$: (a) $\bar{k} = 10$ and $\bar{k} = 30$; (b) $\bar{k} = 2.5$ and $\bar{k} = 5$.

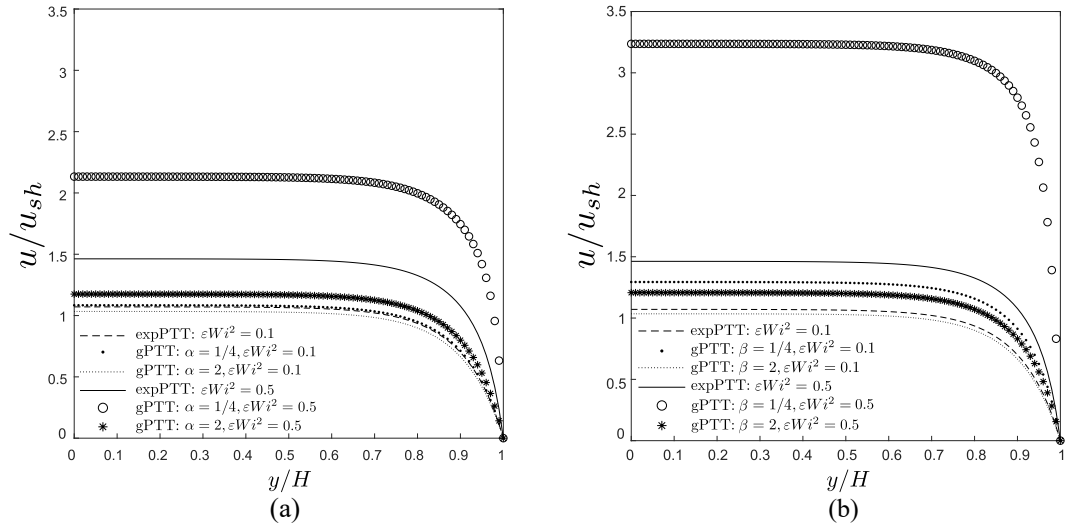


Figure 4.24: Velocity profiles calculated using Eq. (4.132) for the pure EO flow considering different values of ϵWi^2 and different values of α and β for $\bar{k} = 10$: (a) $\beta = 1$; (b) $\alpha = 1$. The velocity profiles were obtained from Eq. (4.132) and the cases for expPTT correspond to $\alpha = \beta = 1$.

the effect of α . Note that both α and β play a role contrary to ϵ in the classical PTT model, that is, decreasing α and β , which leads to an increase of the net rate of destruction of network junctions in the physical model of the polymer, the fluid becomes more thinning, reducing the friction between junctions [3]. The fact that β plays a stronger role on the thinning effect comes from the fact that the new function of the trace of the stress tensor presents higher numerical values for $\beta \ll 1$ when

the argument is smaller than ≈ 1 (the case of the EO flow presented here).

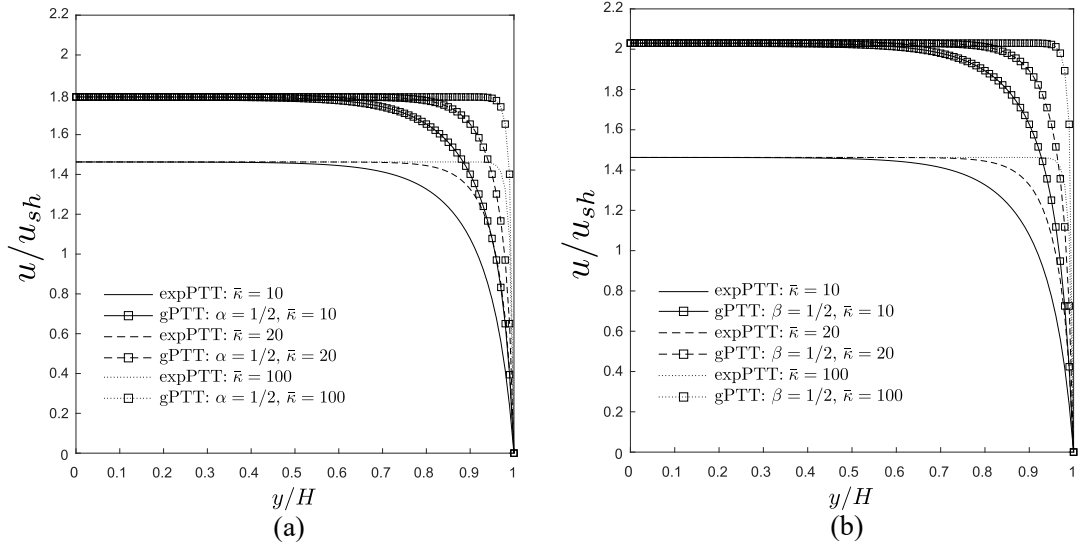


Figure 4.25: The effect of $\bar{\kappa}$ on transverse velocity profiles for EO at $\varepsilon Wi^2 = 0.5$: (a) $\beta = 1$; (b) $\alpha = 1$. The velocity profiles were obtained from Eq. (4.132) and the cases with expPTT correspond to $\alpha = \beta = 1$.

Fig. 4.25 compares transverse velocity profiles for the EO flow considering three different values of $\bar{\kappa}$, at fixed $\varepsilon Wi^2 = 0.5$: Fig. 4.25 (a) refers to fixed $\beta = 1$, and we observe the expected thinning of the EDL with increasing $\bar{\kappa}$. Similar trends are observed in Fig. 4.25 (b). The highest shear rates occur near the walls and in this region, the effects of α and β will be felt more strongly, as discussed in [3]. Smaller values of these parameters mean that the rate of destruction of junctions increases, that is, the friction between the molecules of the polymer solution decreases, leading to a less resistive flow (stronger shear-thinning). These effects are qualitatively similar to those observed with other shear-thinning fluids, even if quantitatively different. For a constant viscosity fluid, the ratio between the maximum velocity (taking place on the centre plane) and the Helmholtz-Smoluchowski velocity is 1, for high $\bar{\kappa}$, but on increasing shear-thinning effects, this ratio increases, as shown in Fig. 4.26 (a), (b) and Fig. 4.27.

4.4.4.2 Electro-osmotic–pressure driven flow

In the case of mixed EO/PD flows ($\Upsilon \neq 0$), Eq. (4.130) was integrated numerically using Simpson's Rule in MATLAB software (version R2018a). The influence of the new model on the velocity profile was assessed considering $\Upsilon = -1$ and $\Upsilon = 1$.

Fig. 4.28 shows velocity profiles obtained numerically for the EO+PD flow with $\Upsilon = -1$ and $\Upsilon = 1$, using the gPTT constitutive model. When $\alpha = 1$ and $\beta = 1$, the results match those presented in [52] for the exponential PTT model. Note that negative values of Υ correspond to a favourable pressure gradient, whereas $\Upsilon > 0$ corresponds to adverse pressure forcing. We can also see the effect of other independent dimensionless numbers on the transverse profile and the

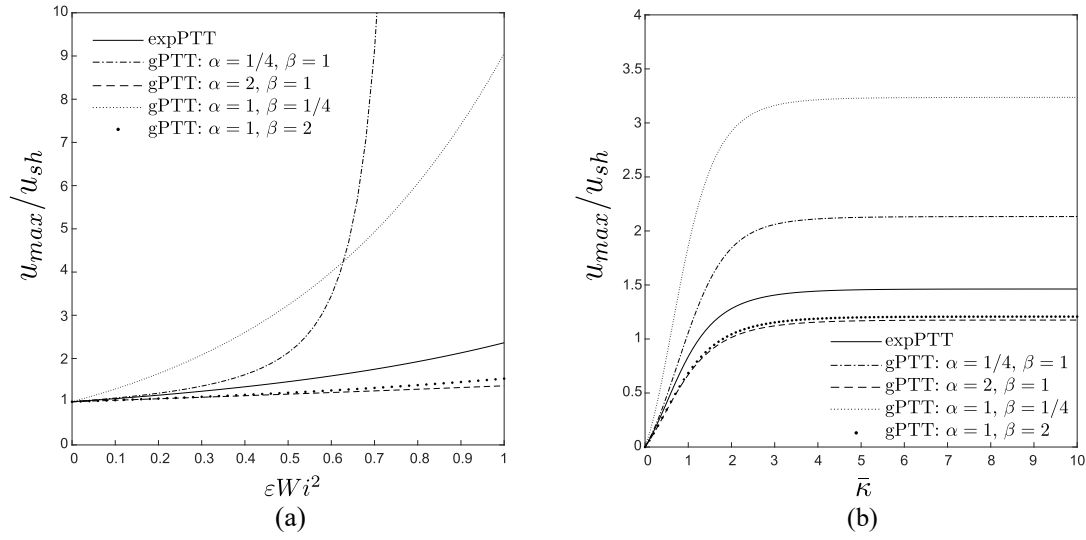


Figure 4.26: Ratio between maximum velocity and u_{sh} as a function of the relevant dimensionless numbers: (a) $\bar{\kappa} = 10$; (b) $\varepsilon Wi^2 = 0.5$. The velocities were obtained from Eq. (4.132) and the cases with expPTT correspond to $\alpha = \beta = 1$.

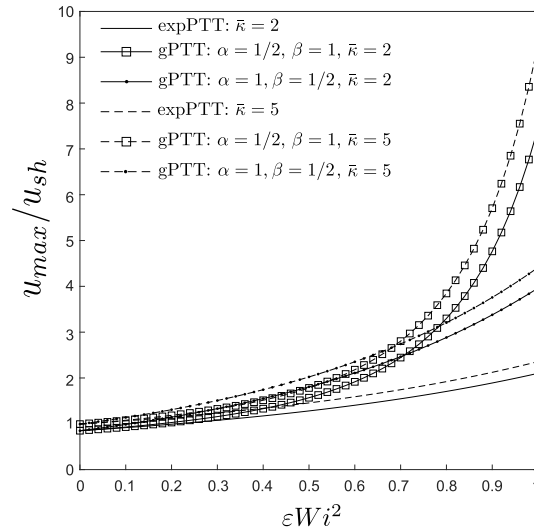


Figure 4.27: Ratio between maximum velocity and u_{sh} as a function of εWi^2 for different values of $\bar{\kappa}$, α and β . The velocities were obtained from Eq. (4.132) and the cases with expPTT correspond to $\alpha = \beta = 1$.

effect of parameters α and β in the velocity profiles. The quantities that previously increased the dimensionless flow rate in pure EO are also seen to increase the flow rate for EO+PD through enhanced shear-thinning effects, and in earlier works, much has been reported and discussed about other shear-thinning viscoelastic models (e.g., refer to [51] for the sPTT model, and to [65] for the PTT model).

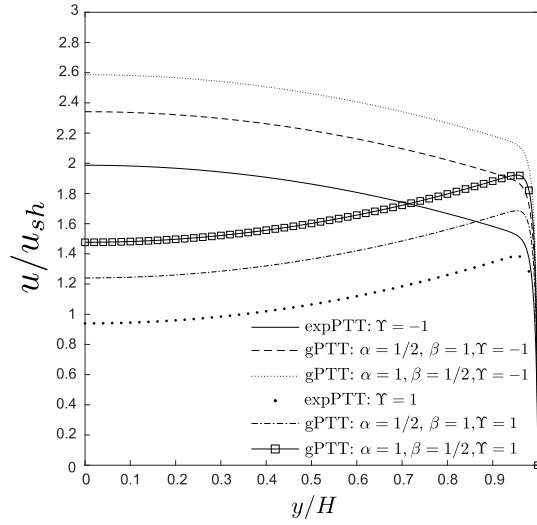


Figure 4.28: Velocity profiles obtained numerically for mixed EO/PD flow with $\Upsilon = -1$, $\Upsilon = 1$, $\bar{\kappa} = 100$ and $\varepsilon Wi^2 = 0.5$. The velocity profiles were obtained numerically using Eq. (4.130) and the cases expPTT correspond to $\alpha = \beta = 1$.

4.4.4.3 The influence of ξ on the flow stability and flow characteristics

For $\xi \neq 0$ a non-monotonic behaviour of the shear stress curve is obtained beyond a critical shear rate. By following the steps presented in [3, 65], one obtains the following formula for the critical shear rate (at the wall), $|\dot{\gamma}_c|$:

$$\lambda |\dot{\gamma}_c| = \frac{\Gamma(\beta)}{\sqrt{\xi(2-\xi)}} E_{\alpha,\beta} \left(\frac{\varepsilon(1-\xi)}{\xi(2-\xi)} \right), \quad (4.136)$$

which corresponds to a critical value of Wi given by

$$|Wi_c| = \frac{\coth(\bar{\kappa})}{2\sqrt{\xi(2-\xi)}}. \quad (4.137)$$

Above this limit, no physically admissible solution of Eq. (4.134) is obtained.

A comparison between the different stability formulae, obtained for the different functions of the trace of the stress tensor, is shown in [3].

To assess the influence of the coefficient ξ on the fluid flow, we will now compare the results obtained with the analytical solution for pure EO flow with the results obtained from the numerical integration of Eq. (4.135). The numerical results were obtained using Simpson's quadrature rule to approximate the integral. We will consider different values of Wi and ξ ranging from 0.001 to 0.1.

Fig. 4.29 shows the maximum velocity at the centre of channel as a function of the ξ , for pure EO flow with $\beta = 1$, $\alpha = 1/4$, $\bar{\kappa} = 10$ and $\varepsilon = 0.5$ and $Wi = 1$ and 0.5. The full line represents the solution obtained for $\xi = 0$ and the dashed line is a guide to the eye for the numerical solution. The inset shows the results obtained for $Wi = 0.5$.

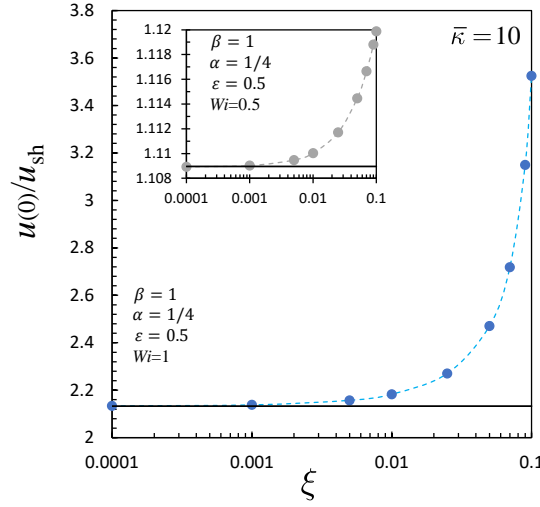


Figure 4.29: Maximum velocity at the channel centreplane as a function of the ξ parameter. Pure EO flow with $\beta = 1$, $\alpha = 1/4$, $\bar{\kappa} = 10$ and $\varepsilon = 0.5$ and $Wi = 1$ and 0.5 . The full line represents the asymptotic solution obtained for $\xi = 0$ (a constant value) and the dashed line is a guide to the eye for the numerical solution (represented by the symbols). The inset shows the results obtained for $Wi = 0.5$.

The influence of ξ on the maximum velocity increases Wi , non-linearly. Indeed, for $Wi = 1$, we obtain increases in the maximum velocity up to 65% when ξ increases from 10^{-3} to 10^{-1} , whereas for $Wi = 0.5$, the maximum velocity is only 1% higher. This difference is expected since Wi has a strong influence on the flow rate.

4.4.4.4 The Debye–Hückel approximation

In section 4.4.2, the Poisson–Boltzmann equation (4.119) was simplified assuming the Debye–Hückel approximation. Here, we consider a more general case, and write Eq. (4.119) in non-dimensional form as [107, 108]:

$$\frac{d^2 \bar{\psi}}{d\bar{y}^2} = \bar{\kappa}^2 \sinh(\bar{\psi}), \quad (4.138)$$

where $\bar{\psi} = [(ez)/(k_B T)] \psi$. Eq. (4.138) can be integrated assuming non-overlapping Debye layers valid for large $\bar{\kappa}$, and $\bar{\psi} = \bar{\psi}_0$ at $\bar{y} = 1$, leading to [107]:

$$\bar{\psi} = 4 \operatorname{arctanh} \left(\tanh(\bar{\psi}_0/4) e^{\bar{\kappa}(\bar{y}-1)} \right). \quad (4.139)$$

The corresponding velocity profile for $\xi = 0$ and pure EO flow can then be obtained by numerical integration using, for example, Simpson's rule. The velocity profile for $\bar{y} \in [0, 1]$ is given by

$$\bar{u}(\bar{y}) = \int_{\bar{y}}^1 \left(\frac{\Gamma(\beta)}{\bar{\psi}_0} \frac{4\bar{\kappa} \tanh\left(\frac{\bar{\psi}_0}{4}\right) e^{\bar{\kappa}(z-1)}}{1 - \tanh^2\left(\frac{\bar{\psi}_0}{4}\right) e^{2\bar{\kappa}(z-1)}} E_{\alpha,\beta} \left[\frac{32\varepsilon Wi^2}{\bar{\psi}_0^2} \left(\frac{\tanh\left(\frac{\bar{\psi}_0}{4}\right) e^{\bar{\kappa}(z-1)}}{1 - \tanh^2\left(\frac{\bar{\psi}_0}{4}\right) e^{2\bar{\kappa}(z-1)}} \right)^2 \right] \right) d\bar{z} \quad (4.140)$$

We now compare in Fig. 4.30 the velocity profiles for a pure EO flow considering the Debye–Hückel approximation and the full solution obtained by Eq. (4.140), using Simpson’s Rule.

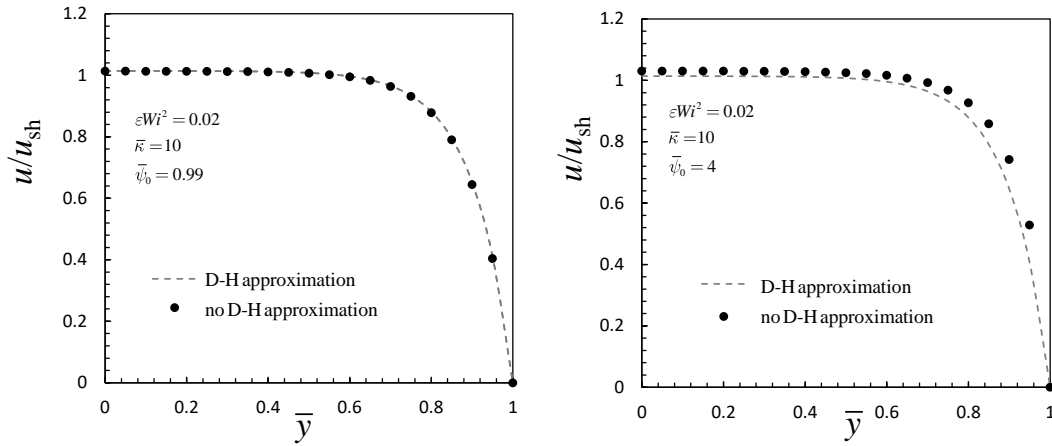


Figure 4.30: Comparison between velocity profiles for the exponential PTT model with $\bar{\kappa} = 10$ and $\varepsilon Wi^2 = 0.02$ for $\bar{\psi}_0 = 0.99$ and 4. Dashed line: solution obtained with the Debye–Hückel approximation; dots: solution obtained without the Debye–Hückel approximation (numerically solving Eq. (4.140)).

Fig. 4.30 shows the velocity profiles obtained for the exponential PTT model for $\bar{\psi}_0 = 0.99$ and 4. We consider the numerical solutions of Eq. (4.140) obtained with and without the Debye–Hückel approximation. It can be seen that for $\bar{\psi}_0 = 0.99$, the Debye–Hückel approximation is valid, while for $\bar{\psi}_0 = 4$, the two solutions become different, especially near the wall. Fig. 4.31 compares the velocity profiles obtained with both the exponential ($\alpha = 1, \beta = 1$) and gPTT models without invoking the Debye–Hückel approximation. The solutions were obtained by numerically integrating Eq. (4.140) with $\beta = 1, \alpha = \{1, 0.8, 0.5\}, \bar{\kappa} = 5$ and $\varepsilon Wi^2 = 0.2$. It is interesting to note that at low $\bar{\psi}_0$ the maximum velocity increases only 4% with the reduction of α whereas for higher $\bar{\psi}_0$, there is a 32% increase in the maximum velocity (in comparison with the exponential PTT model for $\alpha = \beta = 1$).

4.4.5 Conclusions

This work presented new analytical and semi-analytical solutions for electro-osmotic and mixed electro-osmotic/pressure-driven flows of a viscoelastic fluid modelled by the gPTT model, respec-

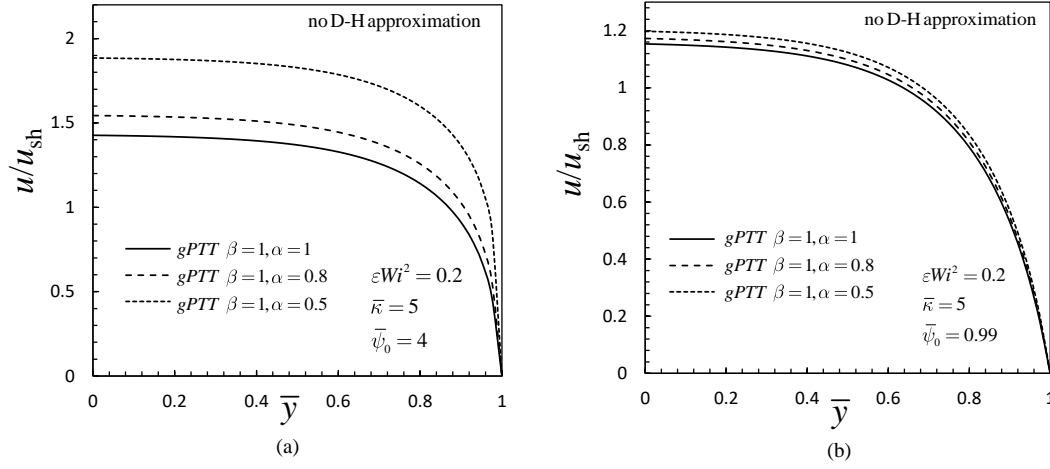


Figure 4.31: Velocity profiles obtained for both the exponential and gPTT models considering $\bar{\psi}_0 = 0.99$ and 4. Solutions obtained by numerically solving Eq. (4.140) with $\beta = 1$, $\alpha = 1, 0.8, 0.5$, $\bar{\kappa} = 5$ and $\varepsilon Wi^2 = 0.2$.

tively. From these solutions, the influence of the model parameters on the velocity profile was assessed. The new model allows a broader description of flow behaviour than the more classical descriptions, and therefore, it can be considered in modelling complex viscoelastic flows. Numerical solutions were also presented for high zeta potential. The analytical and numerical solutions presented in this work are helpful for validating CFD codes and also allow a better understanding of the model behaviour in simple shear flows.

Appendix A: Finite sized ionic species

The Boltzmann distribution breaks down when taking into account finite-sized ionic species. Therefore, a modified Poisson–Boltzmann equation for the ionic distribution that takes these effects into account leads to [107, 109, 110]:

$$\frac{d^2\psi}{dy^2} = \frac{2n_0ez}{\epsilon} \frac{\sinh\left(\frac{ez}{k_B T}\psi\right)}{1 - \Theta + \Theta \cosh\left(\frac{ez}{k_B T}\psi\right)}, \quad (4.141)$$

where Θ is the steric factor, representing the excluded volume effects owing to the finite size of the ionic species. This is a nonlinear differential equation, and in order to obtain the induced potential distribution, the procedure used in [107] was followed.

The shear rate can be obtained as a function of the zeta potential, recalling that $\tau_{xy} = \epsilon E_x \frac{d\psi}{dy}$ [107]. Considering Eq. (4.127) for $\xi = 0$, it leads to

$$\frac{d\bar{u}}{d\bar{y}} = \frac{-\Gamma(\beta)}{\bar{\psi}_0} \frac{d\bar{\psi}}{d\bar{y}} E_{\alpha,\beta} \left[\frac{2\varepsilon Wi^2}{\bar{\kappa}^2 \bar{\psi}_0^2} \left(\frac{d\bar{\psi}}{d\bar{y}} \right)^2 \right]. \quad (4.142)$$

For a low zeta potential, the size of the ionic species is negligible, the Debye–Hückel approximation applies and we obtain the solutions derived previously. For a high zeta potential [107, 108], Eq. (4.141) in non-dimensional form simplifies to

$$\frac{d^2\bar{\psi}}{d\bar{y}^2} = \frac{\bar{\kappa}^2 \sinh(\bar{\psi})}{1 - \Theta + \Theta \cosh(\bar{\psi})} \approx \frac{\bar{\kappa}^2}{\Theta} \quad (4.143)$$

which together with the boundary conditions $(d\bar{\psi}/d\bar{y})|_{\bar{y}=0} = 0$ and $\bar{\psi}(1) = \bar{\psi}_0$, lead to

$$\bar{\psi} = \bar{\psi}_0 + \frac{\bar{\kappa}^2(\bar{y}^2 - 1)}{2\Theta}. \quad (4.144)$$

The corresponding velocity profile can be obtained numerically, for example, using Simpson's Rule for $\bar{y} \in [0, 1]$:

$$\bar{u}(\bar{y}) = \int_{\bar{y}}^1 \frac{\Gamma(\beta)}{\bar{\psi}_0} \frac{\bar{\kappa}^2 z}{\Theta} E_{\alpha,\beta} \left[\frac{2\varepsilon Wi^2}{\bar{\psi}_0^2} \left(\frac{\bar{\kappa} z}{\Theta} \right)^2 \right] d\bar{z} \quad (4.145)$$

The higher the steric factor, the lower the induced transverse EDL field will be, and a lower volumetric flow rate will be obtained. This effect is shown in Fig. 4.32, where the velocity profiles for both the exponential and gPTT models are plotted (considering $\Theta = 0.2$ and 0.25 and a high zeta potential $\bar{\psi}_0 = 4$).

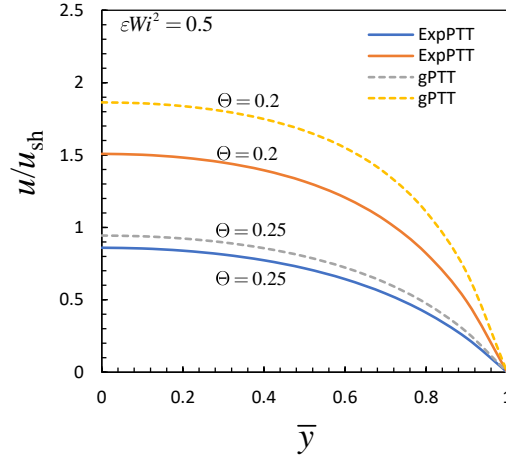


Figure 4.32: Velocity profiles for both the exponential and gPTT models considering $\Theta = 0.2$ and 0.25 and a high zeta potential ($\bar{\psi}_0 = 4$). Dashed line: pure EO flow with $\beta = 1$, $\alpha = 0.8$; full line: pure EO flow with $\beta = 1$, $\alpha = 0.8$. $\bar{\kappa} = 1$ and $\varepsilon Wi^2 = 0.5$.

As expected, the gPTT model allows one to obtain a higher flow rate due to the higher rate of destruction of junctions in the polymer entanglements when α decreases. Note also the non-linear increase of the flow rate with decreasing α at constant Θ , showing the complex interaction between the rate of destruction of junctions and the steric effect.

4.5 The effect of asymmetric zeta potentials on the electro-osmotic flow of complex fluids⁵

Abstract: Electrokinetic flows driven by electro-osmotic forces are especially relevant in micro and nano-devices, presenting specific applications in medicine, biochemistry, and miniaturized industrial processes. In this work, we integrate analytical solutions with numerical methodologies to explore the fluid dynamics of viscoelastic electro-osmotic/pressure driven fluid flows (described by the generalised Phan-Thien-Tanner constitutive equation) in a micro-channel under asymmetric zeta potential conditions. The constitutive equation incorporates the Mittag-Leffler function with two parameters (α and β), which regulate the rate of destruction of junctions in a network model. We analyze the impact of the various model parameters on the velocity profile and observe that our newly proposed model provides a more comprehensive depiction of flow behavior compared to traditional models, rendering it suitable for modeling complex viscoelastic flows.

Keywords: gPTT model, Mittag-Leffler function, eletro-osmotic flow under asymmetric zeta potential, analytical solutions

4.5.1 Introduction

Electro-osmosis is a flow-forcing method with particular applicability in medicine, biochemistry and miniaturised industrial processes, being suitable for flows in micro and nano-devices. In this type of flow, an external potential difference between the inlet and outlet of the channel induces the flow of an electrolyte. This potential difference acts on the ions that are not balanced near the wall region, because of the interaction between the dielectric channel walls and the fluid. Since these fluid layers have a higher concentration of counter-ions (ions with the opposite charge of the wall) this fluid will move by the action of the applied electric field, which then drags by viscous forces, the neutral core as a solid body [41]. This subject has undergone thorough examination in the past, firts regarding Newtonian fluids [42–49] and more recently non-Newtonian fluids [50–57, 65, 111].

This study focuses on investigating the electro-osmotic (EO) flow of viscoelastic fluids within microchannels, particularly under the influence of asymmetric zeta potentials at the channel walls. Asymmetric zeta potentials may arise in various manufacturing techniques due to the use of different materials at distinct walls [58], such as materials with differing dielectric properties. For instance, in soft lithography, microchannels are often made of polydimethylsiloxane (PDMS), while the top wall is typically constructed from glass for optical access or another material for a different purpose [58].

⁵A.M. Ribau, L.L. Ferrás, M.L. Morgado, M. Rebelo, F.T. Pinho, and A.M. Afonso. The effect of asymmetric zeta potentials on the electro-osmotic flow of complex fluids. Submitted to *Journal of Engineering Mathematics*.

Given the significance of this topic, it is crucial to reference relevant literature where the influence of asymmetric zeta potentials has already been explored.

For instance, Afonso et al. (2011) [58] provided insightful analytical solutions for combined EO and pressure-driven flows of viscoelastic fluids under asymmetric zeta potentials at the channel walls. The viscoelastic fluids analyzed were described by the linear Phan-Thien–Tanner (PTT) model and the finite extensible nonlinear elastic model with Peterlin's (FENE-P) approximation. Escandón et al. (2015) [59] presented both analytical and numerical solutions for transient EO flows in microchannels. Their study encompassed symmetric and asymmetric uniform zeta potentials and concerned with Maxwell fluids which are devoid of a variable viscosity that may be important for high rates of shear.

Sadek and Pinho (2019) [60] contributed with analytical solutions for the oscillatory shear flow of viscoelastic fluids induced by EO forcing. They specifically explored the case of a straight microchannel with asymmetric wall zeta potentials for the purpose of measuring linear viscoelastic fluid properties, hence their rheological model was the multi-mode upper-convected Maxwell model. Their analysis investigated the impact of relevant dimensionless parameters on normalized velocity profiles when an external potential field was applied.

Sanchez et al. (2023) [61] obtained analytical solutions for an electrokinetic battery comprising parallel plates, driven by osmotic flow. Their work involved the use of the Debye–Hückel approximation to calculate the electric double layer (EDL) potential coupled with asymmetric hydrodynamic slip. The authors explicitly addressed asymmetries both in the Navier slip lengths and zeta potentials, providing insights into the interplay of these boundary conditions.

In our current investigation, the focus is on the application of the gPTT model, incorporating the Mittag-Leffler function as a function of the trace of the stress tensor. This model introduces two fitting constants, enhancing its capability to describe the rheological properties of viscoelastic fluids [3]. Initially explored in Couette and pressure-driven flows, as well as combined EO/pressure-driven and annular flows (refer to [28, 29, 40, 56]), the gPTT model has been recently scrutinized in studies addressing EO flow.

Teodoro et al. [62] derived an approximate and a numerical solution for laminar viscoelastic fluid flow through a parallel flat plate microchannel driven by EO and external pressure forces. Their approach incorporates a nonlinear Navier slip law at the wall, depicting a power-law behavior on shear stress. The Debye–Hückel approximation for the electric potential in the EDL is applied, assuming symmetric zeta potentials at the wall. Additionally, Hernandez et al. [63] investigated numerically the EO flow in a microchannel with a viscoelastic fluid, using the gPTT model as a constitutive equation to explore the thermodiffusion effect, comparing results with those obtained through the linear PTT model [64].

In this study, we develop a new semi-analytical solution for the EO flow of viscoelastic fluids (described by gPTT constitutive equation) in microchannels, under asymmetric wall zeta potentials. Our investigation explores the influence of both pure EO and the combined effects of forces (EO and pressure gradient) in the fluid flow, taking into account the fluid rheology, the EDL thickness, and the ratio of wall zeta potentials. These findings, together with the developed analytical solutions,

provide valuable insights for industries involved in this field. Furthermore, the obtained results can be used as effective tools for validating Computational Fluid Dynamics (CFD) codes.

The remainder of this paper is organized as follows: the next section presents the governing equations, followed by the new semi-analytical solution in section 4.5.3, the discussion of the results in section 4.5.4 and the closure of the paper in section 4.5.5.

4.5.2 Governing equations

The equations governing the flow of an isothermal incompressible fluid are the continuity equation

$$\nabla \cdot \mathbf{u} = 0, \quad (4.146)$$

and the linear momentum equation

$$\rho \frac{D\mathbf{u}}{Dt} = -\nabla p + \nabla \cdot \boldsymbol{\tau} + \rho_e \mathbf{E} \quad (4.147)$$

where \mathbf{u} is the velocity vector, $\frac{D}{Dt}$ is the material derivative, p is the pressure, t is the time, ρ is the fluid density, $\boldsymbol{\tau}$ is the extra-stress tensor, \mathbf{E} is the electric field and ρ_e is the electric charge density in the fluid.

The EO flow in a microchannel under asymmetric zeta potentials of a viscoelastic gPTT fluid is shown in Fig. 4.33, where x , y and z , represent the streamwise, transverse and spanwise directions, respectively, and the channel width is $2H$. We assume the flow within the channel to be fully-developed, E_x is the applied external electric field in the streamwise direction and ρ_e is associated with the spontaneously formed electric double layers, that in here are assumed not to be affected by the imposed electric field.

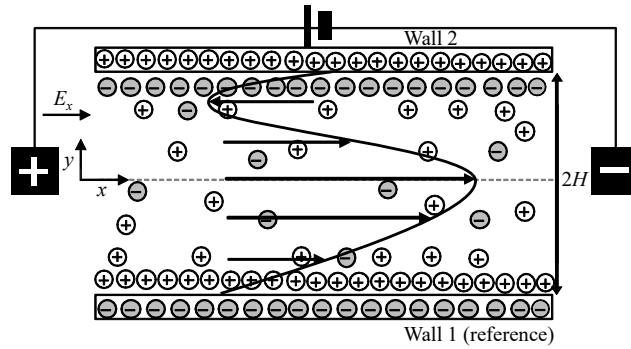


Figure 4.33: Schematic of the flow in a parallel plate microchannel.

The electric field is related to a potential, Φ , by $\mathbf{E} = -\nabla\Phi$, where $\Phi = \psi + \phi$, where ϕ is the applied streamwise potential and ψ is the equilibrium induced potential at the channel walls, that is associated with the interaction between the ions of the fluid and the dielectric properties of the wall. The induced potential ψ can be assumed independent of the applied potential ϕ provided the latter is not too strong [65]. At the walls, the no-slip condition is applied and also asymmetric

zeta potentials are considered. Since the flow is fully-developed, the velocity and stress fields only depend on the transverse coordinate y [58].

4.5.2.1 Constitutive equation

To obtain a closed system of equations, a constitutive equation for the extra-stress tensor, $\boldsymbol{\tau}$, must be defined. In 2019 Ferrás et al. [3] proposed a new differential rheological model based on the Phan-Thien–Tanner constitutive equation (PTT model [21, 22]), derived from the Lodge–Yamamoto type of network theory for polymeric fluids. The new model considers a more general function for the rate of destruction of junctions, the Mittag-Leffler function, where two fitting coefficients are included, in order to achieve additional fitting flexibility [3].

The Mittag–Leffler function is given by,

$$E_{\alpha,\beta}(z) = \sum_{j=0}^{\infty} \frac{z^j}{\Gamma(\alpha j + \beta)}, \quad (4.148)$$

with the Gamma function ($\Gamma(\cdot)$) defined by $\Gamma(t) = \int_0^{\infty} x^{t-1} e^{-x} dx$, where α, β are real and positive values. When $\alpha = \beta = 1$, the Mittag-Leffler function reduces to the exponential function, and when $\beta = 1$ the original one-parameter Mittag-Leffler function, E_{α} is obtained [4].

The gPTT constitutive equation is given by:

$$K(\tau_{kk})\boldsymbol{\tau} + \lambda \overset{\nabla}{\boldsymbol{\tau}} = 2\eta_p \mathbf{D}, \quad (4.149)$$

where τ_{kk} is the trace of the extra stress tensor, λ is the relaxation time, η_p is the polymeric viscosity coefficient, \mathbf{D} is the rate of deformation tensor and the function $K(\tau_{kk})$ is given by:

$$K(\tau_{kk}) = \Gamma(\beta) E_{\alpha,\beta} \left(\frac{\varepsilon \lambda}{\eta_p} \tau_{kk} \right). \quad (4.150)$$

The normalization $\Gamma(\beta)$ is used to ensure that $K(0) = 1$ (for all choices of β) and ε represents the extensibility parameter. $\overset{\nabla}{\boldsymbol{\tau}}$ represents the upper-convected derivative, defined as

$$\overset{\nabla}{\boldsymbol{\tau}} = \frac{\partial \boldsymbol{\tau}}{\partial t} + \mathbf{u} \cdot \nabla \boldsymbol{\tau} - (\nabla \mathbf{u})^T \cdot \boldsymbol{\tau} - \boldsymbol{\tau} \cdot (\nabla \mathbf{u}), \quad (4.151)$$

where $\nabla \mathbf{u}$ is the velocity gradient.

4.5.2.2 Electric potential

When a liquid comes into contact with a dielectric surface, the interactions between the ions and the wall lead to a spontaneous charge distribution within both the fluid and the wall. The wall becomes charged, attracting counter-ions from the fluid while repelling co-ions. Consequently, an electrically charged layer forms in the fluid in close proximity to the wall, known as the electric

double layer (EDL). For more details see [41]. The induced potential field within the EDL, can be given by a Poisson equation:

$$\nabla^2 \psi = -\frac{\rho_e}{\epsilon}, \quad (4.152)$$

where ψ denotes the EDL potential and ϵ is the dielectric constant of the solution. For fully-developed steady flow, this simplifies to:

$$\frac{d^2 \psi}{dy^2} = -\frac{\rho_e}{\epsilon}. \quad (4.153)$$

The net electric-charge density in the fluid, ρ_e , can be given by the Boltzmann distribution:

$$\rho_e = -2n_0 e z \sinh\left(\frac{e z}{k_B T} \psi\right), \quad (4.154)$$

where n_0 is the ion density, e the elementary charge, z the valence of the ions, T the absolute temperature and k_B the Boltzmann constant. Combining this with Eq. (4.153) for the induced potential equation leads to the Poisson-Boltzmann equation:

$$\frac{d^2 \psi}{dy^2} = \frac{2n_0 e z}{\epsilon} \sinh\left(\frac{e z}{k_B T} \psi\right). \quad (4.155)$$

Assuming the Debye-Hückel linearization principle, a valid approximation for small values of ψ [51, 52, 56, 58], the Poisson-Boltzmann equation (Eq. (4.155)) for the, 2D channel flow simplifies to

$$\frac{d^2 \psi}{dy^2} = \kappa^2 \psi, \quad (4.156)$$

where $\kappa^2 = 2n_0 e^2 z^2 / \epsilon k_B T$ is the Debye-Hückel parameter, which is related to the thickness of the Debye layer, $\lambda_D = 1/\kappa$, also called the EDL thickness.

Integrating Eq. (4.156) together with the boundary conditions for different zeta potential at the walls, specifically $\psi(-H) = \xi_1$ and $\psi(H) = \xi_2$, leads to the following induced electric field, ψ :

$$\psi(y) = \xi_1 (\Psi_1 e^{\kappa y} - \Psi_2 e^{-\kappa y}) \quad (4.157)$$

with $\Psi_1 = \frac{R_\xi e^{\kappa H} - e^{-\kappa H}}{2 \sinh(2\kappa H)}$ and $\Psi_2 = \frac{R_\xi e^{-\kappa H} - e^{\kappa H}}{2 \sinh(2\kappa H)}$, where $R_\xi = \frac{\xi_2}{\xi_1}$ denotes the ratio of zeta potentials of the two walls. This equation is valid for $-H \leq y \leq H$, and when $R_\xi = 1$, the symmetric potential profile is recovered [51, 56].

With the induced potential, the electric charge density, ρ_e (Eq. (4.154) with the Debye-Hückel linearization principle) becomes

$$\rho_e = -\epsilon \kappa^2 \xi_1 (\Psi_1 e^{\kappa y} - \Psi_2 e^{-\kappa y}) = -\epsilon \kappa^2 \xi_1 \Omega^-(y). \quad (4.158)$$

where the operator $\Omega^\pm(y) = \Psi_1 e^{\kappa y} \pm \Psi_2 e^{-\kappa y}$ is a hyperbolic function of the transverse variable y which depends on the ratio of zeta potentials and the thickness of the Debye layer.

4.5.3 Semi-analytical solution for the EO flow of a gPTT fluid under asymmetric zeta potentials

We derive the analytical solution considering a fully-developed flow for EO of a gPTT fluid under asymmetric zeta potentials (cf. Fig. 4.33). The momentum equation, Eq. (4.147), simplifies to

$$\frac{d\tau_{xy}}{dy} = P_x - \rho_e E_x, \quad (4.159)$$

where $P_x \equiv \frac{dp}{dx}$ is a constant streamwise pressure gradient, τ_{xy} the shear stress and $E_x \equiv -\frac{d\phi}{dx}$ is the imposed constant streamwise gradient of electric potential. This equation is valid regardless of the rheological constitutive equation considered.

In spite of this simplification, the rheological model is capable to fit well the shear-thinning viscosity as well as normal stress. The model parameters can control the thinning rate and the onset of the thinning behavior and also improve the fitting for shear (weak) flows, when considering polymer solutions.

So, the constitutive equation for the gPTT model for this flow (section 4.5.2.1) can be further simplified, leading to:

$$K(\tau_{kk})\tau_{xx} = 2\lambda\dot{\gamma}\tau_{xy}, \quad (4.160)$$

$$K(\tau_{kk})\tau_{yy} = 0, \quad (4.161)$$

$$K(\tau_{kk})\tau_{xy} = \eta_p\dot{\gamma}, \quad (4.162)$$

where the velocity gradient $\dot{\gamma}$ is a function of y ($\dot{\gamma}(y) \equiv \frac{du}{dy}$) and $\tau_{kk} = \tau_{xx} + \tau_{yy} + \tau_{zz}$ is the trace of the extra stress tensor. Under fully-developed flow conditions, $\tau_{zz} = 0$, thus the trace of the extra stress tensor becomes $\tau_{kk} = \tau_{xx}$.

Using Eq. (4.158), we can now integrate Eq. (4.159) resulting in the following shear stress distribution:

$$\tau_{xy} = \epsilon\kappa\xi_1 E_x \Omega^+(y) + P_x y + c_1, \quad (4.163)$$

where c_1 is a shear-stress integration constant, obtained later from the boundary conditions.

Dividing Eq. (4.160) by Eq. (4.162), $K(\tau_{xx})$ cancels out, and an explicit relationship between the streamwise normal stress and the shear stress is found:

$$\tau_{xx} = 2\frac{\lambda}{\eta_p}\tau_{xy}^2. \quad (4.164)$$

Now combining Eqs. (4.162), (4.164), (4.163) and (4.150) the following velocity gradient profile is obtained,

$$\dot{\gamma}(y) = \frac{\Gamma(\beta)}{\eta_p} E_{\alpha,\beta} \left(\frac{2\varepsilon\lambda^2}{\eta_p^2} (\epsilon\kappa\xi_1 E_x \Omega^+(y) + P_x y + c_1)^2 \right) (\epsilon\kappa\xi_1 E_x \Omega^+(y) + P_x y + c_1), \quad (4.165)$$

which can be rewritten in dimensionless form as

$$\frac{d\bar{u}}{d\bar{y}} = \Gamma(\beta) E_{\alpha,\beta} \left(\frac{2\varepsilon Wi^2}{\bar{\kappa}^2} \left(Y\bar{y} - \bar{\kappa} \bar{\Omega}^+(\bar{y}) + \bar{\tau}_1 \right)^2 \right) \left(Y\bar{y} - \bar{\kappa} \bar{\Omega}^+(\bar{y}) + \bar{\tau}_1 \right), \quad (4.166)$$

where $Wi = \lambda\kappa u_{sh}$ is the Weissenberg number and u_{sh} is the Helmholtz-Smoluchowski EO velocity, defined as $u_{sh} = -\frac{\epsilon\xi_1 E_x}{\eta_p}$, $\bar{u} = \frac{u}{u_{sh}}$, $\bar{y} = \frac{y}{H}$, $\bar{\kappa} = \kappa H$ and $\bar{\tau}_1 = \frac{\tau_1 H}{u_{sh}}$ ($\tau_1 = c_1/\eta_p$). The non-dimensional parameter $Y = -\frac{H^2 P_x}{\epsilon\xi_1 E_x}$ represents the ratio of pressure to EO driving forces and $\bar{\Omega}^+(\bar{y}) = \bar{\Psi}_1 e^{\bar{\kappa}\bar{y}} + \bar{\Psi}_2 e^{-\bar{\kappa}\bar{y}}$, with $\bar{\Psi}_1 = \frac{R_\xi e^{\bar{\kappa}} - e^{-\bar{\kappa}}}{2\sinh(2\bar{\kappa})}$ and $\bar{\Psi}_2 = \frac{R_\xi e^{-\bar{\kappa}} - e^{\bar{\kappa}}}{2\sinh(2\bar{\kappa})}$.

For pure EO flow, $Y = 0$, the velocity profile can be obtained by integrating the velocity gradient profile (Eq. (4.166)), subjected to the no-slip boundary condition at the top (+) or bottom (-) walls, $\bar{u}(\bar{y} = \pm 1) = 0$. Simplifying Eq. (4.166) we obtain,

$$\bar{u}(\bar{y}) = \Gamma(\beta) \sum_{j=0}^{\infty} \left(\frac{2\varepsilon Wi^2}{\bar{\kappa}^2} \right)^j \frac{1}{\Gamma(\alpha j + \beta)} \left(\int_{-1}^{\bar{y}} \left(-\bar{\kappa} \bar{\Omega}^+(\bar{z}) + \bar{\tau}_1 \right)^{2j+1} d\bar{z} \right), \quad (4.167)$$

with z a dummy variable.

Following some algebraic manipulations, Eq. (4.167) can be further simplified, resulting in the subsequent nested sum expression for the velocity profile,

$$\bar{u}(\bar{y}) = \Gamma(\beta) \left(\sum_{j=0}^{\infty} \frac{2\varepsilon Wi^2}{\bar{\kappa}^2 (\Gamma(\alpha j + \beta))} \left[\sum_{m=0}^{2j+1} \binom{2j+1}{m} (\bar{\tau}_1)^m \left\{ \sum_{i=0}^{2j+1-m} \binom{2j+1-m}{i} \frac{(-\bar{\kappa} \bar{\Psi}_1)^{2j-m-i+1} (-\bar{\kappa} \bar{\Psi}_2)^i}{\bar{\kappa} (2j-2i-m+1)} e^{(2j-2i-m+1)\bar{\kappa}\bar{y}} \right\} \right] \right) + c_2, \quad (4.168)$$

with c_2 obtained using $\bar{u}(1) = 0$, and being given by,

$$c_2 = -\Gamma(\beta) \left(\sum_{j=0}^{\infty} \frac{2\varepsilon Wi^2}{\bar{\kappa}^2 (\Gamma(\alpha j + \beta))} \left[\sum_{m=0}^{2j+1} \binom{2j+1}{m} (\bar{\tau}_1)^m \left\{ \sum_{i=0}^{2j+1-m} \binom{2j+1-m}{i} \frac{(-\bar{\kappa} \bar{\Psi}_1)^{2j-m-i+1} (-\bar{\kappa} \bar{\Psi}_2)^i}{\bar{\kappa} (2j-2i-m+1)} e^{(2j-2i-m+1)\bar{\kappa}} \right\} \right] \right). \quad (4.169)$$

$\bar{\tau}_1$ is obtained by solving numerically $\bar{u}(-1) = 0$.

4.5.4 Results and discussion

4.5.4.1 Assessment of the series solution

In this section, we compare the numerical solution of the velocity profile given by of Eq. (4.167) (obtained by a numerical quadrature rule, and referred to as *numerical solution*), with the analytical solution obtained by Eq. (4.168). The numerical results were obtained using the *Mathematica* software.

For the *numerical solution*, we first obtain $\bar{\tau}_1$ using the secant method to find the root of,

$$\Gamma(\beta) \sum_{j=0}^{\infty} \left(\frac{2\varepsilon Wi^2}{\bar{\kappa}^2} \right)^j \frac{1}{\Gamma(\alpha j + \beta)} \left(\int_{-1}^1 \left(-\bar{\kappa} \bar{\Omega}^+ (\bar{z}) + \bar{\tau}_1 \right)^{2j+1} d\bar{z} \right) = 0. \quad (4.170)$$

The $\bar{\tau}_1$ value obtained is then substituted in Eq. (4.167), and the numerical velocity profile is finally obtained.

The analytical solution given by Eq. (4.168) is composed by an infinite series. Therefore, we need to access the number of terms required in the series to achieve a precise and accurate solution. To do this, we used as a reference the *numerical solution*.

The new truncated solution is obtained from Eq. (4.168), truncating the sum with $j + 1$ terms. To validate the solution it was considered 201 equidistant mesh points along the channel height ($2H$) and measured the root mean squared error (RMSE) obtained at these points. The error is calculated by,

$$RMSE = \sqrt{\frac{1}{n} \sum_{i=1}^n (\bar{u}(\bar{y})_{num} - u(\bar{y})_t)^2},$$

where $\bar{u}(\bar{y})_{num}$ is the numerical value of the velocity and $\bar{u}(\bar{y})_t$ is the velocity value for the truncated series. Three different values of εWi^2 were considered: 0.5, 1 and 2 and two different values for R_ξ : -1 and 0.5 . We set $\beta = 1$ and tested two different values of α , 0.5 and 1.5 . We only change the values of α , because this parameter is the most sensitive to changes in the series.

Table 4.4: RMSE (in percentage) for $\varepsilon Wi^2 = 0.5$ and $\alpha = 0.5$.

j	$R_\xi = 0.5$	$R_\xi = -1$
2	8.834×10^0	5.197×10^0
4	1.819×10^0	8.889×10^{-1}
8	4.78×10^{-2}	1.597×10^{-2}
16	2.207×10^{-4}	1.472×10^{-4}

Tables 4.4, 4.5, 4.6 show the RMSE, in percentage, for $\varepsilon Wi^2 = 0.5$, 1 and 2 respectively, and considering $\alpha = 0.5$, $R_\xi = 0.5$ and -1 . As the number of terms in the series (Eq. (4.168)) increase, the error decreases. This parametric study provides insights into the behavior of the truncated solution. For instance, as εWi^2 increases (refer to Table 4.5 and 4.6), and with $R_\xi = 0.5$, the series

Table 4.5: RMSE (in percentage) for $\varepsilon Wi^2 = 1$ and $\alpha = 0.5$.

j	$R_\xi = 0.5$	$R_\xi = -1$
2	1.038×10^2	4.550×10^1
4	5.23×10^1	1.889×10^1
8	9.679×10^0	2.433×10^0
16	1.092×10^{-1}	1.198×10^{-2}
20	6.757×10^{-3}	5.342×10^{-4}

Table 4.6: RMSE (in percentage) for $\varepsilon Wi^2 = 2$ and $\alpha = 0.5$.

j	$R_\xi = 0.5$	$R_\xi = -1$
2	1.503×10^3	2.660×10^2
4	1.226×10^3	1.585×10^2
8	6.571×10^2	4.63×10^1
16	7.132×10^1	2.118×10^0
20	1.546×10^1	3.042×10^{-1}

solution exhibits slower convergence. On the other hand, for lower εWi^2 values, the series solution converges much more rapidly.

Table 4.7 show the RMSE in percentage, for $\varepsilon Wi^2 = 2$, $\alpha = 1.5$ and considering $R_\xi = 0.5$ and -1 . Notably, as α increases, the error decreases more rapidly with an increase in the number of terms in the series (even for high values of εWi^2). We experimented with a higher number of terms in the series for cases with high εWi^2 and low α , and found that a favorable balance between computation time, simplicity, and solution accuracy could be achieved for $j = 20$.

Table 4.7: RMSE (in percentage) for $\varepsilon Wi^2 = 2$ and $\alpha = 1.5$.

j	$R_\xi = 0.5$	$R_\xi = -1$
2	7.898×10^0	4.268×10^0
4	2.231×10^{-1}	9.7×10^{-2}
8	2.635×10^{-4}	1.927×10^{-4}

The velocity profiles obtained by the *numerical solution* of Eq. (4.167) and the analytical solution obtained by Eq. (4.168) for different j are shown in Figures 4.34 and 4.35, where u/u_{sh} is the normalised velocity profile. These particular results indicate that the velocity profile converges to the correct profile as the number of terms in the series increases, and that this convergence is slower for lower values of α .

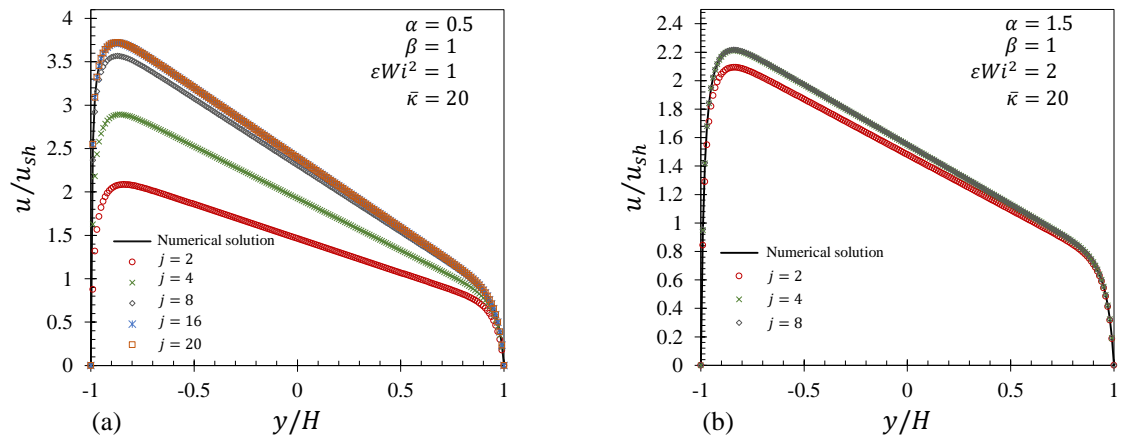


Figure 4.34: Velocity profiles for $\beta = 1$, $R_\xi = 0.5$ and $\bar{\kappa} = 20$. (a) $\alpha = 0.5$, $\epsilon Wi^2 = 1$; (b) $\alpha = 1.5$, $\epsilon Wi^2 = 2$.

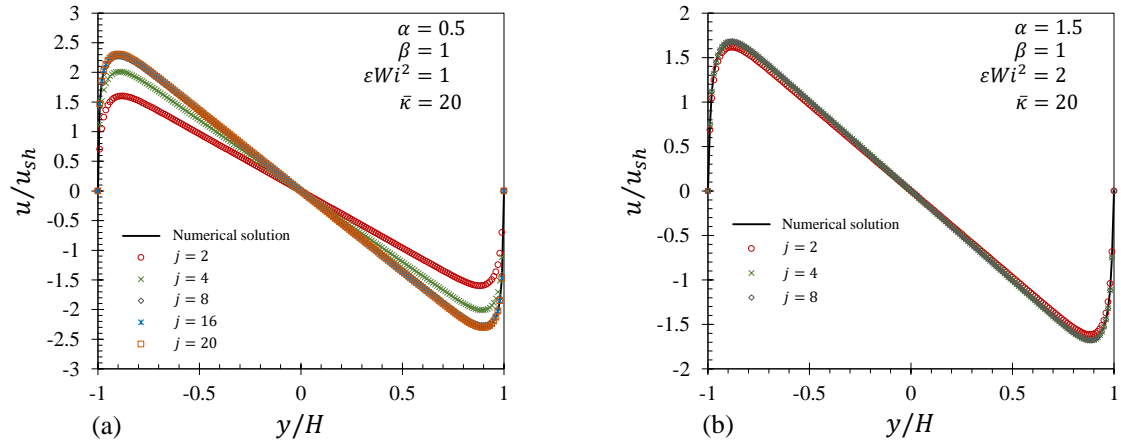


Figure 4.35: Velocity profiles for $\beta = 1$, $R_\xi = -1$ and $\bar{\kappa} = 20$. (a) $\alpha = 0.5$, $\epsilon Wi^2 = 1$; (b) $\alpha = 1.5$, $\epsilon Wi^2 = 2$.

4.5.4.2 Discussion

4.5.4.2.1 Pure EO and asymmetric zeta potentials

In this section, we explore the impact of the Mittag-Leffler function parameters, α and β , on the distribution of the velocity profile under pure EO driving forces (across the channel). We consider different values of ϵWi^2 and R_ξ , allowing for a comparison of results with those obtained for the exponential PTT model.

Fig. 4.36 compares the velocity profiles obtained for EO flow under asymmetric zeta potentials considering two different ϵWi^2 values and different values of α (Fig. 4.36 (a)) and β (Fig. 4.36 (b)) for $\bar{\kappa} = 20$ and $R_\xi = 0.5$.

In Fig. 4.36 (a) ($\beta = 1$), we observe that for increasing ϵWi^2 and decreasing α the flow rate increases, leading to an increase of the *skewed pluglike* profile. In Fig. 4.36 (b) ($\alpha = 1$), a similar

qualitative behaviour is obtained, i.e., increasing εWi^2 and decreasing β , the flow rate increases. However, there are quantitative differences with the effect of α being stronger than the effect of β .

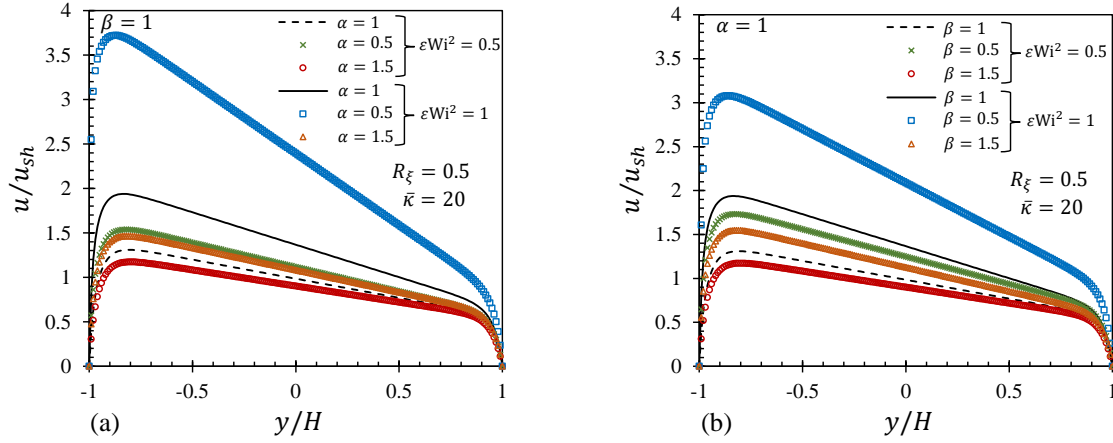


Figure 4.36: Velocity profiles for $R_\xi = 0.5$, $\bar{\kappa} = 20$ and $\varepsilon Wi^2 = 0.5, 1$ (a) $\beta = 1$, $\alpha = 0.5, 1, 1.5$; (b) $\alpha = 1$, $\beta = 0.5, 1, 1.5$.

Fig. 4.37 compares the velocity profiles obtained for EO flow under asymmetric zeta potentials considering two different εWi^2 values and different values of α (Fig. 4.37 (a)) and β (Fig. 4.37 (b)) at $\bar{\kappa} = 20$ and $R_\xi = -1$.

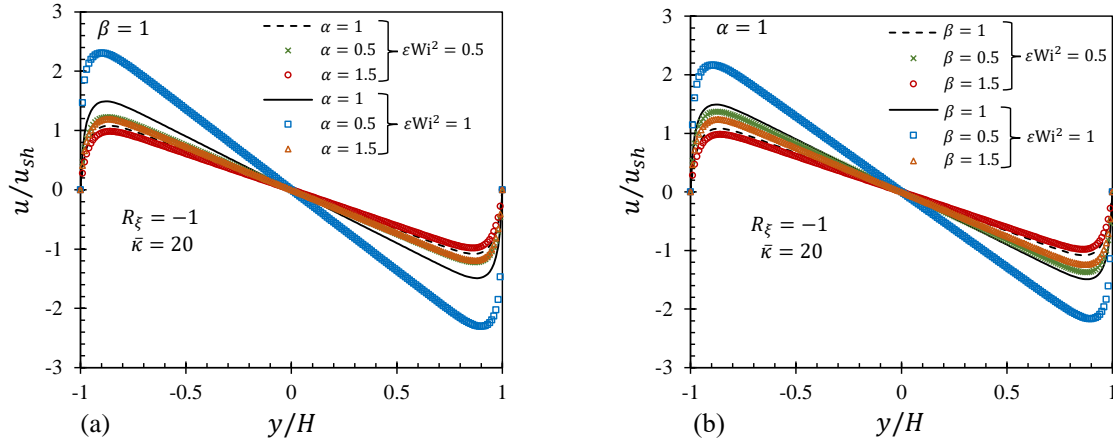


Figure 4.37: Velocity profiles for $R_\xi = -1$, $\bar{\kappa} = 20$ and $\varepsilon Wi^2 = 0.5, 1$ (a) $\beta = 1$, $\alpha = 0.5, 1, 1.5$; (b) $\alpha = 1$, $\beta = 0.5, 1, 1.5$.

In Fig. 4.37 (a) ($\beta = 1$), we observe that for increasing εWi^2 and decreasing α the flow rate increases, leading to an increase of an *anti-symmetric pluglike* profile. In Fig. 4.37 (b) ($\alpha = 1$) a similar qualitative behaviour is obtained, i.e., on increasing εWi^2 and decreasing β , the flow rate increases. However, there are quantitative differences with the effect of α being stronger than the effect of β . The pronounced flow with the increasing of εWi^2 is associated with the shear-thinning behaviour of the fluid.

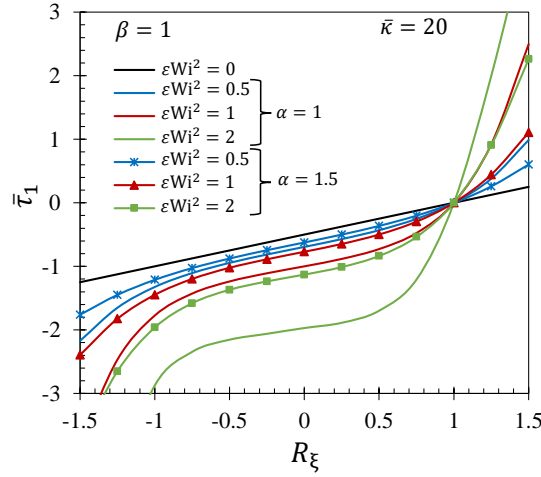


Figure 4.38: Variation of $\bar{\tau}_1$, for purely EO viscoelastic flow, as a function of the ratio of zeta potentials, R_ξ considering $\bar{\kappa} = 20$, $\beta = 1$ and $\alpha = 1, 1.5$.

Fig. 4.38 shows the variation of coefficient $\bar{\tau}_1$, for a purely EO viscoelastic flow, as a function of the ratio of zeta potentials, R_ξ . We consider $\alpha = \beta = 1$ (which corresponds to the exponential PTT model) and $\alpha = 1.5$ and $\beta = 1$. By looking at the results, we see that for $R_\xi = 1$ we have that $\bar{\tau}_1 = 0$, being in accordance with the results obtained for the symmetric case studied by Afonso et al. [51, 58]. For $R_\xi < 1$, $\bar{\tau}_1$ is always negative, decreasing with the increase of ϵWi^2 , indicating that the shear stress is also decreasing as ϵWi^2 increases. For $R_\xi > 1$, $\bar{\tau}_1$ is always positive and increases with ϵWi^2 , which indicates that the shear stress is higher as we increase the shear-thinning behaviour of the fluid. It was not considered the case $\alpha < 1$, due to convergence problems when using high values of ϵWi^2 .

Since one of the goals of this work is to provide a tool for validating future numerical implementations of this model in general numerical codes, the *Mathematica* numerical codes used to obtain the solution are provided as supplementary material.

4.5.4.2.2 Mixed driving forces and asymmetric zeta potentials

For combined EO and pressure-driven flows Eq. (4.166) has to be integrated numerically if $\Upsilon \neq 0$. The influence of the new model on the velocity profile was assessed considering $\Upsilon = 2.5$ and $R_\xi = 0.5$ and $\Upsilon = -2$ and $R_\xi = -1$. We also considered different values for α and β .

Fig. 4.39 presents the velocity profiles obtained for a combined EO/pressure gradient forcing under asymmetric zeta potentials. We consider two different ϵWi^2 values and different values of α (Fig. 4.39 (a)) and β (Fig. 4.39 (b)) for $\bar{\kappa} = 20$, $R_\xi = 0.5$ and $\Upsilon = 2.5$ (adverse pressure gradient).

In Fig. 4.39 (a) ($\beta = 1$) and (b) ($\alpha = 1$), the velocity profiles show a double peak due to the retarding action of the pressure gradient. We observe a consistent pattern, related to what was found in Fig. 4.36, where an increase in ϵWi^2 and a decrease in α correspond to an increase in the flow rate. Notably, the impact of α on the flow rate is more pronounced compared to the effect of β .

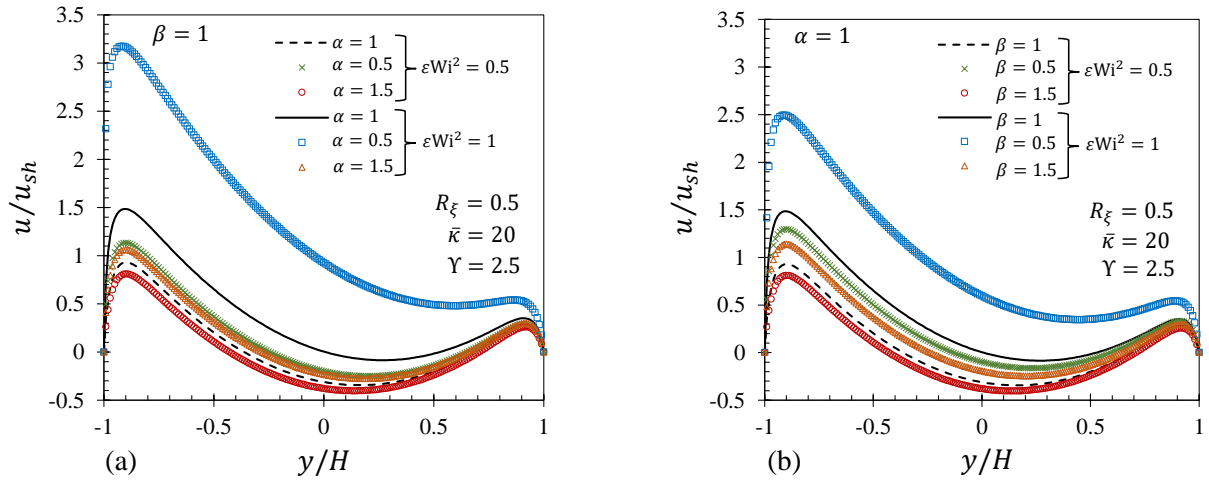


Figure 4.39: Velocity profiles for $R_\xi = 0.5$, $Y = 2.5$, $\bar{\kappa} = 20$ and $\varepsilon Wi^2 = 0.5, 1$ (a) $\beta = 1$, $\alpha = 0.5, 1, 1.5$; (b) $\alpha = 1$, $\beta = 0.5, 1, 1.5$.

In Fig. 4.40, we keep the parameters consistent with those in Fig. 4.39, except for the updated values of $R_\xi = -1$ and $Y = -2$ (indicating a favorable pressure gradient).

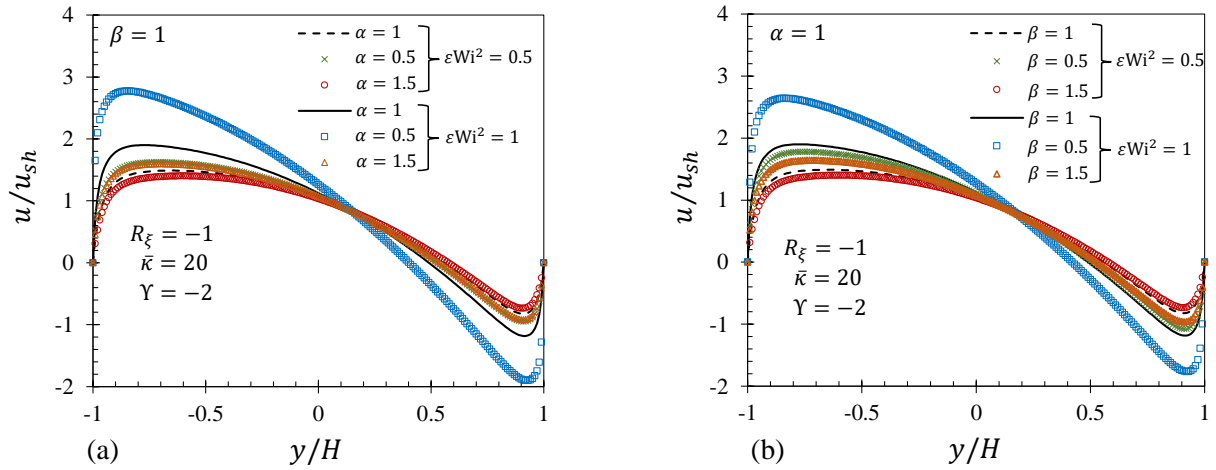


Figure 4.40: Velocity profiles for $R_\xi = -1$, $Y = -2$, $\bar{\kappa} = 20$ and $\varepsilon Wi^2 = 0.5, 1$ (a) $\beta = 1$, $\alpha = 0.5, 1, 1.5$; (b) $\alpha = 1$, $\beta = 0.5, 1, 1.5$.

In Fig. 4.40, (a) with varying α and setting $\beta = 1$, and (b) with varying β and setting $\alpha = 1$, the velocity profiles exhibit an *increase* with the increase of εWi^2 and a decrease in α . This phenomenon is attributed to shear-thinning effects, resulting in higher shear rates near the walls.

Remark: The diverse array of flow behaviors observed, stemming from the variation in different model parameters and flow conditions, offers valuable insights for understanding and predicting the flow patterns of rheologically characterized viscoelastic fluids. While the analysis presented here provides insights into such behavior, it does not comprehensively cover all possible flows of interest, given the limited number of parameter values considered. To facilitate more

targeted studies, we share the codes used in this research, enabling the industrial sector and academia to replicate and further develop these results.

4.5.5 Conclusions

We have developed an analytical solution expressing the velocity profile in a series form for the EO flow of a gPTT fluid. This solution was used to illustrate how various model parameters impact the velocity profiles. As anticipated, a decrease in α and β for the same εWi^2 leads to an increase in flow velocity. Consequently, when $R_\xi > 0$, a more pronounced skewed pluglike profile is observed, whereas $R_\xi < 0$ results in a more pronounced anti-symmetric pluglike profile.

The influence of β is less evident due to its dual role in affecting the rate of destruction of junctions. It serves as a parameter in the Mittag-Leffler function and also functions as a normalization factor. This dual impact contributes to the subtlety of its influence. Our newly proposed model offers a broader description of flow behavior compared to traditional models, making it applicable in the modeling of complex viscoelastic flows.

These analytical and semi-analytical solutions not only serve as valuable tools for validating CFD codes but also enhance our comprehension of the model's behavior in simple shear flows. This expanded understanding facilitates more accurate modeling of complex viscoelastic flows.

Chapter 5

More in numerical studies

5.1 Flow structures identification through proper orthogonal decomposition: the flow around two distinct cylinders⁶

Abstract: Numerical simulations of fluid flows can produce a huge amount of data and inadvertently important flow structures can be ignored, if a thorough analysis is not performed. The identification of these flow structures, mainly in transient situations, is a complex task, since such structures change in time and can move along the domain. With the decomposition of the entire data set into smaller sets, important structures present in the main flow and structures with periodic behaviour, like vortices, can be identified. Therefore, through the analysis of the frequency of each of these components and using a smaller number of components, we show that the Proper Orthogonal Decomposition can be used not only to reduce the amount of significant data, but also to obtain a better and global understanding of the flow (through the analysis of specific modes). In this work, the von Kármán vortex street is decomposed into a generator base and analysed through the Proper Orthogonal Decomposition for the 2D flow around a cylinder and the 2D flow around two cylinders with different radii. We consider a Newtonian fluid and two non-Newtonian power-law fluids, with $n = 0.7$ and $n = 1.3$. Grouping specific modes, a reconstruction is made, allowing the identification of complex structures that otherwise would be impossible to identify using simple post-processing of the fluid flow.

Keywords: proper orthogonal decomposition (POD); Navier–Stokes equations; computational fluid dynamics (CFD); von Kármán vortex street

⁶A.M. Ribau, N.D. Gonçalves, L.L. Ferrás, and A.M. Afonso. Flow structures identification through proper orthogonal decomposition: The flow around two distinct cylinders. *Fluids*, 6(11):384, 2021.

5.1.1 Introduction

The Proper Orthogonal Decomposition (POD) method was first introduced by Lumley in 1967 [9], and it allows for decomposing almost any flow into an infinite set of eigenfunctions or modes. The objective of the POD method is to reduce the model in a way that it can capture the most important and reliable information with much less data and effort. This method is famous in Computational Fluid Dynamics (CFD) because it reduces the simulation time and allows for predicting the fluid flow based only on the most important modes.

Since 1967, several versions of the POD method (and even new methods) were proposed in the literature, being adapted to specific cases and branches of engineering (it should be remarked that, in the first fifteen years, the only works on this topic are from Lumley itself, some co-workers, and Ph.D. students [69]).

The method has become very popular and has been applied to a wide variety of engineering problems going from fluid mechanics to bio-engineering, having different names for the same procedure: Karhunen–Loève Decomposition, Principal Components Analysis (PCA), Singular Systems Analysis, and Singular Value Decomposition (SVD) (please see the review papers [67, 68]). To name all the works on the POD method [112] would be a tedious task that is out of the scope of this work, although some of these works are worth mentioning.

Regarding POD, Selin Aradag et al. [70] developed a couple of methods (the Hybrid Filtered POD (HFPOD) approach (see also [71]) and the Fast Fourier Transform (FFT)-based 3D Filtered POD (FFTPOD)) to deal with the difficulty encountered when using simple POD for three-dimensional (3D) structures. Using the HFPOD method, large-scale structures associated with von Kármán's vortex street, as well as their phase and amplitude variations, can be identified quantitatively. FFTPOD enables modeling 3D flows without being contaminated by small-scale turbulent structures while capturing the large-scale features of the flow, like von Kármán's vortex street. The filtering steps (in the HFPOD method) must be repeated until most small-scale structures are qualitatively eliminated. A spanning phase is provided by the HFPOD, but the FFTPOD is able to deal with 3D geometry, making it a promising alternative to the Hybrid POD for 3D flows.

For a space-time POD problem, for statistically stationary flows, Aaron et al. [72] investigated the Spectral Proper Orthogonal Decomposition (SPOD). This model produces modes that oscillate at a single frequency. In their study, the authors demonstrated how SPOD modes articulate coherently with development in space and time, in contrast to general POD space-modes. Moreover, SPOD modes were found to be optimally averaged Dynamic Mode Decompositions (DMD), resulting from an ensemble model DMD problem for stationary flows. In this sense, SPOD modes represent dynamic structures in the same sense as DMD modes while also incorporating the statistical variability of turbulent flows.

It should be mentioned that the POD method is not the only technique used in the literature to predict complex fluid flows with less effort. We have, for example, Machine Learning (ML) that is now a hot topic on this subject. In fact, the POD method is a feature selection method used in Data Mining processes, to reduce the dimension of the process [76] (in this area, the POD

method goes by the name of PCA). Thus, combining the CFD simulations and ML algorithms to simultaneously reduce computational cost and time, retain physical insight by focusing on the prediction of flow-fields, and keep the ability to access information or to make adjustments is already a reality [77].

The flow around one cylinder is well understood and documented in the literature. See, for example, [81]. Regarding more recent literature on the use of POD to study the flow around bluff bodies, we have the works by Bergmann et al. [82] where they studied the optimal rotary control of the cylinder wake using POD. Huan Ping et al. [83] also studied the wake dynamics behind a rotary oscillating cylinder. They used POD to extract the energetic modes that govern the dynamics of the flow, and also to characterize the spatially evolving nature of the forced wake as it undergoes a transition from the near-wake two-layer shedding pattern to the far-wake Kármán-like shedding pattern. The authors concluded that only a few modes allowed for reconstructing the near-wake accurately, while more modes must be retained to ensure an accurate approximation of the far-wake. Riches et al. [84] used POD to analyze the wake-dynamics of a low-mass ratio circular cylinder undergoing vortex-induced vibrations. Most of the more recent works are now flow around cylinders with different surface texture/geometry.

For the flow around two cylinders, we have works on flows around side-by-side circular cylinders with the same dimensions [85–87], and a study with two cylinders in a staggered configuration where the data processed by the POD method were obtained from experimental measurements of flow fields using the Particle Image Velocimetry (PIV) method [88]. Works on the flow around side-by-side circular cylinders of different radii seems to be nonexistent.

In this work, a simple POD method is used to compute the 2D flow around a single cylinder, and, around two cylinders of different radii. The novelty of this work is:

- the use of POD not to reduce (and compile) the amount of information on the flow (has happens in most studies), but to rather show that the POD can be used to capture flow structures and flow physics that would be impossible to *observe* without a mode analysis. Highlighting, in this way, this ability of the POD method;
- to further understand the flow around two cylinders of different radii, through the use of POD and classical CFD. By decomposing this complex 2D flow, we have a better comprehension of the impact that a certain obstacle has in areas of interest.

We present a detailed study on complex 2D flows, and it is shown that the energy drop-off for higher order modes is much less steep when the complexity of the 2D flow increases.

It should be mentioned that we do not consider turbulent flows. The idea is to fully understand the mode decomposition in an oscillatory flow around two parallel cylinders of different dimensions.

This work is organized as follows: first, we present the basics of POD. Then, numerical simulations for the 2D flow past a cylinder are performed, considering a Newtonian fluid and two non-Newtonian power-law fluids with $n = 0.7$ and $n = 1.3$. The most important modes are identified for this well known case. Then, we perform a numerical study on the 2D flow past two cylinders of different radii (for both Newtonian and power-law fluids). This specific flow destroys the possibility

of forming a symmetric pattern over time and increases the difficulty in grouping different modes. We discuss in detail the dynamics of the fluid flow and the reconstruction procedure. The document ends with the conclusions.

5.1.2 Equations and numerical method

The equations governing the flow of an isothermal incompressible fluid are the continuity:

$$\nabla \cdot \mathbf{u} = 0, \quad (5.1)$$

and the momentum equations,

$$\rho \frac{D\mathbf{u}}{Dt} = -\nabla p + \nabla \cdot \boldsymbol{\tau}, \quad (5.2)$$

where $\frac{D}{Dt}$ is the material derivative, p is the pressure and ρ the fluid density, together with the constitutive equation $\boldsymbol{\tau} = 2\mu\mathbf{D}$, where \mathbf{D} is the rate of deformation tensor and μ is the viscosity. For a Newtonian fluid, μ is constant.

5.1.2.1 Non-Newtonian power-Law fluid

For a non-Newtonian power-law fluid, the constitutive equation for $\boldsymbol{\tau}$ is now given by:

$$\boldsymbol{\tau} = \eta(\dot{\gamma})\mathbf{D} \quad (5.3)$$

where $\eta(\dot{\gamma})$ is the viscosity function, given by:

$$\eta(\dot{\gamma}) = K\dot{\gamma}^{n-1} \quad (5.4)$$

with K being the consistency index, n the power-law index, and $\dot{\gamma}$ the second invariant of the rate of deformation tensor (for simple shear flows, $\dot{\gamma}$ is just the shear rate).

For the study with the power-law fluid, the generalized Reynolds number is given by [89, 90],

$$Re_{gen} = \frac{6\rho U^{(2-n)} D^n}{K [(4n+2)/n]^n}, \quad (5.5)$$

where U is the imposed mean velocity at the inlet. When $n = 1$, the model reduces to the classical Reynolds number Re ,

$$Re = \frac{\rho U D}{\mu}, \quad (5.6)$$

with $\eta(\dot{\gamma}) = K = \mu$ a constant viscosity.

5.1.2.2 Von Kármán vortex street

A von Kármán Vortex street is a repeating pattern of swirling vortices. This happens due to vortex shedding, which is responsible for the unsteady separation of flow of a fluid around a blunt body.

When studying this phenomenon, an important dimensionless number is the Strouhal number (named after the Czech physicist, Vincenc Strouhal (1850–1922)). This dimensionless number is a key parameter for oscillating flows because it describes the relation between the length-scale of the blunt body, the vortex shedding frequency and the flow velocity [77]. The Strouhal number is defined by

$$St = \frac{fD}{U}, \quad (5.7)$$

where f is the vortex shedding frequency and D is the diameter of the blunt body. This dimensionless number can be related to Re . According to Roshko [91], for approximately $50 < Re < 150$, the relationship between St and Re is given by

$$St = 0.212 \left(1 - \frac{21.2}{Re} \right). \quad (5.8)$$

5.1.2.3 Proper orthogonal decomposition

To implement the POD method, we assumed that all data are saved in a matrix with a $(\phi_1, \phi_2, \dots, \phi_{N_e})^T$ shape, saving one time step in each column. Thus, we obtained a matrix Φ with N_e by N_t elements:

$$\Phi = \begin{bmatrix} \phi_{1,1} & \phi_{1,2} & \cdots & \phi_{1,N_t} \\ \phi_{2,1} & \phi_{2,2} & \cdots & \phi_{2,N_t} \\ \vdots & \vdots & \ddots & \vdots \\ \phi_{N_e,1} & \phi_{N_e,2} & \cdots & \phi_{N_e,N_t} \end{bmatrix} \quad (5.9)$$

where N_e is the number of elements to study and N_t are the time steps.

For the study proposed in this work, the data saved in matrix Φ corresponds to the velocity components, u and v , and the pressure, p , obtained after performing a CFD simulation. Thus, in each column of matrix Φ , $(u_1, u_2, \dots, u_{N_E}, v_1, v_2, \dots, v_{N_E}, p_1, p_2, \dots, p_{N_E})^T$ are saved, where N_E is the number of elements of the mesh. We can also consider other properties, such as temperature or viscosity.

Each column of Φ can be written as a linear combination of orthonormal vectors or modes, \mathbf{u} . These modes are unitary and orthogonal. Therefore, the matrix of the modes, \mathbf{U} , is given by

$$\mathbf{U} = \begin{bmatrix} u_{1,1} & u_{1,2} & \cdots & u_{1,N_m} \\ u_{2,1} & u_{2,2} & \cdots & u_{2,N_m} \\ \vdots & \vdots & \ddots & \vdots \\ u_{N_e,1} & u_{N_e,2} & \cdots & u_{N_e,N_m} \end{bmatrix} \quad (5.10)$$

where N_m is the number of modes. This way, each element of matrix Φ can be written as:

$$\phi_{i,t} = \sum_{m=1}^{N_m} u_{i,m} a_{m,t} \quad (5.11)$$

where $i \in \{1, 2, \dots, N_e\}$, $t \in \{1, 2, \dots, N_t\}$ and $a_{m,t}$ are the temporal coefficients.

Eq. (5.11) in the matrix form becomes:

$$\mathbf{\Phi} = \mathbf{U} \cdot \mathbf{A}. \quad (5.12)$$

where \mathbf{A} is the matrix of the temporal coefficients and is equal to

$$\mathbf{A} = \begin{bmatrix} a_{1,1} & a_{1,2} & \cdots & a_{1,N_t} \\ \vdots & \vdots & \ddots & \vdots \\ a_{N_m,1} & a_{N_m,2} & \cdots & a_{N_m,N_t} \end{bmatrix} \quad (5.13)$$

Matrices \mathbf{U} and \mathbf{A} are obtained by the autocovariance matrix \mathbf{R} that is given by

$$\mathbf{R} = \frac{1}{N_e} \mathbf{\Phi} \cdot \mathbf{\Phi}^T \quad (5.14)$$

whose eigenvectors are the columns of matrix \mathbf{U} . Matrix \mathbf{A} is obtained by:

$$\mathbf{A} = \mathbf{U}^T \cdot \mathbf{\Phi}. \quad (5.15)$$

The distribution of the matrix \mathbf{U} columns is directly related to the corresponding eigenvalues. This way, the first columns of \mathbf{U} are the ones showing a higher variation of the temporal coefficients, and therefore the ones that gather more relevant information. Thus, we reconstruct matrix $\mathbf{\Phi}$, where only the modes that are more relevant are considered. Since $N_m < N_e$, it brings:

$$\mathbf{\Phi} \approx \tilde{\mathbf{U}} \cdot \tilde{\mathbf{A}} = \tilde{\mathbf{\Phi}} \quad (5.16)$$

where $\tilde{\mathbf{U}}$ is the matrix with the first more relevant modes and $\tilde{\mathbf{A}}$ is the matrix with the temporal coefficients that correspond to the first more relevant modes, and $\tilde{\mathbf{\Phi}}$ is the spatial reconstruction of the properties in study. For more information on this subject, please consult [113–115] for a detailed explanation on the POD method implemented in this work.

5.1.2.4 Numerical method

The system of equations (Eqs. (5.1) and (5.2)) were solved numerically using the software ANSYS Fluent version 2020 R2.

To perform the simulations, the velocity and pressure fields at $t = 0$ were obtained in the following manner:

- First, a steady-state solution was calculated for $Re = 100$;
- Second, the previous solution was used as an initial guess ($t = 0$) for the velocity and pressure fields, in the steady-state turbulent numerical simulation considering $Re = 500$. This simulation allowed the development of the characteristic von Kármán vortex street.
- Third, the steady-state solution obtained for $Re = 500$ was used as the initial guess for our transient simulations with $Re = 100$.

The pressure–velocity coupling was done using the SIMPLE method. To discretize the pressure gradient, the Least Squares Cell Based scheme was used, and, for the discretization of the advective terms, the Second-Order Upwind scheme was considered. The transient term was approximated by a first order implicit scheme. The POD analysis was performed with MATLAB R2018a.

In the next section, more details are presented regarding the geometry and meshes used along the work.

5.1.3 Case study: flow around a single cylinder

In this section, we present some results on the flow around a single cylinder that will be used fully in the analysis of the flow around two cylinders (for comparison).

5.1.3.1 Geometry, boundary conditions and mesh

Fig. 5.1 (a) shows the geometry of the flow around a cylinder. The left bold-dashed line represents the inlet and the right dashed one the outlet. The cylinder has a diameter $D = 0.1$ m and is placed $5D$ away from the inlet and $15D$ from the outlet. The inlet has a height $10D$. Regarding boundary conditions, we have imposed pressure at the outlet, and imposed at the inlet a uniform velocity profile that is constant in time. At the top and bottom walls of the channel, we consider full slip, and at the wall of the cylinder the usual empirical no-slip boundary condition was assumed.

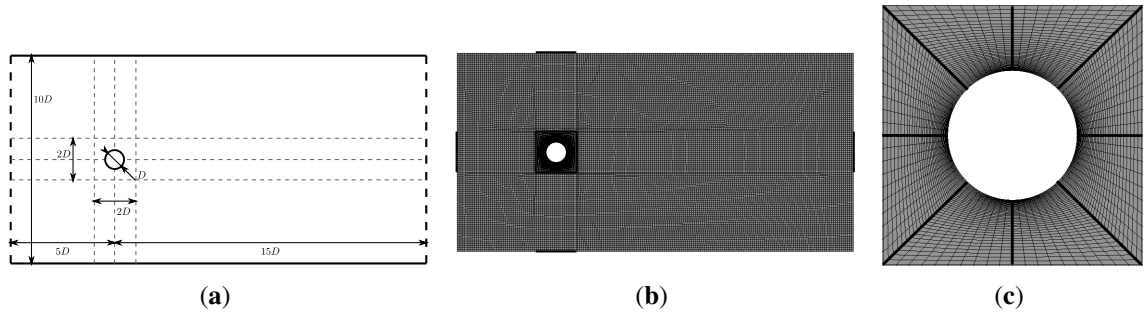


Figure 5.1: (a) Geometry of the flow around one cylinder. The left dashed line represents the inlet and the right dashed one the outlet. Mesh of the flow around one cylinder with 23,789 elements: (b) global view with black lines with 10 mm elements; (c) close view around the cylinder.

To study the flow around one cylinder, we first perform a mesh study. We consider three meshes: one with 12,976 elements, one with 23,789 elements, and a more refined one with 48,570 elements. For each mesh, a simulation with 1000 time-steps was performed, and the drag coefficient on the cylinder wall was calculated. Then, we determined the average drag coefficient, $\overline{c_d}$, for each mesh. The results are presented in Table 5.1.

We calculated an extrapolated value for $\overline{c_d}$ using the Richardson extrapolation technique,

$$\overline{c_{d_e}} \approx \overline{c_{d_{M_1}}} + \frac{\overline{c_{d_{M_1}}} - \overline{c_{d_{M_2}}}}{r^l - 1}, \quad (5.17)$$

Table 5.1: Average drag coefficient values for the three meshes.

Mesh	Number of elements	$\overline{c_d}$
M_1	48570	1.463
M_2	23789	1.470
M_3	12976	1.475

where $\overline{c_{d_e}}$ is the extrapolated value, $\overline{c_{d_{M_1}}}$ is $\overline{c_d}$ for mesh M_1 , $\overline{c_{d_{M_2}}}$ is the $\overline{c_d}$ for mesh M_2 and $\overline{c_{d_{M_3}}}$ is the $\overline{c_d}$ for mesh M_3 . r is the grid refinement ratio and l is the order of the method. We see that $r \approx 2$, and, in this work, we assumed that $l = 2$. Using Eq. (5.17), we obtained $\overline{c_{d_e}} \approx 1.477$.

We measured the relative error (Eq. (5.18)) for each mesh and obtained a good trade-off between accuracy and computational cost for mesh M_2 . The error E was small (about 0.42%):

$$E = \frac{|\overline{c_{d_e}} - \overline{c_{d_{M_2}}}|}{|\overline{c_{d_e}}|} = 0.42\%. \quad (5.18)$$

Based on these results, the subsequent numerical simulations will be performed on mesh M_2 .

Fig. 5.1 (b) shows a global view of the chosen mesh M_2 and Fig. 5.1 (c) shows a zoomed view of the mesh around the cylinder. The cell size was set to 0.0025 m along the cylinder surface region, 0.01 m along bold lines of Fig. 5.1 (b) and 0.02 m on the rest of the domain. The cell size growth rate was 1.2, and, along the edges in bold (Fig. 5.1 (c)), a bias type procedure was used with a bias factor of 10.

5.1.3.2 Rheological properties

To perform the numerical simulations, we first considered a Newtonian fluid with the rheological properties of water at a temperature of 20 °C, that is, density $\rho = 10^3 \text{ kg.m}^{-3}$, and viscosity $\mu = 10^{-3} \text{ Pa.s}$. We considered a Reynolds number of 100, which for a cylinder with diameter $D = 0.1 \text{ m}$, leads to an imposed inlet velocity U of 10^{-3} m.s^{-1} . Then, we performed the numerical simulations with a non-Newtonian power-law fluid, where $Re_{gen} = 100$, $\rho = 10^3 \text{ kg.m}^{-3}$, $D = 0.1 \text{ m}$ and $U = 10^{-3} \text{ m.s}^{-1}$ is the imposed inlet velocity. We will consider two fixed values for the power-law index n : 0.7 and 1.3. Thus, from Eq. (5.5), we conclude that $K = 0.00039 \text{ Pa.s}^{0.7}$ and $0.0026 \text{ Pa.s}^{1.3}$, respectively.

5.1.3.3 Results and discussion

The transient simulation with $Re = 100$ was performed and the first 10λ seconds ($\lambda = \frac{20D \times 10D}{10D \times u}$) were ignored to avoid the strong influence of the initial conditions. Note that λ is an approximate measure of the residence time, that is, the time a particle takes to go from the inlet to the outlet. The study and analysis was focused on the subsequent 10λ seconds of data.

To set the maximum time step of the numerical simulation, a maximum Courant number (C) of 1 was considered. A $C \leq 1$ leads to $\delta t_{CFD} \leq \frac{\delta x}{u_{max}} = \frac{0.0025}{0.001} = 2.5 \text{ s}$. To use the POD method, we considered the data of every 20 time-steps, i.e., $\delta t_{POD} = 50 \text{ s}$, resulting into 400 time-steps to be

analyzed.

Fig. 5.2 (a)–(c) show the streamlines and the vorticity sign map at $t = 20\lambda$, for a Newtonian fluid, and non-Newtonian power-law fluids with $n = 0.7$ and $n = 1.3$, respectively.

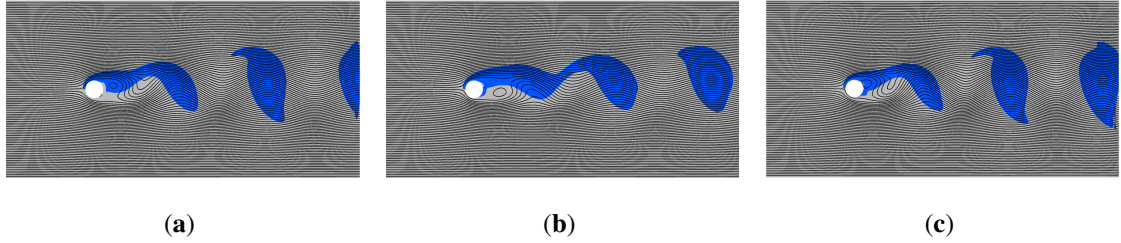


Figure 5.2: Flow around a single cylinder. Streamlines and vorticity sign (blue represents positive values and grey negative values) at $t = 20\lambda$ seconds for: **(a)** Newtonian fluid; **(b)** non-Newtonian power-law fluid with $n = 0.7$; **(c)** non-Newtonian power-law fluid with $n = 1.3$.

In Fig. 5.2 (a), we see that vortices detach from the cylinder rear with diameter of about $5D$, and, from Eq. (5.8), for $Re = 100$, we have $St \approx 0.17 \approx 1/5.88$. Therefore, the structures behind the cylinder are about six times bigger than the cylinder, or three times bigger with an alternating sign of rotation. The oscillatory behaviour downstream from the cylinder is perceptible, and the vortices on Fig. 5.2 (c) have a similar behaviour to the ones presented in Fig. 5.2 (a) for the Newtonian fluid.

In this work, due to the high computational effort and the existence of low information on the neglected modes, only the first 20 eigenvalues and modes were calculated.

Fig. 5.3 (a)–(c) show the relative weight of the eigenvalues associated with each modes, for the three fluids described before. For all cases, we see a fast decrease of the relative weight of the eigenvalues associated with each mode. In Fig. 5.3 (a), the weights attributed to the first, second, and third eigenvalues are 98%, 0.98%, and 0.95%, respectively. In Fig. 5.3 (b), the weights are 99%, 0.5%, and 0.47%, respectively. Finally, in Fig. 5.3 (c), the weights are 97.2%, 1.3%, and 1.3%. All figures show residual weights attributed to the remaining modes, leading to the conclusion that only three modes allow the reconstruction of the flow.

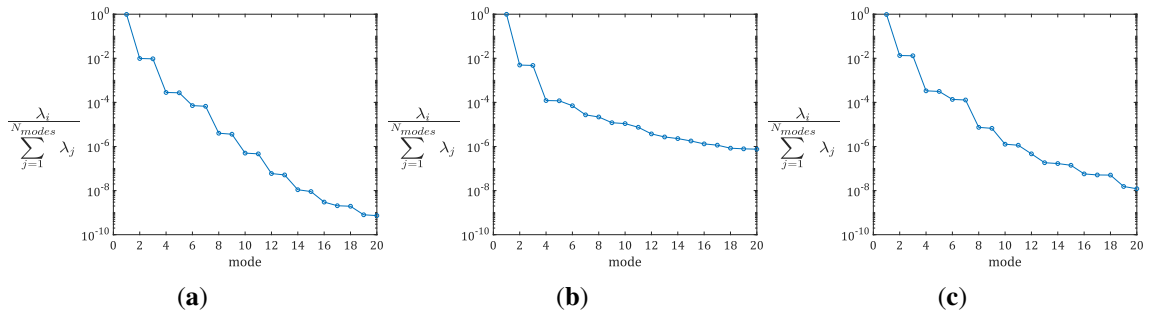
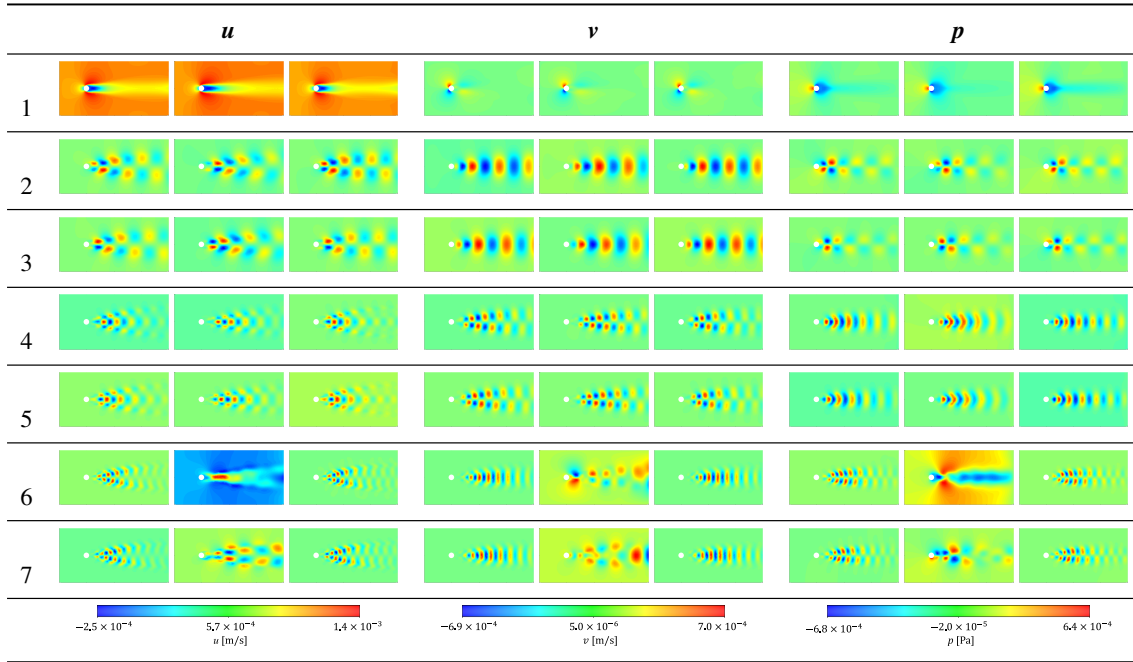


Figure 5.3: Flow around a single cylinder. Relative weight of the eigenvalues associated with each mode: **(a)** Newtonian fluid; **(b)** power-law fluid with $n = 0.7$; **(c)** power-law fluid with $n = 1.3$.

Table 5.2 presents the most important modes of u , v , and p (for each component u , v and p , we have from left to right: a Newtonian fluid, a power-law fluid with $n = 0.7$, and a power-law fluid with $n = 1.3$.).

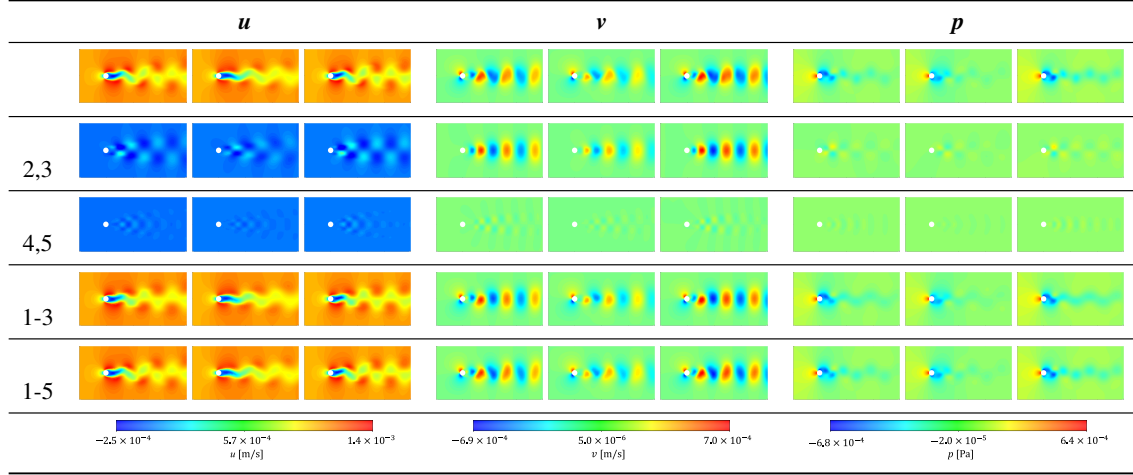
Table 5.2: Most important modes (1 to 7) of u , v and p for the flow around a single cylinder. For each component u , v and p , we have from left to right: a Newtonian fluid, a power-law fluid with $n = 0.7$ and a power-law fluid with $n = 1.3$.



Analysing the modes in Table 5.2, we see that the first mode is symmetric and has the main features of the flow without the oscillating components. For the Newtonian fluid and the power-law fluid with $n = 1.3$, the modes after mode 1 are similar by pairs, with some *delay* between them. We also see that modes 2 and 3 are coherent with vortices. These vortices are about six times larger than the cylinder, as shown in Fig. 5.2. For the power-law fluid with $n = 0.7$, the modes after mode 1 are similar by pairs to modes 2 and 3 and modes 4 and 5, also with some *delay* between them, but mode 6 for u and p seems to be symmetrical again. Note that, from Fig. 5.3 (b), after mode 5, the modes do not pair, having residual contributions. Therefore, it will be more difficult to analyse their contribution. We would probably need more simulation time or a smaller time-step to make a better analysis. We can see that, for the power-law fluid with $n = 1.3$, the results are similar to the Newtonian case, and this may be explained by the dilatant, or shear-thickening behaviour (increase in apparent viscosity at higher shear rates). The flow is more sensible to the shear-thinning obtained for $n = 0.7$, and therefore we have differences and similarities with the Newtonian results for $n = 0.7$ and $n = 1.3$, respectively.

Table 5.3 shows a comparison between the original data obtained from the simulation and the partial reconstruction at $t = 20\lambda$ (for each component u , v and p , we have from left to right: a Newtonian fluid, a power-law fluid with $n = 0.7$, and a power-law fluid with $n = 1.3$).

Table 5.3: Comparison between the original (first row of images) data versus the partial reconstruction at $t = 20\lambda$ seconds (the modes used in the reconstruction are shown in the first column). For each component u , v and p , we have from left to right: a Newtonian fluid, a power-law fluid with $n = 0.7$ and a power-law fluid with $n = 1.3$.



The reconstruction is made with modes 2 and 3, modes 4 and 5, modes 1 to 3 and modes 1 to 5. We see that the reconstruction with modes 2 and 3 allows us to recover the vortices traveling along the domain. With the reconstruction of the first three modes, almost all the structures are perceptible, although slight corrections to their shapes are needed. Comparing the reconstruction with modes 2 and 3, with the reconstruction with modes 4 and 5, we see that they are similar, but with smaller structures on the case of modes 4 and 5. These modes are a first correction to the above referred vortices. When we perform the reconstruction with the first five modes, the velocity and pressure maps become very similar to the original data.

Fig. 5.4 shows an analysis of frequencies of the modes *time coefficients* for the three fluids. The Strouhal numbers (Eq. (5.7)) presented in Fig. 5.4 are calculated considering the frequency with higher energy, D as defined in section 5.1.3.1 and U as defined in section 5.1.3.2. By Eq. (5.8), the Strouhal number with $Re = 100$ is about 0.17.

Analysing the Strouhal numbers in Fig. 5.4 for the Newtonian fluid (top), we obtain $St = 0.175$ that is similar to the one obtained from Eq. (5.8). We can also see that the pair of modes 2 and 3, 4 and 5, 6 and 7, 8 and 9, 10 and 11, have common Strouhal number. This characteristic reveals that each pair is associated with the same flow structure. Furthermore, we notice that higher values of the Strouhal number are multiples of the Strouhal number of modes 2 and 3, so they can be considered as harmonic frequencies, as for example in the square wave function case. These harmonic frequencies result from the non-perfectly round shape of the vortices that travel along the domain.

When we analyse Fig. 5.4 for the power-law fluid where $n = 0.7$, we see that the pairs of modes that now have common Strouhal number are modes 2 and 3, modes 4 and 5, modes 7 and 8, modes 9 and 10 and, finally, modes 6 and 11. Now, modes 7 and 8 have a Strouhal number similar to Strouhal number of modes 2 and 3, the Strouhal number of modes 4 and 5 is about twice the

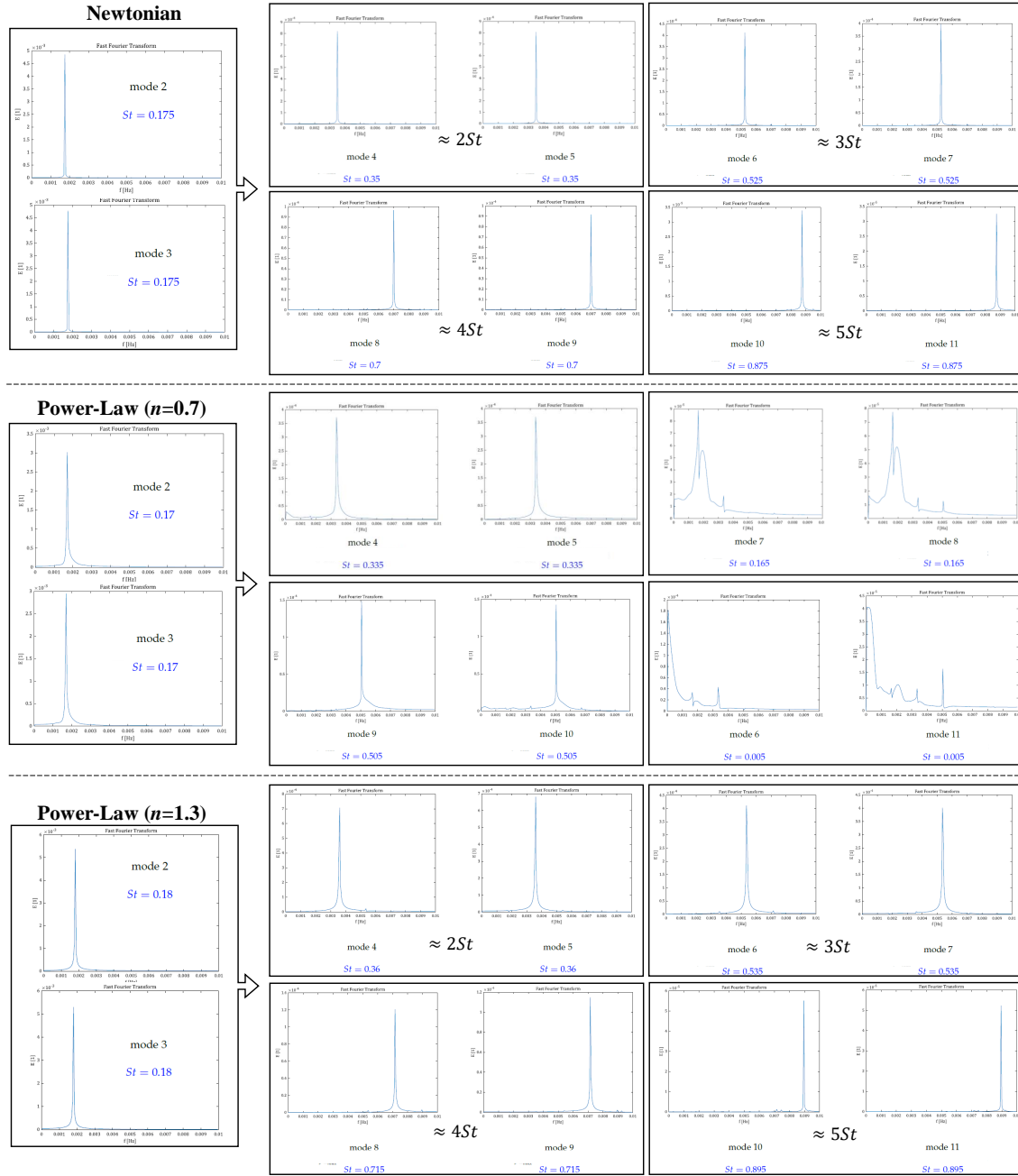


Figure 5.4: Analysis of frequencies of the modes *time coefficients* for a Newtonian fluid (**top**), a non-Newtonian power-law fluid where $n = 0.7$ (**middle**) and a non-Newtonian power-law fluid where $n = 1.3$ (**bottom**).

Strouhal number of modes 2 and 3 and the Strouhal number of modes 9 and 10 is about three times Strouhal number of modes 2 and 3. These mixed results come from the use of another constitutive model for viscosity. The results for a power-law fluid with $n = 1.3$ are similar to the Newtonian ones, with only small differences.

The modes are unitary vectors whose weighted average (the linear combination) forms the original data set. Those weights are the time components and can be used to represent the

importance of each mode. According to Fig. 5.4, we can group the modes by consecutive pairs because of the similar Strouhal number. Therefore, in Fig. 5.5, are represented the pairs of time coefficients for consecutive modes, for the three fluids. We can see that, from the contribution of modes 2 and 3, and 4 and 5, the oscillatory and alternating behaviour is perceived.

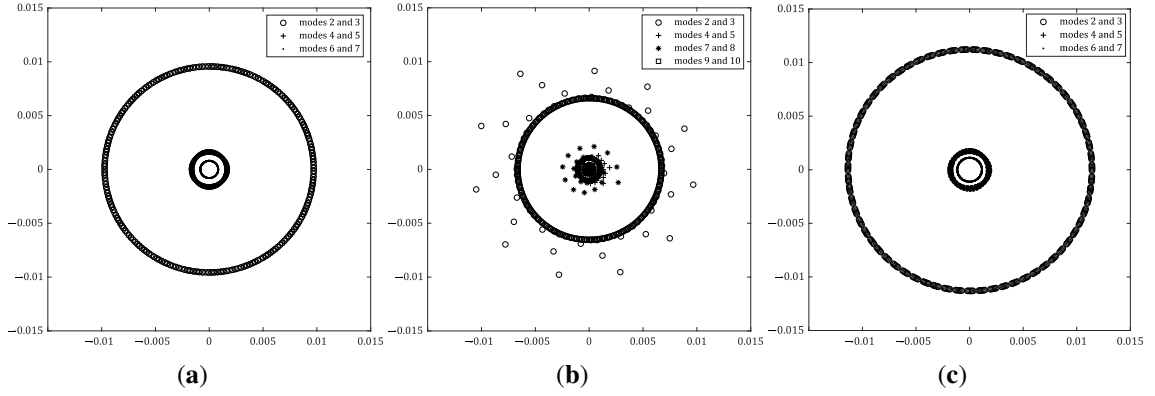


Figure 5.5: Flow around a single cylinder. Pairs of time coefficients of consecutive modes: (a) Newtonian fluid; (b) power-law fluid with $n = 0.7$; (c) power-law fluid with $n = 1.3$.

5.1.4 Case study: flow around two distinct cylinders

We now consider two distinct cylinders that will cause the loss of symmetry and allow us to present the main contribution of this work. We perform a detailed analysis of this flow dynamics, and show that even in these complex cases we can perform a reconstruction of the flow using the basics of the POD method, and therefore obtain a reduction in data analysis and observe *hidden* structures in the flow.

5.1.4.1 Geometry, boundary conditions and mesh

The boundary conditions are the same used for the case of one-cylinder and the geometry is represented in Fig. 5.6 (a). We now have two cylinders: one with radius D (bottom) and the other with radius $1.5D$ (top). The mesh convergence study was similar to the one presented for the flow around a cylinder, being the estimated relative error of the same order. The chosen mesh now has 23944 elements.

Fig. 5.6 (b) presents a global view of the chosen mesh and Fig. 5.6 (c) shows a zoomed view of the mesh around the two cylinders. The cell size was set to 0.0025 m along the cylinders' surface region, 0.01 m along bold lines of Fig. 5.6 (b) and 0.02 m on the rest of the domain. The cell size growth rate is 1.2. Along the bold edges (Fig. 5.6 (c)), a bias type procedure was used with a bias factor of 10. We obtained a mesh with 23944 elements.

5.1.4.2 Rheological properties

For the Newtonian fluid, we have $Re = 100$ near to the smaller cylinder with diameter $D = 0.1$ m and $Re = 150$ near the larger cylinder with diameter $1.5D = 0.15$ m. This way, we kept the imposed

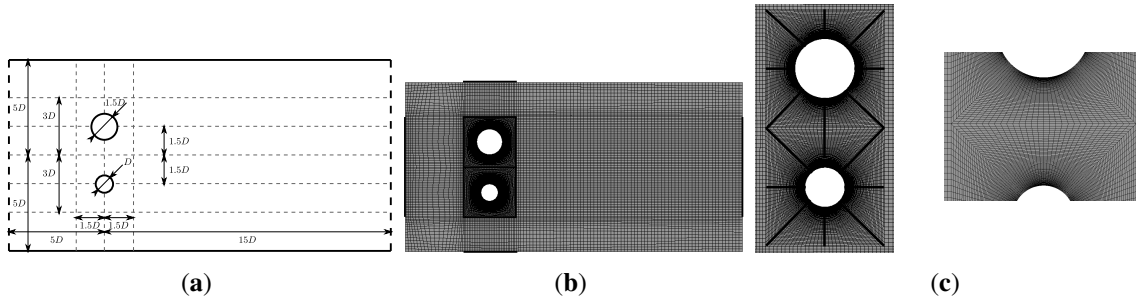


Figure 5.6: (a) Geometry of the flow around two cylinders. The left dashed line represents the inlet and the right dashed one the outlet. Mesh of the flow around two cylinders with 23944 elements; (b) global view with black lines with 10 mm elements; (c) close view around and between the cylinders.

inlet velocity as $U = 10^{-3} \text{ m.s}^{-1}$. For the non-Newtonian power-law, the rheological properties are the same presented in section 5.1.3.2.

5.1.4.3 Results and discussion

The transient simulation was performed, and the first 10λ seconds were again neglected to avoid the strong influence of the initial conditions. The subsequent 10λ seconds of data were then analysed. We considered the same δt_{CFD} and δt_{POD} of the flow around one cylinder.

Fig. 5.7 (a)–(c) present the streamlines and the vorticity sign map for the flow around two cylinders, for the Newtonian fluid, and, the power-law fluids with $n = 0.7$ and $n = 1.3$, respectively. We can see that the oscillatory behaviour downstream the cylinders is perceptible and the vortices detach from each cylinder rear, with different sizes. Later in time, the vortices that arise from both cylinders interact and new structures are formed, where the individual influence of each cylinder is no more clear, when compared to the one-cylinder case. From Eq. (5.8) for $Re = 100$ (smaller cylinder), we have $St \approx 0.17$ and consequently the structures behind the cylinder are about six times bigger than the cylinder itself. Near the bigger cylinder, with diameter $1.5D$, a $Re = 150$ corresponds to $St \approx 0.18$ and vortices are slightly bigger.

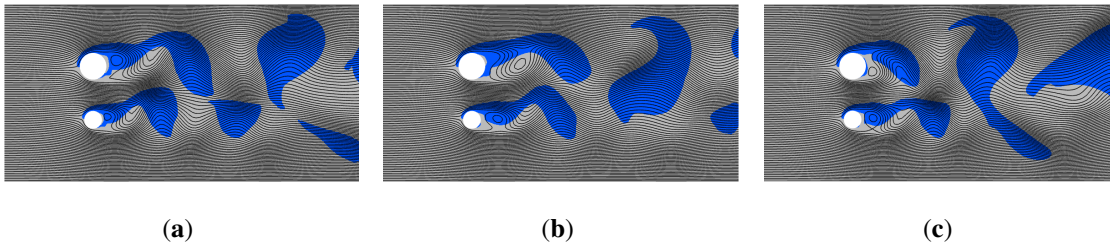


Figure 5.7: Streamlines and vorticity sign (blue represents positive values and grey negative values) at $t = 20\lambda$ for: (a) Newtonian fluid; (b) power-law fluid with $n = 0.7$; (c) power-law fluid with $n = 1.3$.

In order to better understand the dynamics of this flow, we provide simulation videos with the flow fields u, v and p (please see the Supplementary Material). Some snapshots/instant of the

evolution in time of the velocity component u are shown in Fig. 5.8. The figures are numbered from 1 to 15, with 1 representing $t \approx 0$ s and 15 representing $t \approx 2.3$ s of simulation. From instants 1 to 5, the flow in the wake of the cylinders is similar, although the different scales generate different structures that lead to the asynchronous flow verified in instant 6. These asynchronous flow results in the formation of higher velocity structures that *detach* from the main flow in the wake of the cylinder. This analysis alone is still insufficient to fully understand the influence of the one cylinder over the other. Therefore, we will now present a detailed analysis based on POD, and show that these methods allow one to unveil the origin and evolution of the different structures.

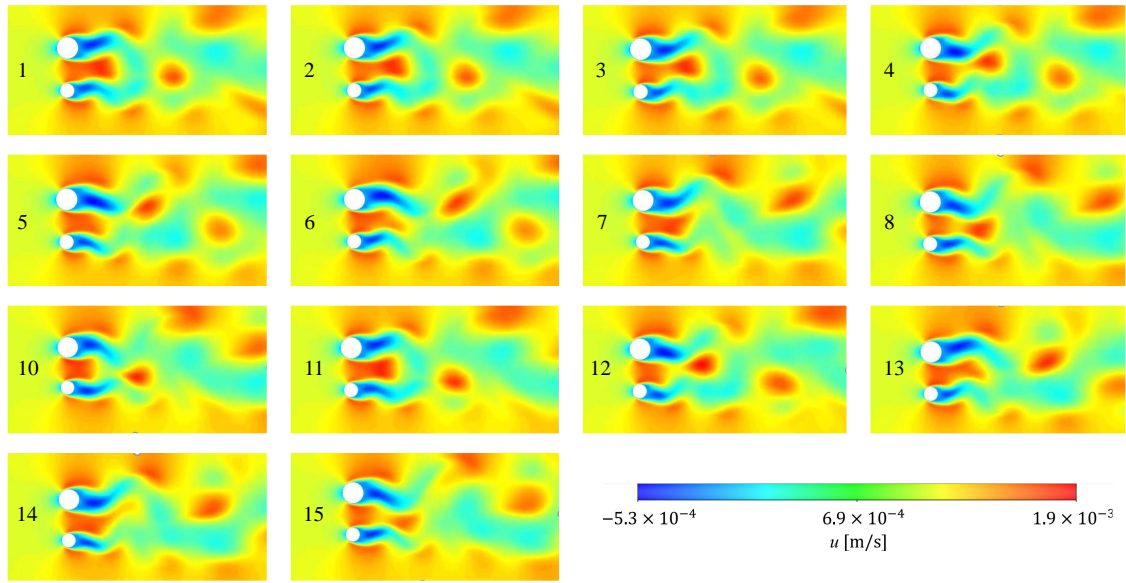


Figure 5.8: Evolution, in time, of the first component, u , of the velocity profile. The numbers 1 to 15 establish the order of occurrence, with 1 representing $t \approx 0$ s and 15 representing $t \approx 2.33$ s. These instants were extracted from the Supplementary Material provided together with this work.

As for the case of one cylinder, we only considered the first 20 eigenvalues and modes. Fig. 5.9 (a)–(c) show the relative weight of the eigenvalues associated with each mode, for a Newtonian fluid, a power-law fluid with $n = 0.7$ and a power-law fluid with $n = 1.3$, respectively.

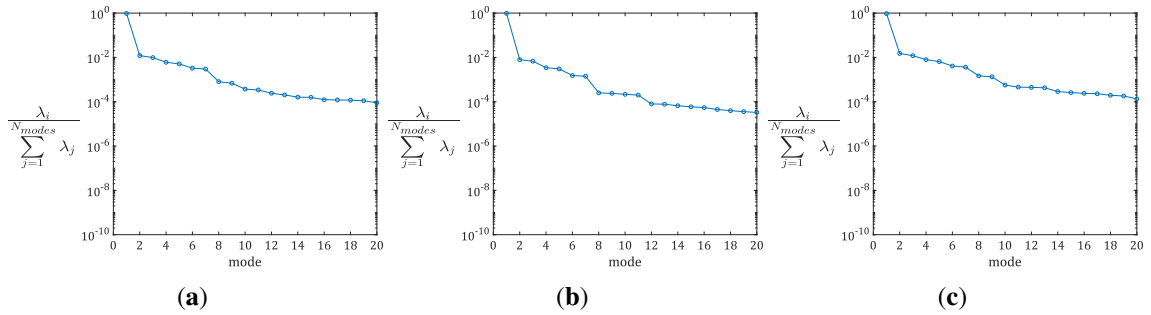


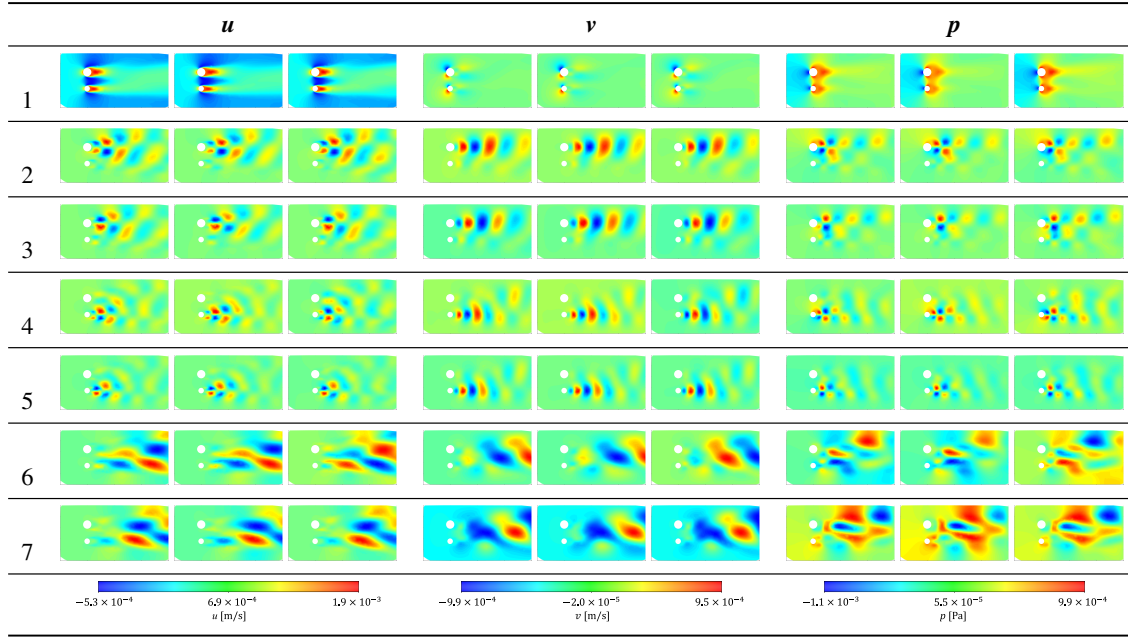
Figure 5.9: Relative weight of the eigenvalues associated with each mode, for: (a) Newtonian fluid; (b) power-law fluid with $n = 0.7$; (c) power-law fluid with $n = 1.3$.

In all figures, we see a fast decrease of the relative weight of the eigenvalues associated with each mode. In Fig. 5.9 (a), the weight attributed to the first, second and third eigenvalues is 95.7%, 1.21% and 0.98%, respectively. In Fig. 5.9 (b), the weights are 97.5%, 0.79% and 0.67%. In Fig. 5.9 (c), the weights are 94.5%, 1.5% and 1.2%.

This leads to the conclusion that with two cylinders, the importance of the first modes is not so clear as in the one-cylinder case. The existence of a second cylinder with different frequencies associated and the interaction of the structures that emerge from the distinct cylinders lead to the use of a higher number of frequencies and modes, to correctly predict/reconstruct the flow.

Table 5.4 shows the most important modes of u , v and p , for the flow around two cylinders (for each component u , v and p , we have from left to right: a Newtonian fluid, a power-law fluid with $n = 0.7$ and a power-law fluid with $n = 1.3$).

Table 5.4: Most important modes (1 to 7) of u , v and p for the flow around two cylinders. For each component u , v and p , we have from left to right: a Newtonian fluid, a power-law fluid with $n = 0.7$ and a power-law fluid with $n = 1.3$.

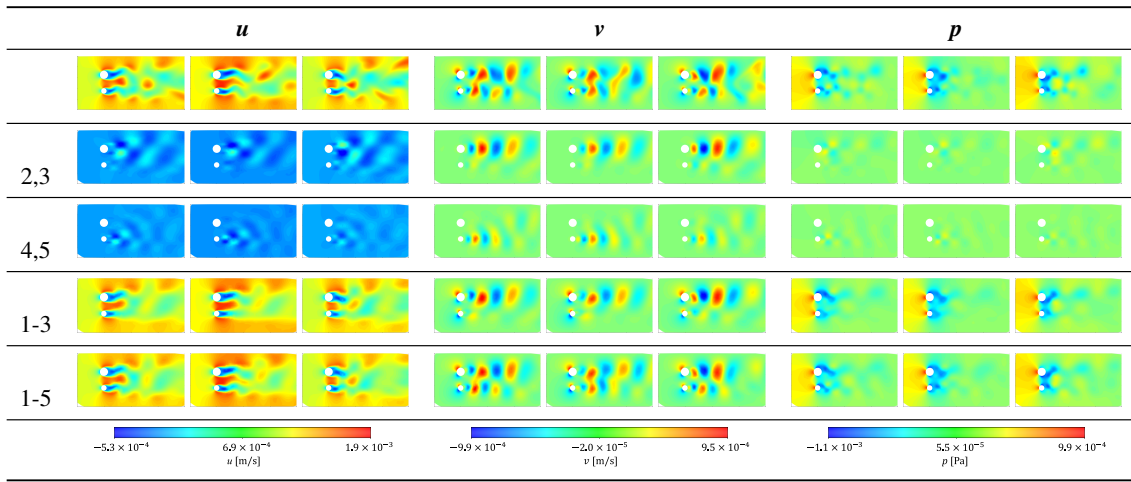


We see that the first mode has the main features of the flow, but without the oscillating components. Mode 1 is in close agreement with the ensemble average (as expected). Notice that the values of u , v and p for mode 1 are symmetrical of what was *supposed* to happen. This happens because this mode is multiplied by the temporal coefficients that, in this case, are negative. Modes 2 and 3 are related to vortices that detach from the top cylinder, whereas modes 4 and 5 can be associated with the bottom cylinder. In modes 2 and 3, we can see flow structures of the top cylinder in front of the bottom cylinder, and that type of influence is hard to see without a decomposition by modes like we perform in here. Unlike the flow around one cylinder, the modes after mode 5 are not *similar by pairs* neither easily associated with some meaningful flow structure.

In order to better understand this phenomena, Table 5.5 shows a comparison between the original data and the partial reconstruction at $t = 20\lambda$, for the three fluids (for each component

u , v and p , we have from left to right: a Newtonian fluid, a power-law fluid with $n = 0.7$ and a power-law fluid with $n = 1.3$). From these results, we conclude that the partial reconstruction with just modes 2 and 3 recovers the bigger vortices traveling along the domain associated with the top cylinder. When modes 4 and 5 are considered, we capture the smaller vortices downstream the bottom cylinder (in a short distance from the cylinder). In the reconstruction with the first five modes almost all the structures are perceptible, although slight corrections are missing.

Table 5.5: Comparison between the original (first row of images) data versus the partial reconstruction at $t = 20\lambda$ (the modes used in the reconstruction are shown in the first column). For each component u , v and p , we have from left to right: a Newtonian fluid, a power-law fluid with $n = 0.7$ and a power-law fluid with $n = 1.3$.



Due to the different vortices that are formed along time and space, the task of finding a direct relationship between the modes and the exact structures is really hard to perform. Although we have plotted the velocity fields obtained for the Newtonian fluid at $t = 10\lambda$, $t = 15\lambda$ and $t = 20\lambda$ seconds (together with the velocity fields obtained for the modes 2 and 3, and, modes 4 and 5). These results are shown in Fig. 5.10.

From Fig. 5.10, it is clear that the relationship between modes 2,3 and modes 4,5 and the top and bottom cylinders prevails along time. In addition, we may conclude that the both reconstructions still have information on both cylinders. The isolated vortices are not completely retrieved, but the association is clear. It is also noticeable that, if the spatial characteristics are preserved, the temporal ones are merged. The intensity of each vortex pattern (represented by the vector lengths) is proportional to the vortices at this position in the decomposed dataset. When the velocity components are decomposed, the intensity of the vectors (vector length) coincides with the local averaged kinetic energy.

Notice that the original data for variables u , v and p , with 23,944 elements along 400 time steps are saved into a matrix with $(3 \times 23,944 \times 400)$ about 28.7 million values that needs to be stored. Due to computational limitations of the MATLAB software in the calculations of the elements applying the POD method (the same happened for the flow around one cylinder), we only considered one fifth of the elements. The data were saved into a matrix of $(3 \times 4789 \times 400)$

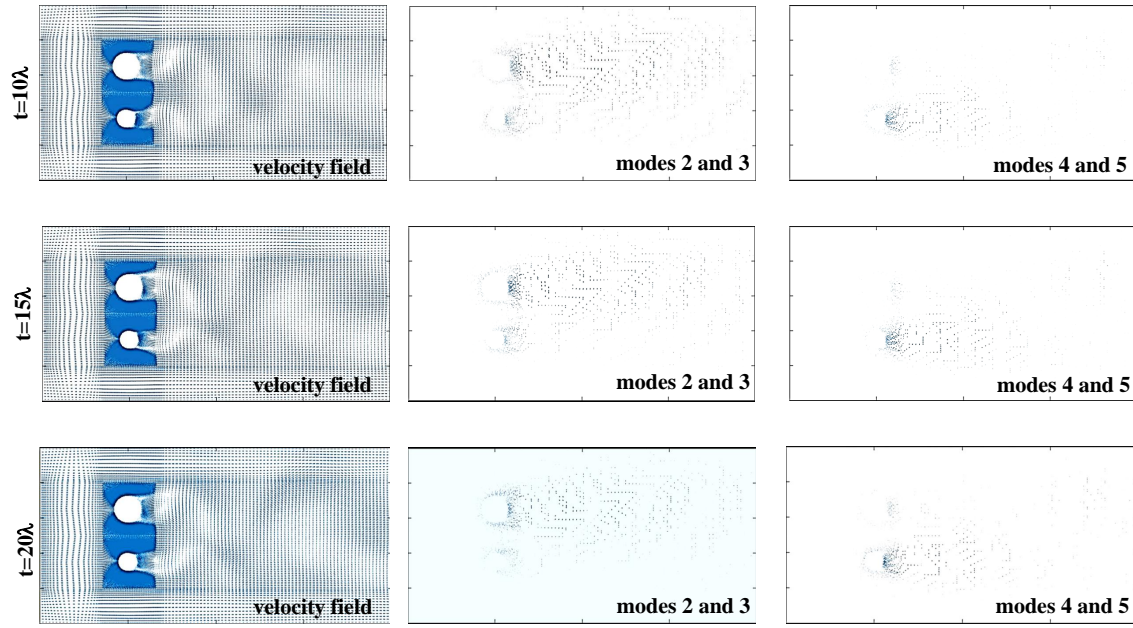


Figure 5.10: Velocity fields obtained for the Newtonian fluid at $t = 10\lambda$, $t = 15\lambda$ and $t = 20\lambda$ seconds (together with the velocity fields obtained for the modes 2 and 3, and, modes 4 and 5).

about 5.7 million entries. The reconstruction made with just five modes only needs $(3 \times 4789 \times 5)$ storage that is 71,835 values. This is a reduction of 98.75% with no significant loss of information, resulting in significant savings.

In Fig. 5.11, an analysis of the frequencies of the modes *time coefficients* is performed. The Strouhal numbers presented in the figure are calculated considering the frequency with higher energy, the diameter of the bottom cylinder, D , and the mean velocity U .

By Eq. (5.8), the Strouhal number for $Re = 100$ is about 0.17 and for $Re = 150$ the Strouhal number is 0.18. We can relate these predicted Strouhal numbers to the ones presented in Fig. 5.11 for the Newtonian fluid. Therefore, analysing the frequencies of modes 2 and 3, we see that $St = 0.155$ and the difference to the predicted Strouhal for the top cylinder (considering the diameter $1.5D$) is about 30%. For modes 4 and 5, we have $St = 0.22$ that, when compared with the value predicted by Eq. (5.8) for the bottom cylinder, shows a deviation of about 30%.

As in the flow around one cylinder, Fig. 5.11 shows that modes greater than one seem to be organized in pairs, revealing the need for the combination of two structures to correctly model the evolution of the flow structures along the domain.

In Fig. 5.11 we also see that for the three fluids the Strouhal numbers are very similar, meaning that the flow characteristics induced by the two cylinders are more important than the rheology of the fluids.

In Tables 5.4 and 5.5 we saw that modes 2 and 3 were associated with the top cylinder. Thus, taking that into account, we can derive some conclusions related to the Strouhal numbers and how do they relate with the other modes represented in Fig. 5.11. Therefore, we see that modes 6 and 7 have a Strouhal number approximately half the Strouhal number of modes 2 and 3, whereas the

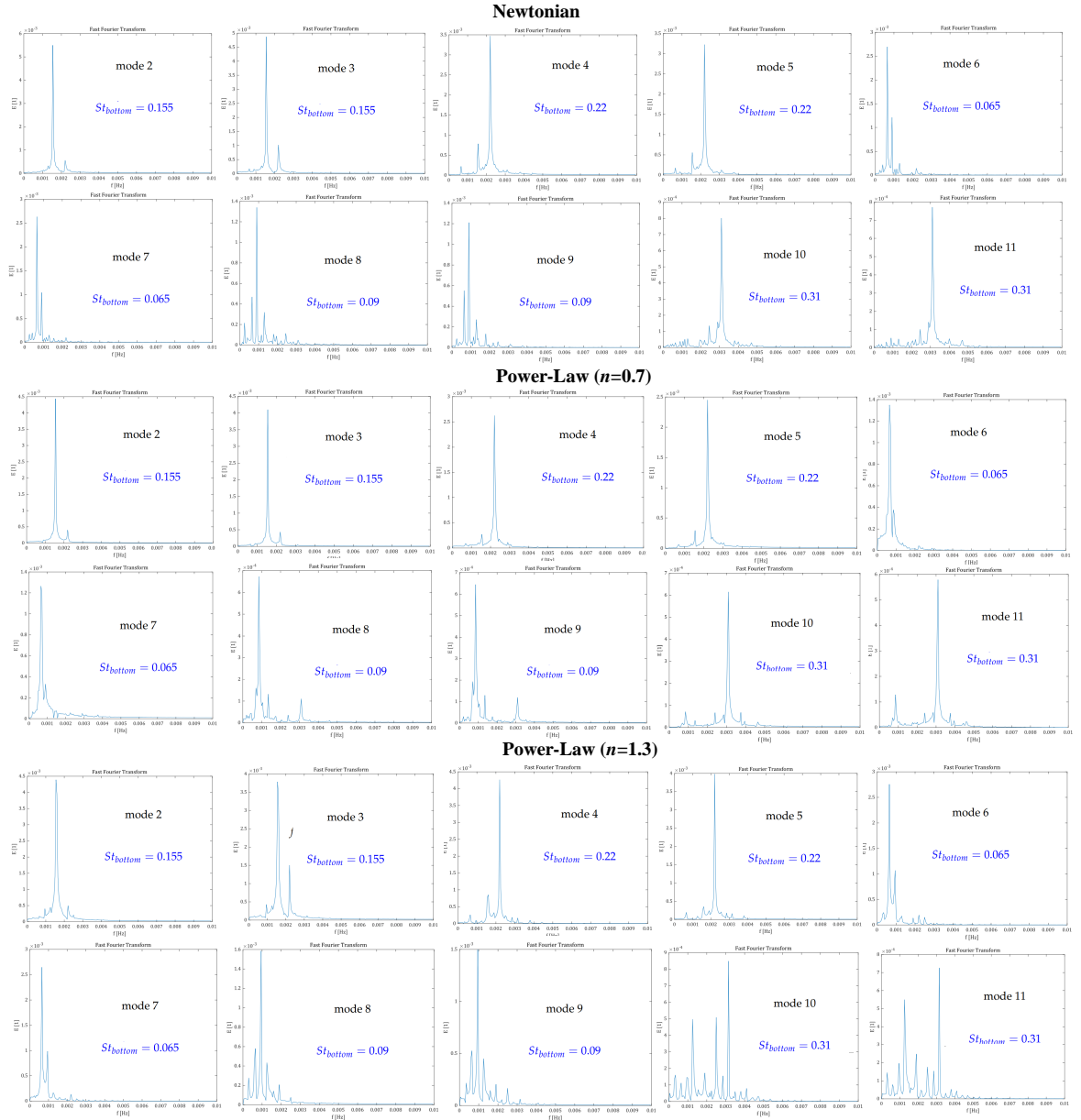


Figure 5.11: Analysis of frequencies of the modes *time coefficients* for a Newtonian fluid (**top**), a non-Newtonian power-law fluid where $n = 0.7$ (**middle**) and a non-Newtonian power-law fluid where $n = 1.3$ (**bottom**).

Strouhal number of modes 10 and 11 is twice the value obtained for modes 2 and 3. Thus, we conclude that modes 6 and 7 and modes 10 and 11 are related to the same flow structures of modes 2 and 3.

In Fig. 5.11, for the case of a Newtonian fluid, we also notice that the Strouhal number calculated for the second most important frequency of modes 2 and 3 is the Strouhal number associated with modes 4 and 5, and vice versa. This means that the flow structure associated with modes 4 and 5 interferes with the flow structures associated with modes 2 and 3, and vice versa. The same happens to modes 6 and 7 and modes 8 and 9. This means that the flow structures

associated with modes 8 and 9 interfere with the flow structure associated with modes 6 and 7, and vice versa.

In Fig. 5.11, for the case of a power-law fluid with $n = 0.7$, we also notice that the Strouhal number calculated for the second most important frequency of modes 2 and 3 is the Strouhal number associated with modes 4 and 5 (the flow structure associated with modes 4 and 5 interferes with the flow structure associated with modes 2 and 3, and vice versa), but this relationship is not observed for the other modes. This is due to the use of a different constitutive model for the viscosity.

Finally, in Fig. 5.11, for the power-law fluid with $n = 1.3$, we see that the Strouhal number calculated for the second most important frequency of modes 2 and 3 is the Strouhal number associated with modes 4 and 5, but not the other way around. However, for modes 6 and 7, the Strouhal number calculated for the second most important frequency is associated with modes 8 and 9, and vice versa. This means that the flow structure associated with modes 8 and 9 interferes with the flow structures associated with modes 6 and 7, and vice versa. This is again due to the use of a different constitutive model for the viscosity.

In this case we cannot establish a relationship between the Strouhal numbers in the same way as in the flow around one cylinder. Although, visually we know that the different modes are related to the upper or lower cylinder, thus allowing us to use POD to detect and predict flow feature with much less information.

Fig. 5.12 (a)–(c) show the pairs of time coefficients of consecutive modes, according to frequencies represented in Fig. 5.11 for the Newtonian fluid, the power-law fluid with $n = 0.7$ and the power-law fluid with $n = 1.3$, respectively.

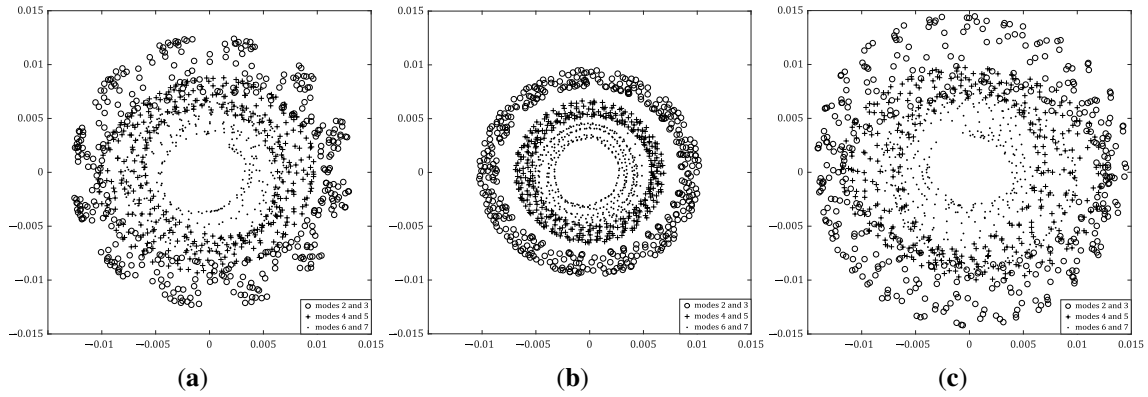


Figure 5.12: Pairs of time coefficients of consecutive modes: (a) Newtonian fluid; (b) power-law fluid with $n = 0.7$; (c) power-law fluid with $n = 1.3$.

The oscillatory and alternating behaviour is observed for modes 2 and 3, modes 4 and 5, and modes 6 and 7.

To compare the weights of the modes taking into account the oscillating behaviour, we considered the reference value (5.19):

$$\sqrt{a_1^2} + \sqrt{a_2^2 + a_3^2} + \sqrt{a_4^2 + a_5^2} + \sqrt{a_6^2 + a_7^2}. \quad (5.19)$$

The modes higher than 7 were not considered due to their small contributions.

For the Newtonian fluid, we see that mode 1, without the oscillatory information, has about 75% of the information in (5.19), whereas modes 2 and 3 have approximately 11.2% of the information in (5.19) (referring to $\sqrt{a_2^2 + a_3^2}$), modes 4 and 5 have approximately 8% of the information in (5.19) (referring to $\sqrt{a_4^2 + a_5^2}$) and modes 6 and 7 have approximately 6% of the information in (5.19) (referring to $\sqrt{a_6^2 + a_7^2}$).

For the non-Newtonian power-law fluid where $n = 0.7$, mode 1, without the oscillatory information, has about 79.5% of the information in (5.19), whereas modes 2 and 3 have approximately 9.7% of the information in (5.19) (referring to $\sqrt{a_2^2 + a_3^2}$), modes 4 and 5 have approximately 6.5% of the information in (5.19) (referring to $\sqrt{a_4^2 + a_5^2}$) and modes 6 and 7 have approximately 4.3% of the information in (5.19) (referring to $\sqrt{a_6^2 + a_7^2}$). When comparing with the Newtonian fluid, we see that the time weights show a smaller decrease, for pairs of modes after mode 1, but an increase for mode 1. Finally, the non-Newtonian power-law fluid where $n = 1.3$, mode 1, without the oscillatory information, has about 72.7% of the information in (5.19), whereas modes 2 and 3 have approximately 12.1% of the information in (5.19) (referring to $\sqrt{a_2^2 + a_3^2}$), modes 4 and 5 have approximately 8.8% of the information in (5.19) (referring to $\sqrt{a_4^2 + a_5^2}$) and modes 6 and 7 have approximately 6.3% of the information in (5.19) (referring to $\sqrt{a_6^2 + a_7^2}$). When comparing with the Newtonian fluid and with the non-Newtonian power-law where $n = 0.7$, we see that the time weights show a smaller decrease on mode 1, but an increase on the pairs of modes after mode 1.

Looking at the results obtained for the Newtonian fluid, the non-Newtonian power-law fluid where $n = 0.7$, and with the non-Newtonian power-law fluid where $n = 1.3$, we conclude that the first modes are the ones that carry most of the information and with only a few modes we also can reconstruct the simulation.

By using two cylinders with different radii, we get different hidden structures in the flow, and using the modes and the frequencies of the modes *time coefficients*, some structures can be related to the influence of one cylinder over the other. This gives us a better understanding of the flow.

For ease of understanding of the results presented above, the interested reader can find Supplementary Material, including the videos obtained for the flow around two cylinders (for both the velocity and pressure variables).

5.1.5 Conclusions

We performed a detailed study on the flow around a single and two distinct cylinders, by decomposing the von Kármán vortex street data into a generator base that was analysed through the Proper Orthogonal Decomposition. We considered a Newtonian fluid, and two power-law fluids with $n = 0.7$ and $n = 1.3$. The behaviour obtained for the Newtonian fluid and the power-law fluid with $n = 1.3$ (case of one cylinder) is similar, for the range shear rates considered. The power-law fluid with $n = 0.7$ shows a more erratic behaviour that could still be captured by the POD method.

We showed that the original POD method can be used to detect and predict flow feature with much less information. A visualization of the influence of each mode on the fluid flow allowed us to infer on the possible reconstruction of the flow features. We also showed the possibility of using the analysis of the frequencies of the temporal coefficients to group modes automatically, or by grouping using visual analysis. By adding an extra cylinder (with a different radius), we obtained different hidden structures in the flow and some of these structures were related to the top cylinder or others related to the bottom cylinder. A detailed analysis of the flow dynamics revealed the complexity of such flow.

This work aims to inspire other researchers to use the original POD method for decomposing complex flows and better identify meaningful flow structures.

Supplementary Materials: For ease of understanding of the results presented above, the interested reader can find as supplementary material, the videos obtained for the flow around two cylinders (for both the velocity and pressure variables). We present the reconstruction of the flow by considering different modes and enhance the visualization of different flow structures. The following are available online at <https://drive.google.com/file/d/1RbQ0mNtr-wKY-rAAg0k-vWKHj7AWB1sc/view?usp=sharing>.

Part IV

Conclusions and outlook

Chapter 6

Conclusions

This work presents new semi-analytical and numerical solutions in canonical flows, considering viscoelastic fluids modelled by the gPTT model. The gPTT viscoelastic model considers the Mittag-Leffler function instead of the classical linear and exponential functions of the trace of the extra-stress tensor and uses two new fitting parameters. With the obtained solutions, the influence of the model parameters on the velocity profile were studied. This new model allows a wider description of the flow behaviour, when compared to more classical descriptions, thus it can be considered in modelling complex viscoelastic flows. The analytical and numerical solutions presented in this work are helpful for validating CFD codes, and also allow a better understanding of the model behaviour in simple shear flows.

In this work, a detailed study was also performed on the flow around two parallel side-by-side cylinders with different radii, by decomposing the von Kármán vortex street data into a generator base that was analysed through the POD method. For that purpose, a Newtonian fluid, and two power-law fluids with $n = 0.7$ and 1.3 were considered. This study showed that the original POD method can be used to detect and predict flow features with much less information. The visualization of the influence of each mode on the fluid flow allowed to infer on the possible reconstruction of the flow and also allowed to use the analysis of the frequencies of the modes' time coefficients to group modes using visual analysis. By adding an extra cylinder with different radii, different complex structures in the flow were obtained and some of these structures were related to the top cylinder while others were related to the bottom cylinder. A detailed analysis of the flow dynamics revealed the complexity of such flow.

The POD method was also applied in a planar flow past a cylinder, but now considering a gPTT fluid under creeping flow conditions, $Re = 0.01$, and two Weissenberg numbers, $Wi = 1.2$ and 1.25 . A flow phenomena similar to a von Kármán vortex street downstream of the cylinder was observed and the POD method was applied to decompose the flow into a generator base. Again, with the POD method, flow features were detected and predicted with much less information and from the visualization of the influence of each mode on the fluid flow, a reconstruction of the flow was performed. With the analysis of the frequencies of the time coefficients, it was again possible to group modes using visual analysis and also by calculating the RMSE between the original dataset and the reconstruction obtained.

Finally, for the flow past a cylinder using the POD analysis made for the flow with $Wi = 1.2$, a prediction of the reconstruction of the flow at $Wi = 1.25$ was obtained and compared with the original simulation at $Wi = 1.25$. The RMSE between the original and the reconstructed normal stresses fields was obtained, and it was below 1, being higher when stresses are at their maximum, as expected. Therefore, the prevision is worst when the fields are close to the maximum value of the oscillations. The performed analysis can be used to better identify meaningful flow structures and also to obtain new data at different conditions with significantly lower cost.

Chapter 7

Outlook

In this work new analytical and semi-analytical solutions for canonical flows modelled by the gPTT viscoelastic model were obtained and the influence of the model parameters on the velocity profile were studied. For strong flows (e.g., extensional flows) a lack of solutions still exists where this model could be applied and its parameters could be studied, a subject that can be explored in the future.

The huge amount of data obtained when performing a numerical simulation is a problem when CFD investigations are carried on. In this thesis the simple POD method was applied to help overcome this problem, by decomposing the flow into a generator base, and use it to detect and predict flow features with much less information. Being the POD method a feature selection method use in machine learning processes, and since in this work it was used to reconstruct the flow with much less information, one thing that can be done in the future is to apply the POD method to several numerical simulations and then use a neural network model for modelling the POD time coefficients and, this way, obtain numerical approaches for multiple flow conditions.

The numerical simulations carried out in this work were on the flow around two parallel side-by-side cylinders with different radii and also on the planar flow past a single cylinder. In the last case, the viscoelastic model used was the gPTT and, for the conditions applied, the presence of vortex shedding, bearing similarities with the von Kármán vortex street downstream of a cylinder for Newtonian fluids at higher Reynolds numbers were found. A deeper analysis of the flow, based on more numerical simulation results, can be done in the future, allowing to better understand the observed phenomena.

Part V

References

References

- [1] R.B. Bird, R.C. Armstrong, and O. Hassager. *Dynamics of Polymeric Liquids, Volume 1: Fluid Mechanics*. Dynamics of Polymeric Liquids. Wiley, 1987. ISBN 9780471802457.
- [2] L.L. Ferrás, M.L. Morgado, M. Rebelo, R.T. Leiva, A. Castelo, G. H. McKinley, and A.M. Afonso. Recent Advances in Complex Fluids Modeling. In Farhad Ali, editor, *Fluid Flow Problems*, chapter 2. IntechOpen, Rijeka, 2019.
- [3] L.L. Ferrás, M.L. Morgado, M. Rebelo, G.H. McKinley, and A.M. Afonso. A generalised Phan-Thien–Tanner model. *Journal of Non-Newtonian Fluid Mechanics*, 269:88–99, jul 2019.
- [4] R. Gorenflo, A.A. Kilbas, F. Mainardi, S.V. Rogosin, et al. *Mittag-Leffler functions, related topics and applications*. Springer, 2020.
- [5] F. Chinesta, A. Ammar, A. Leygue, and R. Keunings. An overview of the proper generalized decomposition with applications in computational rheology. *Journal of Non-Newtonian Fluid Mechanics*, 166(11):578–592, 2011.
- [6] A. Ammar, B. Mokdad, F. Chinesta, and R. Keunings. A new family of solvers for some classes of multidimensional partial differential equations encountered in kinetic theory modeling of complex fluids. *Journal of Non-Newtonian Fluid Mechanics*, 139(3):153–176, 2006.
- [7] A. Ammar, B. Mokdad, F. Chinesta, and R. Keunings. A new family of solvers for some classes of multidimensional partial differential equations encountered in kinetic theory modelling of complex fluids: Part II: Transient simulation using space-time separated representations. *Journal of Non-Newtonian Fluid Mechanics*, 144(2-3):98–121, 2007.
- [8] W.H.A. Schilders, H.A. Van der Vorst, and J. Rommes. *Model order reduction: theory, research aspects and applications*, volume 13. Springer, 2008.
- [9] J.L. Lumley. The structure of inhomogeneous turbulent flows. *Atmospheric Turbulence and Radio Wave Propagation*, pages 166–178, 1967.
- [10] A.M. Afonso. *Further developments on theoretical and computational rheology*. PhD thesis, Faculdade de Engenharia da Universidade do Porto, 2010.

- [11] L.L. Ferrás. *Theoretical and numerical studies of slip flows*. PhD thesis, Universidade do Minho, Escola de Engenharia, 2012.
- [12] F.A. Morrison. *Understanding rheology*, volume 1. Oxford University Press, New York, 2001.
- [13] F.A. Cruz. *Computational analysis of purely-elastic flow instabilities and transition to elastic turbulence in microscale flows of viscoelastic fluids*. PhD thesis, Faculdade de Engenharia da Universidade do Porto, 2018.
- [14] E.C. Bingham. *An investigation of the laws of plastic flow*. Number 278. US Government Printing Office, 1917.
- [15] I. Newton. *Philosophiae naturalis principia mathematica*. Benjamin Motte, London, 1687.
- [16] J.C. Maxwell. IV. On the dynamical theory of gases. *Philosophical Transactions of the Royal Society of London*, (157):49–88, 1867.
- [17] R.J. Poole. The Deborah and Weissenberg numbers. In *The British Society of Rheology, Rheology Bulletin*, volume 53, pages 32–39, 2012.
- [18] J.G. Oldroyd. On the formulation of rheological equations of state. *Proceedings of the Royal Society of London. Series A. Mathematical and Physical Sciences*, 200(1063):523–541, 1950.
- [19] D.O.A. Cruz and F.T. Pinho. Skewed Poiseuille-Couette flows of sPTT fluids in concentric annuli and channels. *Journal of Non-Newtonian Fluid Mechanics*, 121(1):1–14, 2004.
- [20] H. Giesekus. A simple constitutive equation for polymer fluids based on the concept of deformation-dependent tensorial mobility. *Journal of Non-Newtonian Fluid Mechanics*, 11(1-2):69–109, 1982.
- [21] N. Phan-Thien and R.I. Tanner. A new constitutive equation derived from network theory. *Journal of Non-Newtonian Fluid Mechanics*, 2(4):353–365, jul 1977.
- [22] N. Phan-Thien. A nonlinear network viscoelastic model. *Journal of Rheology*, 22(3): 259–283, jun 1978.
- [23] L.L. Ferrás, A.M. Afonso, M.A. Alves, J.M. Nóbrega, and F.T. Pinho. Annular flow of viscoelastic fluids: Analytical and numerical solutions. *Journal of Non-Newtonian Fluid Mechanics*, 212:80–91, oct 2014.
- [24] I. Podlubny. *Fractional Differential Equations: An Introduction to Fractional Derivatives, Fractional Differential Equations, to Methods of Their Solution and Some of Their Applications*. ISSN. Elsevier Science, 1998. ISBN 9780080531984.

- [25] H.M. Laun. Description of the non-linear shear behaviour of a low density polyethylene melt by means of an experimentally determined strain dependent memory function. *Rheologica Acta*, 17(1):1–15, 1978.
- [26] W.R. Schowalter. The behavior of complex fluids at solid boundaries. *Journal of Non-Newtonian Fluid Mechanics*, 29:25–36, 1988.
- [27] C.L.M.H. Navier. Mémoire sur les lois du mouvement des fluides—presented in (1822). *Mémoires l'Acad Royale des Sciences de l'Institut de France*, 2:375–393, 1827.
- [28] A.M. Ribau, L.L. Ferrás, M.L. Morgado, M. Rebelo, and A.M. Afonso. Semi-Analytical Solutions for the Poiseuille-Couette Flow of a Generalised Phan-Thien–Tanner Fluid. *Fluids*, 4(3):129, jul 2019.
- [29] A.M. Ribau, L.L. Ferrás, M.L. Morgado, M. Rebelo, and A.M. Afonso. Analytical and numerical studies for slip flows of a generalised Phan-Thien–Tanner fluid. *ZAMM - Journal of Applied Mathematics and Mechanics / Zeitschrift für Angewandte Mathematik und Mechanik*, 100(3), jan 2020.
- [30] F.T. Pinho and P.J. Oliveira. Axial annular flow of a nonlinear viscoelastic fluid - an analytical solution. *Journal of Non-Newtonian Fluid Mechanics*, 93(2-3):325–337, 2000.
- [31] M.P. Escudier, P.J. Oliveira, and F.T. Pinho. Fully developed laminar flow of purely viscous non-Newtonian liquids through annuli, including the effects of eccentricity and inner-cylinder rotation. *International Journal of Heat and Fluid Flow*, 23(1):52–73, 2002.
- [32] M.P. Escudier, P.J. Oliveira, F.T. Pinho, and S. Smith. Fully developed laminar flow of non-Newtonian liquids through annuli: comparison of numerical calculations with experiments. *Experiments in Fluids*, 33:101–111, 2002.
- [33] R.K. Bhatnagar. Steady laminar flow of visco-elastic fluid through a pipe and through an annulus with suction or injection at the walls. *Journal of the Indian Institute of Science*, 45(4):127, 1963.
- [34] M. Mostafaiyan, K. Khodabandehlou, and F. Sharif. Analysis of a viscoelastic fluid in an annulus using Giesekus model. *Journal of Non-Newtonian Fluid Mechanics*, 118(1):49–55, 2004.
- [35] M. Mirzazadeh, M.P. Escudier, F. Rashidi, and S.H. Hashemabadi. Purely tangential flow of a PTT-viscoelastic fluid within a concentric annulus. *Journal of Non-Newtonian Fluid Mechanics*, 129(2):88–97, 2005.
- [36] M.T. Ravanchi, M. Mirzazadeh, and F. Rashidi. Flow of Giesekus viscoelastic fluid in a concentric annulus with inner cylinder rotation. *International Journal of Heat and Fluid Flow*, 28(4):838–845, 2007.

- [37] M.M. Mohseni and F. Rashidi. Analysis of axial annular flow for viscoelastic fluid with temperature dependent properties. *International Journal of Thermal Sciences*, 120:162–174, 2017.
- [38] L.L. Ferrás, A.M. Afonso, M.A. Alves, J.M. Nóbrega, and F.T. Pinho. Analytical and numerical study of the electro-osmotic annular flow of viscoelastic fluids. *Journal of Colloid and Interface Science*, 420:152–157, 2014.
- [39] R.B. Bird, W.E. Stewart, and E.N. Lightfoot. Transport phenomena. *John Wiley Sons, Inc.*, 1960.
- [40] A.M. Ribau, L.L. Ferrás, M.L. Morgado, M. Rebelo, F.T. Pinho, and A.M. Afonso. Analytical study of the annular flow of a generalised Phan-Thien–Tanner fluid. *Acta Mechanica*, pages 1–11, 2023.
- [41] H. Bruus. *Theoretical microfluidics*, volume 18. Oxford University Press, 2007.
- [42] D. Burgreen and F.R. Nakache. Electrokinetic flow in ultrafine capillary slits. *The Journal of Physical Chemistry*, 68(5):1084–1091, 1964.
- [43] C.L. Rice and R. Whitehead. Electrokinetic flow in a narrow cylindrical capillary. *The Journal of Physical Chemistry*, 69(11):4017–4024, 1965.
- [44] S. Arulanandam and D. Li. Liquid transport in rectangular microchannels by electroosmotic pumping. *Colloids and Surfaces A: Physicochemical and Engineering Aspects*, 161(1): 89–102, 2000.
- [45] P. Dutta and A. Beskok. Analytical solution of combined electroosmotic/pressure driven flows in two-dimensional straight channels: finite Debye layer effects. *Analytical Chemistry*, 73(9):1979–1986, 2001.
- [46] S. Das and S. Chakraborty. Analytical solutions for velocity, temperature and concentration distribution in electroosmotic microchannel flows of a non-Newtonian bio-fluid. *Analytica Chimica Acta*, 559(1):15–24, 2006.
- [47] C.L.A. Berli and M. Olivares. Electrokinetic flow of non-Newtonian fluids in microchannels. *Journal of Colloid and Interface Science*, 320(2):582–589, 2008.
- [48] C. Zhao and C. Yang. An exact solution for electroosmosis of non-Newtonian fluids in microchannels. *Journal of Non-Newtonian Fluid Mechanics*, 166(17-18):1076–1079, 2011.
- [49] C. Zhao and C. Yang. Electro-osmotic mobility of non-Newtonian fluids. *Biomicrofluidics*, 5(1):014110, 2011.
- [50] C. Zhao and C. Yang. Electrokinetics of non-Newtonian fluids: a review. *Advances in Colloid and Interface Science*, 201:94–108, 2013.

- [51] A.M. Afonso, M.A. Alves, and F.T. Pinho. Analytical solution of mixed electro-osmotic/pressure driven flows of viscoelastic fluids in microchannels. *Journal of Non-Newtonian Fluid Mechanics*, 159(1-3):50–63, 2009.
- [52] L.L. Ferrás, A.M. Afonso, M.A. Alves, J.M. Nóbrega, and F.T. Pinho. Electro-osmotic and pressure-driven flow of viscoelastic fluids in microchannels: Analytical and semi-analytical solutions. *Physics of Fluids*, 28(9):093102, 2016.
- [53] S. Das and S. Chakraborty. Transverse electrodes for improved DNA hybridization in microchannels. *AIChE Journal*, 53(5):1086–1099, 2007.
- [54] P. Goswami, J. Chakraborty, A. Bandopadhyay, and S. Chakraborty. Electrokinetically modulated peristaltic transport of power-law fluids. *Microvascular Research*, 103:41–54, 2016.
- [55] R. Sarma, N. Deka, K. Sarma, and P. K. Mondal. Electroosmotic flow of Phan-Thien–Tanner fluids at high zeta potentials: An exact analytical solution. *Physics of Fluids*, 30(6), 2018.
- [56] A.M. Ribau, L.L. Ferrás, M.L. Morgado, M. Rebelo, M.A. Alves, F.T. Pinho, and A.M. Afonso. A study on mixed electro-osmotic/pressure-driven microchannel flows of a generalised Phan-Thien–Tanner fluid. *Journal of Engineering Mathematics*, 127(1), mar 2021.
- [57] K. N. Vasista, S. K. Mehta, S. Pati, and S. Sarkar. Electroosmotic flow of viscoelastic fluid through a microchannel with slip-dependent zeta potential. *Physics of Fluids*, 33(12), 2021.
- [58] A.M. Afonso, M.A. Alves, and F.T. Pinho. Electro-osmotic flow of viscoelastic fluids in microchannels under asymmetric zeta potentials. *Journal of Engineering Mathematics*, 71: 15–30, 2011.
- [59] J. Escandón, E. Jiménez, C. Hernández, O. Bautista, and F. Méndez. Transient electroosmotic flow of Maxwell fluids in a slit microchannel with asymmetric zeta potentials. *European Journal of Mechanics-B/Fluids*, 53:180–189, 2015.
- [60] S.H. Sadek and F.T. Pinho. Electro-osmotic oscillatory flow of viscoelastic fluids in a microchannel. *Journal of Non-Newtonian Fluid Mechanics*, 266:46–58, 2019.
- [61] G. Sánchez, F. Méndez, and E.A. Ramos. Electrokinetic cells powered by osmotic gradients: an analytic survey of asymmetric wall potentials and hydrophobic surfaces. *Journal of Physics D: Applied Physics*, 56(35):355501, 2023.
- [62] C. Teodoro, O. Bautista, F. Méndez, and J. Arcos. Mixed electroosmotic/pressure-driven flow for a generalized Phan–Thien–Tanner fluid in a microchannel with nonlinear Navier slip at the wall. *European Journal of Mechanics-B/Fluids*, 97:70–77, 2023.
- [63] A. Hernández, A. Mora, J.C. Arcos, and O. Bautista. Joule heating and Soret effects on an electro-osmotic viscoelastic fluid flow considering the generalized Phan-Thien–Tanner model. *Physics of Fluids*, 35(4), 2023.

- [64] A. Hernández, J. Arcos, J. Martínez-Trinidad, O. Bautista, S. Sánchez, and F. Méndez. Thermodiffusive effect on the local Debye-length in an electroosmotic flow of a viscoelastic fluid in a slit microchannel. *International Journal of Heat and Mass Transfer*, 187:122522, 2022.
- [65] S. Dhinakaran, A.M. Afonso, M.A. Alves, and F.T. Pinho. Steady viscoelastic fluid flow between parallel plates under electro-osmotic forces: Phan-Thien–Tanner model. *Journal of Colloid and Interface Science*, 344(2):513–520, 2010.
- [66] A.M. Ribau, L.L. Ferrás, M.L. Morgado, M. Rebelo, F.T. Pinho, and A.M. Afonso. The effect of asymmetric zeta potentials on the electro-osmotic flow of a viscoelastic fluid. *Under preparation*.
- [67] P. Holmes, J.L. Lumley, G. Berkooz, and C.W. Rowley. *Turbulence, coherent structures, dynamical systems and symmetry*. Cambridge University Press, 2012.
- [68] G. Berkooz, P. Holmes, and J.L. Lumley. The proper orthogonal decomposition in the analysis of turbulent flows. *Annual Review of Fluid Mechanics*, 25(1):539–575, 1993.
- [69] N. Aubry. On the hidden beauty of the proper orthogonal decomposition. *Theoretical and Computational Fluid Dynamics*, 2(5-6):339–352, 1991.
- [70] S. Aradag, S. Siegel, J. Seidel, K. Cohen, and T. McLaughlin. Filtered POD-based low-dimensional modeling of the 3D turbulent flow behind a circular cylinder. *International Journal for Numerical Methods in Fluids*, 66(1):1–16, 2011.
- [71] X. Ma and G. Karniadakis. A low-dimensional model for simulating three-dimensional cylinder flow. *Journal of Fluid Mechanics*, 458:181–190, 2002.
- [72] A. Towne, O. Schmidt, and T. Colonius. Spectral proper orthogonal decomposition and its relationship to dynamic mode decomposition and resolvent analysis. *Journal of Fluid Mechanics*, 847:821–867, 2018.
- [73] M.A. Mendez, M.T. Scelzo, and J.M. Buchlin. Multiscale modal analysis of an oscillating impinging gas jet. *Experimental Thermal and Fluid Science*, 91:256–276, 2018.
- [74] M.A. Mendez, M. Balabane, and J.M. Buchlin. Multi-scale proper orthogonal decomposition of complex fluid flows. *Journal of Fluid Mechanics*, 870:988–1036, 2019.
- [75] M.A. Mendez, D. Hess, B.B. Watz, and J.M. Buchlin. Multiscale proper orthogonal decomposition (mPOD) of TR-PIV data—a case study on stationary and transient cylinder wake flows. *Measurement Science and Technology*, 31(9):094014, 2020.
- [76] V. Kotu and B. Deshpande. *Predictive analytics and data mining: concepts and practice with rapidminer*. Morgan Kaufmann, 2014.

- [77] S. Arntzen. Prediction of flow-fields by combining high-fidelity CFD data and machine learning algorithms. Master's thesis, Delft University of Technology, 2019.
- [78] S. Hijazi, M. Freitag, and N. Landwehr. POD-Galerkin reduced order models and physics-informed neural networks for solving inverse problems for the Navier–Stokes equations. *Advanced Modeling and Simulation in Engineering Sciences*, 10(1):1–38, 2023.
- [79] P. Wu, F. Qiu, W. Feng, F. Fang, and C. Pain. A non-intrusive reduced order model with transformer neural network and its application. *Physics of Fluids*, 34(11):115130, 2022.
- [80] L. Sirovich. Turbulence and the dynamics of coherent structures. III. Dynamics and scaling. *Quarterly of Applied Mathematics*, 45(3):583–590, 1987.
- [81] M. Schäfer, S. Turek, F. Durst, E. Krause, and R. Rannacher. *Benchmark computations of laminar flow around a cylinder* In Flow simulation with high-performance computers II. Springer, 1996.
- [82] M. Bergmann, L. Cordier, and J.P. Brancher. Optimal rotary control of the cylinder wake using proper orthogonal decomposition reduced-order model. *Physics of Fluids*, 17(9):097101, 2005.
- [83] H. Ping, H. Zhu, K. Zhang, R. Wang, D. Zhou, Y. Bao, and Z. Han. Wake dynamics behind a rotary oscillating cylinder analyzed with proper orthogonal decomposition. *Ocean Engineering*, 218:108185, 2020.
- [84] G. Riches, R. Martinuzzi, and C. Morton. Proper orthogonal decomposition analysis of a circular cylinder undergoing vortex-induced vibrations. *Physics of Fluids*, 30(10):105103, 2018.
- [85] M. Sakai, Y. Sunada, T. Imamura, and K. Rinoie. Experimental and Numerical Flow Analysis Around Circular Cylinders Using POD and DMD. In *44th AIAA Fluid Dynamics Conference*, page 3325, 2014.
- [86] W. Zhang, C. Chen, and D.J. Sun. Numerical simulation of flow around two side-by-side circular cylinders at low Reynolds numbers by a POD-Galerkin spectral method. *J. Hydrodyn. Ser. A*, 24(1):82–88, 2009.
- [87] S. Singha, K.K. Nagarajan, and K.P. Sinhamahapatra. Numerical study of two-dimensional flow around two side-by-side circular cylinders at low Reynolds numbers. *Physics of Fluids*, 28(5):053603, 2016.
- [88] R. Vitkovicova, Y. Yokoi, and T. Hyhlik. Identification of structures and mechanisms in a flow field by POD analysis for input data obtained from visualization and PIV. *Experiments in Fluids*, 61:1–21, 2020.

- [89] F. Delplace and J.C. Leuliet. Generalized Reynolds number for the flow of power law fluids in cylindrical ducts of arbitrary cross-section. *The Chemical Engineering Journal and the Biochemical Engineering Journal*, 56(2):33–37, 1995. ISSN 0923-0467.
- [90] S. Dhinakaran, M.S.N. Oliveira, F.T. Pinho, and M.A. Alves. Steady flow of power-law fluids in a 1:3 planar sudden expansion. *Journal of Non-Newtonian Fluid Mechanics*, 198: 48–58, aug 2013.
- [91] A. Roshko. *On the development of turbulent wakes from vortex streets*. PhD thesis, California Institute of Technology, 1952.
- [92] A.M. Ribau, N.D. Gonçalves, L.L. Ferrás, and A.M. Afonso. Flow Structures Identification through Proper Orthogonal Decomposition: The Flow around Two Distinct Cylinders. *Fluids*, 6(11):384, 2021.
- [93] D.G. Baird and M. Renardy. Report on the VIIth international workshop on numerical methods in non-Newtonian flow. *Journal of Non-Newtonian Fluid Mechanics*, 43(2-3):386, 1992.
- [94] M.A. Alves, P.J. Oliveira, and F.T. Pinho. Numerical methods for viscoelastic fluid flows. *Annual Review of Fluid Mechanics*, 53:509–541, 2021.
- [95] S. Peng, T. Tang, J. Li, M. Zhang, and P. Yu. Numerical study of viscoelastic upstream instability. *Journal of Fluid Mechanics*, 959:A16, 2023.
- [96] S. Varchanis, C.C. Hopkins, A.Q. Shen, J. Tsamopoulos, and S.J. Haward. Asymmetric flows of complex fluids past confined cylinders: A comprehensive numerical study with experimental validation. *Physics of Fluids*, 32(5):053103, 2020.
- [97] F. Pimenta and M.A. Alves. Stabilization of an open-source finite-volume solver for viscoelastic fluid flows. *Journal of Non-Newtonian Fluid Mechanics*, 239:85–104, 2017.
- [98] F. Pimenta and M.A. Alves. Numerical simulation of electrically-driven flows using Open-FOAM. *arXiv preprint arXiv:1802.02843*, 2018.
- [99] F. Pimenta and M.A. Alves. Conjugate heat transfer in the unbounded flow of a viscoelastic fluid past a sphere. *International Journal of Heat and Fluid Flow*, 89:108784, 2021.
- [100] F. Pimenta and M.A. Alves. RheoTool. <https://github.com/fppimenta/rheoTool>, 2016.
- [101] M.A. Alves, F.T. Pinho, and P.J. Oliveira. The flow of viscoelastic fluids past a cylinder: finite-volume high-resolution methods. *Journal of Non-Newtonian Fluid Mechanics*, 97 (2-3):207–232, 2001.
- [102] A.M. Alexandre, P.J. Oliveira, F.T. Pinho, and M.A. Alves. The log-conformation tensor approach in the finite-volume method framework. *Journal of Non-Newtonian Fluid Mechanics*, 157(1-2):55–65, 2009.

- [103] P.J. Oliveira and F.T. Pinho. Analytical solution for fully developed channel and pipe flow of Phan-Thien–Tanner fluids. *Journal of Fluid Mechanics*, 387:271–280, 1999.
- [104] R. Keunings. Finite element methods for integral viscoelastic fluids. *Rheology Reviews*, pages 167–195, 2003.
- [105] P.K. Mondal, U. Ghosh, A. Bandopadhyay, D. DasGupta, and S. Chakraborty. Pulsating electric field modulated contact line dynamics of immiscible binary systems in narrow confinements under an electrical double layer phenomenon. *Soft Matter*, 10(42):8512–8523, 2014.
- [106] S. Mukherjee, S.S. Das, J. Dhar, S. Chakraborty, and S. DasGupta. Electroosmosis of viscoelastic fluids: Role of wall depletion layer. *Langmuir*, 33(43):12046–12055, 2017.
- [107] S. Mukherjee, P. Goswami, J. Dhar, S. Dasgupta, and S. Chakraborty. Ion-size dependent electroosmosis of viscoelastic fluids in microfluidic channels with interfacial slip. *Physics of Fluids*, 29(7):072002, 2017.
- [108] A. Bandopadhyay and S. Chakraborty. Electrokinetically induced alterations in dynamic response of viscoelastic fluids in narrow confinements. *Physical Review E*, 85(5):056302, 2012.
- [109] I. Borukhov, D. Andelman, and H. Orland. Steric effects in electrolytes: A modified Poisson-Boltzmann equation. *Physical Review Letters*, 79(3):435, 1997.
- [110] M.Z. Bazant, K. Thornton, and A. Ajdari. Diffuse-charge dynamics in electrochemical systems. *Physical Review E*, 70(2):021506, 2004.
- [111] A.M. Afonso, M.A. Alves, and F.T. Pinho. Analytical solution of two-fluid electro-osmotic flows of viscoelastic fluids. *Journal of Colloid and Interface Science*, 395:277–286, 2013.
- [112] M. Balajewicz. *A New Approach to Model Order Reduction of the Navier-Stokes Equations*. PhD thesis, Duke University, 2012.
- [113] A. Liné. Eigenvalue spectrum versus energy density spectrum in a mixing tank. *Chemical Engineering Research and Design*, 108:13–22, 2016.
- [114] A. Liné, J.C. Gabelle, J. Morchain, D. Anne-Archard, and F. Augier. On POD analysis of PIV measurements applied to mixing in a stirred vessel with a shear thinning fluid. *Chemical Engineering Research and Design*, 91(11):2073–2083, 2013.
- [115] P. Torres, N.D. Goncalves, C.P. Fonte, M.M. Dias, J.C.B. Lopes, A. Liné, and R.J. Santos. Proper Orthogonal Decomposition and Statistical Analysis of 2D Confined Impinging Jets Chaotic Flow. *Chemical Engineering & Technology*, 42(8):1709–1716, 2019.